



HAL
open science

Study of new porous materials for silicon microfabricated column development in gas chromatography

David Lefebvre

► **To cite this version:**

David Lefebvre. Study of new porous materials for silicon microfabricated column development in gas chromatography. Other. Université Claude Bernard - Lyon I, 2014. English. NNT : 2014LYO10314 . tel-01867825

HAL Id: tel-01867825

<https://theses.hal.science/tel-01867825>

Submitted on 4 Sep 2018

HAL is a multi-disciplinary open access archive for the deposit and dissemination of scientific research documents, whether they are published or not. The documents may come from teaching and research institutions in France or abroad, or from public or private research centers.

L'archive ouverte pluridisciplinaire **HAL**, est destinée au dépôt et à la diffusion de documents scientifiques de niveau recherche, publiés ou non, émanant des établissements d'enseignement et de recherche français ou étrangers, des laboratoires publics ou privés.

THESE DE L'UNIVERSITE DE LYON

Délivrée par

L'UNIVERSITE CLAUDE BERNARD LYON 1

Ecole Doctorale de Chimie de Lyon (ED 206)

DIPLOME DE DOCTORAT

(arrêté du 7 août 2006)

Spécialité : Chimie

soutenue publiquement le 15 décembre 2014

par

Monsieur David LEFEBVRE

TITRE :

Etude de nouveaux matériaux poreux pour le
développement de micro-colonnes en silicium pour la
chromatographie en phase gazeuse

Directrice de thèse : Madame Chloé THIEULEUX

Co-directrice de thèse : Madame Florence RICOUL

JURY :

Madame	Bernadette CHARLEUX
Monsieur	Oliver TRAPP
Monsieur	Christophe PIJOLAT
Monsieur	Vincent DUGAS
Madame	Florence RICOUL
Madame	Chloé THIEULEUX
Monsieur	Pierre PUGET

THESE DE L'UNIVERSITE DE LYON

Délivrée par

L'UNIVERSITE CLAUDE BERNARD LYON 1

Ecole Doctorale de Chimie de Lyon (ED 206)

DIPLOME DE DOCTORAT

(arrêté du 7 août 2006)

Spécialité : Chimie

soutenue publiquement le 15 décembre 2014

par

Monsieur David LEFEBVRE

TITRE :

Study of new porous materials for silicon micro-fabricated column development in gas chromatography

Directrice de thèse : Madame Chloé THIEULEUX

Co-directrice de thèse : Madame Florence RICOUL

JURY :

Madame	Bernadette CHARLEUX
Monsieur	Oliver TRAPP
Monsieur	Christophe PIJOLAT
Monsieur	Vincent DUGAS
Madame	Florence RICOUL
Madame	Chloé THIEULEUX
Monsieur	Pierre PUGET

Remerciements

Ce manuscrit conclut trois années de thèse effectuées au CEA-LETI au « Laboratoire de Chimie des Matériaux et des Interfaces » du SBSC. Je tiens tout d'abord à remercier Françoise VINET, et Gilles MARCHAND, pour la chance qu'ils m'ont accordée en m'accueillant au sein du laboratoire. Je remercie aussi Pierre PUGET, qui a su susciter chez moi l'intérêt pour les microanalyseurs de gaz et avec qui j'ai pu discuter tout au long de ces trois ans jusqu'au jour de ma soutenance pour laquelle il a accepté de faire partie du jury.

Bien sûr, je remercie aussi du fond du cœur Florence RICOUL pour avoir encadré mes travaux au jour le jour. Elle a toujours été disponible en cas de difficulté et elle a su m'aider tout en me laissant l'autonomie dont j'avais besoin pour faire progresser ce travail.

Mes remerciements vont aussi particulièrement à ma directrice de thèse Chloé THIEULEUX pour son accompagnement et la pertinence de ses remarques scientifiques. J'ai pris beaucoup de plaisir à travailler avec elle malgré l'éloignement géographique de son laboratoire.

Je remercie également Bernadette CHARLEUX, avec qui nous avons pu redéfinir la bonne orientation de ces travaux. Ses conseils ont été d'une grande aide et sa présence dans le jury m'a fait honneur.

Je tiens à remercier spécialement Oliver TRAPP (de l'université de Heidelberg) et Christophe PIJOLAT (de l'école nationale des Mines de Saint Etienne) pour m'avoir fait l'honneur d'accepter d'être les rapporteurs de ce manuscrit.

Je remercie également Vincent DUGAS (Université Lyon I) d'avoir accepté de présider ce jury.

Merci à Mireille MARET, sans qui les manip SAXS à l'ESRF n'auraient pas été possibles. Merci aussi à Vincent JOUSSEAUME qui nous a lui aussi accompagné dans cette aventure du week end de Pâques. Merci à Dominique LAFOND qui m'a formé pour l'imagerie MEB. Merci à Laurent VEYRE pour son aide précieuse durant mes séjours au LCOMS, et pour les mesures de DRX. Merci à Séverine VIGNOUD et Marjorie VRIGNAUD pour l'aide qu'elles ont pu

m'apporter sur les dernières mesures d'Adsorption/Désorption durant la rédaction. Merci à Thomas BORDY pour la gestion de la salle gaz et tous ses petits bricolages très efficaces, et à l'équipe APIX : Régis BARATTIN, Mélanie PETITJEAN et Vincent GOUTTENOIRE pour m'avoir accueilli dans le monde de la GC. Et enfin, merci aux nombreux techniciens de la Salle Blanche, Guillaume COSTA pour les mesures au Zetamètre et qui sait où tout se trouve en salle, Caroline FONTELAYE pour sa bonne humeur et pour sa tolérance à FIP radio, mais aussi Nadine DAVID, Amélie BELLEMIN-COMTE, Manu ALESSIO et Martine COCHET pour la techno.

Mes remerciements s'adressent également à toutes les personnes qui sont passées par la pièce 201, avec qui nous avons eu de nombreuses conversations enrichissantes sur divers projets, mais surtout avec qui j'ai eu le bonheur de partager tant de café, gâteaux, thés, tisanes et éclat de rires : Caro, Séverine, Guillaume (les 3, même si le dernier n'était pas vraiment de la 201), Hélène, Marjo, Jordi, Régis, Mélanie, Claire, Sandra, Louise, Julien (les 2), Arnaud, Murielle, Pascal, Antoine, Frédérique, Anne-Claude, Florence, Pierre...

Et bien sûr, ils s'adressent aussi aux Post-Doc et Thésard du service (et plus), adeptes ou non des jeudis au O'Callaghan, avec qui il était si facile de se serrer les coudes dans les moments moins faciles : Prisca, Emilie, Fabien, John, Frédéric, Allan, PH, Mathilde, Jess, Arnaud, Julie, Lisa, en plus de ceux déjà cités ci-dessus.

Enfin, je tiens bien évidemment à remercier ma famille : mes parents, grand parents, parrain et marraine, mais aussi mon frère et mes deux sœurs qui n'ont jamais vraiment compris les détails de mon travail mais qui ont toujours réussi à trouver les bons mots pour m'encourager. Je reste aussi admiratif de Laetitia, qui a réussi à me supporter tout au long de ces trois années et pour bien d'autres à venir.

Ces remerciements ne seraient pas complets non plus sans citer mes collocs François, puis Tim et Charlotte, les nombreux amis dont les noms ne pourraient rentrer dans ces 2 petites pages, FIP radio pour la musique, la slackline et le yoga pour la détente, et la bibliothèque de l'ALAS pour ses choix très pertinents de BD pour la lecture.

Enfin, un grand merci à tous ceux que j'ai oublié ici et dont l'aide n'a pas été moins importante pour moi au cours de ces 3 ans, et qui, j'espère, me le pardonneront.

UNIVERSITE CLAUDE BERNARD - LYON 1

Président de l'Université

M. François-Noël GILLY

Vice-président du Conseil d'Administration

M. le Professeur Hamda BEN HADID

Vice-président du Conseil des Etudes et de la Vie
Universitaire

M. le Professeur Philippe LALLE

Vice-président du Conseil Scientifique

M. le Professeur Germain GILLET

Directeur Général des Services

M. Alain HELLEU

COMPOSANTES SANTE

Faculté de Médecine Lyon Est – Claude Bernard

Directeur : M. le Professeur J. ETIENNE

Faculté de Médecine et de Maïeutique Lyon Sud –
Charles Mérieux

Directeur : Mme la Professeure C. BURILLON

Faculté d'Odontologie

Directeur : M. le Professeur D. BOURGEOIS

Institut des Sciences Pharmaceutiques et
Biologiques

Directeur : Mme la Professeure C. VINCIGUERRA

Institut des Sciences et Techniques de la
Réadaptation

Directeur : M. le Professeur Y. MATILLON

Département de formation et Centre de Recherche
en Biologie Humaine

Directeur : Mme. la Professeure A-M. SCHOTT

COMPOSANTES ET DEPARTEMENTS DE SCIENCES ET TECHNOLOGIE

Faculté des Sciences et Technologies

Directeur : M. F. DE MARCHI

Département Biologie

Directeur : M. le Professeur F. FLEURY

Département Chimie Biochimie

Directeur : Mme Caroline FELIX

Département GEP

Directeur : M. Hassan HAMMOURI

Département Informatique

Directeur : M. le Professeur S. AKKOUCHE

Département Mathématiques

Directeur : M. le Professeur Georges TOMANOV

Département Mécanique

Directeur : M. le Professeur H. BEN HADID

Département Physique

Directeur : M. Jean-Claude PLENET

UFR Sciences et Techniques des Activités Physiques
et Sportives

Directeur : M. Y.VANPOULLE

Observatoire des Sciences de l'Univers de Lyon

Directeur : M. B. GUIDERDONI

Polytech Lyon

Directeur : M. P. FOURNIER

Ecole Supérieure de Chimie Physique Electronique

Directeur : M. G. PIGNAULT

Institut Universitaire de Technologie de Lyon 1

Directeur : M. le Professeur C. VITON

Ecole Supérieure du Professorat et de l'Education

Directeur : M. le Professeur A. MOUGNIOTTE

Institut de Science Financière et d'Assurances

Directeur : M. N. LEBOISNE

Abstract

Miniaturization in Gas Chromatography opens the way to low cost, low gas and low power consumption portable devices, which offer *in-situ* analysis and avoid tedious transport of samples to laboratories. Since the first micro-fabricated column in the late 1970's, the main focus was directed to the separation of heavy molecular weight hydrocarbons, with 5 or more carbon atoms.

In this work, we have developed sol-gel mesostructured silica stationary phases for the separation of light alkanes (from one to 5 carbon atoms) in micro-fabricated columns, following two different procedures: i) the deposition of a sol-gel thin film by dynamic coating directly into the GC capillary or on micro-fabricated columns or ii) the layer-by-layer (LbL) deposition of silica nanoparticles (SNPs) on micro-fabricated columns.

The influence of the sol-gel process coating parameters on the final thickness of the stationary phase was studied on short capillary columns. Various ordered or disordered mesostructures were yielded by varying the nature and the concentration of the structure directing agent (SDA), thus allowing the obtention of columns with different retention strengths. Interestingly, the less organized layers led to the columns with the highest retention, comparable with commercial columns for stationary phases being 30 times thinner.

The process was successfully transposed to micro-fabricated columns. The obtained micro-columns showed promising efficiencies and the highest number of theoretical plates per meter (th.p./m) reported to date for ethane (7500 th.p./m).

Finally, we investigated an alternative way to coat GC micro-columns directly with mesostructured silica nanoparticles using an LbL process. The process was first evaluated for commercial non porous SNPs. Then it was successfully applied to mesostructured custom SNPs and further validated for the full-wafer simultaneous coating of 35 columns.

Overall, this work demonstrated the use of mesostructured silica as an effective stationary phase for light alkane's separation on GC micro-fabricated columns.

Résumé

En chromatographie en phase gazeuse, la miniaturisation ouvre la voie pour de nouveaux appareils portables, consommant peu d'énergie et de gaz et permettant des analyses directement sur site en évitant ainsi le transport d'échantillons. Depuis les années 70, l'essentiel des travaux s'est focalisé sur les hydrocarbures les plus lourds, avec 5 atomes de carbones ou plus.

Ce travail expose le développement de nouvelles phases stationnaires de silice mésostructurées pour la séparation des alcanes légers (avec moins de 5 atomes de carbones) dans des colonnes micro-fabriquées, suivant deux procédés différents : i) le dépôt dynamique *in-situ* d'un sol directement dans les colonnes capillaires ou micro-fabriquées, ou ii) le dépôt couche-par-couche de nanoparticules de silices (SNPs) sur les micro-colonnes.

L'influence des paramètres du dépôt sol-gel sur l'épaisseur finale de la phase stationnaire a été étudiée sur des colonnes capillaires courtes. En modifiant la nature et la concentration de l'agent structurant, il a été possible d'obtenir différentes mésostructures plus ou moins ordonnées et de modifier le pouvoir rétentif de la colonne. Curieusement, les structures les moins organisées ont montré la rétention la plus importante vis-à-vis des alcanes, comparable à celle de colonnes commerciales, mais pour une épaisseur de phase stationnaire 30 fois plus faible.

Le procédé a été adapté avec succès aux colonnes micro-fabriquées. Les colonnes obtenues montrent des efficacités de séparation prometteuses, et le plus grand nombre de plateau théorique par mètre (th.p./m) rapporté à ce jour pour l'éthane (7500 th.p./m).

Finalement, un procédé alternatif par dépôt couche-par-couche a été étudié pour déposer directement des nanoparticules de silice comme phase stationnaire dans les micro-colonnes. Ce procédé a d'abord été évalué pour des SNPs commerciales non poreuses. Puis il a été appliqué avec succès au dépôt de SNPs mésostructurées, synthétisées au laboratoire, et validé pour le dépôt pleine-plaque de 35 micro-colonnes en simultané.

Dans l'ensemble, ce travail démontre l'efficacité des phases stationnaires en silice mésostructurée pour la séparation des alcanes légers par des colonnes micro-fabriquées.

Résumé substantiel

La chromatographie en phase gazeuse (CPG) est une des techniques analytiques les plus utilisées pour la séparation et la quantification des liquides organiques ou mélanges gazeux. Elle est utilisée dans de nombreuses industries : pétrochimie, pharmacie, agroalimentaire, surveillance de l'environnement, ou détection d'explosifs...

Les appareils de CPG conventionnels sont déjà capables d'analyses très complexes, mais ils restent d'encombrants équipements de laboratoire, grands consommateurs d'énergie. Le transport des échantillons jusqu'au laboratoire pose des problèmes de délais ou de perte d'intégrité des échantillons, préjudiciables pour certaines applications.

La miniaturisation des différents composants (préconcentrateur, injecteur, colonne, détecteur...) grâce aux technologies MEMS (MicroSystèmes Electro-Mécaniques), d'un chromatographe ouvre la voie pour des appareils portables, consommant peu d'énergie et de gaz, qui permettront des analyses directement sur site. De tels systèmes intégrés de CPG sont actuellement en cours de développement au CEA/LETI.

Élément clef du chromatographe, la colonne est responsable de la séparation des analytes qui permet leur détection. La qualité de la séparation, la résolution des pics et le temps d'analyse dépendent des propriétés de la phase stationnaire, en fonction de la complexité de l'échantillon. De ce fait, depuis la fin des années 70, les colonnes sont l'objet de nombreux efforts de miniaturisation. Cependant, l'essentiel des travaux s'est focalisé sur les hydrocarbures les plus lourds, avec 5 atomes de carbones ou plus, et seuls quelques récents travaux se sont intéressés à la séparation des alcanes de 1 à 5 carbones.

Ce travail réalisé en collaboration avec le laboratoire C2P2 de Lyon a pour but d'étudier les propriétés de la silice mésostructurée en tant que phase stationnaire dans les colonnes micro-fabriquées pour la séparation des alcanes légers. Deux procédés ont été développés : i) le dépôt *in-situ* d'un sol par dépôt dynamique, directement dans les colonnes capillaires et micro-fabriquées, détaillé dans les chapitres II à IV, ou ii) le dépôt couche par couche de nanoparticules silicique dans des colonnes micro-fabriquées, détaillé dans le chapitre V.

Ce manuscrit s'articule en 5 grands chapitres :

Le chapitre I est un chapitre bibliographique permettant de mettre en évidence l'état de l'art le plus proche et le contexte scientifique du présent projet.

Le chapitre II présente l'optimisation du procédé sol-gel. Un agent structurant (SDA), le CTAB, a été utilisé pour augmenter et structurer la porosité de la phase stationnaire finale. Une faible dilution du sol a été utilisée pour permettre de maximiser la quantité de silice finale par volume de sol déposée. L'épaisseur finale dépend aussi des paramètres du dépôt (pression et durée d'introduction du sol) qui ont été étudiés en détails. Le procédé a ainsi montré des similitudes avec le dépôt par trempage, dans la mesure où l'épaisseur déposée est proportionnelle à la vitesse du dépôt (une vitesse élevée étant obtenue pour une pression élevée et un temps de dépôt court). Finalement, un procédé avec une vitesse de dépôt modérée a été préféré pour favoriser une bonne répétabilité du procédé : une variation des coefficients de rétentions des colonnes de quelques pourcents seulement a été observée. Des colonnes double-couche ont également pu être réalisées, présentant ainsi une rétention double de celle d'une colonne avec une simple couche, sans perte de la finesse des pics.

Le chapitre III présente l'étude de l'influence de la nature du SDA et du rapport molaire SDA/Si sur la structuration de la phase stationnaire et ses propriétés chromatographiques. Des techniques d'imagerie comme le MEB ou le SAXS ont été utilisées pour obtenir des informations sur les caractéristiques physiques des phases stationnaires. La synthèse à l'échelle du g d'une poudre modèle a été développée pour faciliter l'adsorption d'azote mais sa structure s'est révélée malheureusement trop différente de celles des films minces. Des phases stationnaires mésostructurées (structures en « trou de vers », cubiques ou hexagonales) ont été effectivement observées sur colonnes capillaires avec le CTAB, les pluronics F68 et F127 respectivement, pour des rapports SDA/Si élevés. Cependant, l'affinité de la phase stationnaire vis-à-vis des alcanes est la plus grande pour des rapports SDA/Si faible, pour lesquels aucun ordre de la mesostructure n'a été observée. Des colonnes obtenues avec le pluronic F68 présentent une rétention pour les alcanes similaire à des colonnes commerciales Si-PLOT®, mais avec une phase stationnaire 30 fois plus fine, donc une affinité 30 fois plus importante.

Le chapitre IV présente le transfert de ce procédé à des colonnes micro-fabriquées. Du fait de la géométrie particulière de ces colonnes, les phases stationnaires obtenues ne sont pas parfaitement homogènes et s'accumulent dans les coins du canal. Par ailleurs, seule l'utilisation du CTAB a abouti à des colonnes fonctionnelles, les conditions de suppression des Pluronic n'étant pas compatibles avec la limite de tenue en température de la colle utilisée pour l'assemblage des colonnes. Les colonnes obtenues avec le CTAB montrent des efficacités de séparation prometteuses, et le plus grand nombre de plateau théorique par mètre (th.p./m) rapporté à ce jour pour l'éthane (7500 th.p./m). Elles ont aussi été utilisées avec succès pour la séparation avec gradient thermique de mélanges complexes de gaz naturel.

Finally, in chapter V, an alternative procedure is studied to deposit directly silica nanoparticles as a stationary phase in micro-columns by layer-by-layer deposition. In a first step, the efficiency of the procedure was demonstrated on commercial silica nanoparticles, non-porous, using a cationic polyelectrolyte (polyallylamine hydrochloride). Despite encouraging performances, these phases do not show enough retention for light alkanes, probably due to a lack of developed surface. Silica mesostructured nanoparticles, not commercially available with a satisfying size distribution, were therefore synthesized by two ways: i) the synthesis of mesostructured shells, and ii) the synthesis of silica mesostructured nanoparticles catalyzed by amines. However, it was found that the cationic structuring agent used changed the surface charge of silica particles, which required the change of the cationic polyelectrolyte for an anionic one (polystyrene sulfonate) and the adjustment of ionic forces during deposition, with the addition of NaCl to 10^{-2} M. These conditions allowed the realization of a conformal and homogeneous deposition of aminosilica nanoparticles on micro-fabricated columns. Unfortunately, these could not be tested in HPLC due to assembly problems. Wafers were therefore specifically fabricated so that the cap could be sealed by anodic bonding after the deposition of the beads. A deposition was realized on a wafer of 35 micro-columns, which were then tested in chromatography, with promising performances.

In conclusion, this work demonstrates the efficiency of silica mesostructured stationary phases for the separation of light alkanes on micro-fabricated columns. It opens interesting perspectives for miniaturization and integration of these in fully miniaturized systems. Moreover, the versatility of these phases and the numerous possibilities of post-functionalization of silica open the way to a much more important field of applications.

Table of content

Introduction 1
Chapter I. Literature Review 7
Chapter II. Thin film coating: Process development 41
Chapter III. Thin film coating: SDA impact on the stationary mesostructures phase and chromatographic performances 69
Chapter IV. Micro-fabricated columns: Sol-gel coating 99
Chapter V. Micro-fabricated columns: Nanoparticles layer by layer coating 121
Conclusion 149
Appendix A. Experimental part 155
Appendix B. Laminar flow through columns 175

Table of figures

Fig. I.1 – Illustration of the three main components of a gas chromatograph: the injector, the column and the detector, and a two compound-sample profile through the separation process	11
Fig. I.2 – Agilent 6890 gas chromatograph used in the laboratory. In (a) the oven door is closed and the auto-sampler is in place, and in (b) the oven cavity is open and we can see a typical capillary column, coiled into a cylinder.....	12
Fig. I.3 – Schematic of a split inlet from ref. ¹ The sample is injected via the syringe, and only a fraction goes through the column while the remaining is evacuated through the split vent, improving peak sharpness.	13
Fig. I.4 – Illustration of the three main types of GC columns: wall coated open tubular (WCOT), porous layer open tubular (PLOT) and packed columns. The stationary phase is represented in plain orange.	15
Fig. I.5 – Typical chromatograph of a sample with one un-retained and two retained compounds.....	18
Fig. I.6 – Adsorption standard enthalpy of n-alkanes plotted vs. carbon number using silica gels with various pores diameters as stationary phases, from the work of A. Kiselev and Y. Yashin. ⁶⁷ The mean diameter of the silica gel pores (in Å): 1 – 32; 2 – 46; 3 – 70; 4 – 104; 5 – 140; 6 – 250; 7 – 1100; 8 – 710; 9 – 1700; 10 – 4100.	20
Fig. I.7 – Illustration of the three main phenomena responsible for band broadening in GC	22
Fig. I.8 – Van Deemter plot of column HETP (<i>or H</i> , in red) as a function of mobile phase average velocity <i>u</i> , illustrating the contributions of the three phenomena responsible for band broadening.....	23
Fig. I.9 – Golay plot of column efficiency <i>H</i> (in black) against mobile phase average velocity <i>u</i> , illustrating the different contributions to band broadening.....	24
Fig. I.10 – Examples of recently commercialized portable gas chromatographs: (a) Torion portable GC-MS Tridion™, (b) Inficon portable GC Explorer™, (c) Vernier Mini GC plus™ for college and high-school experiments, (d) Defiant portable GC for air, soil and water analysis FROG 4000™, (e) Airmet Explorer GC system and (f) Ametek 292B Portable Natural Gas Chromatograph.....	27
Fig. I.11 – Photograph of a gas chromatograph integrated on a planar silicon wafer fabricated by Terry and coworkers at Stanford University.	29
Fig. I.12 – Illustration of the two main route for stationary phase deposition in a micro-fabricated column (cross-sectional view of the substrate). (a) The column is sealed by a cover plate and the stationary phase is introduced in the channel. (b) The stationary phase is deposited on the silicon wafer before sealing the cover plate.	30
Fig. II.1 – Schematic representation of the pH-dependence of hydrolysis (H) and condensation (C) and dissolution (D) of TEOS, from C. J. Brinker. ⁶	45
Fig. II.2 – Three different materials from the M41S family. ¹⁸	46
Fig. II.3 – Scheme for the liquid-crystal templating mechanism proposed by Mobil scientists: (1) silicate aggregation around organized micellar rods (liquid-crystal templating or LCT) and (2) formation of surfactant-silicate rods on the basis of organic-inorganic interactions (cooperative self-assembly or CSA). ¹⁷	46
Fig. II.4 – Illustration of the formation of ordered mesostructured silica by the EISA strategy. ³⁰	48
Fig. II.5 – Principles of a) spin coating and b) dip coating for thin film deposition. ³⁷	48
Fig. II.6 – Illustration (a) and photograph (b) of the experimental apparatus.	49
Fig. II.7 – Illustration of the different steps of column coating. Steps a. to d. are explained in the text.	50
Fig. II.8 – Simplified view of the column pretreatment: opening of siloxane bridges to form silanols on which the stationary phase can covalently bond by condensation.....	51
Fig. II.9 – Contact angle of water on the column walls as a function of the pretreatment duration, measured by capillary effect. Activation times over 30 minutes are not necessary.	52
Fig. II.10 – Thermal treatment and a typical chromatograph of the removal of the CTAB from the column.	54
Fig. II.11 - Influence of the porosity on the separation of light alkanes.....	55
Fig. II.12 – Plug length as a function of time for a 1.5m long capillary with a 100µm diameter. Sols' viscosities are 0.001 and 0.01 kg.m ⁻¹ .s ⁻¹ . Differences in travel times between the complete model and equation 1.7. are 0.45s and 0.7s (respectively 1.25% and 0.19% of error)	58
Fig. II.13 – Influence of coating speed on the retention of light alkanes using the following sol composition: TEOS:F68 = 1:0.005. Isothermal separation of light alkanes (methane 2000 ppm, ethane to pentane, 500 ppm each), T=30°C, inlet pressure 12psi, Vinj=0.2µL, 1m column, 100µm diameter, plug length and speed calculated in MATLAB, based on the model of Appendix B.2.3.	60

Fig. II.14 – Graphic representation of the analogy between a. dip coating and b. capillary coating.	60
Fig. II.15 – Column retention (for butane) versus pressure. At the time of the 1 st process, columns were made directly one meter long, without cutting their extremities prior to GC testing. This was corrected for the 2 nd process, and columns were made 1.5m long, and cut to 1 m for GC tests, but there was still no fabric to wipe the capillary end after immersion. The final optimized process included this last addition.	61
Fig. II.16 – Reproducibility study for CTAB columns.	63
Fig. II.17 – Reproducibility study for F68 columns.	63
Fig. II.18 – Comparison of multilayer and single layer columns chromatographic performances.	64
Fig. III.1– Phase diagram of the mesostructures obtained with EISA of the system CTAB/Si _{1.25} (OH) _{1.5} /EtOH/H ₂ O, from Grosso and coworkers. ³	74
Fig. III.2 – Phase diagram of a CTAB mesostructured silica sol, showing the domain of existence of three micellar phases as a function of the CTAB/Si molar ratio and the aging time of the initial sol at 40°C. ⁵ The initial sol composition is the same as the one used in this work.	75
Fig. III.3– Phase diagram of the mesostructures obtained with EISA of the system F127/TiO _x Cl _y (OH) _z /EtOH/H ₂ O, from Grosso and coworkers. ³	75
Fig. III.4 – BET analysis of capillary columns with krypton. (a) BET krypton adsorption isotherm for a coated and an uncoated capillary. (b) 4 repetitions of the same measurement: signal is too low for a quantitative study.	76
Fig. III.5 – Picture and schematic cross section of the experimental set-up for sol-gel synthesis under azote flow. 77	77
Fig. III.6 – Setup 1 for SAXS observations of the stationary phase inside the capillary segments of column on the BM2 beamline at ESRF. Picture of the experimental bench (a), and schematic drawings of the side view (b), and top view(c), with the normal directions to the wall represented in red arrows.	78
Fig. III.7 – Setup 2 for SAXS observations of capillaries coaxial to the X-ray beam. (a) Pictures of the dispositive: capillaries are placed side by side, coaxial to the axis. (b) Schematic drawing of the capillary side view.	79
Fig. III.8 – (a to c) SEM pictures and thickness measurements of various stationary phases at 100 k magnification. (d) Zoom at 350 k magnification of the stationary phase with F127/Si = 0.005.	80
Fig. III.9 – Representative stationary phase thickness in a column as measured with the SEM. Each point is calculated as the average of 3 measurements. The average and standard deviation of the measurements are indicated on the figure.	80
Fig. III.10 – Stationary phase thickness of the films coated with different CTAB/Si ratios, measured by SEM.	81
Fig. III.11 – SAXS data for CTAB mesoporous stationary phases, coated at a pressure of 1 bar. CTAB/Si ratios are 0.05 (a), 0.10 (b) and 0.14 (c). Data presented are the result of the subtraction of the signal for the capillary column minus a reference capillary without stationary phase.	82
Fig. III.12 – Radial integration of SAXS data for the 3 columns prepared at 1 bar. The signal maximum for the interference ring is found at 1.18 or 1.20 nm ⁻¹ for the columns prepared with CTAB/Si molar ratios of 0.10 and 0.14 respectively. No peak is observed for the column prepared with a CTAB/Si molar ratio of 0.05.	83
Fig. III.13 – XRD analysis of powders synthetized in “column like conditions” for varying CTAB/Si molar ratios.	83
Fig. III.14 – Retention properties of columns coated at 1 bar with a sol gel stationary phase as a function of CTAB/Si molar ratios.	84
Fig. III.15 – Affinity of the stationary phase towards propane for various CTAB/Si molar ratios. Similar results are observed regardless of the coating pressure used.	85
Fig. III.16 – Adsorption standard enthalpy towards light alkanes of the columns coated at 1 bar with a sol gel stationary phase with various CTAB/Si molar ratios.	85
Fig. III.17 – Stationary phase thickness of the films coated with varying F68/Si ratios, measured by SEM.	86
Fig. III.18 – SAXS data for F68 mesoporous stationary phases. (a) F68/Si = 0.0033, coated at 1 bar (the picture is similar to the one with F68/Si = 0.0017, not represented), (b) F68/Si = 0.005, coated at 1 bar, (c) F68/Si = 0.005, coated at 4 bar, and (d) F68/Si = 0.010, coated at 1 bar.	87
Fig. III.19 – Radial integration of SAXS data for the columns coated with F68. The ratios between peak coordinates (indicated on the figure), for the column coated with F68/Si ratio of 0.010, correspond to a face-centered cubic structure for the reciprocal lattice. The x-coordinate of the first peak coincides with the maximum of the diffuse peak for the column coated at 4 bar, and is centered on 0.66 nm ⁻¹	88
Fig. III.20 – Perpendicular (a) and coaxial (b) SAXS pictures of the column coated with F68/Si = 0.01. There is a small deviation (around 2 or 3 %) between the values measured in the two pictures.	88
Fig. III.21 – XRD analysis of powders synthetized in “column like conditions” for varying F68/Si molar ratios.	89

Fig. III.22 – N ₂ adsorption/desorption isotherms of the mesostructured powders synthesized in “column like conditions” using F68 as SDA. The desorption isotherms are in open symbols.....	90
Fig. III.23 – Retention properties towards alkane for columns coated at 1 bar as a function of F68/Si molar ratios. Stationary phase affinity is plotted with red circle dots and retention is plotted with black square dots.....	90
Fig. III.24 – Adsorption standard enthalpy towards light alkanes of the columns coated at 1 bar with a sol gel stationary phase with various F68/Si molar ratios.....	91
Fig. III.25 – Stationary phase thickness of the films coated with varying P123 or F127/Si ratios, measured by SEM.	92
Fig. III.26 – Perpendicular (a) and coaxial (b) SAXS pictures of the column coated with F127/Si = 0.005.	92
Fig. III.27 – Retention properties of columns coated with a sol gel stationary phase with various P123/Si (in filled symbols) or F127/Si (in unfilled symbols) molar ratios. Retention is plotted with black square dots and the stationary phase affinity is plotted with in red circle dots.....	93
Fig. III.28 – Adsorption standard enthalpy towards light alkanes of the columns coated at 1 bar with a sol gel stationary phase with various P123 and F127/Si molar ratios.....	94
Fig. III.29 – Column affinity for the various SDA and SDA/Si ratios studied in this work.	94
Fig. III.30 – Comparison of the chromatographs of a commercial Silica PLOT column and a mesostructured silica capillary column with F68/Si = 0.0033. Isothermal (30°C) separation of a methane to n-pentane mixture, on 1 meter long column with an internal diameter of 320µm (Silica PLOT) and 100µm (mesostructured silica). (a) The time scale is linear, and (b) in logarithmic scale for better readability until C5. (c) Number of theoretical plate per meter for methane to butane, and separation factor between methane and ethane (well over 1.5 for both)	95
Fig. IV.1 – Flow and shear stress profile through channels of different cross-sections calculated with COMSOL for a pressure gradient of 1 Bar/m and a fluid dynamic viscosity of 2.10 ⁻⁵ Po (Helium at 30°C).....	103
Fig. IV.2 – Coating velocity contour lines in the moving referential attached to the sol for a square column.	104
Fig. IV.3 – MEB pictures of the stationary phase in the corner of the channel (a), along the bottom (b-c), and on the sides of the channel (d to f).	105
Fig. IV.4 – MEB pictures of the bottom (a) and the sides (b-c) of the channel. Stationary phase does not form a continuous film but small beads (in dark in the pictures).	105
Fig. IV.5 – MEB pictures showing stationary phase pooling in the corners. As the result of gel contraction during gelation and annealing, the stationary phase come off the wall (a), break in two (b) or both (c-f). Pictures (a-d) are taken at the bottom of the channel (silicon part) and corners are slightly round. Pictures (e-f) are taken on the top, at the junction between the silicon and the silica cover plate.....	106
Fig. IV.6 – Time position and speed of an un-retained compound inside a micro-column with 25cm long capillary connections. Square cross section are 80x80µm and rectangle ones are 40x120µm. T* and u _{col} stand for the ratio of time and the average velocity inside the micro-column area.....	108
Fig. IV.7 – Picture of a micro-column during coating. The filled part can be seen and controlled by the change of contrast of the channel color.	109
Fig. IV.8 – Pictures of the capillaries glued to the chip for coating (a.). The capillary are plugged but the glue does not fill the holes so it can be removed with a scalpel. Definitive gluing is shown in (b.). The glue fills the holes and the gluing is more resistant to pressure, but it is not reversible.....	109
Fig. IV.9 – Illustration of the effect of connections on column efficiency. An uncoated capillary is added at the entry of the column (a). The resulting retention time $t_r' > t_r$ (b), so N is usually higher for the coated column with a capillary connection. But as Δt_r is unchanged (the connection is uncoated, so the same time is added to each separation), the separative power of the column is in fact poorer (c).	110
Fig. IV.10 – Influence of diameter and length of the entry (a.) and exit (b.) capillaries on Neff for different values of k, in a square section micro-column (80µm x 80µm x 1.33m). Theoretical values are calculated with MATLAB (the model equations are presented in Appendix B.2.3). Optimum Neff is presented in the z-axis, and the optimal working pressure is represented by the color sale.....	112
Fig. IV.11 - Entry capillary length influence on efficiency. Carrier speed: 82 cm/s. For ethane and propane, N increases with capillary length whereas Neff decreases, as predicted. For butane, both decreases with capillary length (this can be explained as we are working largely above optimum speed for butane, as we will see in IV.3.3)	113
Fig. IV.12 – Golay plot for a micro-column coated with a mesostructured CTAB sol-gel stationary phase. CTAB:Si molar ratio 0.1:1, sol dilution 1:3 in volume with ethanol, coating pressure and introduction time of 1 Bar and approximately 6 seconds. Column dimensions: 80µm x 80µm x 1.33m, connections: 25cm 100µm diameter capillaries. Working pressures between 5 and 40 psi.....	114
Fig. IV.13 – Comparison of our work with the work of J. Vial and coworkers ⁴	115

Fig. IV.14 – Kovatz plot for C2-C5 n-alkanes at 40°C. The expected linear relationship is verified.	116
Fig. IV.15 – Thermodynamic evaluation of a sol-gel micro-column. Van't Hoff plots (a) show an expected linear correlation. It gives access to the adsorption heat (b) (slope) and $\ln(k_{\infty})$ at infinite temperature (c) (y-intercept) which are both linear function of carbon number	117
Fig. IV.16 – Separation of a natural gas like mixture of light alkanes: (1) methane (28%), (2) ethane (4%), (3) propane (1%), (4) iso- and n-butane (2000ppm), (5) neo-, iso- and n-pentane (500ppm). Complete separation of all pairs is achieved in 40 s, starting from 30°C with a ramp of 80°C/min. The resolution of the worst pair: n-butane/isobutane $R = 1.8$. Separation could be completed in 30 s, starting from 50°C, but n-butane/isobutane resolution dropped to $R=1.47$. Inlet pressure = 20psi; $V_{inj} = 0.2 \mu\text{L}$; column $1.33 \text{ m} \times 80 \mu\text{m} \times 80 \mu\text{m}$	117
Fig. V.1 – Illustration of the LbL process for the deposition of PAH and SNP bilayers, taken from ¹	126
Fig. V.2 – Thickness of the deposited film as a function of the number of bilayers for two SNP solutions.	126
Fig. V.3 – SEM pictures of the SNP LbL coating (30 bilayers) on a silicon chip with micropillars.	127
Fig. V.4 – SEM pictures of a micro-column channel cross-section, coated with 30 SNP layers. (a) 10 μm thick ordyl film at the top of the channel, (magnification: 2 k). (b) Picture of a corner at the bottom of the channel (magnification 10 k). (c) Picture of the 30 layers of SNPs at high magnification (200 k)	128
Fig. V.5 – Chromatographs of the two micro-columns with 30 layers of commercial SNPs. Isothermal (30°C) separation of pentane, heptane, octane and toluene at 20 psi.	129
Fig. V.6 – TEM pictures of the core-shell mesostructured SNP before templates removal.....	131
Fig. V.7 – SEM picture of calcined mesoporous SNP. Magnification $\times 500 \text{ k}$. TEOS:CTAB:Arg:H ₂ O = 1:0.07:0.03:250.	132
Fig. V.8 – Adsorption isotherms of calcined mesoporous SNP. Formulations are TEOS:CTAB:Arg:H ₂ O = 1:0.10:0.03:250 (#1), 1:0.07:0.03:250 (#2), 1:0.05:0.015:250 (#3) and 1:0.035:0.015:250 (#4).	132
Fig. V.9 – SEM pictures of the commercial mesoporous silica nanoparticles. (a) Commercial mesoporous nanoparticles: the particles are very polydisperse in size. (b and c) Silicon substrate after 3 deposition cycles at different magnification (indicated on the pictures)	133
Fig. V.10 – SEM pictures (100 k magnification) of the silicon substrate after 1 deposition cycle of 5 minutes (a) and 15 minutes (b), and (c) after 4 deposition cycles (15 minutes for the 1 st , then 5 minutes).	135
Fig. V.11 – Zeta potential measurements of the silicon substrate surface: 1) after the layer of PEI, 2) after the first layer of PSS, 3) after the first layer of mesoporous SNP.....	136
Fig. V.12 – SEM pictures (100 k magnification) of the silicon substrate after 1 deposition cycle, with SNP deposition times of 30 minutes (a) 45 minutes (b), and 60 minutes (c), and after 2 coating cycles with a SNP deposition time of 30 minutes (d).....	137
Fig. V.13 – SEM pictures of the silicon substrate after 1 deposition cycle. HCl (until pH = 4) (a and c) or NaCl (0.1 M) (b and c) was added to the mesoporous SNP solution before coating.. Magnification is indicated on the pictures.	138
Fig. V.14 – SEM pictures (50 k magnification) of the silicon substrate after 1 deposition cycle of 15 minutes. NaCl 10^{-2} M (a), 10^{-3} M (b) and 10^{-4} M (c) was added to the mesoporous SNP solution prior to coating.	138
Fig. V.15 – Zeta potential measurements of the silicon substrate surface charge 1) after the layer of PEI, 2) after the first layer of PSS, 3) after the first layer of mesoporous SNP (deposited with NaCl = 10^{-2} M). The measure is repeated 4) after 2 complete deposition cycles, and 5) after the addition of a third layer of PSS.....	139
Fig. V.16 – SEM pictures of the coating obtained inside the channels of a micro-column after 20 deposition cycles with PSS 1 mg/mL and arginine catalyzed mesoporous SNP with 10^{-2} M of NaCl. (a), (b) and (c) present respectively the channel bottom, side and bottom corner. (d) is a zoomed picture of the coating, (e) top corner and (f) side view of a channel bottom. Magnification is indicated on the pictures.	140
Fig. V.17 – SEM pictures of the coating obtained inside the channels of a micro-column after 20 deposition cycles with PSS 1 mg/mL and arginine catalyzed mesoporous SNP diluted 4 times in deionized water, before addition of 10^{-2} M of NaCl. (a) and (b) present respectively the channel side and bottom corner. (c) Side view of a channel. Magnification is indicated on the pictures.	140
Fig. V.18 – Process flow for the realization of full wafer LbL deposited stationary phase for micro-columns with anodically bonded cover plate.	141
Fig. V.19 – Picture of a wafer after the deposition of the first PEI layer.....	142
Fig. V.20 – Picture of the wafer after glass cover plate anodic bonding.	142
Fig. V.21 – SEM pictures of the stationary phase deposited by LbL full wafer coating. (a) Large view. (b and c) Pictures in the top first 20 μm of the channel. (d and e) Bottom of the channel, and zoom on a coated area. Zoom on a particle cluster (f) and cross section view (g) of the median part of the channel.....	143

Fig. V.22 – Isothermal (30°C) separation of methane to n-pentane (500 ppm each) at 20 psi. Butane and pentane are separated from the others. The saturation of the stationary phase is clearly visible on the quantity of sample introduced increases.....	144
Fig. A.1 – Experimental set-up for the sol preparation	160
Fig. A.2 – Picture of the coating apparatus.	161
Fig. A.3 – (a) process flow and (b) picture of a column illustrating the serpentine four-leaf clover design.....	164
Fig. A.4 – SAXS experimental set-up with capillaries perpendicular (a) or coaxial (b) to the beam.	167
Fig. A.5 – Picture of the glass container, placed into the oven for powder synthesis in “column like” conditions..	169
Fig. A.6 – Process flow for the full wafer LbL deposition of mesoporous silica nanoparticles.....	173

Tables

Table I-1 – Comparison of the A, B and C terms of eq I.14 found in the literature. *no value given for B and C (the model was developed for un-retained compounds)	34
Table II-1 – Influence of the sol dilution on the retention of the stationary phases. Coating conditions are detailed in Appendix A.2.2.....	56
Table II-2 – Influence of coating time, pressure and sol viscosity on plug length and plug speed (when changed one at a time); and their observed effect on the deposited thickness, as presented in the next paragraphs.....	57
Table II-3 – Viscosity calculated using <i>equation II.7</i> and film coating thickness measured by SEM.....	59
Table III-1 – CTAB/Si molar ratios that were investigated.....	81
Table III-2 – F68/Si molar ratios that were investigated.	86
Table III-3 – ads N ₂ adsorption characteristics for powders synthesized in “column like conditions”.....	89
Table III-4 – F127/Si and P123/Si molar ratios that were investigated.	91
Table A-1 – Ethanol and SDA quantities used for the synthesis	160
Table A-2 – coating parameters used for the study of dilution influence on column’s retention (Chapter II.3.1.2)	163
Table A-3 – SDA quantities, dissolved in 4.5 mL of ethanol, for powder synthesis.....	168

List of abbreviations

BET	Brunauer, Emmett and Teller theory
C _i	alkane with i Carbon atoms
CSA	Cooperative Self-Assembly
CTAB	CetylTrimethylAmmonium Bromide
DRIE	Deep Reactive-Ion Etching
EISA	Evaporation Induced Self-Assembly
F127	Pluronic F127 (polyoxyethylene-polyoxypropylene-polyoxyethylene: EO ₇₃ -PO ₂₈ -EO ₇₃)
F68	Pluronic F68 (EO ₁₀₁ -PO ₅₆ -EO ₁₀₁)
FID	Flame Ionization Detector
GC	Gas Chromatography
HETP	Height Equivalent to a Theoretical Plate
LbL	Layer-by-Layer
LCT	Liquid Cristal Templating
LPG	Liquid Petroleum Gas
MCM	Mobile Corporation Materials
MEMS	Micro-Electro-Mechanical Systems
MS	Mass Spectrometry
MVD	Molecular Vapor Deposition
N ₂ ads./des.	Nitrogen adsorption desorption
P123	Pluronic P123 (EO ₂₀ -PO ₇₀ -EO ₂₀)
PAH	PolyallylAmine Hydrochloride
PDMS	PolyDiMethylSiloxane
PECVD	Plasma Enhanced CVD
PEI	PolyEthylenImine
PLOT	Porous Layer Open Tubular column
PSS	PolyStyrene Sulfonate
SAXS	Small Angle X-ray Scattering
SBA	Santa Barbara Amorphous materials
SDA	Structure Directing Agent
SEM	Scanning Electron Microscopy
SNP	Silica NanoParticles
TCD	Thermal Conductivity Detector
TEM	Transmission Electron Microscopy
TEOS	TetraEthyl OrthoSilicate
TLCT	True LCT
VOC	Volatile Organic Compounds
WCOT	Wall Coated Open Tubular column
XRD	X-Ray Diffraction

Introduction

Gas chromatography (GC) is one of the most used analytical techniques for the separation and quantification of organic liquids or volatile mixtures. It is used in a wide variety of industries: petrochemical, environmental monitoring, product purification, or explosive detection.

Conventional GC apparatus are already capable of performing complex analyses but are quite bulky and power consuming. Moreover, samples transport to the laboratory generates additional delay and potential loss of sample integrity which can be detrimental to some applications. Indeed, chemical process monitoring may require real time feedback, possible only through on-line analyses. Likewise, many applications such as environment monitoring would benefit from portable GC equipment, which can be used directly on site.

Following recent advances in miniaturization, various portable GC devices are now commercialized. They are the result of the integration of the different modules of a classical GC (preconcentrator, injector, column, detector...) that are miniaturized most of the time thanks to MEMS (Micro-Electro-Mechanical systems) technologies. Such integrated GC devices are under development at CEA/LETI, as it is still necessary to develop and optimize each of the modules to obtain the most efficient system.

As a key element of GC systems, the column is responsible for the separation of the analytes to allow their detection with the best sensitivity and selectivity. Its physical properties and its stationary phase nature determine the separation quality, the peak resolution and the analysis time, depending on the initial mixture complexity. Consequently, since the end of the 70's, columns are the object of numerous miniaturization efforts. Technologies coming from the microelectronic were used to etch several meters long-columns into small silicon chips of a few centimeters square.

Such attempts were supported by a theory according to which it is possible to control total flow and resolution independently with a rectangular channel cross-section. Indeed, the efficiency of circular capillary columns is greater when their diameter is small, but the smaller their diameter is, the smaller the column volume is and thus the maximum sample volume that can be analyzed. On the other hand, by choosing the width and height of a rectangular cross-section column independently, it is possible to improve column efficiency (small width) without any loss of column volume (high height).

Moreover, such small and compact columns have a low thermal inertia. They can be easily connected to a resistive system or a Peltier device to perform fast and low power consuming temperature management. This opens the way to faster and more power efficient analyses that could be of great advantage for portable systems.

However, although it is quite simple to fabricate columns with dimensions compatible to GC needs, the stationary phase deposition remains quite complex. Indeed, usual deposition techniques used for capillary columns are difficult to transpose to the particular geometry of these micro-fabricated columns, and particularly to column channels with high aspect ratios. They often result in uneven coatings with stationary phase accumulations in the corner of the channels.

A lot of work has also been directed to prevent this phenomenon, either by improving the deposition techniques of already existing stationary phases, mainly in liquid phase, or by developing new stationary phases that can be deposited as monolayers or by gas phase processes. However, until recently, most of these works focused on intermediate molecular weight hydrocarbons separation, with 5 or more carbon atoms. Only few recent works have examined applications for lighter hydrocarbons (1 to 5 carbon atoms), and only with moderate reported efficiencies.

Among other materials, porous silica stationary phases can separate light alkanes, as these analytes interact with the silica surface by adsorption reactions. Thus, in the present project realized in collaboration with C2P2 laboratory at CPE Lyon, we have developed a process to deposit porous mesostructured silica as a stationary phase for light alkane separation. This silica coating was prepared by sol-gel process *via* a templating route. Our idea was to benefit from the recent developments on ordered mesoporous materials that allow high specific area and a considerable control of pore size and geometry to test these materials as stationary phases inside GC columns and to study the influence of porosity on separation. Although the influence of porosity is easier to study on capillary columns, we still aimed at generating micro-fabricated column coatings.

In the first part of this work, the principles of gas chromatography and the recent efforts towards miniaturization of GC systems and in particular of the column will be described.

In the second part, we will focus on sol-gel thin film deposition process and how to adapt it to the constraints of a closed channels. In particular, we will study the influence of the coating parameters on the thickness of the final stationary phases.

Then, we will investigate the influence of different structure directing agents on the porous structure and the retention properties of the stationary phases.

In a fourth part, we will demonstrate the portability of the process to micro-fabricated columns and how our columns compare with the state of the art.

Introduction

In the fifth chapter, another type of deposition process, which allows an easier characterization of the porous structure and is particularly adapted to the micro-fabricated columns, will be presented.

At the end of the manuscript, conclusion and open perspectives will be given.

Chapter I.

Literature Review

I.1. Gas chromatography	11
I.1.1. General principle.....	11
I.1.2. Gas chromatograph.....	12
I.1.2.1. <i>The injector</i>	12
I.1.2.2. <i>The detector</i>	13
I.1.2.3. <i>The column</i>	14
I.1.3. Commonly used stationary phases.....	16
I.1.3.1. <i>Gels and liquids for WCOT columns</i>	16
I.1.3.2. <i>Solid adsorbents for packed columns</i>	16
I.1.3.3. <i>Solid adsorbents for PLOT columns</i>	17
I.1.3.4. <i>Sol-gel strategies for GC stationary phases</i>	17
I.1.4. Columns performances.....	18
I.1.4.1. <i>The chromatogram</i>	18
I.1.4.2. <i>Thermodynamic evaluation</i>	19
I.1.4.3. <i>Adsorption properties of light hydrocarbons on silica</i>	20
I.1.4.4. <i>Column efficiency evaluation – plate number and HETP</i>	21
I.1.4.5. <i>Band broadening – Van Deemter equation</i>	21
I.1.4.6. <i>Open tubular column efficiency – Golay equation</i>	23
I.1.4.7. <i>Column capacity</i>	25

I.2. Towards portable GC	26
I.2.1. The quest for miniaturization	26
I.2.1.1. Commercialized micro-GC.....	26
I.2.1.2. Toward the next generation of portable devices.....	27
I.2.2. Micro-columns.....	28
I.2.2.1. Micro-column fabrication process.....	28
I.2.2.2. Major stationary phases for micro-columns.....	30
I.2.2.3. Temperature management of micro-fabricated columns.....	32
I.2.3. Micro-column evaluation.....	33
I.2.3.1. Modification of the Golay equation coefficients.....	33
I.2.3.2. Influence of the capillary connections.....	34
I.3. Conclusion	35
I.4. References	37

I.1. Gas chromatography

Chromatography is an analytical technique aiming at the separation, identification and quantification of the different compounds of a mixture. Gas chromatography, or GC, refers to the use of this technique with volatile or vaporized gaseous mixtures.

We will first briefly describe how the apparatus works and its different constitutive. We will then focus on the heart of the separation mechanism, the column itself and its stationary phase. In the next section, we will detail how it is possible to evaluate the column's performances and to compare several columns. Finally we will consider miniaturization efforts on GC systems.

I.1.1. General principle

A gas chromatograph comprises three main elements: the injector, the column and the detector (Fig. I.1). The sample is injected into the injector, where it is vaporized (if not already gaseous). Then, it is carried through the column by a carrier gas, also called the mobile phase, where it interacts with an adsorbing material, named the stationary phase by opposition. As the different compounds progress through the column, they adsorb and desorb differently on the stationary phase, and are therefore more or less delayed, depending on their affinity with the adsorbent. As illustrated in Fig. I.1, two compounds (in blue and red, with their corresponding mixture in purple) arrive to the detector as two different separated peaks.

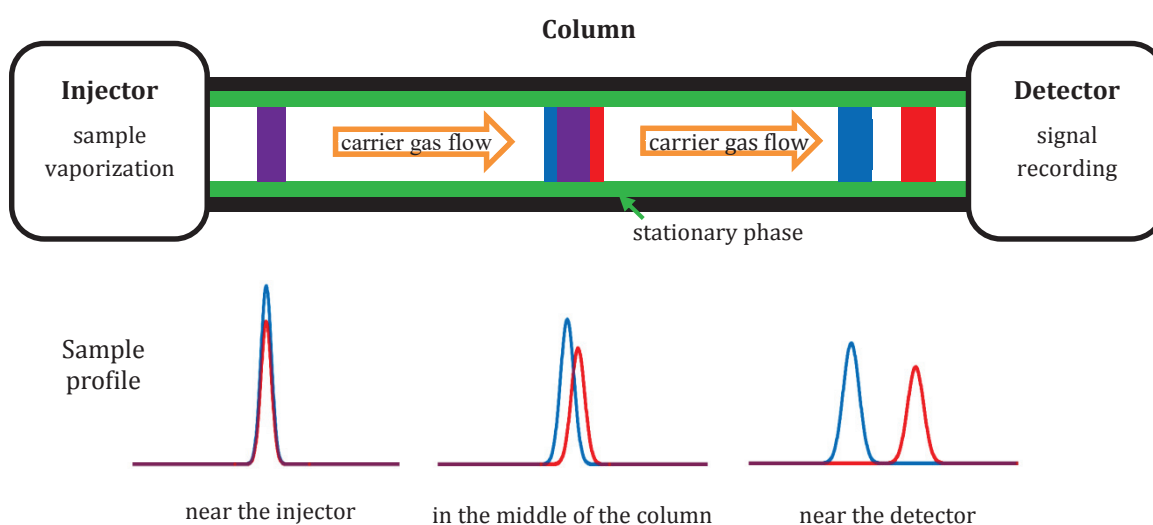


Fig. I.1 - Illustration of the three main components of a gas chromatograph: the injector, the column and the detector, and a two compound-sample profile through the separation process

I.1.2. Gas chromatograph

Fig. I.2 presents a standard GC apparatus used in our laboratory. It is composed of an injector, a detector and a column (as detailed afterwards) wound in coil form and located in an oven for temperature programming. An electronic interface with a computer controls the system for data recording and processing. The gas supply requires additional equipment such as a carrier gas bottle, a hydrogen generator or bottle and an air compressor (not present in the picture). Usually, an automatic sampler for liquid samples is added to the equipment.

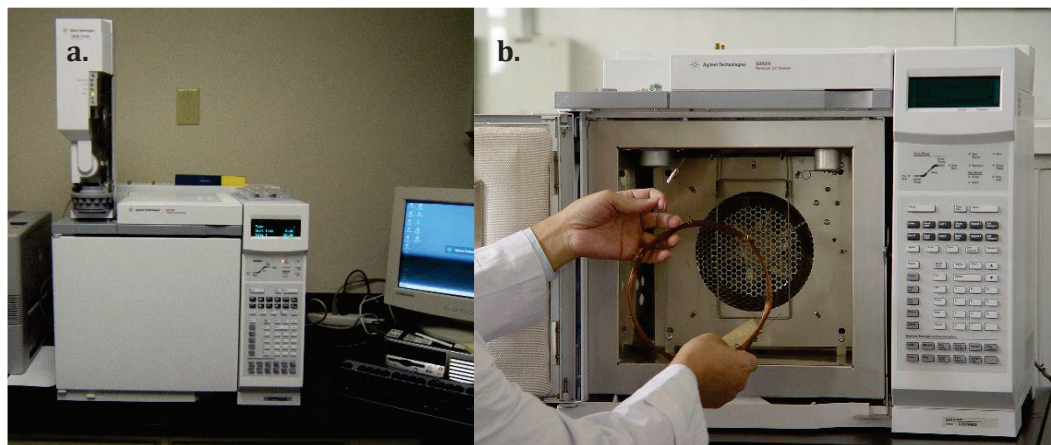


Fig. I.2 – Agilent 6890 gas chromatograph used in the laboratory. In (a) the oven door is closed and the auto-sampler is in place, and in (b) the oven cavity is open and we can see a typical capillary column, coiled into a cylinder.

It is obvious that such equipment is not portable, and analyses thus often require tedious transport of the sample to the laboratory. Due to the equipment price, the maintenance, the human operating, power and helium consumptions, GC apparatus is relatively expensive.

I.1.2.1. The injector

Fig. I.3 illustrates the usual configuration of the injection unit. The sample is injected with a syringe, handled manually or by a robot, through a septum into the pressurized gas liner. From there, a part of the sample goes directly in the column while the rest is evacuated in the split vent. The split ratio, which is the flow ratio between the column and the split vent, determines what fraction of the sample is really injected. A high split ratio, although it decreases the quantity of sample introduced, can help to reduce the injected peak dispersion as the sample is flushed faster from the glass liner. The septum purge is used to clean the septum between each injection in order to reduce sample pollution.

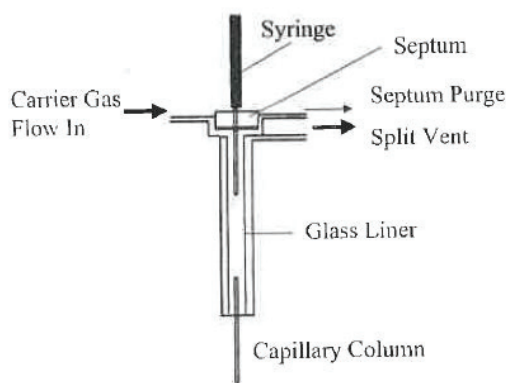


Fig. I.3 – Schematic of a split inlet from ref.¹ The sample is injected via the syringe, and only a fraction goes through the column while the remaining is evacuated through the split vent, improving peak sharpness.

In case of gaseous samples, it is also possible to use an injection valve system. In this case the sample is injected through a sample loop which is further switched to the main flow line for unloading the sample at the head of the GC column. Of course, recent advances in the field brought those injection systems to new levels of performances. Extremely short injection pulses (of the order of the millisecond) can be achieved through dual valve injection systems to fulfill the needs of ultra-fast GC.²⁻³ The miniaturization of the injector to a few centimeters square silicon chip is another technical breakthrough.⁴⁻⁷

However, such systems are not commercialized yet on standard apparatus and are not used in this work.

I.1.2.2. The detector

At the end of the column, the detector records the signal of the different compounds as they get out. The physical value detected depends of the detector's type.

I.1.2.2.1. Flame ionization detector (FID)

This type of detection is based on the generation of a voltage difference due to the ionization of the organic compounds in a hydrogen flame. The as obtained signal is proportional to the number of C-H bonds present in the ionization chamber. This Flame Ionization Detector (FID) is one of the most widely used as it is quite sensitive (low detection and quantification limits). However, it can only detect organic molecules and requires hydrogen supply, which can be a serious limitation towards portability.

Such detectors were successfully miniaturized to silicon chip dimensions by S. Zimmermann and his group.⁸⁻⁹

I.1.2.2.2. Thermal conductivity detector (TCD)

The Thermal Conductivity Detector (TCD) is based on the measure of the difference in thermal conductivity between the column flow and a carrier gas reference flow. It usually consists of four resistors forming a Wheatstone bridge, two of them being immersed in the main column flow and the two others in the reference flow. The resistors are continuously heated by a constant voltage, and as an analyte passes through the main flow line, it changes the thermal conductivity of the resistors' surroundings, thus changing their temperature and resistance value.

TCD generally shows poorer performances than FID, but is universal and can detect all analytes (except the carrier gas itself). Moreover, no other gases than the carrier one is required for GC analysis.

As such, TCD was used in the first miniaturized GC apparatus,⁴ and was extensively reported in the literature.¹⁰⁻¹⁴

I.1.2.2.3. Other types of detectors

Many other types of detector exist: optical, gravimetric, mass spectrometry (MS), *etc.* The latter is also widely used, as it gives information on the compounds mass and their fragmentation mechanism which allow to identify the molecular structure of unknown samples. Miniaturized and MEMS based MS detectors have also been reported.¹⁵⁻¹⁷

Other types of miniaturized detectors include MEMS gas sensors with gravimetric detection,¹⁸ such as the nano-cantilevers developed at the laboratory.¹⁹⁻²⁰

I.1.2.3. The column

GC columns are capillary tubings filled by an adsorbing material. Typical columns have inner diameters between 100 μm and 1 mm and lengths comprised between 5 cm to 50 m. As illustrated in Fig. I.4, columns are usually classified into three categories, depending if the adsorbing material is either packed in the column, or coated on its inner walls either in a liquid or in a solid form:

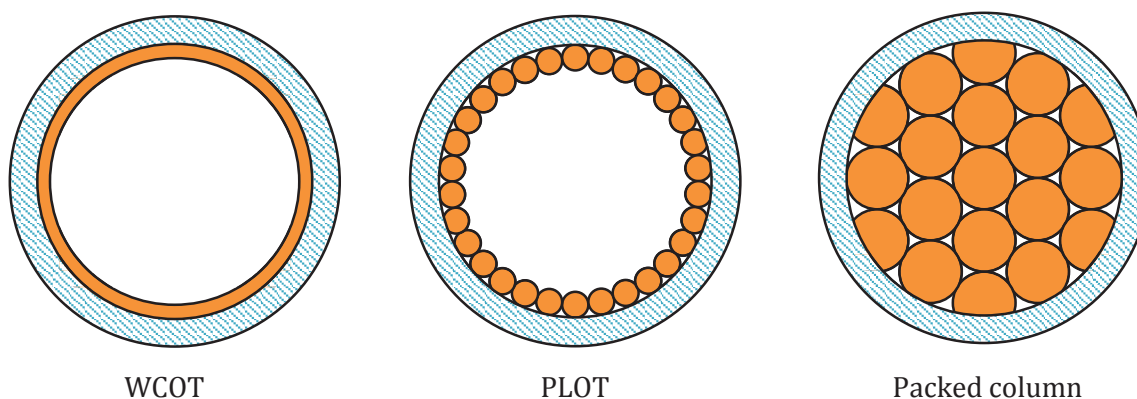


Fig. I.4 – Illustration of the three main types of GC columns: wall coated open tubular (WCOT), porous layer open tubular (PLOT) and packed columns. The stationary phase is represented in plain orange.

1.1.2.3.1. Packed columns

Packed columns are filled with a porous monolith or porous solid beads and retention involves surface physisorption. The columns' lengths are often short to compensate the high pressure drops induced by their low permeability.

They were the first columns used in GC, but were progressively replaced by open tubular columns, developed by M. Golay in 1957,²¹ and generalized in 1979 after the introduction of fused silica tubings.²²

Indeed, open tubular columns offer numerous advantages over packed columns, such as drastically improved resolutions, reduction of analysis time, smaller sample requirements and higher sensitivities.¹

1.1.2.3.2. Wall coated open tubular (WCOT) columns

WCOT columns are open tubular columns coated with a thin layer of gel adsorbent material. They are the most used type of GC column. Retention mechanism is assured by the dissolution of the analytes in the liquid polymeric stationary phase. They are usually relatively long thanks to their high permeability.

1.1.2.3.3. Porous layer open tubular (PLOT) columns

PLOT columns are also open tubular columns, but coated with a thin film of porous solid structure. Although they look quite similar to WCOT columns, their retention mechanism is quite different as the analytes are physisorbed onto the surface of the material. PLOT and WCOT columns have similar length but the stationary phase of the former is thicker.

I.1.3. Commonly used stationary phases

The GC column can be considered as the central part of the gas chromatograph, as it is responsible for separation. Considering its major impact on the success and the quality of the separation, the stationary phase is chosen in accordance with the sample to analyze.

In this work, we will focus our efforts on the separation of light alkanes (from C₁ to C₄/C₅) as they present a high interest for petrochemical industries. In the next paragraph, we will therefore present the main stationary phase families used in this application field.

I.1.3.1. Gels and liquids for WCOT columns

Contemporary liquid GC stationary phases belong to two main families, polysiloxanes and polyethylene glycol phases.

- Polysiloxanes are the most widely used stationary phases in GC.¹ They offer high solute diffusivities and excellent chemical and thermal stability. Because a variety of functional groups can be incorporated into the structure, they exhibit a wide range of polarities, from non-polar to polar phases.²³⁻²⁴ However, their use is limited to volatile compounds such as light alkanes (one to three carbons), unless used with a very long column to compensate the low retention coefficients.²⁵
- Polyethylene glycol phases are the major alternatives to polysiloxanes, due to their high polarity and unique selectivity.
- Among the other existing stationary phase for GC, it is worth noting the more recent advances on ionic liquid²⁶ and cyclodextrin²⁷ stationary phases.

These last families are generally used for the separation of more polar compounds or specific functionalized group¹ but are not really adapted to the separation of light volatile alkanes.

Overall, stationary phases with low polarity have the best inertness and compliance to high temperature and are preferably chosen if their separative power is sufficient.

I.1.3.2. Solid adsorbents for packed columns

Light hydrocarbons and permanent gases are traditionally separated on columns which are packed with adsorbing materials such as porous polymers, molecular sieves or carbonaceous materials.¹ Silica and alumina gel have also been reported.²⁸

Monolithic columns, although initially developed for gas chromatography,²⁹⁻³⁰ have acquired a major importance for high-performance electrochromatography or liquid

chromatography.³¹ They reemerged recently in GC, and were thoroughly studied by A. A. Korolev *et al.*³² Monolith made of silica,³³⁻³⁴ polydivinylbenzene³⁵⁻³⁸ or acrylate polymers³⁷⁻³⁹ were successfully prepared and used for fast separation of light hydrocarbons and permanent gases at relatively high pressure and with different types of carrier gas⁴⁰⁻⁴² (including less commonly used carbon dioxide and nitrogen dioxide).

Although packed and monolithic materials are well suited for the analysis of volatile mixture due to their low permeability,⁴³ they often require short column length (thus with a lower efficiency), or high working pressures (not available with standard GC apparatus). The fast analysis of light alkanes (methane to butane) that was reported in packed⁴⁴ and monolithic³³ columns has required the use of pressures as high as 64 or 82 bar (for analysis time of 0.15 and 15 s respectively).

I.1.3.3. Solid adsorbents for PLOT columns

PLOT columns usually use the same adsorbent materials as those used in packed columns but they also benefit from all the advantages of open tubular columns: i) greater efficiencies as predicted by M. Golay⁴⁵⁻⁴⁶ and ii) faster separations with fewer instrument requirements (lower pressures).⁴⁷

A review by Z. Ji *et al.* in 1999,⁴⁷ lists the principal PLOT stationary phases and applications. Light hydrocarbons separation is one of the major applications of PLOT columns and can be achieved with virtually all materials: alumina, silica, porous polydivinylbenzene polymers, molecular and carbon sieves.

A first approach for coating alumina adsorbents into a capillary column is the direct oxidation a thin layer of the column aluminum walls.⁴⁸ The second and more common approach is similar to the coating of liquid stationary phase: dissolution in a solvent, insertion and evaporation of the solvent.⁴⁹⁻⁵⁰

However in both cases, the as obtained stationary phase is quite thick (several μm) which firstly is not adapted to the functionalization of micro-fabricated narrow columns. Moreover it is believed that thinner film could open the way to faster analysis and column bleed reduction.⁴⁷

I.1.3.4. Sol-gel strategies for GC stationary phases

Sol-gel processes have already been widely used in electrochromatography⁵¹ and occasionally in GC⁵² to grow an intermediate silica layer between the capillary walls and the effective stationary phase. Adding this layer as two major advantages: i) roughness increase

of the capillary walls which increases the stationary phase surface, and ii) covalent bonding of the stationary phase to the column, thus limiting bleeding.

This technique was first reported in GC applications by Wang and coworkers.⁵³ It allowed the stabilization of PDMS stationary phases. It has also been used afterwards for the stabilization of polyethylene glycol,⁵⁴ crown ether,⁵⁵ cyclodextrin,⁵⁶⁻⁵⁷ or crown ether stationary phases.

However, examples of direct *in-situ* formation of the stationary phase are limited and include silica monoliths (see § I.1.3.2), alumina porous layers,⁵⁸ and one example of a mesostructured silica stationary phase.⁵⁹

I.1.4. Columns performances

I.1.4.1. The chromatogram

Fig. I.5 displays a typical chromatogram showing one un-retained and two retained compounds.

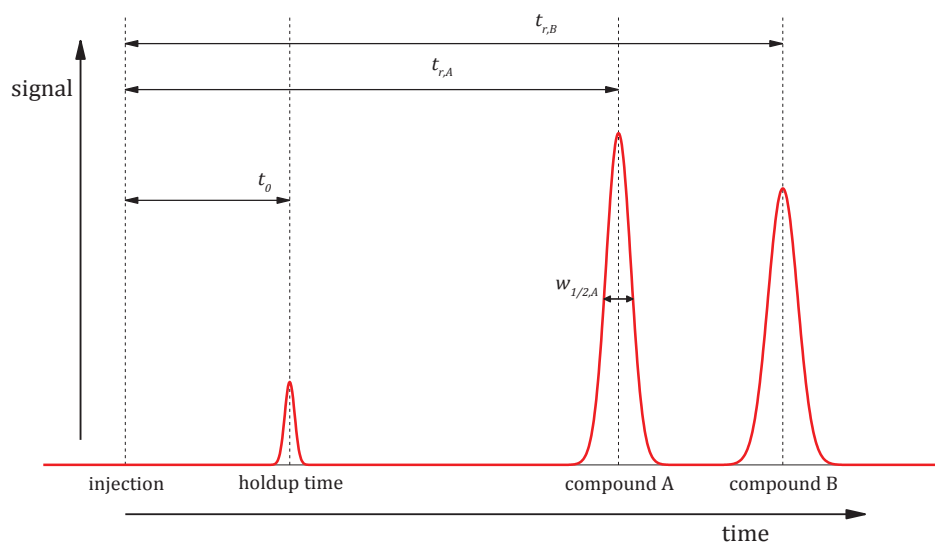


Fig. I.5 – Typical chromatograph of a sample with one un-retained and two retained compounds.

The un-retained compound peak is used to calculate the holdup time or dead time t_0 (average time needed for the carrier gas to go through the column) and with the column length L , the average speed \bar{u} can be obtained:

$$\bar{u} = \frac{L}{t_0} \quad I.1.$$

Supposing a laminar flow, one can also calculate these values knowing the geometry of the column, and the pressure used. Nowadays, most GC software programs give such values as directions, but the exact value can be subjected to instrumentation imprecisions. Moreover, for some geometries (such as square or rectangular micro-columns') or for packed columns, calculations can be difficult, approximate or even impossible.

From the retained compounds peaks, the determination of the retained time t_r and the half-height width $w_{1/2}$ gives a measure of peak thinness. Generally, the area under each peak is proportional to the injected quantity of each analyte (in the linear domain of the detector). For this purpose, it is often important that the two peaks of interest do not overlap. This criterion is measured by the resolution between two species:

$$R_{AB} = 1.18 \frac{t_{r,B} - t_{r,A}}{w_{1/2,A} + w_{1/2,B}} \quad I.2.$$

Two analytes are considered to be completely separated when $R_{AB} > 1.5^1$. However, in particular cases (compounds in similar quantities, high signal to noise ratio) a value of 1 or even 0.75 can be sufficient.

I.1.4.2. Thermodynamic evaluation

The ability of a column to retain a particular analyte is measured by a dimensionless number: the retention factor k . It is measured experimentally:

$$k = \frac{t_r - t_0}{t_0} \quad I.3.$$

Being always positive, k is close to 0 for species with few interactions with the stationary phase, and is high (and not limited) for species with a strong affinity. It is equal to the ratio of a component fraction in the stationary phase ($C_s.V_s$) on its fraction in the mobile phase ($C_m.V_m$), and thus is linked to the equilibrium constant of adsorption K :

$$k = \frac{C_s V_s}{C_m V_m} = \frac{K}{\beta} \quad I.4.$$

β represents the phase ratio, the ratio of the volume of the mobile phase on the volume of the stationary phase. However, measuring the exact volume of the stationary phase, especially for complex geometries (micro-columns) is difficult.

The equilibrium constant of adsorption of an analyte on the stationary phase is itself a function of i) $\Delta_r H^0$ and $\Delta_r S^0$, the standard enthalpy and entropy of the adsorption reaction

respectively and also ii) the temperature T (in K°) and the ideal gas constant R ($8.314 \text{ J.K}^{-1}.\text{mol}^{-1}$):

$$-RT \ln K = \Delta_r H^0 - T \Delta_r S^0 \quad I.5.$$

Consequently, the retention depends on the temperature of separation, and decreases as temperature increases. It is also possible to have access to the standard adsorption enthalpy by calculating the slope of the $\ln(k)$ plot as a function of $1/RT$ (referred as “Van’t Hoff plot”). The y-intercept of this plot corresponds to $\Delta_r S^0/R + \ln \beta$, and will be referred to $\ln k_\infty$ in this work (i.e. $\ln(k)$ at infinite temperature).

I.1.4.3. Adsorption properties of light hydrocarbons on silica

Hydrocarbons adsorption mechanism and thermodynamics on silica have been studied by various methods:⁶⁰⁻⁶⁷ chromatographic evaluation (Van’t Hoff plot), spectroscopy and microgravimetric measurements.

Interactions between the alkanes and silica are predominantly due to Debye forces. Debye forces are Van Der Waals weak intermolecular forces, which exist between a permanent dipole (polar silica) and an induced dipole (non-polar alkane molecules). Therefore, alkanes’ retention increases with their polarizability, which is proportional with the molecular size, the carbon number and the boiling point. Besides, the adsorption standard enthalpy of n-alkanes has been reported to vary linearly with carbon number,^{65, 67} as shown in Fig. I.6.

Another property of alkane adsorption on silica is the pronounced concave shape of the adsorption isotherm.⁶²⁻⁶⁴ In ideal GC, K is independent of the analyte’s concentration and the isotherm is linear, which leads to symmetrical peaks. However, a curved isotherm will result in a front tailing (convex isotherm), or, in our case of a concave isotherm, to peak tailing.

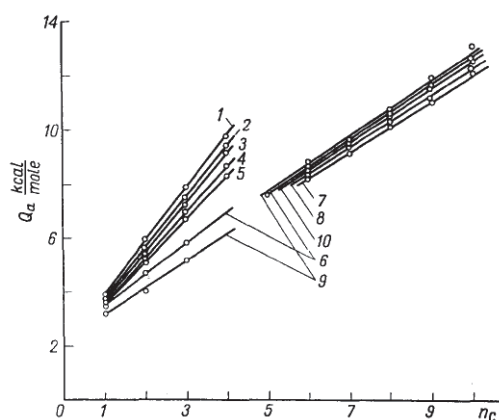


Fig. I.6 – Adsorption standard enthalpy of n-alkanes plotted vs. carbon number using silica gels with various pores diameters as stationary phases, from the work of A. Kiselev and Y. Yashin.⁶⁷ The mean diameter of the silica gel pores (in Å): 1 – 32; 2 – 46; 3 – 70; 4 – 104; 5 – 140; 6 – 250; 7 – 1100; 8 – 710; 9 – 1700; 10 – 4100.

I.1.4.4. Column efficiency evaluation – plate number and HETP

The resolving power of a column is traditionally defined as a number of theoretical plates, N . This definition comes from an analogy with distillation columns, which are assumed to be divided into a number of zones within which there is perfect equilibrium between gaseous and adsorbed analytes. Although this image is not valid for chromatographic columns, where separation is a continuous process along the column, it still gives a measurement of efficiency.

N is determined experimentally from an isothermal analysis using equation I.6:

$$N = 5.545 \left(\frac{t_r}{w_{1/2}} \right)^2 \quad I.6.$$

To compare the efficiency of two different columns, it is often preferable to use the Height Equivalent to a Theoretical Plate, HETP or H (i.e. N divided by the column length L), as it is independent of column length and thus more representative of the stationary phase. H is given in equation I.7.

$$H = \frac{L}{N} \quad I.7.$$

Using these definitions, resolution of two adjacent peaks can also be written as follows:

$$R_{AB} = \frac{1}{4} \sqrt{N} \frac{\alpha - 1}{\alpha} \frac{k_B}{k_B + 1} \quad I.8.$$

where α is the ratio of the retention coefficient k_B/k_A and B the later-eluted compound.

The first term of this equation (\sqrt{N}) indicates the need to maximize the number of plates on the column to achieve good separations. The second ($\frac{\alpha-1}{\alpha}$) and third ($\frac{k_B}{k_B+1}$) terms takes into account respectively the difficulty to separate peaks with similar retention factors (when $\alpha \rightarrow 1, \frac{\alpha-1}{\alpha} = 0$); and the difficulty to separate compounds that are only slightly retained (when $k_B \rightarrow 0, \frac{k_B}{k_B+1} = 0$).

I.1.4.5. Band broadening – Van Deemter equation

Plate theory predicts that chromatographic peaks have Gaussian shapes in optimal conditions. Thus, peak broadening is due to the sum of different phenomena, illustrated in Fig. I.7:

- A multi-path effect, A , also called Eddy diffusion. It results from the difference in path length followed by two different molecules along the column. This effect should *a priori* occur only in packed columns as molecules make their way around the obstacles; it is independent of velocity.
- The effect of longitudinal diffusion, B/u . As the sample travels through the column, it diffuses and spread along the column. It is proportional to the diffusion coefficient of the analyte in the carrier gas, D_m , and is inversely proportional to the average speed of the carrier gas: the fastest the analyte is carried through the column, the less time it has to diffuse.
- The resistance to mass transfer effect, $C.u$. It is the result of radial diffusion and variations in carrier gas speed through the column cross-section (carrier gas speed is maximum at the center of the column and null at the sides and in the stationary phase). It is composed of two terms; they are inversely proportional to the diffusion of the analytes in the carrier gas and in the stationary phase (the faster the analytes diffuse, the more homogenous is their average speed); and they are proportional to the average velocity of the carrier gas (the higher it is, the higher are the variations of velocity across the column cross-section)

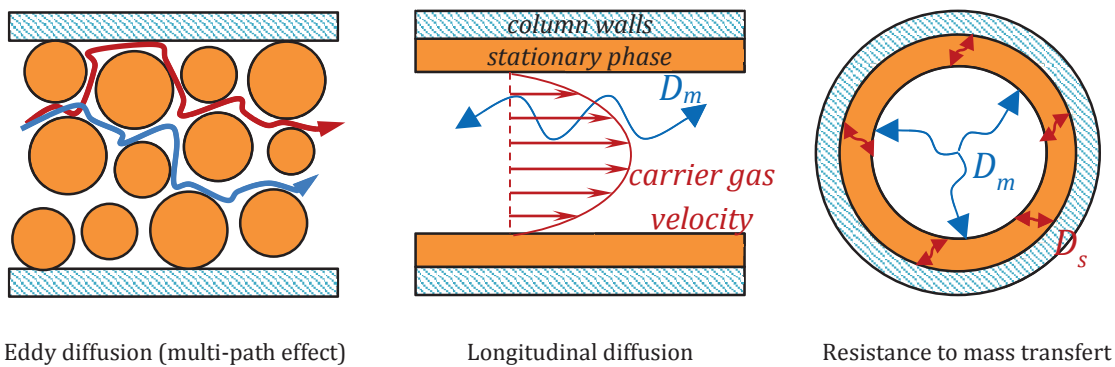


Fig. I.7 - Illustration of the three main phenomena responsible for band broadening in GC

These phenomena are represented in the Van Deemter equation (equation I.9), which is illustrated on Fig. I.8:

$$H = A + \frac{B}{u} + Cu \tag{I.9}$$

It is easy to see on the plot that the column efficiency goes through a minimum. This minimum corresponds to the mobile phase optimal velocity at which the column shows the maximum of theoretical plates, and thus the best separation properties.

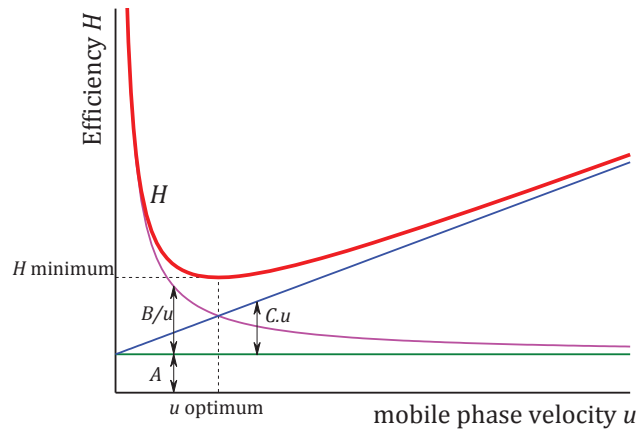


Fig. I.8 – Van Deemter plot of column HETP (or H , in red) as a function of mobile phase average velocity u , illustrating the contributions of the three phenomena responsible for band broadening.

I.1.4.6. Open tubular column efficiency – Golay equation

In our work, we will exclusively use open tubular columns, so the Eddy diffusion coefficient of the Van Deemter disappears. However, the equation is not necessarily simplified, as we have to take into account several other parameters such as the gas compressibility and the extra-column band broadening.

In open tubular round-cross-section capillary columns, H is given by the extended Golay equation I.10:⁴⁵⁻⁴⁶

$$H = \frac{2D_m}{u} jf + \frac{1 + 6k + 11k^2}{24(k + 1)^2} \frac{r^2}{D_m} u \frac{f}{j} + \frac{2k}{3(k + 1)^2} \frac{d_s^2}{D_s} u + \frac{\Delta t^2}{L(k + 1)^2} u^2 \quad I.10.$$

Or in shortened form as:

$$H = \frac{B}{u} jf + \left(C_m \frac{f}{j} + C_s \right) u + Du^2 \quad I.11.$$

Where j and f are respectively the Martin-James and Golay-Giddings gas compression factors, k the retention coefficient of the analyte, r and L the radius and length of the column respectively, d_s the thickness of the stationary phase, D_m and D_s the coefficient of diffusion of the analyte in the mobile and stationary phase respectively and Δt the time dispersion of the analyte peak at the entry of the column (also referred as extra-band broadening).

The shortened form takes the same form as the Van Deemter equation, but with i) the A term equal to zero, ii) the added gas compressibility effects, and iii) a D term which accounts

for extra band broadening. This equation form also makes the distinction between resistance to mass transfer occurring in the mobile phase (C_m) and in the stationary phase (C_s).

The gas compression factors j and f are defined in equations I.12 and I.13 respectively, with P being the ratio of the column inlet pressure on the outlet pressure.

$$j = \frac{3(P^2 - 1)}{2(P^3 - 1)} \quad I.12.$$

$$f = \frac{9(P^4 - 1)(P^2 - 1)}{8(P^3 - 1)^2} \quad I.13.$$

Few parameters can be played with to optimize the column efficiency. The most evident one is to minimize extra-band broadening effects but it is not always so easy, especially for short columns with poorly retained compounds. The second possibility is to choose a thin stationary phase in which the analytes diffuse rapidly, thus reducing the C_s term. It is possible to reduce C_m to a certain extent with narrow bore columns (small diameter), as they generate higher pressure drops and have smaller capacities. The only way to reduce B is to change the carrier gas to change the diffusion coefficient of the analyte, but it has the opposite effect on C_s and C_m .

The typical contribution to band broadening of each term of the Golay equation is illustrated on Fig. I.9 with arbitrary values for the coefficients. We see that the extra-column band dispersion can be relatively important at high velocities, especially for poorly retained analytes (see equation I.10). We can also note that the contributions of the resistance to mass transfer from the mobile and the stationary phases now differ in form. Thus, the asymptote form of the Golay plot at high velocities can give information on the potential limiting mechanism responsible for band broadening (asymptote linear with u or u^2).

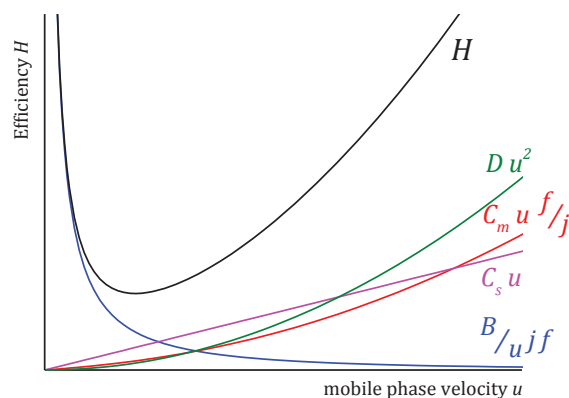


Fig. I.9 – Golay plot of column efficiency H (in black) against mobile phase average velocity u , illustrating the different contributions to band broadening.

All parameters of the extended Golay equation depend on physical characteristics of the analyte and of the mobile and the stationary phases.

I.1.4.7. Column capacity

Of course, there are also other parameters that are susceptible to adversely affect column efficiency, such as sample overloading. Overloading is caused by an excess of injected analyte that saturates the stationary phase. This often results in broader peaks with front or peak tailing and reduced efficiency.

The maximum analyte quantity that it is possible to inject in a column without overloading it is called column capacity. It is usually large enough for most samples in classic GC applications, although it is often an issue for the short columns used in fast GC.

I.2. Towards portable GC

As seen in paragraph I.1.2, a gas chromatograph is quite bulky, expensive and unsuited to portable use. As we will see now, there are already a few miniaturized gas chromatographs that are commercially available and designed for a portable use. However, further miniaturization of the different compounds, especially the column, is still needed in order to further reduce costs and power consumption (optimization of the thermal management) but also to improve system integration. Thus, there is a need for new stationary phases and coating processes compatible with miniaturized columns, particularly for the separation of light volatile alkanes.

I.2.1. The quest for miniaturization

GC miniaturization opens the way to low cost and low gas / power consumption portable devices. Allowing on-site analyses, the risk of potential sample integrity loss during storage and transport would be minimized. Thus, many of the recent developments in GC deal with the miniaturization of the different components of the chromatograph (injector, detector, and mainly the column and its thermal management), as revealed by recent reviews in this field.⁶⁸⁻⁷⁷

Cited applications are numerous, and include for example the analysis of the atmosphere of enclosed spaces and compartments (car passenger compartment, household), the analysis of surface waters and soils, the detection of explosives and chemical warfare components, and the on-field real-time monitoring of oil contents.

I.2.1.1. Commercialized micro-GC

As a result of the recent advances in GC miniaturization, a number of portable GC devices are now commercialized by various companies: some examples are presented in Fig. I.10. These devices were developed thanks to i) the size reduction of some components of the gas chromatograph (injection system, valves, actuators, column, detector and electronics components...), ii) the use of air as carrier gas or small pressurized bottles and iii) the integration of batteries and on-board electronics.

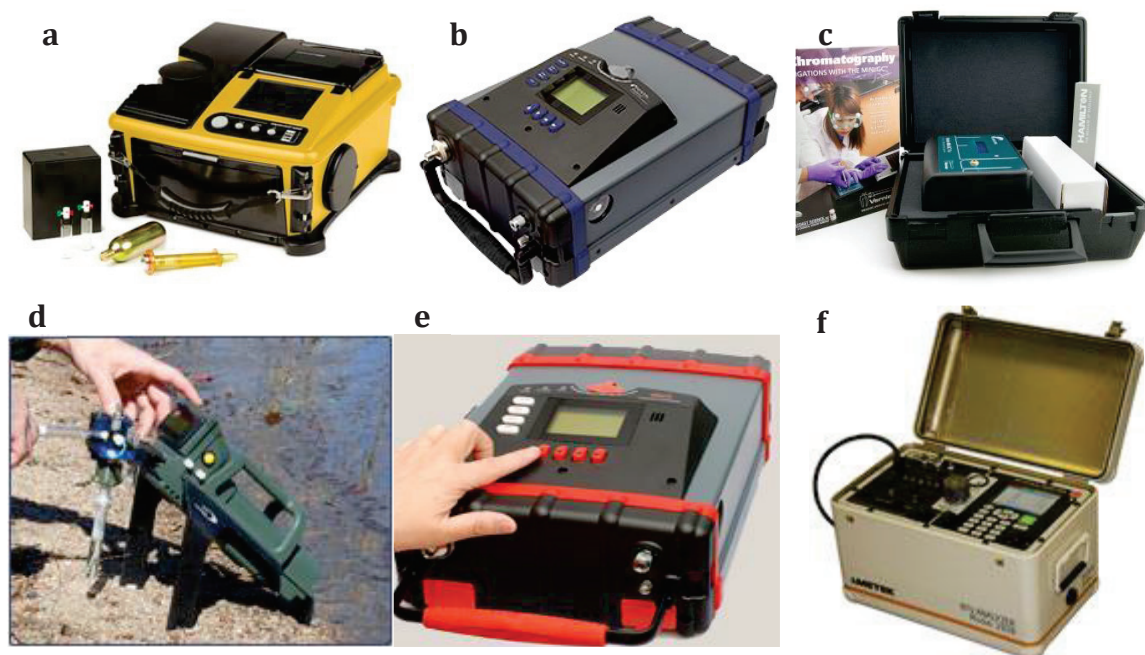


Fig. I.10 – Examples of recently commercialized portable gas chromatographs: (a) Torion portable GC-MS Tridion™, (b) Inficon portable GC Explorer™, (c) Vernier Mini GC plus™ for college and high-school experiments, (d) Defiant portable GC for air, soil and water analysis FROG 4000™, (e) Airmet Explorer GC system and (f) Ametek 292B Portable Natural Gas Chromatograph.

This major advance enables GC analyses to be performed almost anywhere, with apparatus of reduced cost, but such apparatus still face some limitations: autonomy of only a few hours and a lack of sensitivity. Moreover, devices prices are usually still above 30k€, and the separations are mostly isothermal, thus limiting the number of analytes to be analyzed and increasing the analysis time.

I.2.1.2. Toward the next generation of portable devices

The perspectives given to miniaturized GC systems are numerous and could overcome these limitations. The integration of multiple micro-fabricated components such as micro-preconcentrators,⁷⁸⁻⁸² micropumps and microvalves,⁸³⁻⁸⁵ injectors,⁴⁻⁷ and detectors,⁸⁻¹⁴ would lead to further miniaturization of the whole system with a reduced power consumption and the possibility of reduced production costs associated with batch fabrication. Additionally resistive heating of micro-fabricated columns could open the way to fast thermal management with low power consumption⁶⁹⁻⁷¹ (*vide infra*).

Although commercial portable equipments already include some of these miniaturized components on silicon, micro-fabricated columns are mostly reserved for lab developments because they do not yet propose the same advantages as capillary columns in term of stationary phase versatility and efficiency.⁶⁸

In particular, since the first micro-fabricated column in the late 1970's,⁴ most of the work was focused on intermediate molecular weight hydrocarbons separation, with 5 or more carbon atoms; only a few recent articles being dedicated to lighter hydrocarbons, but with moderate efficiencies.⁸⁶⁻⁹⁰ Thus, there is still a need for stationary phase developments and optimizations.

I.2.2. Micro-columns

I.2.2.1. Micro-column fabrication process

I.2.2.1.1. The column etching process

In 1979, S. C. Terry and coworkers⁴ reported the fabrication of a whole GC device (injector, column and TCD detector) on a single silicon wafer (Fig. I.11). The 1.5 m long column, 200 μm wide and 30 μm deep was fabricated on a 200 μm thick and 5 cm diameter wafer using photolithographic technologies:

A layer of silicon dioxide, approximately 1 μm thick, was thermally grown on the wafer. Using a standard photoresist and photolithography process, a spiral pattern was defined on the front side of the wafer and the oxide was further removed following this pattern, exposing the silicon surface. The wafer was exposed to an isotropic silicon etching solution, thus yielding a spiral trench of 30 μm deep. The wafer was then re-oxidized and through holes were defined and etched for connections with a similar photolithography process, except that an anisotropic etchant was utilized to minimize the volume of these holes. The wafer was then cleaned, stripped of all oxide and anodically bonded to a Pyrex cover plate, transforming the trench into an enclosed channel. A commercial OV-101 (PDMS) stationary phase was then coated on the inner walls using a standard static coating process (dissolution in a solvent, filling the channel with the solution, removal of the solvent).

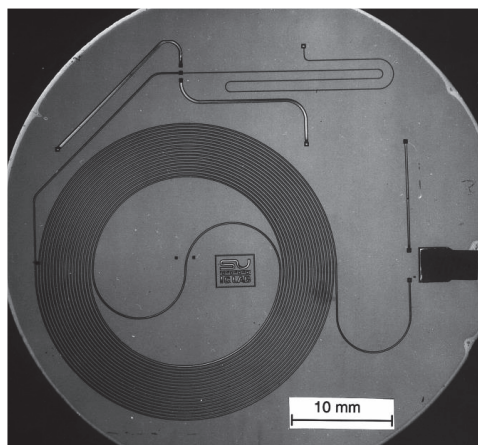


Fig. I.11 – Photograph of a gas chromatograph integrated on a planar silicon wafer fabricated by C. Terry and coworkers at Stanford University.⁴

The introduction of the coating material in its liquid form yielded a condensation phenomenon at corners and curvatures leading to a non-homogeneous layer coverage and thus to poor column performances. Yet, liquid coating remained the main coating process, as several attempts were undertaken to generate more homogeneous coverage, by adding column pretreatment, or changing the viscosity of the coating solution.

Nevertheless, several technologies were developed to avoid the strongly asymmetric semi-circular channels obtained with isotropic etching. The fabrication of quasi-circular channels was developed by two main routes: buried column technology⁹¹⁻⁹² and wafer-wafer aligned bonding.⁹³ However, these technologies imply complex processes with the addition of multiple steps or alignment constraints that are not easy to settle concomitantly.

The anisotropic technology deep reactive ion etching has been used with similar fabrication steps as that developed in 1979, and resulted in the fabrication of square and rectangle channels.⁹⁴ The advantages of such channels are the space gain on the wafer for columns of identical cross-section and length and the possibility to choose the column width independently of the section area, with potential theoretical advantages⁹⁵ (i.e. the possibility to control separately the column's efficiency and flow by choosing respectively the width and depth of the channel).

Another advantage is the possibility to create various high aspect ratio structures such as micro pillars inside the channel bed as described by various authors.⁹⁶⁻⁹⁷

1.2.2.1.2. Stationary phase deposition

Stationary phase deposition in such micro-fabricated column is possible through two different pathways, as illustrated on Fig. I.12. The most reported route (a) is to close the etched channel by bonding a cover plate to a silicon chip first and then to introduce the

stationary phase inside the column. This route is particularly adapted to liquid coating processes as it is easy to fill the channel with a liquid before evaporating the solvent. This route can also be used to produce packed columns by packing particles inside the channel or with vapor processes for growing carbon nanotubes. The advantage of this method is that the stationary phase deposited does not have to go through the process of cover bonding which could alter it (as an example, anodic bonding requires temperature over 350°C and the use of a high voltage).

The second route (b) has the main advantage to be a collective fabrication process (all the column on one wafer can be treated simultaneously). Here, the stationary phase is deposited before the bonding of the cover plate, mostly through a vapor process (chemical vapor deposition, plasma enhanced vapor deposition, sputtering...) although liquid processes have been reported (layer by layer coating for example).

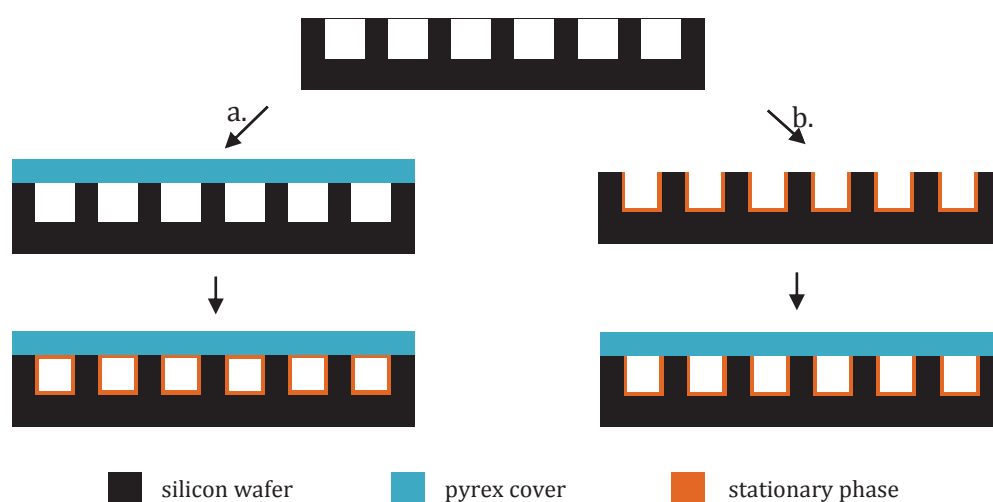


Fig. I.12 - Illustration of the two main route for stationary phase deposition in a micro-fabricated column (cross-sectional view of the substrate). (a) The column is sealed by a cover plate and the stationary phase is introduced in the channel. (b) The stationary phase is deposited on the silicon wafer before sealing the cover plate.

I.2.2.2. Major stationary phases for micro-columns

An exhaustive review of the different stationary phases reported for GC micro-fabricated columns was published recently by I. Azzouz and co-workers.⁶⁸ Most of the works presented in the next paragraphs are taken from this reference publication and completed with few recent relevant articles.

I.2.2.2.1. Polymer based stationary phases

Liquid and gel stationary phases are the phases that have received most of the attention since the pioneering work of S. C. Terry.⁴ Mainly, commercial PDMS and derivative stationary

phases with various polarities were used in a vast majority.^{94, 98-105} The applications of such columns are the separation of volatile organic compounds (VOC) or various other moderately volatile organic molecules (with 5 or more carbon atoms). However, despite the efforts put into the realization of conform film depositions with only minimal corner pooling, the best efficiencies reported do not exceed 5500 theoretical plates per meter¹⁰² on open tubular designs.

These performances were improved by the use of semi-packed or small width multi-channel designs for the micro-columns,^{97, 106} improving sample capacity and efficiency up to 10,000 th.p./m, but still for heavier hydrocarbons.

The separation of light alkanes (methane to butane) was reported once on a PECVD deposited PDMS stationary phase, but the micro-column needed to be cooled down to 10°C in order to achieve an acceptable separation of methane and ethane.⁹⁰

An effective way of increasing the column efficiency was developed by M. Agah *et al.* at Virginia Tech.¹⁰⁷⁻¹⁰⁹ They settled a process to coat a monolayer of octadecylthiol on an intermediate gold layer using sulfur-gold bondings. The high homogeneity of the organic layer and the absence of corner pooling on channels with a high aspect ratio resulted in really very high efficiencies: 20,000 th.p./m.¹⁰⁹ The same method was implemented to multicapillary channels and resulted in lower efficiency but higher column capacity¹⁰⁷. Finally, this thiol-gold technology also enabled the use of other thiol functionalized stationary phase such as highly polar 6-mercapto-1-hexanol for the separation of alcohol and other polar compounds.¹¹⁰ However, this type of stationary phase was intended for high boiling point compounds.

1.2.2.2.2. *Packed solid stationary phases*

It is possible to pack micro-fabricated columns with commercial adsorbents traditionally used for packed columns. The process is often tedious, as the column is usually filled under vacuum with constant mechanical shaking.^{87, 111} A mixture of CO₂, methane, ethane and ethylene was separated with a 75 cm column packed with Carboxen 1000 at 60°C in 8 min.⁸⁷ The column yielded 900 th.p. (1200 th.p./m). Aromatic volatile compounds' separations with packed micro-columns were also reported.

In a recent PhD thesis,¹¹² silica porous monoliths for micro-fabricated columns were developed and they allowed methane to n-butane separation in 2 minutes with 1750 th.p./m in a 1 m long channel. In this case no packing stage was necessary: the porous silica synthesis was performed *in situ* and enabled to fill the whole channel section

I.2.2.2.3. Porous layer stationary phases

Porous layered open tubular micro-fabricated-columns are rarely described in the literature. Carbon nanotubes were used for their high surface-to-volume ratio and their chemical and thermal stability. Fast GC separations of heavy hydrocarbons (more than C₆) were reported with high speed temperature programming.¹¹³⁻¹¹⁴ However, it did not offer enough retention for permanent gases and light alkanes separations, although a patent from B. Bourlon *et al.* suggested this possibility.¹¹⁵

J. Vial and coworkers proposed a very interesting route for porous thin film deposition in micro-fabricated columns by sputtering.⁸⁸ Various materials were deposited, including graphite,¹¹⁶ alumina⁸⁹ and silica.^{88-89, 116} Silica coated columns coated showed the best results for light alkanes separations. Methane to n-pentane were separated in 50 seconds on 2.2 m long columns, and the separation time was further reduced to 7 s with proper thermal management. These results confirm that a silica stationary phase is a promising candidate for the separation of volatile compounds. However, relatively thick layers of sputtered silica were used to ensure the complete separation of ethane from methane, and efficiencies were limited to 2500 th.p./m for open tubular designs. It was increased to 5000 th.p./m with a semi-packed design⁸⁸ but a loss of permeability was observed and the use of higher pressures was needed.

It is also worth noting the development of PLOT micro-columns by D. Wang and coworkers.¹¹⁷ Here, a thin layer of porous silica was deposited onto the walls of micro-columns with a “layer-by-layer” process, by alternatively dipping them in a polyelectrolyte solution and a silica nanoparticles solution. The as-obtained silica layer was further grafted with some alkyl chains (octadecyl) through a silanization reaction and the columns were used to separate organochloride or hydrocarbons with high boiling points (C₁₀ to C₁₇).

Such an approach could be used with mesoporous particles to form a mesoporous silica thin film susceptible to separate light alkanes. This idea will be developed in chapter V.

I.2.2.3. Temperature management of micro-fabricated columns

I.2.2.3.1. Temperature management technologies

Traditionally, capillary columns are wound in coil and placed in an oven for temperature programming. Due to their volume (around 10 dm³), conventional GC ovens generally have high power consumption (>2000 watt) and are limited to low heating rate and long cooling times between two analyses. Temperature programming is usually limited to 40°C/min to 100°C/min.¹¹⁸

Resistive heating is a good alternative to provide fast and low power consumption thermal management. It has already been implemented with success to capillary columns^{3,69-71} with heating rates as high as 240°C/s.³ Despite some disadvantages including complex manufacturing, inconvenient column maintenance and sometimes efficiency losses due to uneven heating,⁷⁰ thermal management implementation shows a real potential for portable GC applications to speed up analysis time and enhance the range of compounds to be analyzed.

1.2.2.3.2. *Micro-fabricated column resistive heating*

One of the advantages of micro-fabricated columns technology is the facility to implement efficient thermal management by resistive heating.⁷¹ Resistive heating generally consists of metallic filaments deposited directly on the chip by electro- or plasma-deposition. Metals usually used are gold, platinum, tungsten and chromium-nickel alloys chosen for their compatibility with the micro-electronic deposition techniques, their high conductivity and their resistance to oxidation. Fast and homogeneous chip heating systems with low power consumption (< 20 watt) were obtained in various works, achieving heating rates between 10 and 60°C/s.^{100, 113-114, 116, 119}

Of course, such fast temperature management requires a cooling system to bring the column back to its initial temperature in a short time as well, before any further analysis can be undertaken. Indeed, if cooling time is too long, reducing only analysis time won't increase the analysis rate. However, such systems have been poorly reported excepted for some mentions of Peltier devices.^{70, 93}

1.2.3. Micro-column evaluation

1.2.3.1. Modification of the Golay equation coefficients

Standard theories for open-tubular GC columns (see § I.1.4.6), assume circular cross-section columns and thus are not applicable to micro-columns fabricated through a DRIE process. The theory for rectangular channels was described in various studies by M. Golay,¹²⁰ J. Giddings and coworkers,¹²¹ G. Spangler,¹²²⁻¹²⁴ and H. Ahn and S. Brandani.¹²⁵

These works suggest that the C_m term of the resistance to mass transfer in the mobile phase changes as the result of the new geometry. Equation I.14 presents the form of C_m :

$$C_m = \frac{A + B k + C k^2}{96(k + 1)^2} \frac{w^2}{D_m} \quad I.14.$$

In the equation, w is the width (smaller dimension) of the channel or the diameter for circular geometries. The values of coefficients A , B and C are summarized in Table I-1; α being equal to 1 and to ∞ for square or rectangular channels with infinite height (α stands for the ratio between the long and the small lengths of the cross-section).

	Golay ^{46, 120}		Giddings ¹²¹	Spangler ¹²²	Ahn et Bradani ¹²⁵	
	capillary	$\alpha = \infty$	$\alpha = \infty$	$\alpha = \infty$	$\alpha = 1$	$\alpha = \infty$
A	1	7.48	0.9	0.9	1.608	7.269
B	6	*	8.3	2	9.220	41.11
C	11	*	25.5	35	15.61	65.84

Table I-1 – Comparison of the A, B and C terms of eq I.14 found in the literature. *no value given for B and C (the model was developed for un-retained compounds)

The most recent theory developed by H. Ahn *et al.*¹²⁵ proposes coefficients that vary as a function of α and takes into account the influence of the aspect ratio on the gas flow but also on the interactions between the analyte and the stationary phase.

I.2.3.2. Influence of the capillary connections

Even if micro-fabricated columns are eventually integrated in micro-electro-mechanical systems with only minimal dead volume losses in the connections, most columns require capillary connections for linking to other components of the chromatograph (injector and detector). As most micro-columns are dedicated to fast analyses, their length is usually small, and the length of the capillary connections is no more negligible. Moreover, it is not always possible to coat the column without coating the connections, which makes it hard to evaluate the intrinsic performances of the micro-column.

Connections have an influence on the average velocity of the mobile phase, especially as the average velocity can be very different between the column and the connection depending of their geometry. The connections also add extra column band broadening and reduce the column's efficiency. It can be calculated using equation I.11, with $k = 0$, as there is usually no retention in the connections. Experimental observations will be given in Chapter IV.

I.3. Conclusion

In this chapter, we have described the general principles of GC and the main components of a gas chromatograph, including the injector, the detector and the column. Columns are generally classified into three categories, depending of the nature of their stationary phase. WCOT columns are the most common type of columns and are perfectly adapted to the separation of compounds with moderate to low volatility. However, the separation of lighter compounds and permanent gases would necessitate the use of extremely long columns and is not compatible with fast and portable GC.

Light alkanes and permanent gases are commonly separated with packed or PLOT columns. Packed columns generally show low permeability and thus require the use of higher pressures and have often a poorer resolution than PLOT columns. Among PLOT columns, silica is often used as a stationary phase for light alkanes separation, and the manufacture of thinner silica layers is believed to help the bleed reduction and the increase of columns performances.

Columns performances are generally evaluated according to Golay's theory of the HETP, which is an extension of Van Deemter's theory for open tubular columns. The affinity between the stationary phase and the analyte can also be evaluated with Van't Hoff plots that give access to the standard enthalpy of the adsorption reaction.

In the last part of the chapter, the development of micro-fabricated columns and their strong potential for portable GC systems is highlighted. The micro-fabricated columns are usually manufactured with standard micro-electronic processes, with different geometries with respect to those of capillary columns. As a result, stationary phase coating presents several challenges among which the stationary phase pooling in the corners, which is detrimental for efficiency. Most developments aiming at reducing this phenomenon were mostly dedicated to gel and liquid coatings, which are not adapted to the separation of volatile compounds such as light alkanes.

Besides, some works were dedicated to the development of solid coatings, such as silica or alumina, which are traditionally used for these types of separations. These works comprise packed micro-columns and the recent work of J. Vial and coworkers on sputtered silica. Silica appears to be a promising candidate for light alkanes' separation, especially if a thin and highly porous layer (thus more retentive) could be deposited.

Finally, we have seen how the Golay theory is impacted by the micro-fabricated columns geometry and how extra column broadening due to connections can be taken into account.

In the next chapter, we will show our results concerning the coating of capillary columns with mesostructured silica thin films by a sol-gel process using a templating route. We will present our experimental set-up designed for capillary columns coatings and the process' parameters influencing the stationary phase thickness and the chromatographic performances.

I.4. References

1. Grob, R. L.; Barry, E. F., *Modern Practice of Gas Chromatography*. Wiley: **2004**.
2. Gross, G. M.; Prazen, B. J.; Grate, J. W.; Synovec, R. E., *Analytical Chemistry* **2004**, *76* (13), 3517-3524.
3. Reid, V. R.; McBrady, A. D.; Synovec, R. E., *Journal of Chromatography A* **2007**, *1148* (2), 236-243.
4. Terry, S. C.; Jerman, J. H.; Angell, J. B., *IEEE Transactions on Electron Devices* **1979**, *26* (12), 1880-1886.
5. Dziuban, J. A.; Mróz, J.; Szczygielska, M.; Małachowski, M.; Górecka-Drzazga, A.; Walczak, R.; Buła, W.; Zalewski, D.; Nieradko, Ł.; Łysko, J.; Koszur, J.; Kowalski, P., *Sensors and Actuators A: Physical* **2004**, *115* (2-3), 318-330.
6. Nachef, K.; Marty, F.; Donzier, E.; Bourlon, B.; Danaie, K.; Bourouina, T., *Journal of Microelectromechanical Systems* **2012**, *21* (3), 730-738.
7. Nachef, K.; Bourouina, T.; Marty, F.; Danaie, K.; Bourlon, B.; Donzier, E., *Journal of Microelectromechanical Systems* **2010**, *19* (4), 973-981.
8. Zimmermann, S.; Wischhusen, S.; Müller, J., *Sensors and Actuators, B: Chemical* **2000**, *63* (3), 159-166.
9. Zimmermann, S.; Krippner, P.; Vogel, A.; Müller, J., *Sensors and Actuators, B: Chemical* **2002**, *83* (1-3), 285-289.
10. Sorge, S.; Pechstein, T., *Sensors and Actuators, A: Physical* **1997**, *63* (3), 191-195.
11. Yu, C. M.; Lucas, M.; Koo, J. C.; Stratton, P.; DeLima, T.; Behymer, E. In *High performance hand-held gas chromatograph*, American Society of Mechanical Engineers, Dynamic Systems and Control Division (Publication) DSC, 1998; pp 481-486.
12. Cruz, D.; Chang, J. P.; Showalter, S. K.; Gelbard, F.; Manginell, R. P.; Blain, M. G., *Sensors and Actuators, B: Chemical* **2007**, *121* (2), 414-422.
13. Narayanan, S.; Agah, M., *Journal of Microelectromechanical Systems* **2013**, *22* (5), 1166-1173.
14. Kaanta, B. C.; Chen, H.; Lambertus, G.; Steinecker, W. H.; Zhdaneev, O.; Zhang, X. In *High sensitivity micro-thermal conductivity detector for gas chromatography*, Proceedings of the IEEE International Conference on Micro Electro Mechanical Systems (MEMS), 2009; pp 264-267.
15. Pau, S.; Pai, C. S.; Low, Y. L.; Moxom, J.; Reilly, P. T. A.; Whitten, W. B.; Ramsey, J. M., *Physical Review Letters* **2006**, *96* (12).
16. Blain, M. G.; Riter, L. S.; Cruz, D.; Austin, D. E.; Wu, G.; Plass, W. R.; Cooks, R. G., *International Journal of Mass Spectrometry* **2004**, *236* (1-3), 91-104.
17. Badman, E. R.; Cooks, R. G., *Journal of Mass Spectrometry* **2000**, *35* (6), 659-671.
18. Fanget, S.; Hentz, S.; Puget, P.; Arcamone, J.; Matheron, M.; Colinet, E.; Andreucci, P.; Duraffourg, L.; Meyers, E.; Roukes, M. L., *Sensors and Actuators, B: Chemical* **2011**, *160* (1), 804-821.
19. Arcamone, J.; Niel, A.; Gouttenoire, V.; Petitjean, M.; David, N.; Barattin, R.; Matheron, M.; Ricoul, F.; Bordy, T.; Blanc, H.; Ruellan, J.; Mercier, D.; Pereira-Rodrigues, N.; Costa, G.; Agache, V.; Hentz, S.; Gabriel, J. C.; Baleras, F.; Marcoux, C.; Ernst, T.; Duraffourg, L.; Colinet, E.; Myers, E. B.; Roukes, M. L.; Andreucci, P.; Ollier, E.; Puget, P. In *VLSI silicon multi-gas analyzer coupling gas chromatography and NEMS detectors*, Technical Digest - International Electron Devices Meeting, IEDM, 2011; pp 29.3.1-29.3.4.
20. Martin, O.; Gouttenoire, V.; Villard, P.; Arcamone, J.; Petitjean, M.; Billiot, G.; Philippe, J.; Puget, P.; Andreucci, P.; Ricoul, F.; Dupré, C.; Duraffourg, L.; Bellemin-Comte, A.; Ollier, E.; Colinet, E.; Ernst, T., *Sensors and Actuators, B: Chemical* **2014**, *194*, 220-228.
21. Golay, M. J. E., *Analytical Chemistry* **1957**, *29* (6), 928-932.
22. Dandeneau, R. D.; Zerenner, E. H., *Journal of High Resolution Chromatography* **1979**, *2* (6), 351-356.
23. Haken, J. K., *Journal of Chromatography A* **1977**, *141* (3), 247-288.
24. Haken, J. K., *Journal of Chromatography A* **1984**, *300* (C), 1-77.
25. Averill, W.; Ettore, L. S., *Nature* **1962**, *196* (4860), 1198-1199.
26. Vidal, L.; Riekkola, M. L.; Canals, A., *Analytica Chimica Acta* **2012**, *715*, 19-41.
27. Xiao, Y.; Ng, S. C.; Tan, T. T. Y.; Wang, Y., *Journal of Chromatography A* **2012**, *1269*, 52-68.
28. Greene, S. A., *Analytical Chemistry* **1957**, *29* (7), 1055.
29. Schnecko, H.; Bieber, O., *Chromatographia* **1971**, *4* (3), 109-112.

30. Hileman, F. D.; Sievers, R. E.; Hess, G. G.; Ross, W. D., *Analytical Chemistry* **1973**, 45 (7), 1126-1130.
31. Guiochon, G., *Journal of Chromatography A* **2007**, 1168 (1-2), 101-168.
32. Svec, F.; Kurganov, A. A., *Journal of Chromatography A* **2008**, 1184 (1-2), 281-295.
33. Korolev, A. A.; Shiryayeva, V. E.; Popova, T. P.; Kurganov, A. A., *Journal of Analytical Chemistry* **2007**, 62 (4), 313-318.
34. Korolev, A. A.; Popova, T. P.; Shiryayeva, V. E.; Kurganov, A. A., *Russian Journal of Physical Chemistry A* **2005**, 79 (3), 457-460.
35. Korolev, A. A.; Shiryayeva, V. E.; Popova, T. P.; Kozin, A. V.; D'Yachkov, I. A.; Kurganov, A. A., *Polymer Science - Series A* **2006**, 48 (8), 779-786.
36. Viktorova, E. N.; Korolev, A. A.; Ibragimov, T. R.; Kurganov, A. A., *Polymer Science - Series A* **2012**, 54 (5), 385-392.
37. Kanatyeva, A.; Korolev, A.; Shiryayeva, V.; Popova, T.; Kurganov, A., *Journal of Separation Science* **2009**, 32 (15-16), 2635-2641.
38. Shiryayeva, V. E.; Popova, T. P.; Korolev, A. A.; Dianov, M. E.; Kurganov, A. A., *Petroleum Chemistry* **2011**, 51 (4), 308-310.
39. Viktorova, E. N.; Korolev, A. A.; Ibragimov, T. R.; Kanat'Eva, A. Y.; Kurganov, A. A., *Polymer Science - Series A* **2013**, 55 (3), 204-211.
40. Korolev, A. A.; Shiryayeva, V. E.; Popova, T. P.; Kurganov, A. A., *Journal of Separation Science* **2011**, 34 (16-17), 2362-2369.
41. Korolev, A.; Shyrjaeva, V.; Popova, T.; Kurganov, A., *Journal of Chromatography A* **2011**, 1218 (21), 3267-3273.
42. Korolev, A. A.; Shiryayeva, V. E.; Popova, T. P.; Kurganov, A. A., *Journal of Analytical Chemistry* **2011**, 66 (2), 184-188.
43. Kurganov, A., *Analytica Chimica Acta* **2013**, 775, 25-40.
44. Jonker, R. J., *Analytical Chemistry*® **1982**, 54 (14), 2447-2456.
45. Golay, M. J. E., *Nature* **1963**, 199 (4891), 370-371.
46. Golay, M. J. E., *Analytical Chemistry* **1968**, 40 (2), 382-384.
47. Ji, Z.; Majors, R. E.; Guthrie, E. J., *Journal of Chromatography A* **1999**, 842 (1-2), 115-142.
48. Petitjean, D. L.; Leftault, C. J., *Journal of Chromatographic Science* **1963**, 1 (3), 18-21.
49. Schwartz, R. D.; Brasseaux, D. J.; Shoemake, G. R., *Analytical Chemistry* **1963**, 35 (4), 496-499.
50. Kirkland, J. J., *Analytical Chemistry* **1963**, 35 (9), 1295-1297.
51. Malik, A., *Electrophoresis* **2002**, 23 (22-23), 3973-3992.
52. Collinson, M. M., *Critical Reviews in Analytical Chemistry* **1999**, 29 (4), 289-311.
53. Wang, D.; Chong, S. L.; Malik, A., *Analytical Chemistry* **1997**, 69 (22), 4566-4576.
54. Shende, C.; Kabir, A.; Townsend, E.; Malik, A., *Analytical Chemistry* **2003**, 75 (14), 3518-3530.
55. Zeng, Z.; Qiu, W.; Xing, H.; Huang, Z., *Analytical Sciences* **2000**, 16 (8), 851-854.
56. Liang, M.; Qi, M.; Zhang, C.; Fu, R., *Journal of Chromatography A* **2004**, 1059 (1-2), 111-119.
57. Wang, D. X.; Abdul, M., *Chinese Journal of Analytical Chemistry* **2007**, 35 (3), 360-364.
58. Sidelnikov, V. N.; Patrushev, Y. V.; Belov, Y. P., *Journal of Chromatography A* **2006**, 1101 (1-2), 315-318.
59. Patrushev, Y. V.; Sidel'nikov, V. N.; Kovalev, M. K.; Mel'gunov, M. S., *Russian Journal of Physical Chemistry A* **2008**, 82 (7), 1202-1205.
60. Vinh-Thang, H.; Huang, Q.; Eić, M.; Trong-On, D.; Kaliaguine, S., *Langmuir* **2005**, 21 (11), 5094-5101.
61. Newalkar, B. L.; Choudary, N. V.; Turaga, U. T.; Vijayalakshmi, R. P.; Kumar, P.; Komarneni, S.; Bhat, T. S. G., *Microporous and Mesoporous Materials* **2003**, 65 (2-3), 267-276.
62. Newalkar, B. L.; Choudary, N. V.; Turaga, U. T.; Vijayalakshmi, R. P.; Kumar, P.; Komarneni, S.; Bhat, T. S. G., *Chemistry of Materials* **2003**, 15 (7), 1474-1479.
63. Hernández, M. A.; Velasco, J. A.; Asomoza, M.; Solís, S.; Rojas, F.; Lara, V. H.; Portillo, R.; Salgado, M. A., *Energy and Fuels* **2003**, 17 (2), 262-270.
64. Newalkar, B. L.; Choudary, N. V.; Kumar, P.; Komarneni, S.; Bhat, T. S. G., *Chemistry of Materials* **2002**, 14 (1), 304-309.
65. Dernovaya, L. I.; Eltekov, Y. A., *Journal of Chromatography* **1990**, 520, 47-54.
66. Hertl, W.; Hair, M. L., *Journal of Physical Chemistry* **1968**, 72 (13), 4676-4682.
67. Kiselev, A. V.; Yashin, Y. I., *Petroleum Chemistry: U.S.S.R* **1965**, 4 (3), 221-228.
68. Azzouz, I.; Vial, J.; Thiébaud, D.; Haudebourg, R.; Danaie, K.; Sassiati, P.; Breviere, J., *Analytical and Bioanalytical Chemistry* **2014**, 406 (4), 981-994.
69. Jacobs, M. R.; Hilder, E. F.; Shellie, R. A., *Analytica Chimica Acta* **2013**, 803, 2-14.

70. Wang, A.; Tolley, H. D.; Lee, M. L., *Journal of Chromatography A* **2012**, *1261*, 46-57.
71. Smith, P. A., *Journal of Chromatography A* **2012**, *1261*, 37-45.
72. Ohira, S. I.; Toda, K., *Analytica Chimica Acta* **2008**, *619* (2), 143-156.
73. Dorman, F. L.; Overton, E. B.; Whiting, J. J.; Cochran, J. W.; Gardea-Torresdey, J., *Analytical Chemistry* **2008**, *80* (12), 4487-4497.
74. Wise, K. D., *Sensors and Actuators, A: Physical* **2007**, *136* (1), 39-50.
75. Eiceman, G. A.; Gardea-Torresdey, J.; Dorman, F.; Overton, E.; Bhushan, A.; Dharmasena, H. P., *Analytical Chemistry* **2006**, *78* (12), 3985-3996.
76. Santos, F. J.; Galceran, M. T., *Journal of Chromatography A* **2003**, *1000* (1-2), 125-151.
77. De Mello, A., *Lab on a Chip - Miniaturisation for Chemistry and Biology* **2002**, *2* (3), 48N-54N.
78. Wang, D.; Muhammad, A.; Heflin, J. R.; Agah, M. In *Novel layer-by-layer silica nanoparticles as an adsorbent bed for micro-fabricated preconcentrators*, Proceedings of IEEE Sensors, 2012.
79. Alfeeli, B.; Cho, D.; Ashraf-Khorassani, M.; Taylor, L. T.; Agah, M., *Sensors and Actuators, B: Chemical* **2008**, *133* (1), 24-32.
80. Gràcia, I.; Ivanov, P.; Blanco, F.; Sabaté, N.; Vilanova, X.; Correig, X.; Fonseca, L.; Figueras, E.; Santander, J.; Cané, C., *Sensors and Actuators, B: Chemical* **2008**, *132* (1), 149-154.
81. Tian, W. C.; Chan, H. K. L.; Lu, C. J.; Pang, S. W.; Zellers, E. T., *Journal of Microelectromechanical Systems* **2005**, *14* (3), 498-507.
82. Tian, W. C.; Pang, S. W.; Lu, C. J.; Zellers, E. T., *Journal of Microelectromechanical Systems* **2003**, *12* (3), 264-272.
83. Smits, J. G., *Sensors and Actuators: A. Physical* **1990**, *21* (1-3), 203-206.
84. Van de Pol, F. C. M.; Van Lintel, H. T. G.; Elwenspoek, M.; Fluitman, J. H. J., *Sensors and Actuators: A. Physical* **1990**, *21* (1-3), 198-202.
85. van Lintel, H. T. G.; van De Pol, F. C. M.; Bouwstra, S., *Sensors and Actuators* **1988**, *15* (2), 153-167.
86. Kaanta, B. C.; Chen, H.; Zhang, X., *Journal of Micromechanics and Microengineering* **2010**, *20* (5).
87. Sklorz, A.; Janßen, S.; Lang, W., *Sensors and Actuators, B: Chemical* **2012**.
88. Vial, J.; Thiébaud, D.; Marty, F.; Guibal, P.; Haudebourg, R.; Nachef, K.; Danaie, K.; Bourlon, B., *Journal of Chromatography A* **2011**, *1218* (21), 3262-3266.
89. Haudebourg, R.; Matouk, Z.; Zoghalmi, E.; Azzouz, I.; Danaie, K.; Sassiati, P.; Thiebaut, D.; Vial, J., *Analytical and Bioanalytical Chemistry* **2014**, *406* (4), 1245-1247.
90. Lehmann, U.; Krusemark, O.; Müller, J.; Vogel, A.; Binz, D., Micro machined gas chromatograph based on a plasma polymerised stationary phase. In *Micro Total Analysis Systems 2000*, van den Berg, A.; Olthuis, W.; Bergveld, P., Eds. Springer Netherlands: **2000**; pp 167-170.
91. Tjerkstra, R. W.; de Boer, M.; Berenschot, E.; Gardeniers, J. G. E.; van den Berg, A.; Elwenspoek, M. In *Etching technology for microchannels*, Proceedings of the IEEE Micro Electro Mechanical Systems (MEMS), 1997; pp 147-152.
92. De Boer, M. J.; Tjerkstra, R. W.; Berenschot, J. W.; Jansen, H. V.; Burger, G. J.; Gardeniers, J. G. E.; Elwenspoek, M.; Van Den Berg, A., *Journal of Microelectromechanical Systems* **2000**, *9* (1), 94-103.
93. Lewis, A. C.; Hamilton, J. F.; Rhodes, C. N.; Halliday, J.; Bartle, K. D.; Homewood, P.; Grenfell, R. J. P.; Goody, B.; Harling, A. M.; Brewer, P.; Vargha, G.; Milton, M. J. T., *Journal of Chromatography A* **2010**, *1217* (5), 768-774.
94. Lambertus, G.; Elstro, A.; Sensenig, K.; Potkay, J.; Agah, M.; Scheuering, S.; Wise, K.; Dorman, F.; Sacks, R., *Analytical Chemistry* **2004**, *76* (9), 2629-2637.
95. Martin, M.; Jurado-Baizaval, J. L.; Guiochon, G., *Chromatographia* **1982**, *16* (1), 98-102.
96. Sun, J.; Cui, D.; Chen, X.; Zhang, L.; Cai, H.; Li, H., *Journal of Chromatography A* **2013**, *1291*, 122-128.
97. Ali, S.; Ashraf-Khorassani, M.; Taylor, L. T.; Agah, M., *Sensors and Actuators, B: Chemical* **2009**, *141* (1), 309-315.
98. Lambertus, G. R.; Fix, C. S.; Reidy, S. M.; Miller, R. A.; Wheeler, D.; Nazarov, E.; Sacks, R., *Analytical Chemistry* **2005**, *77* (23), 7563-7571.
99. Agah, M.; Potkay, J. A.; Lambertus, G.; Sacks, R.; Wise, K. D., *Journal of Microelectromechanical Systems* **2005**, *14* (5), 1039-1050.
100. Agah, M.; Lambertus, G. R.; Sacks, R.; Wise, K., *Journal of Microelectromechanical Systems* **2006**, *15* (5), 1371-1378.
101. Reidy, S.; Lambertus, G.; Reece, J.; Sacks, R., *Analytical Chemistry* **2006**, *78* (8), 2623-2630.
102. Radadia, A. D.; Masel, R. I.; Shannon, M. A.; Jerrell, J. P.; Cadwallader, K. R., *Analytical Chemistry* **2008**, *80* (11), 4087-4094.

103. Nishino, M.; Takemori, Y.; Matsuoka, S.; Kanai, M.; Nishimoto, T.; Ueda, M.; Komori, K., *IEEE Transactions on Electrical and Electronic Engineering* **2009**, *4* (3), 358-364.
104. Serrano, G.; Reidy, S. M.; Zellers, E. T., *Sensors and Actuators, B: Chemical* **2009**, *141* (1), 217-226.
105. Sun, J.; Cui, D.; Li, Y.; Zhang, L.; Chen, J.; Li, H.; Chen, X., *Sensors and Actuators, B: Chemical* **2009**, *141* (2), 431-435.
106. Zareian-Jahromi, M. A.; Ashraf-Khorassani, M.; Taylor, L. T.; Agah, M., *Journal of Microelectromechanical Systems* **2009**, *18* (1), 28-37.
107. Shakeel, H.; Agah, M., *Journal of Microelectromechanical Systems* **2013**, *22* (1), 62-70.
108. Zareie, H.; Alfeeli, B.; Zareian-Jahromi, M. A.; Agah, M. In *Self-patterned gold electroplated multicapillary separation columns*, Proceedings of IEEE Sensors, 2010; pp 1526-1529.
109. Zareian-Jahromi, M. A.; Agah, M., *Journal of Microelectromechanical Systems* **2010**, *19* (2), 294-304.
110. Shakeel, H.; Rice, G.; Agah, M. In *First reconfigurable MEMS separation columns for micro gas chromatography*, Proceedings of the IEEE International Conference on Micro Electro Mechanical Systems (MEMS), 2012; pp 823-826.
111. Zampolli, S.; Elmi, I.; Mancarella, F.; Betti, P.; Dalcanale, E.; Cardinali, G. C.; Severi, M., *Sensors and Actuators, B: Chemical* **2009**, *141* (1), 322-328.
112. Azzouz, I. *Etude, réalisation et caractérisation de nouveaux supports pour microsystèmes intégrés de chromatographie en phase gazeuse*. **2013**.
113. Reid, V. R.; Stadermann, M.; Bakajin, O.; Synovec, R. E., *Talanta* **2009**, *77* (4), 1420-1425.
114. Stadermann, M.; McBrady, A. D.; Dick, B.; Reid, V. R.; Noy, A.; Synovec, R. E.; Bakajin, O., *Analytical Chemistry* **2006**, *78* (16), 5639-5644.
115. Bourlon, B.; Wong, J.; Guieze, P., Gas chromatograph column with carbon nanotube-bearing channel. Google Patents: 2011.
116. Haudebourg, R.; Vial, J.; Thiebaut, D.; Danaie, K.; Breviere, J.; Sassiati, P.; Azzouz, I.; Bourlon, B., *Analytical Chemistry* **2013**, *85* (1), 114-120.
117. Wang, D.; Shakeel, H.; Lovette, J.; Rice, G. W.; Heflin, J. R.; Agah, M., *Analytical Chemistry* **2013**, *85* (17), 8135-8141.
118. Leonard, C., *Analytical Chemistry* **1999**, *71* (11), 2123-2129.
119. Reidy, S.; George, D.; Agah, M.; Sacks, R., *Analytical Chemistry* **2007**, *79* (7), 2911-2917.
120. Golay, M. J. E., *Journal of Chromatography A* **1981**, *216* (C), 1-8.
121. Giddings, J. C.; Chang, J. P.; Myers, M. N.; Davis, J. M.; Caldwell, K. D., *Journal of Chromatography A* **1983**, *255* (C), 359-379.
122. Spangler, G. E., *Journal of Microcolumn Separations* **2001**, *13* (7), 285-292.
123. Spangler, G. E., *Analytical Chemistry* **1998**, *70* (22), 4805-4816.
124. Spangler, G. E., *Analytical Chemistry* **2006**, *78* (14), 5205-5207.
125. Ahn, H.; Brandani, S., *AIChE Journal* **2005**, *51* (7), 1980-1990.

Chapter II.

Thin film coating:

Process development

II.1. State of the art	44
II.1.1. The sol-gel process	44
II.1.2. Ordered mesoporous silica	45
II.1.3. Evaporation Induced Self Assembly (EISA)	47
II.1.4. Thin film deposition processes.....	48
II.2. Capillary columns coating	49
II.2.1. Experimental apparatus.....	49
II.2.2. Sol-gel deposition.....	50
II.2.2.1. Sol synthesis	50
II.2.2.2. Column pretreatment.....	51
II.2.2.3. Thin film deposition.....	52
II.2.2.4. Structural agent removal	53
II.3. Process optimization	54
II.3.1. SDA addition.....	54
II.3.1.1. The need of a SDA.....	54
II.3.1.2. Dilution of the sol.....	55
II.3.2. Coating parameters	57
II.3.2.1. Viscosity of the sol	57
II.3.2.2. Sol introduction time	59
II.3.2.3. Pressure influence on the film.....	61
II.3.3. Reproducibility of the stationary phases	62
II.3.4. Multiple layers.....	64
II.4. Conclusion	65
II.5. References	66

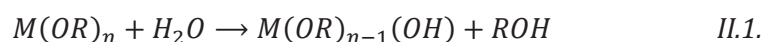
II.1. State of the art

II.1.1. The sol-gel process

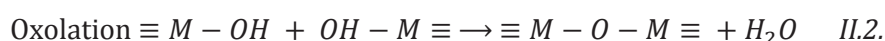
The sol-gel process was first described in 1845 by the French chemist M. Ebelmen.¹⁻² This process allows to synthesize many metal oxides through the polymerization of precursors in solution under soft reaction conditions (low temperatures and pressures). metal-alcoxides precursors, $M(OR)_n$, where M is a metal of coordination number n and R an alkyl group, are generally preferred to metal-halides derivatives. This process is generally carried out in alcohols as solvents, in the presence of a catalyst (base, acid or nucleophile) and a stoichiometric amount of water.

Under these conditions, the precursor is polymerized through two reactions: hydrolysis and condensation.³⁻⁴ First, a colloidal suspension is obtained, called "sol", whose viscosity remain constant till a continuous solid matrix swelled with solvent is formed, namely the gel. When the gel is obtained, a sharp increase of the viscosity occurs; the time needed to reach such high viscosity is commonly called "time of gel".

The polymerization is initiated by the hydrolysis reaction:



The hydrolysis is either complete or incomplete depending the quantity of water or the catalyst used.⁵ Two molecules, even partially hydrolyzed, can further react with each other to form a metal-oxo bridges M-O-M.



These reactions lead to the formation of growing clusters of metallic oxides, which ultimately connect to form a solid network. The sol-gel process is a kinetically driven process in which the physical properties of the final solid are governed by the kinetics of the two aforementioned reactions. Therefore, reaction conditions (solvent nature, pH, concentrations, temperature, water quantity, etc.) strongly influence the characteristics of the final oxide materials. For example, pH drastically modify the hydrolysis and condensation rates of $M(OR)_n$ as shown Fig. II.1 where $M(OR)_n$ is $Si(OEt)_4$ (quoted TEOS for tetraethyl

orthosilicate). In neutral conditions (pH ca. 7), condensation is fast and hydrolysis is slow, whereas the reverse is observed in basic or acidic conditions.

Moreover, basic catalysis favors the formation of hyperbranched clusters, and is therefore adapted to the formation of colloids/particles. At the reverse, acid catalysis favors linear chain growth and is therefore preferred to yield thin films.⁵

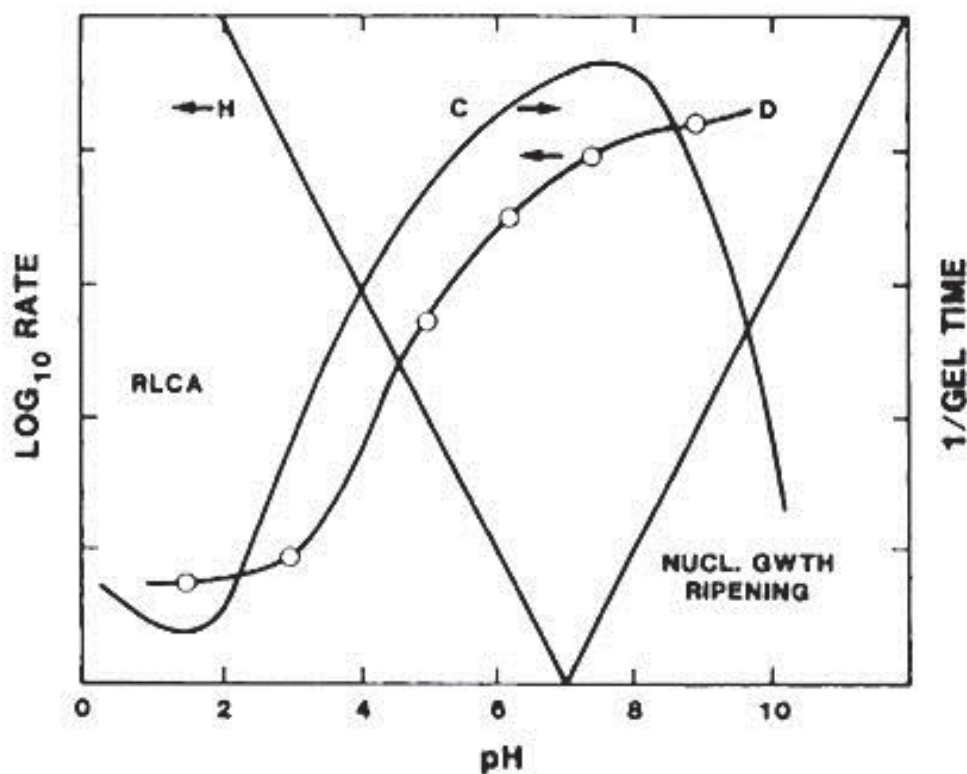


Fig. II.1 - Schematic representation of the pH-dependence of hydrolysis (H) and condensation (C) and dissolution (D) of TEOS, from C. J. Brinker.⁶

In this project, we will focus on the formation of silica materials, although a large variety of oxides can be synthesized by sol-gel process, such as titanium oxide,⁷ or alumina⁸ for example.

II.1.2. Ordered mesoporous silica

The sol-gel process naturally leads to porous materials but the control of the pore calibration within the oxide matrix is difficult. In the 1990s, the discovery of novel mesostructured materials exhibiting a high degree of porous network organization and pore calibration has opened the way to better defined oxide-based materials. Advantages of such materials are numerous: they show an interconnected structure of pores, whose structure type and pore diameter can be adjusted and they present a high surface area (over 1000

m²/g) that can be functionalized by diverse molecules. These new materials were found to be very attractive for numerous applications such as catalysis,⁹ optic¹⁰⁻¹¹ or separation.¹²

Such materials were first obtained and patented around 1970,¹³ although it went mostly unnoticed at that time. They were rediscovered in 1990 by Japanese researchers¹⁴ and later produced and patented in 1992 by researchers from Mobil Company.¹⁵ Such materials were obtained by adding a quaternary ammonium type surfactant ($C_nH_{2n+1}N^+(CH_3)_3$ or C_nTMA^+ , with $12 < n < 18$), to zeolite precursor solutions.¹⁶ This new family of materials, M41S, includes structures of various geometries, such as MCM-41 hexagonal phases, MCM-48 cubic phases, and MCM-50 lamellar phases (MCM standing for Mobil Corporation Materials).¹⁷

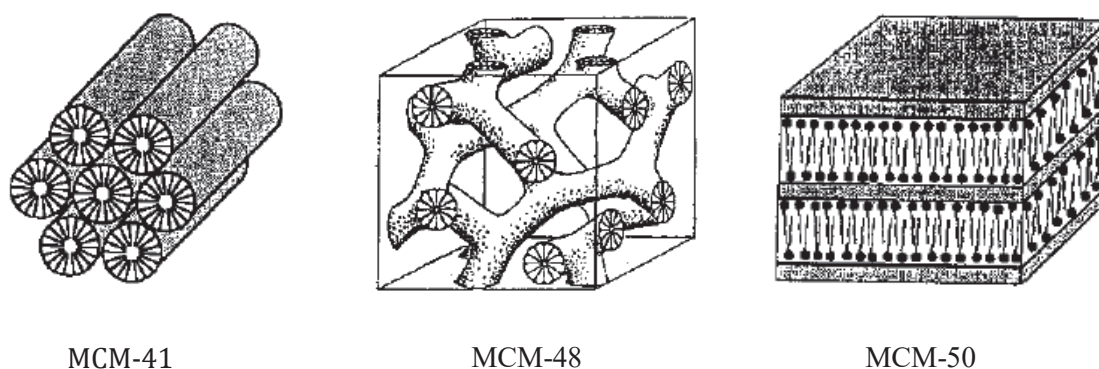


Fig. II.2 – Three different materials from the M41S family.¹⁸

In 1994, Q. Huo *et al.* realized a breakthrough by synthesizing highly mesostructured silica in strongly acidic conditions¹⁹ with anionic or cationic surfactant. In such conditions the polymerization of silicate species is irreversible and leads to linear silicate oligomers which favor more regular morphologies.²⁰

In 1995, P. T. Tanev *et al.* used primary amines as non-ionic surfactants to produce such materials.²¹ This opened the way to the use of various surfactants such as polyethoxylated surfactants,²² and block copolymers.²³⁻²⁴

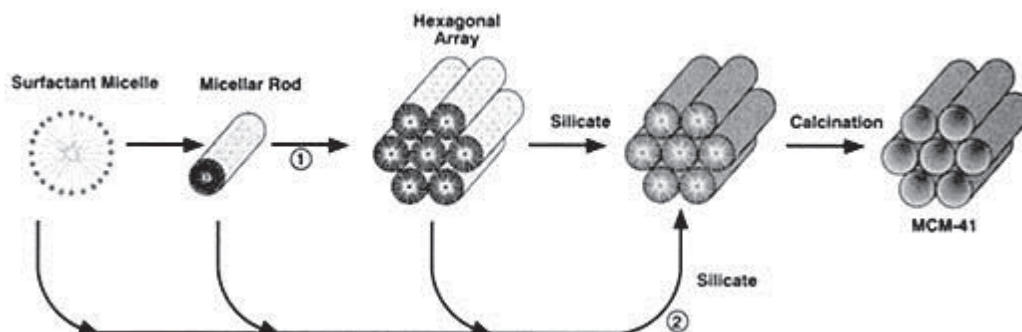


Fig. II.3 – Scheme for the liquid-crystal templating mechanism proposed by Mobil scientists: (1) silicate aggregation around organized micellar rods (liquid-crystal templating or LCT) and (2) formation of surfactant-silicate rods on the basis of organic-inorganic interactions (cooperative self-assembly or CSA).¹⁷

The liquid-crystal templating mechanism proposed by Mobil scientists to explain the formation of such materials is presented in Fig. II.3.¹⁷ It presents two main pathways, liquid-crystal templating (LCT) in which silica aggregates around the surfactant organized mesophase, and cooperative self-assembly (CSA) in which silicates and surfactants interactions establish inorganic-organic mesostructured composites.

The most popular CSA mechanism for the formation of mesostructured solids was proposed by Q. Huo *et al.*^{19, 25} It explains the formation of 3D ordered arrangements by minimizing the interface energy of surfactant/inorganic species, interacting via Coulomb forces. The different types of interactions (electrostatic or Van Der Waals) involved in such mechanism when using non-ionic surfactants are described by F. Hoffman *et al.*²⁶ This mechanism stands particularly well to explain the formation of mesostructures that do not exist in the surfactant phase diagram, such as the SBA-2 type mesostructure.²⁷

On the other hand, “true” LCT mechanism is not common. It often fails to illustrate the formation of such materials as liquid-crystal mesophases are only assembled with a high surfactant concentration.²⁷ On the contrary, MCM-41 can be prepared with only 2 wt% cetyltrimethylammonium bromide (CTAB), and can hardly be formed above 28 wt%, necessary for the hexagonal phase. Nevertheless, various structures can still be formed by TLCT from liquid-crystal mesophases.²⁸⁻²⁹

II.1.3. Evaporation Induced Self Assembly (EISA)

The EISA strategy is derived from the LCT pathway;²⁷ it was first used by C. J. Brinker *et al.*³⁰ and is now really widespread. The sol is prepared in highly diluted conditions (below the micellar concentration), in a volatile solvent, and organization occurs upon solvent evaporation. Starting from solution with a low inorganic condensation degree favors one to obtain materials with an excellent long range ordering, as the silica gel stiffens around the mesophase triggered by solvent evaporation.³¹

The synthesis frequently involves two steps: first, the inorganic precursor (generally TEOS in the case of silica) is pre-hydrolyzed in acidic conditions using alcohol (generally ethanol) as solvent or co-solvent. The structure-directing agent (SDA), diluted in the solvent, is further added to the sol. The second step of the synthesis involves further hydrolysis but mainly cross-linking of the inorganic oligomers by condensation reaction during solvent evaporation. At the final stage of evaporation, the SDA self-assembles in a liquid-crystal phase in the presence of the inorganic oligomers that further condense around the SDA mesophase. An illustration of the EISA mechanism is presented in Fig. II.4.

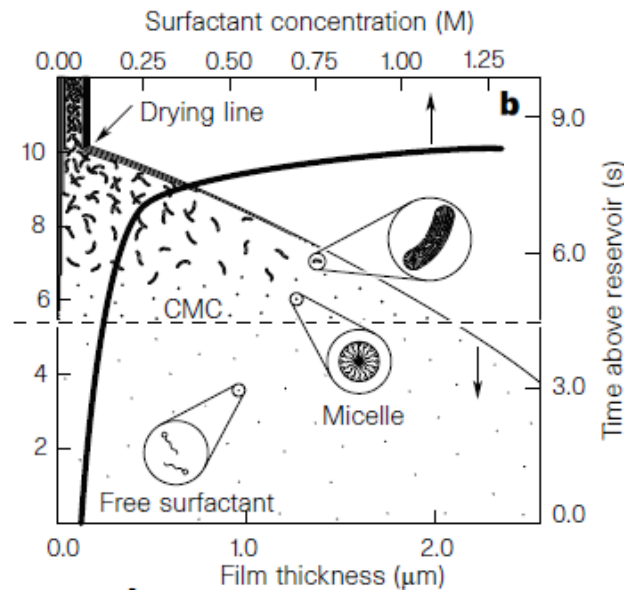


Fig. II.4 – Illustration of the formation of ordered mesostructured silica by the EISA strategy.³⁰

The final mesostructures are affected by various parameters such as the initial cross-linkage degree of the inorganic precursors, the nature of the surfactant, and the ratio of surfactant/precursor. Noteworthy, water concentration, evaporation temperature and rate, and ambient humidity can also have an important influence on the type of structure obtained and its order.³²⁻³⁶

II.1.4. Thin film deposition processes

The two most frequently used thin-film deposition techniques are: a) dip coating and b) spin coating. They are illustrated in Fig. II.5. Just after coating, the solvent included in the sol begins to evaporate, ultimately leading to the EISA process.

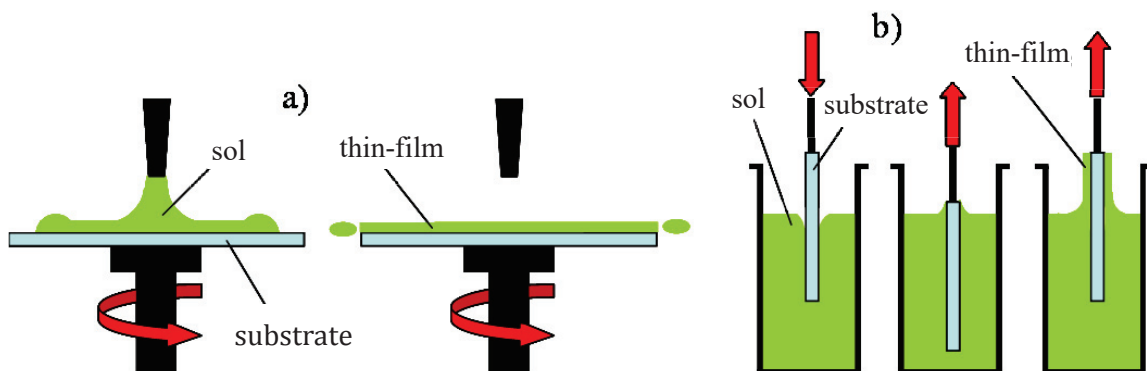


Fig. II.5 – Principles of a) spin coating and b) dip coating for thin film deposition.³⁷

The final thickness of the film depends essentially on the sol concentration (i.e. the amount silicate species in the solution) and the coating speed. However, although coating

thickness increases with coating speed for dip-coating,³⁸⁻³⁹ it is the opposite tendency for spin coating.³⁹⁻⁴⁰ In both cases, the viscosity of the sol also plays a role over film thickness.

However, for our project, neither dip nor spin-coating is applicable. We will therefore adapt traditional coating technique used for gas chromatography column preparation, pushing the sol through the column with a pressure source (directly on the solution itself with a syringe pump for example, or applied by gas).

II.2. Capillary columns coating

II.2.1. Experimental apparatus

As the EISA mechanism depends on the evaporation of the solvent to achieve the desired mesostructure, it seems preferable to dry the sol-gel thin film just after its deposition, just as in dip or spin coating techniques. Thus, contrary to Y. V. Patrushev *et al.*¹² we chose to use a dynamic coating technique for the stationary phase deposition, where the sol plug is directly pushed inside the column by the drying gas under pressure. This process seems judicious as the deposited film thickness often depends on the coating speed and therefore the sol plug will probably move through the column at constant speed.

The experimental set-up presented in Fig. II.6. was designed to meet these process requirements. It ables a convenient way to inject a solution plug through the column, and to rinse it with a nitrogen flux, with only a few handlings.

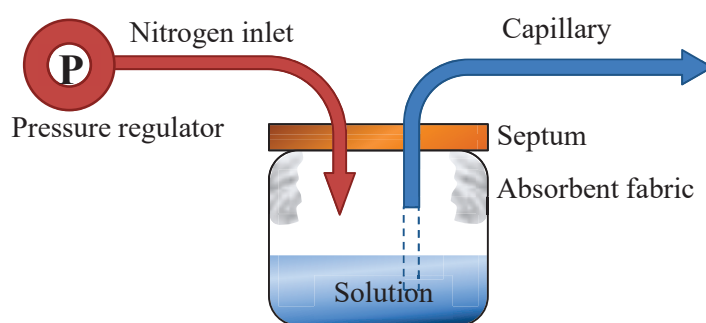


Fig. II.6 – Illustration (a) and photograph (b) of the experimental apparatus.

The solution is at the bottom of a glass vial. Two capillaries enter the vial through a septum, to guaranty the airtightness. The first capillary is linked, via a stainless steel tubing to the pressure regulator of the nitrogen inlet which controls the pressure inside the vial. The second one is the capillary column to be coated.

An absorbent fabric is placed into the vial so it can be used to wash off any excess of solution which could stick to the outer end of the capillary column. Indeed, the column pretreatment may alter the properties of the polyimide outer layer of the column near its opening and make it hydrophilic, so a drop of solution may form there when the column is removed from the sol.

Dynamic coating is easily done by immersing the end of the capillary column in the solution for a short period of time. As long as the capillary is immersed, solution is propelled by the pressure gradient through the column (Fig. II.7.a.). Then it is placed back in the gas part of the vial, and any excess of solution is wiped from the opening (Fig. II.7.b.). Nitrogen further enters the column to push the sol plug (Fig. II.7.c.). Upstream of the plug, some of the solution sticks to the walls of the column, and this thin film is directly dried by the nitrogen flow (Fig. II.7.d.).

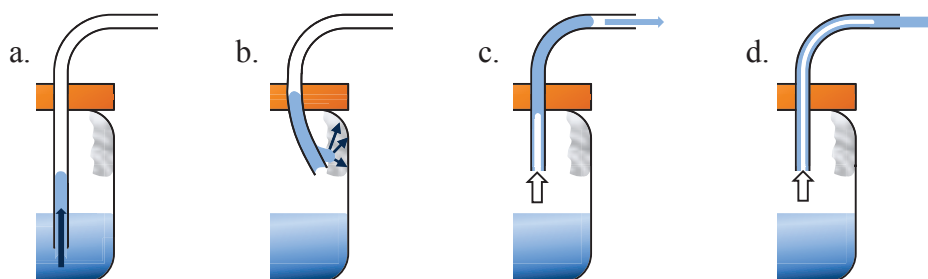


Fig. II.7 – Illustration of the different steps of column coating. Steps **a.** to **d.** are explained in the text.

II.2.2. Sol-gel deposition

II.2.2.1. Sol synthesis

The sol composition is prepared based on the work of J. P. Boilot and co-workers.^{11, 41-44} The pre-hydrolysis of the precursor, namely TEOS ($\text{Si}(\text{OC}_2\text{H}_5)_4$), is performed in acidic conditions. TEOS, water (adjusted at pH 1.25 using hydrochloric acid) and ethanol are mixed with a molar ratio (1:5:3.8). Sol is slightly over-stoichiometric in water. Under these conditions, hydrolysis ends in a few seconds. The sol is then aged at 60°C for one hour, under constant stirring, to achieve condensation (The exact synthesis details are given in the annex A.1.)

An ethanolic solution of the structure directing agent (SDA) is added to the sol just before the coating. The SDA chemical nature and its molar ratio with respect to the silica content are important parameters, influencing the characteristics of the final pore structure. Typically, the SDA used are cetyltrimethylammonium bromide (CTAB) or the poloxamer Pluronic F68

or F68 (polyoxyethylene-polyoxypropylene-polyoxyethylene: EO₇₃-PO₂₈-EO₇₃), with ratios CTAB/TEOS of 0.1, and F68/TEOS of 0.01 typically giving 3D hexagonal or cubic phases on flat substrates using EISA coating.⁴³⁻⁴⁴ The choice of the SDA and its influence will be detailed in chapter III.

However the dilution of the sol by addition of ethanol can modify the final thickness of the silica coating (typically between 50 nm and 300 nm). Its influence will be studied in a following section of the chapter.

II.2.2.2. Column pretreatment

Prior to the coating, the internal surface of the silica capillaries was activated by a solution of water, ethanol and sodium hydroxide (weight ratio 1 : 1.05 : 0.01). The goal of this step is to remove any pollutants from the surface, and to increase surface silanols concentration by hydrolysis of siloxanes bridges. These surface silanols can further react with the sol to form covalent bonds, that increase adherence of the stationary phase to the column walls,⁴⁵ as illustrated in Fig. II.8.

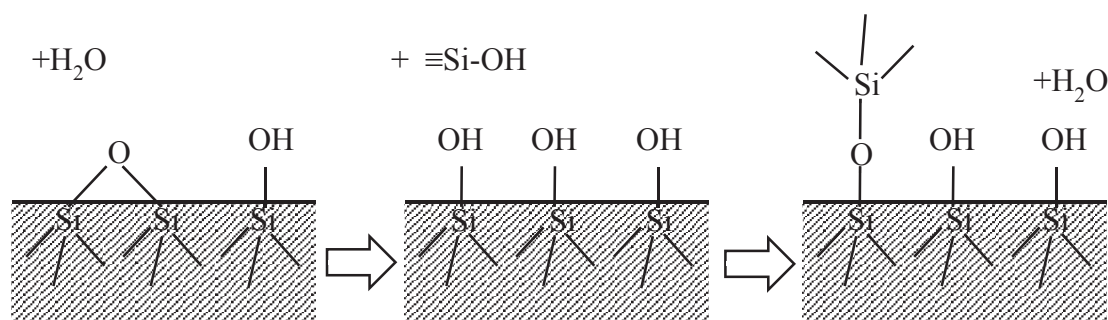


Fig. II.8 – Simplified view of the column pretreatment: opening of siloxane bridges to form silanols on which the stationary phase can covalently bond by condensation.

Once the capillary is activated, it is rinsed with distilled water and dried under nitrogen flow.

This treatment has been developed in the laboratory for washing silicon chip prior to silane deposition by MVD (Molecular Vapor Deposition). Its efficiency is usually assessed by contact angle measurement of water drops on the surface, as the process enhances its wettability. Unfortunately this measurement is not possible in a capillary and we therefore have evaluated the wettability of the capillary surface with a measure of the capillary effect, with the formula:

$$h = \frac{2\gamma \cos \theta}{\rho g r} \quad \text{II.4.}$$

Where γ is the water-air surface tension (0.0728 N.m^{-1} at 20°C), ρ is the density of water (1000 kg.m^{-3}), g is the standard gravity (9.81 m.s^{-2}) and θ the contact angle. It is easy to measure h , the height at which water rises in a $250 \text{ }\mu\text{m}$ diameter capillary ($r = 125 \text{ }\mu\text{m}$), and thus have access to θ .

Fig. II.9 shows the value of the contact angle of untreated capillaries compared to that of capillaries treated during 30 minutes or 2 hours. As wettability is already maximal after 30 minutes of treatment, it was not necessary to wait for two hours. Thus the activation time was fixed to 30 minutes for this study.

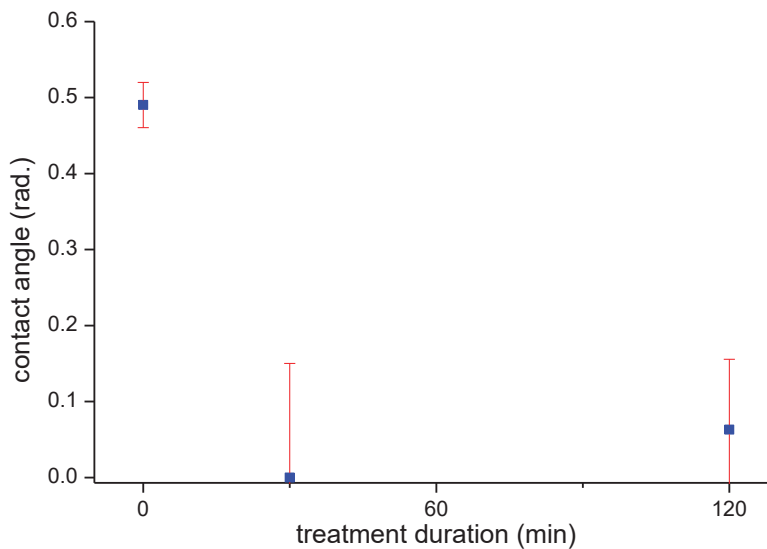


Fig. II.9 – Contact angle of water on the column walls as a function of the pretreatment duration, measured by capillary effect. Activation times over 30 minutes are not necessary.

II.2.2.3. Thin film deposition

After the pretreatment, the thin film is deposited by dynamic coating: a plug of sol is propelled in the capillary by nitrogen pressure. The length of the plug depends on the pressure, the column immersion time and the sol viscosity itself. And once propelled in the column, the plug's speed depends only on its length and its viscosity (if the pressure is kept constant).

Therefore, as the viscosity has no reason to vary, the plug's speed will be constant as long as its length does not vary significantly along its path through the column. To satisfy this condition, the plug's volume (and length) must be large enough so that the volume of the film deposited in its path is small in comparison. This way, the length variation of the plug is negligible along its path and its speed stays constant.

But near the beginning and the ending of the column, as the plug enters or leave the column, its length varies inevitably, and its speed will vary in these regions. To compensate for this phenomenon, the column is made 50% longer than its final length, and both extremities (25% of the final length each) are cut before being used for gas chromatography tests.

Once the stationary phase is deposited, it is dried under a nitrogen flow during 15 minutes at room temperature, and 8 hours at 120°C.

II.2.2.4. Structural agent removal

Once the film is deposited, it is necessary to remove the surfactant so that the pores become available for interaction with gas molecules.

There are several ways to remove the surfactant. The most widely used technique is SDA calcination, even though low temperature processes are sometimes favored. Such low temperature process include extraction of the surfactant by treatment with i) boiling ethanol,⁴⁶ ii) ethanol and isopropanol extraction under ultra-sonication¹¹ or iii) ultraviolet irradiation (photocalcination).⁴⁷ The advantages of low temperature SDA removal are the preservation of organic functionalities included in the sol *via* the use of organosilanes (at the exception of the photocalcination process) and the non-contraction of the silica film.

Indeed, high temperature treatments of mesoporous materials lead to lower pore volumes, lower surface areas, less surface hydroxyl groups, and a higher cross linking degree of silica.²⁷

However, after suffering a heat treatment, mesoporous materials possess a higher hydrothermal stability.^{46, 48} This is an advantage for GC columns, as they are often meant to be used or regenerated up to high temperatures. Hence, high temperature annealing process for SDA removal was used in this work.

The process consisted in our case in annealing the thin film at high temperature under gaz flow for sufficient time as to remove the organic species from the film. CTAB first decomposes in hexadecane and trimethylamine species at temperature between 100°C and 220°C.²⁷ In the case of tri-block copolymers, as pluronic P123, even if they can be starting from 250°C,²³ most authors generally prefer temperatures over 350°C to completely remove organics. Finally, in the case of long chain alkyl surfactant, temperatures between 360 and 550°C are needed for complete removal.²⁷

In the case of our geometry, column temperature treatment is done under constant gas flow through the column. So the gas will drag the surfactant and its degradation products from the thin stationary phase through the column, and increase the removal rate, even at

lower temperature. If the gas is Helium, the surfactant is simply removed but not degraded, and it is possible to monitor the removal by recording the FID signal.

The thermal treatment used for columns with CTAB is presented in Fig. II.10, with the associated chromatograph. As CTAB's melting point is between 235°C and 248°C,⁴⁹ a final temperature of 250°C was held for 4 hours. However, for pluronic type surfactants, even 300°C in an inert gas flow is not enough for complete removal as the molecules at stake are much bigger. It is therefore necessary to perform calcination under wet air flow (dry air flow would have been preferred but was not available) at 300°C (limit temperature of our oven connected to the gas flow) for 12 hours. No signal was recorded in this case, as the air flow was not connected to the GC main flow line and FID.

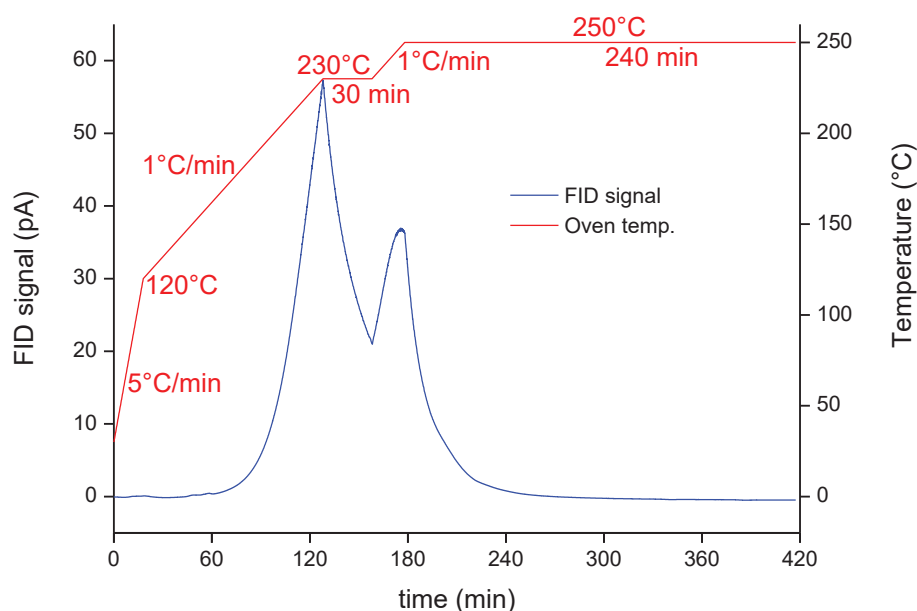


Fig. II.10 – Thermal treatment and a typical chromatograph of the removal of the CTAB from the column.

II.3. Process optimization

II.3.1. SDA addition

II.3.1.1. The need of a SDA

Fig. II.11. compares the retention of light alkanes (methane to butane n-alkanes) at 30°C obtained with different columns with or without SDA, before and after the calcination.

Retention is almost zero for all columns, except for that prepared using CTAB after calcination.

Hence we can conclude that most of the interactions between the stationary phase and the alkane gas that are responsible of retention take place in the mesopores liberated by CTAB removal. The porosity generated by a classical hydrolytic sol-gel is insufficient to have an effect on the retention of light alkanes with less than 5 carbon atoms.

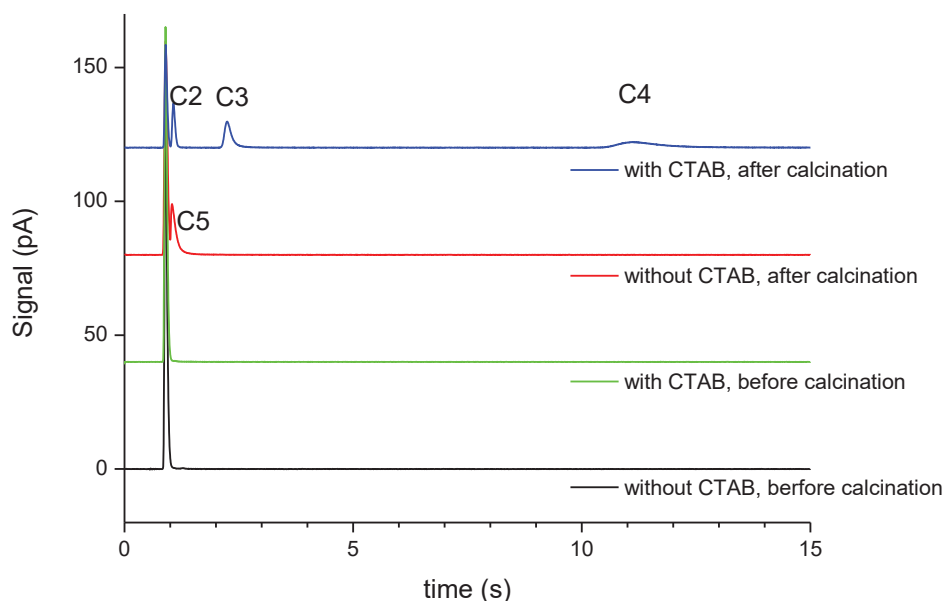


Fig. II.11 - Influence of the porosity on the separation of light alkanes.

Isothermal separation of a mixture of light n-alkanes (methane to pentane, 500 ppm each), $T=30^{\circ}\text{C}$, inlet pressure 12psi, $V_{inj}=0.2\mu\text{L}$, 1m column, 100 μm diameter.

II.3.1.2. Dilution of the sol

The volume of ethanol added to the sol containing SDA dilutes the amount of silica species compared to the total volume of sol. Thus, the same volume of initial solution deposited in the column will result in a thinner stationary phase as dilution increases.

S. Besson *et al.* report that it is easier to achieve a coherent porous structure over the whole thickness with volume dilution EtOH:sol ratios of 3:1 to 9:1 volumes of ethanol, as the deposited films are thinner (between 100 and 300 nm).⁴¹

However, with our process, thicknesses are below 200nm, even for dilution EtOH:sol ratios as low as 1:3. As a result, we preferred to use such low dilution ratios in the following experiments, to maximize the thickness, the retention towards alkanes and the capacity of the final stationary phase.

For a typical sol-gel synthesis, once hydrolysis is finished, the molar ratio of the sol are $\text{Si}(\text{OH})_4$: H_2O : EtOH = 1:1:7.8 and the final molar ratios after dilution ratios between 3:1 to 1:1 are $\text{Si}(\text{OH})_4$: H_2O : EtOH = 1: 1:10.8 to 1:1:26.8. This corresponds to a concentration in silica of 1.41 to 0.94 mol.L⁻¹.

Expecting that the thickness of the column stationary phase, and its retention, scale proportionally to the silica concentration of the sol, we did the following experiments summarized in Table II-1.

We can observe that CTAB structured columns prepared in similar conditions exhibit retention coefficients (only the one for propane is presented in Table II-1) that are proportional to the silica concentration of the sol with a constant ratio of retention over silica concentration for different dilutions.

		silica concentration [Si] (M) / sol : EtOH (vol)	propane retention, k3	k3 / [Si]	relative difference
CTAB/Si (0.1:1)	coating conditions 1	0.94 (D1:1)	0.32	0.34	2%
		0.63 (D1:2)	0.22	0.35	
	coating conditions 2	1.41 (D3:1)	0.61	0.43	4%
		0.94 (D1:1)	0.39	0.41	
	coating conditions 3	1.41 (D3:1)	1.24	0.88	1%
		0.94 (D1:1)	0.82	0.87	
Pluronic F68/Si (0.005:1)	coating conditions 4	1.41 (D3:1)	2.08	1.48	47%
		0.94 (D1:1)	0.74	0.79	

Table II-1 – Influence of the sol dilution on the retention of the stationary phases. Coating conditions are detailed in Appendix A.2.2

In *contrario*, F68 structured columns exhibit non proportional retention coefficient with respect to silica concentration. The result of dilution alone should be a decrease of 1/3 of the retention and stationary phase thickness, as silica concentration for D1:1 dilution is 2/3 of that of D3:1 dilution. However, the retention of the D1:1 column is lower than what is expected from the effect of dilution alone (more than halved), and SEM pictures of the columns indicate the same trend for their final stationary phase thicknesses (40 nm for the D1:1 column and 87 nm for the D3:1 column).

This could be the consequence of the much higher viscosity of pluronic sols, compared to CTAB's ones. Indeed, we will see that the viscosity of the sol, as some other parameters presented in the next paragraph, have an influence on the deposition process. And as the viscosity of the pluronic sols is high, it is also more affected by dilution (as seen later in Table II-3).

II.3.2. Coating parameters

The process presented in this work involves two parameters that it is particularly easy to modify: the pressure and the coating time (i.e. the time during which the capillary entry is immersed in the sol solution). These parameters both have an influence on the plug speed and plug length, as resumed in Table II-2.

For dip and spin coating processes, the viscosity of the sol solution also has an influence on the deposited thickness. Therefore, we also studied this parameter as it is easy to modify the sol viscosity by changing the nature of the SDA and its molar ratio. However, this could also have an effect on the nature of the mesostructure formed, as we will see in chapter III, thus complicate interpretation.

		Plug length	Plug speed	Deposited thickness
Coating time	↗	+	-	-
Pressure	↗	+	+	+
Viscosity	↗	-	-	+

Table II-2 – Influence of coating time, pressure and sol viscosity on plug length and plug speed (when changed one at a time); and their observed effect on the deposited thickness, as presented in the next paragraphs.

As we can see, the influence of this three main parameters are greatly interconnected, and it is difficult, and often not possible to isolate and study the influence of only one of them, keeping everything else constant.

II.3.2.1. Viscosity of the sol

The sol viscosity can be calculated experimentally, assuming a laminar sol flow. When the capillary is immersed in the sol, the pressure in the vial propels it through the column and if considering the flow resistance of the gas as negligible (much lower viscosity than the sol), the plug speed is given by:

$$\bar{u} = \frac{dl}{dt} = \frac{r^2 \Delta P}{8\mu l} \tag{II.5}$$

With r : the radius of the capillary, ΔP : the pressure difference, μ and l : the viscosity and the length of the sol plug respectively.

The length of the plug as a function of time is further obtained by integration of eq. II.5:

$$l = \frac{r}{2} \sqrt{\frac{\Delta P}{\mu} t} \quad \text{II.6.}$$

From eq. II.6, the sol viscosity can be calculated as follows:

$$\mu = \frac{r^2 \Delta P}{4L^2} T \quad \text{II.7.}$$

With L: the length of a capillary and T: the time to fill completely the capillary with the solution.

The bigger error source in this equation is the determination of ΔP as the manometer has only a $\pm 5\%$ precision. A more precise calculation, including the flow resistance of the gas has been done in MATLAB and is presented in Appendix B.2.3 but the precision increase is negligible, as shown in Fig. II.12.

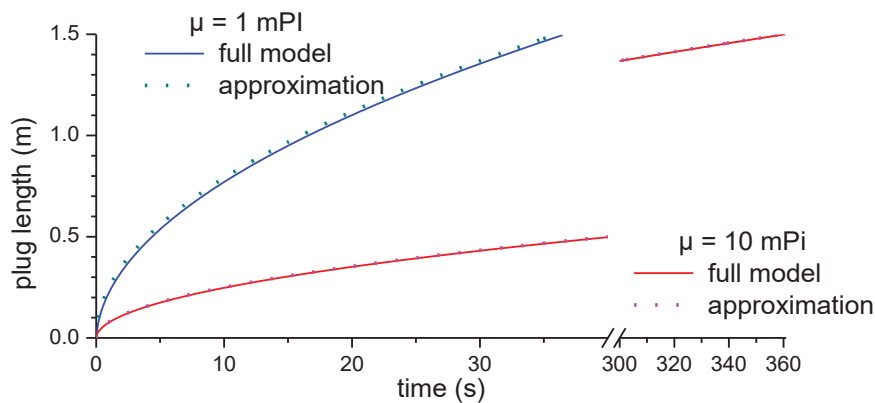


Fig. II.12 – Plug length as a function of time for a 1.5m long capillary with a 100µm diameter. Sols' viscosities are 0.001 and 0.01 kg.m⁻¹.s⁻¹. Differences in travel times between the complete model and equation II.6 are 0.45s and 0.7s (respectively 1.25% and 0.19% of error)

Based on eq. II.7, the viscosity of various sol compositions were calculated and are listed in Table II-3.

As the nature and molar ratio of the SDA affects not only the viscosity of the sol but also the mesostructure of the phase, it is better to study the deposited thickness directly instead of the retention which may be affected by the mesostructure. Overall, an increase of the sol viscosity at constant dilution (except the lines 3 and 7 in gray) results in a thicker stationary phase, as shown in Table II-3, last column.

Of course, a decrease of the viscosity *via* an increased dilution (Table II-3, F68, line 2 and 4) has a greater impact that decreasing viscosity at constant dilution *via* SDA ratio (Table II-3, F68, line 2 and 3). It results from the impact of dilution seen in II.3.1.2.

It is also worth noting that the change in viscosity were studied at constant coating time and pressure, and thus at varying plug length and speed.

Nature	SDA	Dilution	Viscosity ($10^{-3} \cdot \text{kg} \cdot \text{m}^{-1} \cdot \text{s}^{-1}$)	Thickness (nm)
	(Si : SDA) mol. ratio	(sol : EtOH) vol. ratio		
F68	1 : 0.01	3 : 1	16.31 ± 1.30	109 ± 89
F68	1 : 0.005	3 : 1	7.64 ± 0.61	86 ± 28
F68	1 : 0.002	3 : 1	4.64 ± 0.37	77 ± 9
F68	1 : 0.005	1 : 1	4.69 ± 0.38	40 ± 19
CTAB	1 : 0.14	3 : 1	3.84 ± 0.31	69 ± 50
CTAB	1 : 0.10	3 : 1	3.78 ± 0.30	67 ± 49
CTAB	1 : 0.05	3 : 1	3.36 ± 0.27	57 ± 14
CTAB	1 : 0.10	1 : 1	2.61 ± 0.21	x

Table II-3 – Viscosity calculated using *equation II.7* and film coating thickness measured by SEM.

II.3.2.2. Sol introduction time

In the following section the influence of the sol introduction time on the film thickness will be studied. It influences directly the length of the plug introduced in the column, and the plug's speed, which is directly proportional to the inverse of plug length (assuming the flow is laminar through the column). This study was carried out using pluronic type SDAs as CTAB low viscosity prohibits any major modification of the coating speeds while keeping plug lengths under 0.25m and laminar flows with a Reynolds number under 1.

As plug length cannot be directly imaged with enough precision and contrast, plug length and speed will be calculated based on the introduction time of the sol, using the model of Appendix B.2.3 and viscosity values presented in Table II-3.

Fig. II.13 shows columns chromatographs obtained with stationary phases of the same sol composition using different introduction times. We observe that the faster is the coating, the more retention is observed. This indicates that our coating mechanism is probably similar to that taking place with dip coating processes, where the thickness increases with coating speed (the reverse phenomenon is being observed in spin coating processes).

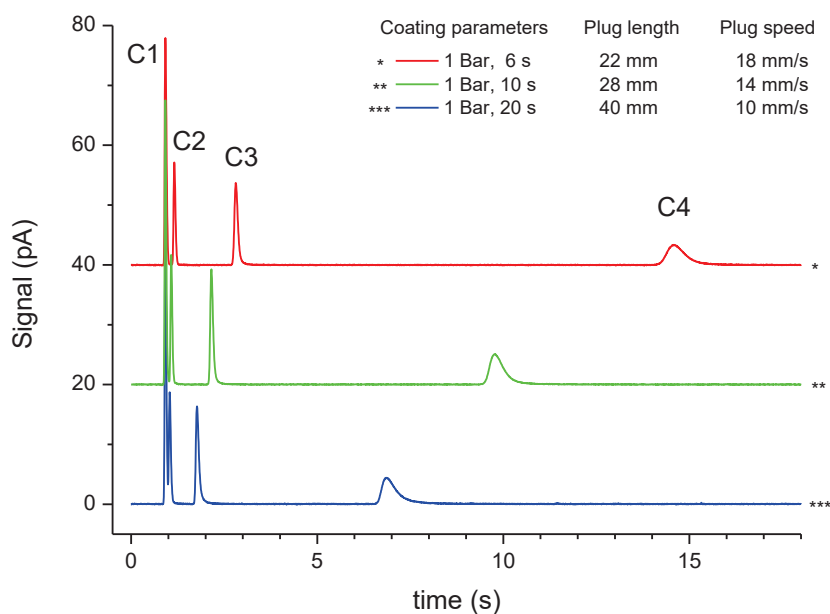


Fig. II.13 – Influence of coating speed on the retention of light alkanes using the following sol composition: TEOS:F68 = 1:0.005. Isothermal separation of light alkanes (methane 2000 ppm, ethane to pentane, 500 ppm each), $T=30^{\circ}\text{C}$, inlet pressure 12psi, $V_{inj}=0.2\mu\text{L}$, 1m column, $100\mu\text{m}$ diameter, plug length and speed calculated in MATLAB, based on the model of Appendix B.2.3.

This analogy with dip coating processes is easier to understand if we change the referential to that of the sol plug. In this referential, the plug is stationary and the capillary moves and drag away the sol in its trail, as represented in Fig. II.14. Differences with dip coating are i) the position of the support with respect to the sol: the capillary surrounds the sol reservoir whereas a substrate being surrounded by sol in the reservoir, and ii) the gravity which has no influence in the capillary coating since the capillary is horizontal and since capillary forces are much greater than gravity.

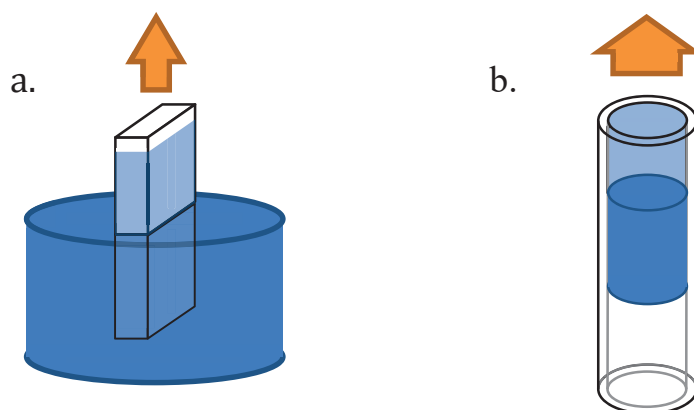


Fig. II.14 – Graphic representation of the analogy between a. dip coating and b. capillary coating.

In the following part of the project, the sol introduction time was chosen to insure maximum process reproducibility as presented in II.2.2.3. It was tuned depending of SDA nature and the pressure in order to insure a reproducible experimental gesture (i.e. 2 seconds or more) and a plug length inferior to roughly 25% of the final column length (i.e. the length of capillary that is removed at each extremity).

II.3.2.3. Pressure influence on the film

Having insight into the pressure influence on the deposited stationary phase is more complex since it influences the speed and length of the coating plug but also changes the drying conditions for the first 15 minutes at ambient temperature. A higher pressure results in a higher gas flow, and probably a faster drying rate.

Its influence was mostly studied at the first stages of the process optimization, using CTAB as SDA, and was evaluated by the value of the retention of the columns for butane, which is supposed to be proportional to the stationary phase thickness. The results, presented in Fig. II.15, show the trend that the one observe by reducing coating time: an increase in coating speed results in an increased deposited thickness.

Once the process optimized, this study was repeated for 4 different SDA conditions, in 2 columns each, and this trend was clearly confirmed.

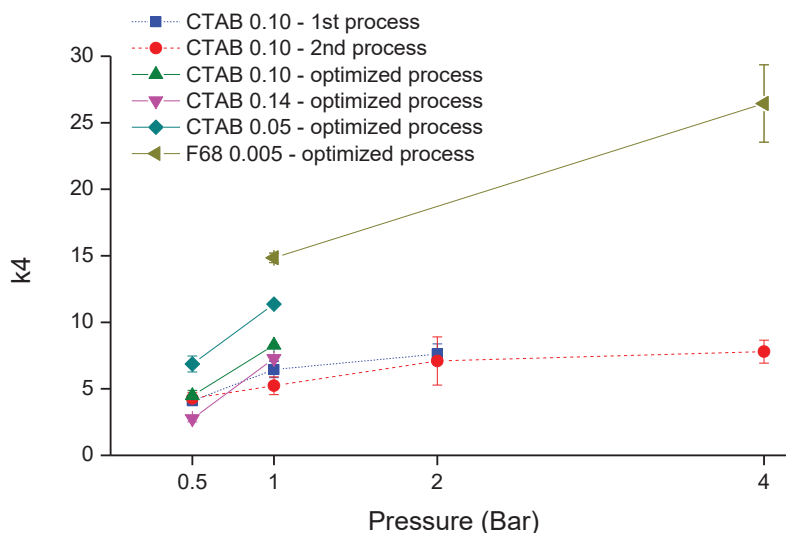


Fig. II.15 – Column retention (for butane) versus pressure. At the time of the 1st process, columns were made directly one meter long, without cutting their extremities prior to GC testing. This was corrected for the 2nd process, and columns were made 1.5m long, and cut to 1 m for GC tests, but there was still no fabric to wipe the capillary end after immersion. The final optimized process included this last addition.

However, columns with high retention factors due to high pressures coatings were sometimes found to less efficient (those obtained at 4 bar with F68 had a lower number of theoretical plates for example). Coatings with high pressure also lead to less reproducibility for the separations, as a slight deviation in coating time leads to higher plug length and speed variations. Thus, coating pressure was often settled to 1 bar, as a reasonable compromise between retention and reproducibility.

II.3.3. Reproducibility of the stationary phases

It is particularly difficult to obtain a reproducible process for coating, as there are many parameters that can affect the final stationary phase. Some of them have been studied and presented in this work (viscosity, coating time and pressure) but others would be worth testing: i) the aging of the gel (under different conditions: drying gas composition and pressure, temperature), and ii) the calcination process.

Reproducibility was first studied for CTAB columns. Columns of 1.5 m long were coated at 2 bars, for 2 seconds. The sol CTAB/Si ratio was fixed at 0.1 and the dilution was 3:1 (sol : ethanol). Columns were dried 15 minutes at ambient temperature and annealed at 250°C for 4 hours under inert gas flow as described in II.2.2.4, cut to 1 meter, and were then analyzed in GC with a mix of light alkanes (methane, ethane, propane, butane and pentane). Methane signal was chosen to calculate the holdup time.

For this first study, no tissue was used to wipe off the capillary entries, as this was not part of the standard protocol at this time. Chromatographic indirect characterizations are summarized in Fig. II.16 which shows the retention factors and efficiencies of the columns included in the study.

Chromatographic performances are similar for these columns; retention factors are in the range of 15% of the mean value. However, efficiencies are more variable, especially for the more retained species. These unsatisfactory results (30% of retention deviation) prohibit discriminating easily variations related to the process or to irreproducibility.

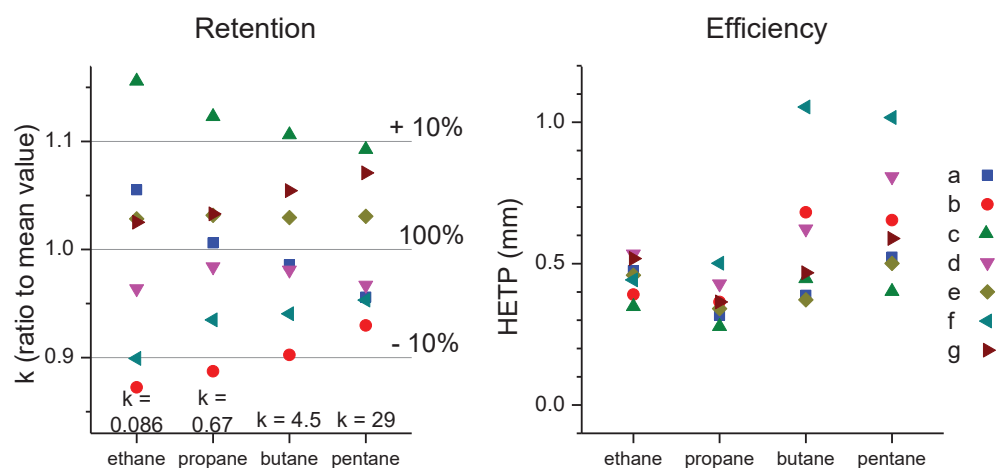


Fig. II.16 – Reproducibility study for CTAB columns.

Indirect characterization of the columns' retention and efficiencies via GC separation of light alkanes.
Capillary's entries are not wiped off at the end of coating (not yet implemented).

To fix this problem, the excess of sol sticking to the capillary ends was wiped at the end of the coating and column reproducibility was found to be increased. These preliminary results in hands, a new set of experiments was carried out using pluronic F68 as SDA, a F68/Si ratio of 0.005, a dilution of 3:1 (sol : ethanol) and coating pressure and time of 1 Bar and 6 seconds respectively. The corresponding results are shown in Fig. II.17. Here, retention factors were found to be really similar, within 3% of the mean value (i.e. a fivefold increase in reproducibility). However, efficiencies were still variable, especially for the most retained species, but were mostly over 2000 th.p./m (HETP < 0.5 mm).

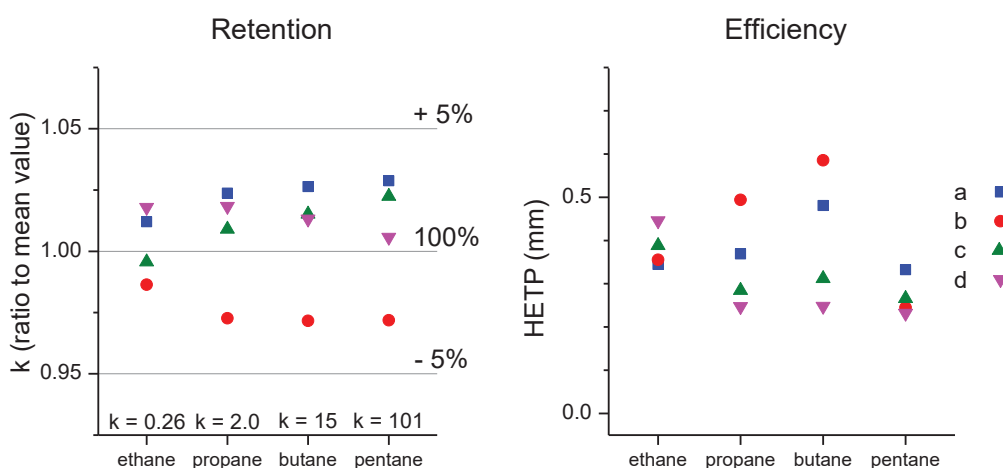


Fig. II.17 – Reproducibility study for F68 columns.

Indirect characterization of the columns' retention and efficiencies via GC separation of light alkanes.

II.3.4. Multiple layers

Thick layers of stationary phase are keys for increases of columns retention and capacity but also for a more robust separation of natural gas mixtures (in which gas concentrations are really variable). However, obtaining thick layers is not easy since the sol dilution was already set at low levels (sol : EtOH = 3:1), and the increase of coating speed would probably lead to losses in efficiency or reproducibility.

Therefore, thicker stationary phases were prepared by the deposition of several layers on top of one another. The additional layers are directly deposited before the removal of the SDA so that the new layer does not fill the pores of the layers underneath, and benefits from the presence of surface silanols to increase the bonding of the supplementary layer.

If the second layer was added directly after coating the first one, or after 15 minutes of drying, no significant increase of retention was observed. Therefore, to ensure a correct coating, the sol was aged at 120°C for 8h (following the standard protocol) between each coating. It is then possible to prepare columns with really high retention coefficients.

A comparison of the chromatographic performances for two double layer columns with respect to two single layer ones is shown in Fig. II.18. Each coating was carried out with a F68/Si ratio of 0.01, a dilution of 3:1 (sol : EtOH), a pressure and an introduction time of 1 bar and 4 seconds respectively.

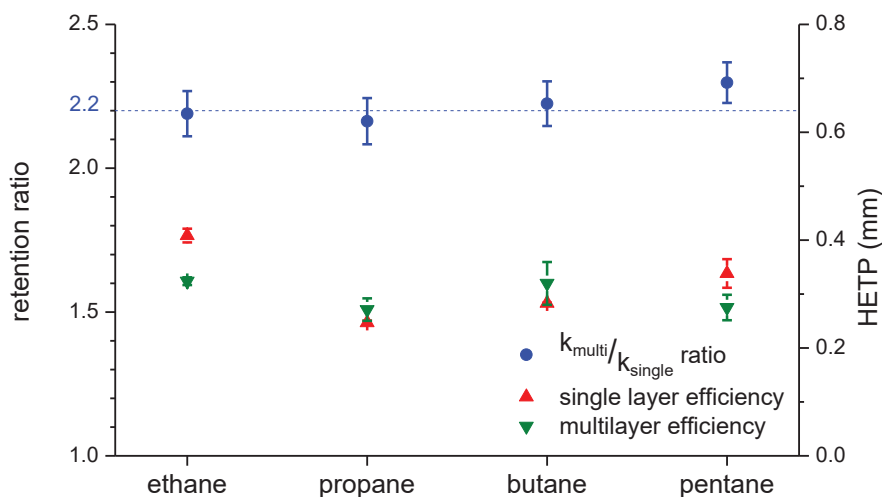


Fig. II.18 – Comparison of multilayer and single layer columns chromatographic performances.

Retention coefficients for the double layer columns are just slightly more than twice those of the single layer columns. This may be due to coating variations or may suggest the easier deposition of a silica layer on top of an ordered silica coating than onto flat no porous silica.

We can also see that the retention ratio is slightly superior for pentane, which could be explained as a result of the single layer column saturation. As the pentane affinity towards the column is high, the injection of a bigger quantity of pentane was needed to observe its signal from the baseline, but the column then saturated and retention time decreased. The phenomenon is not observed with a thicker column which is harder to saturate. Moreover, the efficiency of the separation, measured in terms of HETP was not really affected by the addition of a second layer.

II.4. Conclusion

In this chapter, we studied the coating of GC columns with a mesostructured silica stationary phase obtained *via* a sol-gel process using a templating route. The porosity generated by classical hydrolytic sol-gel was found to be insufficient to separate the targeted molecules (i.e. light alkanes from methane to pentane); therefore the addition of a structure-directing agent was performed to generate the structuration of the silica film (i.e. calibration of the pore mean size and 3D organization of the porous network).

Different experimental parameters (viscosity of the sol, plug length and coating pressure) were studied in order to optimize the coating process. Of these results, it was found that a low sol dilution leads to thicker stationary phases as expected since it maximizes the quantity of silica per volume of sol deposited.

The process of capillary coating was found to be more similar to a dip coating process than a spin coating one with respect to the influence of coating speed on the coating thickness. Coating speed was increased using high pressure flow and low sol introduction time. Therefore a compromise was found between columns with high retentions, which increased with thickness and coating speed and repeatability, which decreased with pressure and short sol introduction time.

Interestingly, it was possible to generate double-layer-stationary phases by repeating our process on a single capillary. These columns exhibited a high retention coefficient (twice those of the single layer-stationary phase), without decrease of the efficiency.

Overall, the optimized process gave reproducible results with small variations of the retention coefficients (only several percent) from one column to the other. Having these results in hands, we decided to study in the present project the impact of the SDA on the final porous structuration of the stationary phase and its influence on the column retention.

II.5. References

1. Ebelmen, J. J., *Comptes Rendus de l'Académie des Sciences* **1844**, 19, 398-400.
2. Ebelmen, J. J., *Comptes Rendus de l'Académie des Sciences* **1845**, 21, 502-505.
3. Schmidt, H.; Scholze, H.; Kaiser, A., *Journal of Non-Crystalline Solids* **1984**, 63 (1-2), 1-11.
4. Livage, J.; Henry, M.; Sanchez, C., *Progress in Solid State Chemistry* **1988**, 18 (4), 259-341.
5. Brinker, C. J.; Scherer, G. W., *Sol-gel science: the physics and chemistry of sol-gel processing*. Academic Press: **1990**.
6. Brinker, C. J., *Journal of Non-Crystalline Solids* **1988**, 100 (1-3), 31-50.
7. Kim, T. Y.; Alhooshani, K.; Kabir, A.; Fries, D. P.; Malik, A., *Journal of Chromatography A* **2004**, 1047 (2), 165-174.
8. Deng, S. G.; Lin, Y. S., *AIChE Journal* **1995**, 41 (3), 559-570.
9. Trong On, D.; Desplantier-Giscard, D.; Danumah, C.; Kaliaguine, S., *Applied Catalysis A: General* **2001**, 222 (1-2), 299-357.
10. Battie, Y. *Mécanismes de croissance in situ et propriétés optiques de nanoparticules d'argent spatialement organisées dans des films diélectriques mésostructures*. Thèse de Doctorat, Université Jean Monnet, Saint-Etienne, **2009**.
11. Matheron, M. *Films mésoporeux hybrides organiques-inorganiques : synthèse, organisation des pores et application en optique ophtalmique*. These de Doctorat, Ecole doctorale de l'Ecole Polytechnique, Palaiseau, **2005**.
12. Patrushev, Y. V.; Sidel'nikov, V. N.; Kovalev, M. K.; Mel'gunov, M. S., *Russian Journal of Physical Chemistry A* **2008**, 82 (7), 1202-1205.
13. Beau, R.; Duchene, J.; Page, M. L., Porous silica particles containing a crystallized phase and method. Google Patents: 1970.
14. Yanagisawa, T.; Shimizu, T.; Kuroda, K.; Kato, C., *Bulletin of the Chemical Society of Japan* **1990**, 63 (4), 988-992.
15. Kresge, C. T.; Leonowicz, M. E.; Roth, W. J.; Vartuli, J. C. Synthetic mesoporous crystalline material. US Patent 5098684, march 24, **1992**.
16. Kresge, C. T.; Leonowicz, M. E.; Roth, W. J.; Vartuli, J. C.; Beck, J. S., *Nature* **1992**, 359 (6397), 710-712.
17. Beck, J. S.; Vartuli, J. C.; Roth, W. J.; Leonowicz, M. E.; Kresge, C. T.; Schmitt, K. D.; Chu, C. T. W.; Olson, D. H.; Sheppard, E. W.; McCullen, S. B.; Higgins, J. B.; Schlenker, J. L., *Journal of the American Chemical Society* **1992**, 114 (27), 10834-10843.
18. Selvam, P.; Bhatia, S. K.; Sonwane, C. G., *Industrial and Engineering Chemistry Research* **2001**, 40 (15), 3237-3261.
19. Huo, Q.; Margolese, D. I.; Ciesla, U.; Feng, P.; Gier, T. E.; Sieger, P.; Leon, R.; Petroff, P. M.; Schüth, F.; Stucky, G. D., *Nature* **1994**, 368 (6469), 317-321.
20. Wan, Y.; Zhao, D., *Chemical Reviews* **2007**, 107 (7), 2821-2860.
21. Tanev, P. T.; Pinnavaia, T. J., *Science* **1995**, 267 (5199), 865-867.
22. Bagshaw, S. A.; Pinnavaia, T. J., *Angewandte Chemie (International Edition in English)* **1996**, 35 (10), 1102-1105.
23. Zhao, D.; Feng, J.; Huo, Q.; Melosh, N.; Fredrickson, G. H.; Chmelka, B. F.; Stucky, G. D., *Science* **1998**, 279 (5350), 548-552.
24. Zhao, D.; Huo, Q.; Feng, J.; Chmelka, B. F.; Stucky, G. D., *Journal of the American Chemical Society* **1998**, 120 (24), 6024-6036.
25. Huo, Q.; Margolese, D. I.; Ciesla, U.; Demuth, D. G.; Feng, P.; Gier, T. E.; Sieger, P.; Firouzi, A.; Chmelka, B. F.; Schüth, F.; Stucky, G. D., *Chemistry of Materials* **1994**, 6 (8), 1176-1191.
26. Hoffmann, F.; Cornelius, M.; Morell, J.; Fröba, M., *Angewandte Chemie - International Edition* **2006**, 45 (20), 3216-3251.
27. Zhao, D.; Wan, Y.; Zhou, W., *Ordered Mesoporous Materials*. Wiley: **2012**.
28. Attard, G. S.; Glyde, J. C.; Göltner, C. G., *Nature* **1995**, 378 (6555), 366-368.
29. Yang, P.; Zhao, D.; Margolese, D. I.; Chmelka, B. F.; Stucky, G. D., *Nature* **1998**, 396 (6707), 152-155.
30. Lu, Y.; Ganguli, R.; Drewien, C. A.; Anderson, M. T.; Jeffrey Brinker, C.; Gong, W.; Guo, Y.; Soyez, H.; Dunn, B.; Huang, M. H.; Zink, J. I., *Nature* **1997**, 389 (6649), 364-368.
31. De A.A. Soler-Illia, G. J.; Crepaldi, E. L.; Grosso, D.; Sanchez, C., *Current Opinion in Colloid and Interface Science* **2003**, 8 (1), 109-126.

32. Grosso, D.; Balkenende, A. R.; Albouy, P. A.; Ayral, A.; Amenitsch, H.; Babonneau, F., *Chemistry of Materials* **2001**, *13* (5), 1848-1856.
33. Grosso, D.; Babonneau, F.; Albouy, P. A.; Amenitsch, H.; Balkenende, A. R.; Brunet-Bruneau, A.; Rivory, J., *Chemistry of Materials* **2002**, *14* (2), 931-939.
34. Grosso, D.; Babonneau, F.; Soler-Illia, G. J. D. A. A.; Albouy, P. A.; Amenitsch, H., *Chemical Communications* **2002**, (7), 748-749.
35. Cagnol, F.; Grosso, D.; Soler-Illia, G. J. D. A. A.; Crepaldi, E. L.; Babonneau, F.; Amenitsch, H.; Sanchez, C., *Journal of Materials Chemistry* **2003**, *13* (1), 61-66.
36. Grosso, D.; Cagnol, F.; Soler-Illia, G. J. D. A. A.; Crepaldi, E. L.; Amenitsch, H.; Brunet-Bruneau, A.; Bourgeois, A.; Sanchez, C., *Advanced Functional Materials* **2004**, *14* (4), 309-322.
37. wikipedia <http://fr.wikipedia.org/wiki/Sol-gel>.
38. Spiers, R. P.; Subbaraman, C. V.; Wilkinson, W. L., *Chemical Engineering Science* **1974**, *29* (2), 389-396.
39. Scriven, L. E., *MRS Online Proceedings Library* **1988**, *121*, null-null.
40. Emslie, A. G.; Bonner, F. T.; Peck, L. G., *Journal of Applied Physics* **1958**, *29* (5), 858-862.
41. Besson, S.; Gacoin, T.; Jacquiod, C.; Ricolleau, C.; Babonneau, D.; Boilot, J. P., *Journal of Materials Chemistry* **2000**, *10* (6), 1331-1336.
42. Besson, S.; Ricolleau, C.; Gacoin, T.; Jacquiod, C.; Boilot, J. P., *Journal of Physical Chemistry B* **2000**, *104* (51), 12095-12097.
43. Besson, S.; Gacoin, T.; Ricolleau, C.; Jacquiod, C.; Boilot, J. P., *Journal of Materials Chemistry* **2003**, *13* (2), 404-409.
44. Besson, S.; Ricolleau, C.; Gacoin, T.; Jacquiod, C.; Boilot, J. P., *Microporous and Mesoporous Materials* **2003**, *60* (1-3), 43-49.
45. Wang, D.; Chong, S. L.; Malik, A., *Analytical Chemistry* **1997**, *69* (22), 4566-4576.
46. Grosso, D.; Balkenende, A. R.; Albouy, P. A.; Lavergne, M.; Mazerolles, L.; Babonneau, F., *Journal of Materials Chemistry* **2000**, *10* (9), 2085-2089.
47. Hozumi, A.; Yokogawa, Y.; Kameyama, T.; Hiraku, K.; Sugimura, H.; Takai, O.; Okido, M., *Advanced Materials* **2000**, *12* (13), 985-987.
48. Zhang, F.; Yan, Y.; Yang, H.; Meng, Y.; Yu, C.; Tu, B.; Zhao, D., *Journal of Physical Chemistry B* **2005**, *109* (18), 8723-8732.
49. chemspider <http://www.chemspider.com/Chemical-Structure.5754.html> (accessed Apr 30, 2014).

Chapter III.

Thin film coating:

SDA impact on the stationary

mesostructures phase and

chromatographic performances

III.1. Ordered mesoporous silica thin films	72
III.1.1. Selected SDAs.....	72
III.1.2. Mesostructure formation mechanism	73
III.1.2.1. <i>The importance of relative humidity</i>	73
III.1.2.2. <i>CTAB mesostructured silica films</i>	74
III.1.2.3. <i>Pluronic mesostructured silica films</i>	75
III.2. Mesostructured silica stationary phases in capillary columns	76
III.2.1. Analytical techniques description for mesostructure characterization	76
III.2.1.1. <i>N₂ and krypton adsorption/desorption measurements</i>	76
III.2.1.2. <i>XRD Measurements</i>	77
III.2.1.3. <i>SAXS Measurements</i>	77
III.2.1.4. <i>SEM measurements</i>	79
III.2.2. Analyses of the CTAB induced stationary phases	81
III.2.2.1. <i>Influence of the CTAB/Si ratio on the physical properties</i>	81
III.2.2.2. <i>Chromatographic performances</i>	84
III.2.3. Analyses of Pluronic F68 induced structured silica stationary phases	86
III.2.3.1. <i>Influence of the F68/Si ratio on the physical properties</i>	86
III.2.3.2. <i>Chromatographic performances</i>	90
III.2.4. Pluronic P123 and F127 induced stationary phases	91
III.2.4.1. <i>Influence of the pluronic/Si ratio on the physical properties</i>	91
III.2.4.2. <i>Chromatographic performances</i>	93
III.3. Comparison between the SDA	94
III.3.1. Influence of the coating step: SDA content and pressure.....	94
III.3.2. Influence of pore size on chromatographic properties	96
III.4. Conclusion	97
III.5. References	98

III.1. Ordered mesoporous silica thin films

In the precedent chapter, we have studied and optimized the parameters (dilution, coating time, pressure, and viscosity) to obtain a reproducible coating process and to maximize the stationary phase thickness.

We saw that the viscosity of the sol, mainly directed by the SDA nature and its concentration, affects the final stationary phase thickness. However, the SDA also modified the texture of the stationary phase, which could drastically change the columns retention properties. Noteworthy, the nature of the SDA affected the pore size, surface area and pore volume but can also modifies the pore-network structuration. These porous structures include 2D hexagonal arrangement of cylindrical pores as observed in the famous MCM-41 mesoporous silica, but also various cubic phases (primitive, body centered or face centered) and 3D hexagonal phases.

In this chapter, we will first rapidly review the different expected structures, depending on the SDA nature and concentration. The external parameters such as the relative humidity which can affect the columns features will also be presented. Finally, the influence of physical characteristics of the different as-obtained silica coatings on the stationary phase retention properties will be highlighted. We will first focus on CTAB as SDA, then on the F68 (poloxamer pluronic F68) and finally on two other pluronics: P123 and F127.

III.1.1. Selected SDAs

The SDA that were used here are listed below:

- CTAB (cetyltrimethylammonium bromide $C_{16}H_{33}N^+(CH_3)_3, Br^-$), a cationic surfactant, is often used for the synthesis of MCM-41 type silicas (2D hexagonal porous network) and MCM-48 type oxides (cubic porous network).
- Pluronic F68 or F68 (polyoxyethylene-polyoxypropylene-polyoxyethylene: $EO_{73}-PO_{28}-EO_{73}$), a nonionic poloxamer, also qualified as copolymer tri-block, is used in the synthesis of SBA-16 (body centered cubic porous network) mesoporous silica; SBA standing for Santa Barbara Amorphous as developed at the University of Santa Barbara.¹
- Pluronic F127 or F127 ($EO_{101}-PO_{56}-EO_{101}$), is used in the synthesis of SBA-16 mesoporous silica, and leads to larger pores than F68 as it is a bigger molecule.¹

- Pluronic P123 or P123 (EO₂₀-PO₇₀-EO₂₀), is used in the synthesis of SBA-15, (2D hexagonal porous network) mesoporous silica.¹

The listed mesostructures are of course not exhaustive, as the SDA concentration and the synthetic conditions (coating parameters, pH...) also play a role.

III.1.2. Mesostructure formation mechanism

III.1.2.1. The importance of relative humidity

For the EISA process used in this work, the mesostructure formation starts during the evaporation. As the solvent evaporates, SDA micelles are formed and they progressively organize into a structured mesophase, from the air interface to the substrate. Simultaneously, the silica condensation and cross-linking occurs around the SDA network. As a result, thicker films often fail to be completely organized as the gel near the substrate is already condensed and rigid before the complete self-organisation of the SDA.² Therefore, it is important to control the experimental conditions to ensure the SDA self-organization before silica gelation and stiffening and the yield of a thin film (which is not too thick).

The condensation rate of the gel also depends on the relative humidity. In high humidity, water will evaporate more slowly or can even dissolve in the gel, delaying gelation, while a dry atmosphere will have the opposite effect. Relative humidity can also have an effect on the stationary phase obtained, as the result of two combined effects:³

- Water present in the stationary phase can solvate the ionic head of the CTAB or gather with the hydrophilic part of the pluronic poloxamers, and results in the swelling of the polar phase.
- The volume fraction of the SDA present in the film decreases as its water content increases.

Thus, the thermodynamically stable mesostructure may change as a result of relative humidity.⁴

In our process, to avoid reproducibility problems, dry nitrogen gas was chosen as the carrier gas instead of compressed air of unknown humidity. Moreover, the film thickness deposited into the capillary columns rarely exceeded 100 nm to ensure the better ordering of the silica coating.

III.1.2.2. CTAB mesostructured silica films

The use of CTAB as a SDA can lead to a wide variety of mesostructures depending on the relative humidity and CTAB concentration, as described in Fig. III.1.³

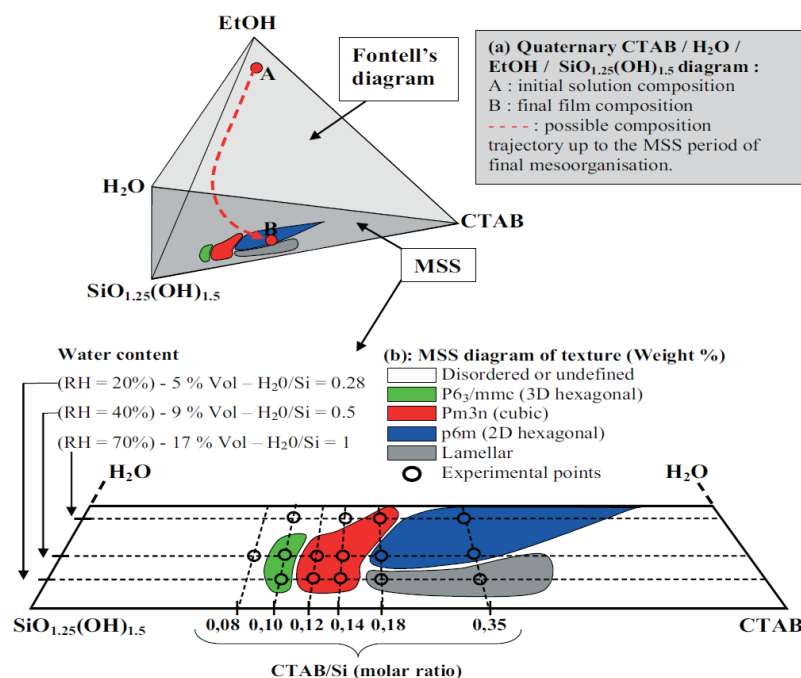


Fig. III.1- Phase diagram of the mesostructures obtained with EISA of the system CTAB/Si_{1.25}(OH)_{1.5}/EtOH/H₂O, from Grosso and coworkers.³

As the ethanol evaporates, the sol composition changes until only water, silica and CTAB remain, as illustrated in the Fontell's diagram. It may lead to various structures, with 3D- or 2D-hexagonal, cubic or lamellar geometry.

Yet, some of these mesostructures are not thermodynamically stable, and may form only if the deposited sol gelifies fast enough around the unstable SDA mesophase (see Fig. III.2).⁵ To ensure the better long-range ordering of the deposited film, it was reported that the precursors in the initial sol should be partially hydrolyzed (2 or 3 Si-O-Si liaisons per precursor).⁶

Such a condition is obtained after aging the initial sol solution for 6 hours at 40°C. More recently, it was shown that similar conditions could be obtained using one hour of aging time at 60°C.⁷ In our study, we took into account such literature precedent to optimize our coating process: the initial composition for our sol was set to TEOS: H₂O:EtOH = 1:5:3.8 and the aging time was 1 hour at 60°C before addition of SDA and coating.

For chromatographic applications, we tried to maximize the specific surface area of the porous adsorbent to increase the probability of interactions between the adsorbent and the

analytes. Therefore, we first focused on a highly structured phase (3D hexagonal phase), with the greater pore volume *a priori* and therefore a CTAB/Si molar ratio of 0.10 was chosen.

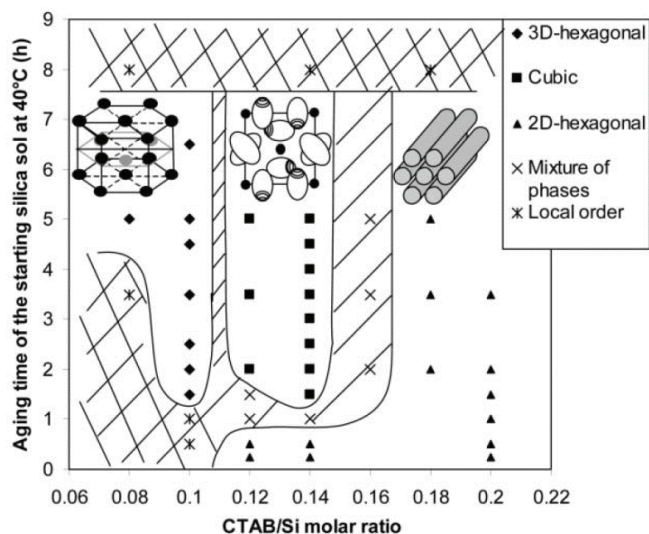


Fig. III.2 – Phase diagram of a CTAB mesostructured silica sol, showing the domain of existence of three micellar phases as a function of the CTAB/Si molar ratio and the aging time of the initial sol at 40°C.⁵ The initial sol composition is the same as the one used in this work.

III.1.2.3. Pluronic mesostructured silica films

In the case of non-ionic block copolymer SDAs, the final oxide structuration was reported to depend on the sol water content and the SDA concentration. This point is illustrated in Fig. III.3, for the preparation of a titanium oxide³ film using pluronic F127.

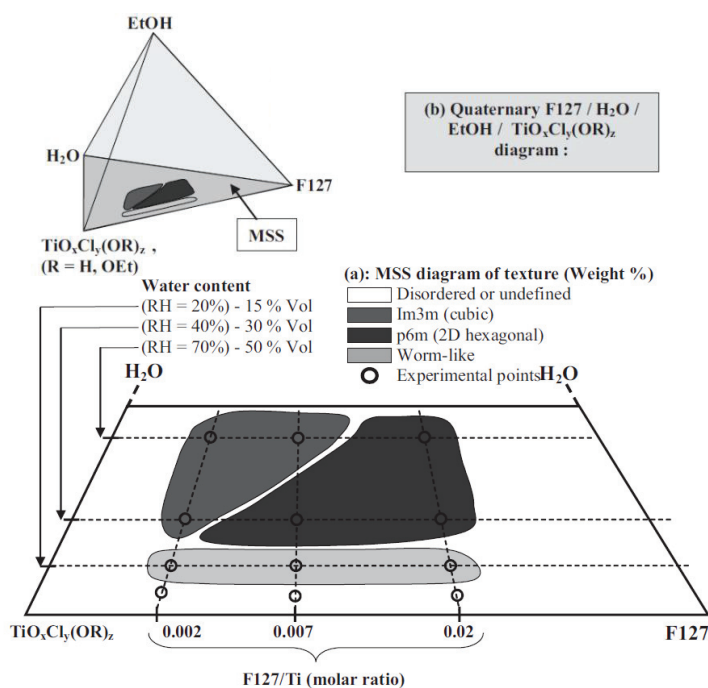


Fig. III.3– Phase diagram of the mesostructures obtained with EISA of the system F127/TiO_xCl_y(OH)_z/EtOH/H₂O, from Grosso and coworkers.³

These SDAs are generally used to obtain big mesopores (up to 30 nm compared to a few nm with CTAB)¹. The structure of the silica walls was also found to be more porous due to the presence of microporous “corona” regions around the mesopores. Such micropores arising from the partial occlusion of the PEO chains at the interface of the mesopores and the silica matrix.⁸⁻⁹

III.2. Mesostructured silica stationary phases in capillary columns

III.2.1. Analytical techniques description for mesostructure characterization

As sol-gel mesostructures obtained by EISA are dependent of the coating conditions (relative humidity, deposited thickness, heating...), we tried as much as possible to characterize the as-obtained films in the capillary columns.

III.2.1.1. N₂ and krypton adsorption/desorption measurements

Our 1 meter long columns exhibit approximately about 0.05 m² of specific surface area, which is too small for proper N₂ adsorption/desorption analysis. Attempts were therefore undertaken to analyze the columns using a more sensitive gas probe: Krypton. The analyses were performed by cutting the columns into small 1 cm long pieces that were introduced in the apparatus cells. As shown in Fig. III.4.a, it is possible to discriminate between an uncoated and a coated capillary, but the calculated BET surface areas were unreliable due to huge base line drift during sample measurements (Fig. III.4.b).

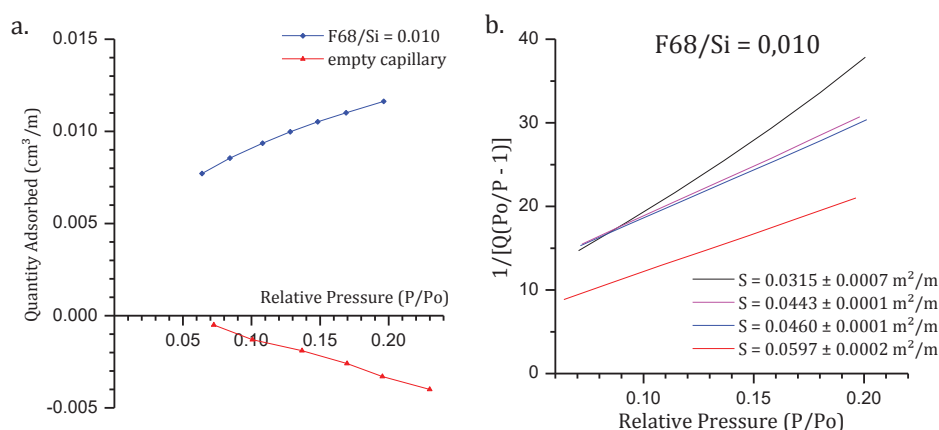


Fig. III.4 – BET analysis of capillary columns with krypton. (a) BET krypton adsorption isotherm for a coated and an uncoated capillary. (b) 4 repetitions of the same measurement: signal is too low for a quantitative study.

Therefore some N_2 ads./des. measurements were also performed on powders produced in bigger quantity. The synthesis procedures to yield these powders were chosen to mimic as best as possible the capillary coating conditions, i.e. the sol compositions were the same and drying of the gel was performed under nitrogen flow. The experimental set-up for the synthesis of the silica gel is illustrated on Fig. III.5. Taps were used to isolate the powder under an inert atmosphere at the end of the drying step and the cap could be removed to recover the powder for further use.

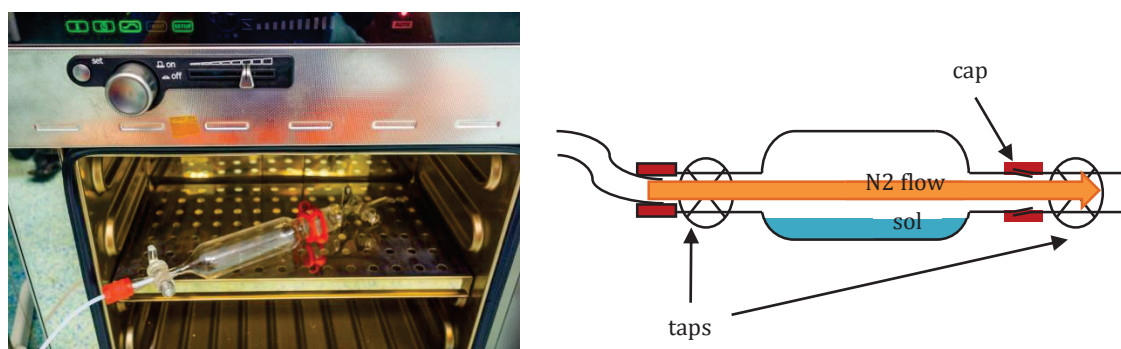


Fig. III.5 – Picture and schematic cross section of the experimental set-up for sol-gel synthesis under azote flow.

The exact synthesis conditions are described in the Experimental section (Annex A.4.).

N_2 ads./des. measurements were used to quantify the specific surface, the pore diameter distribution and the porous volume of the mesostructured silica powders.

III.2.1.2. XRD Measurements

Powder XRD analyses were performed at the diffractometry center Henri Longchambon in Lyon. These XRD data were further compared with the SAXS measurements performed directly on the capillaries, in order to control the matching between silica mesostructures synthesized inside columns or in the glass apparatus.

III.2.1.3. SAXS Measurements

Using high energy synchrotron radiation, small angle X-ray scattering (SAXS) characterization could be performed directly on the stationary phases inside the capillary columns to investigate the order of the silica mesostructure. Indeed, pore-periodicity with the silica framework lead to diffraction peaks visible on the SAXS pictures. Measurements were carried out at the ESRF (European synchrotron radiation facility) in Grenoble at the BM2 beamline, with the help of Mireille Maret, from SIMAP, and Vincent Jousseume from the CEA LETI.

The experimental setup 1 is illustrated in Fig. III.6. Capillary column segments were set perpendicularly to the beam. As the X-ray beam was wider than the capillary internal

diameter (the spot is approximately $150\ \mu\text{m}$ wide), the signal should be the sum of the interactions of the X-rays with stationary phase area oriented along all the direction perpendicular to the capillary axis, as illustrated in Fig. III.6.c. Thus, if the mesoporous structure is well ordered and oriented with respect to the capillary walls, diffraction patterns should be visible, more or less like those obtained for bulk silica powders. However, in the vertical direction (axis of the capillary), our system could present anisotropy which is expected to appear on the SAXS pictures.

In addition to the stationary phase, the beam also passes through the amorphous silica composing the capillary envelope. This layer has a coherence length at about $1.5\ \text{nm}$ which was visible in the SAXS pictures as a ring at $4.2\ \text{nm}^{-1}$ and did not interfere with our measurement since the structures were looking at were much bigger (at least $4\ \text{nm}$).

In this setup, we imaged the stationary phase at different capillary height, and obtained the same spectra, indicating that the stationary phase structure is homogeneous along the capillary length (or at least for several cm).

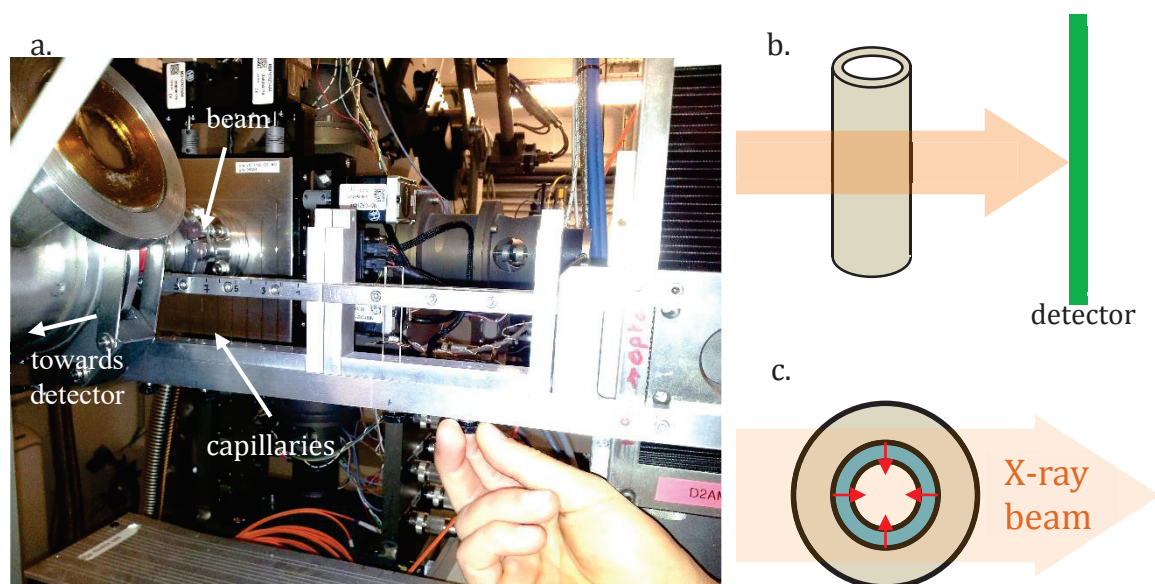


Fig. III.6 – Setup 1 for SAXS observations of the stationary phase inside the capillary segments of column on the BM2 beamline at ESRF. Picture of the experimental bench (a), and schematic drawings of the side view (b), and top view(c), with the normal directions to the wall represented in red arrows.

We have also tried another setup (setup 2) in which capillary segments of around $4\ \text{mm}$ were coaxial to the X-ray beam, as illustrated in Fig. III.7. In this configuration the samples present a circular geometry in the plan perpendicular to the beam that we also found in the diffraction spectra. However aberrations were visible: arcs of high intensity passing through the center of the picture, which were probably due to a slight misalignment of the capillary axis with respect to the beam or to uneven cuttings of the capillary ends.

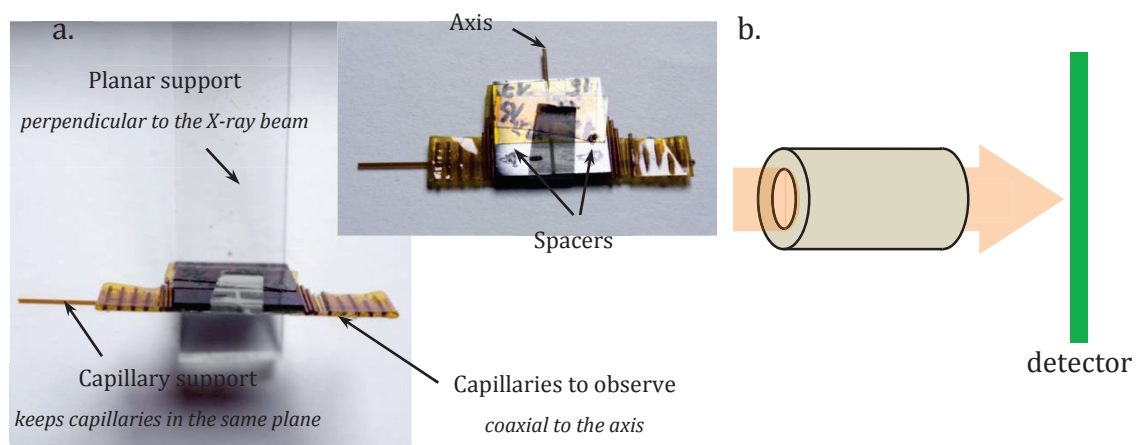


Fig. III.7 – Setup 2 for SAXS observations of capillaries coaxial to the X-ray beam. (a) Pictures of the dispositive: capillaries are placed side by side, coaxial to the axis. (b) Schematic drawing of the capillary side view.

One year before the experiment, we conducted a preliminary study to justify the interest of SAXS measurements. We kept the sample used for this study and tested it one year later, to investigate the effects of sample aging. As the same spectrum was obtained at one year interval, we could show that, in our case, sample aging had no effect on the films and that silica mesostructures were stable over time.

III.2.1.4. SEM measurements

As for chapter II, the thickness of the stationary phase was evaluated on the high resolution Hitachi S 5500 scanning electron microscope of the Nanocharacterization Platform at MINATEC. As silica is an insulator, it charges under the electron beam and makes observations particularly difficult, especially as there is a low contrast between the stationary phase made of porous silica, and the walls made with fused silica.

Charge effects were prevented by using low acceleration voltages between 0.5 and 2 keV, instead of 20 to 30 keV, as it is common in standard SEM instruments. In this configuration, resolution was too weak to obtain information on the porous structure, but, as we can see on typical SEM pictures in Fig. III.8, the contrast was sufficient to observe the interface between the mesoporous silica stationary phase and the fused silica of the walls, and thus, the film thickness measurement was possible.

Generally, 9 small segments were cut every 12.5 cm along the 1 meter long columns and the film thickness was evaluated as the average between the observations of the 9 cross-sections. Fig. III.8 shows representative SEM micrographs of different stationary.

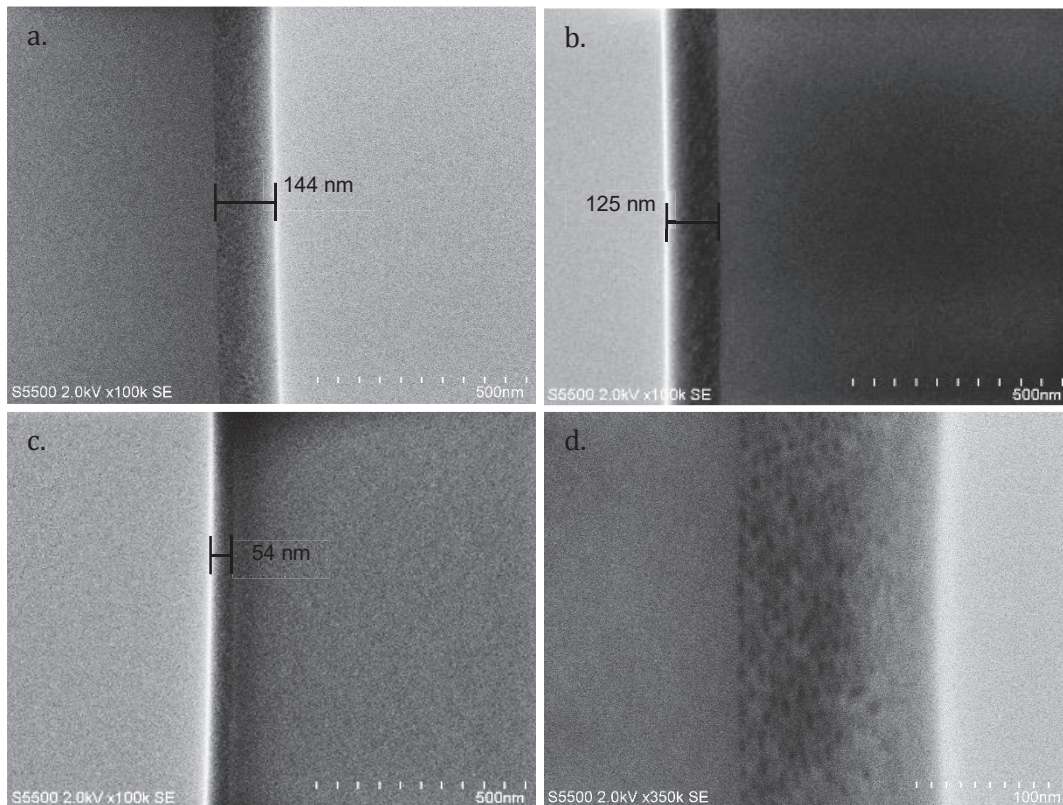


Fig. III.8 – (a to c) SEM pictures and thickness measurements of various stationary phases at 100 k magnification. (d) Zoom at 350 k magnification of the stationary phase with F127/Si = 0.005.

The average thickness of the stationary phase and its relative precision were calculated for each column as the average and standard deviation of these 9 measurements. Fig. III.9 shows a typical set of measurements representative of what we observed. Thereafter, only the average and standard deviation of the stationary phase thicknesses will be presented. As measurement dispersion was generally high, standard deviation was used for the representation of error bars on the different graphs (which are +/- one standard deviation).

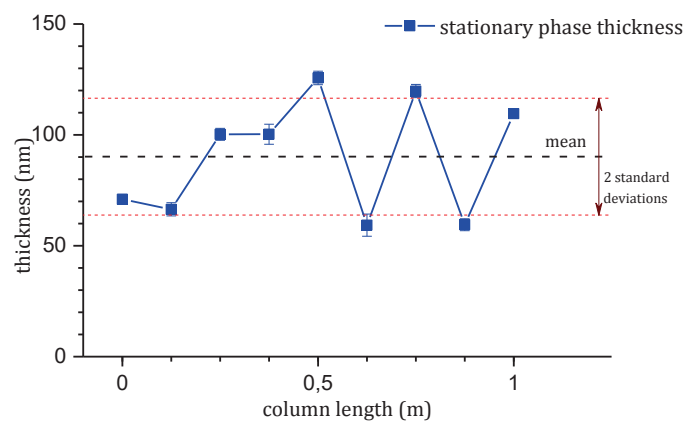


Fig. III.9 – Representative stationary phase thickness in a column as measured with the SEM. Each point is calculated as the average of 3 measurements. The average and standard deviation of the measurements are indicated on the figure.

III.2.2. Analyses of the CTAB induced stationary phases

Stationary phases structured with CTAB were first studied, as CTAB was easily removed by annealing the columns at 250°C under constant helium flow. During annealing, the SDA removal was monitored by the recording of the FID signal, as the column was connected to a GC apparatus (cf Fig II.10). Columns were coated at a pressure of 1 bar, for a coating time of 2 seconds. Similarly to what was done in the literature, we changed the CTAB/Si molar ratio to study its effect on the obtained stationary phase and the chromatographic properties. The expected influence of the different CTAB/Si molar ratios is shown in Table III-1.

CTAB/Si	0.14	0.10	0.05
Possible mesostructuration	Cubic	Hexagonal 3D	-

Table III-1 – CTAB/Si molar ratios that were investigated.

Noteworthy, CTAB/Si molar ratios under 0.10 were also investigated despite the yielding of disordered or vermicular phases in literature precedents because of interesting chromatographic results (see Fig. III.1 and Fig. III.2).

III.2.2.1. Influence of the CTAB/Si ratio on the physical properties

As presented in Fig. III.10, the film thicknesses obtained for the different CTAB/Si ratios were really similar, and not or only slightly affected by the CTAB content in the sol: it increases slightly in average as CTAB concentration increased. This is coherent with the results reported in chapter II, which showed that the viscosity of the CTAB sol was not drastically modified by the CTAB content (Table II-3).

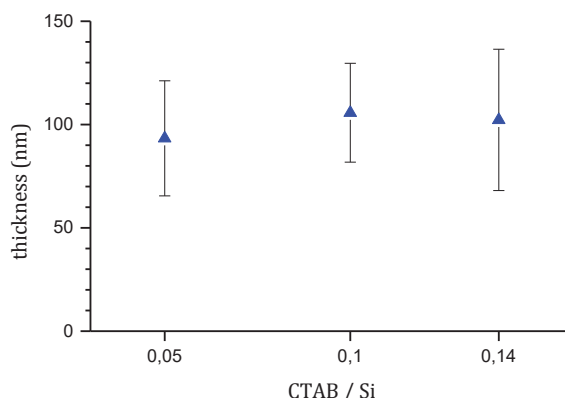


Fig. III.10 – Stationary phase thickness of the films coated with different CTAB/Si ratios, measured by SEM. Error bars are +/- one standard deviation.

Fig. III.11 exhibits the collected SAXS pictures for the three different stationary phases. The data presented here are the result of the subtraction of the obtained signal by the signal of an empty capillary used as reference. For the two stationary phases using a CTAB/Si ratio over 0.1 (Fig. III.11.b and c), the spectra present a diffraction ring, which suggests some ordering of the mesostructures, probably a worm-like structure with a constant inter-pore distance.

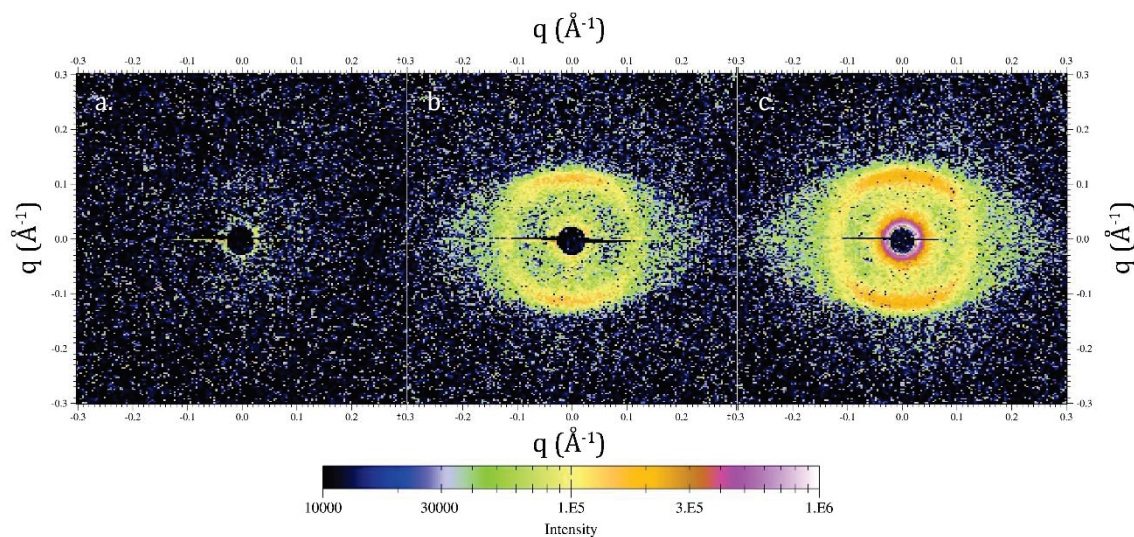


Fig. III.11 – SAXS data for CTAB mesoporous stationary phases, coated at a pressure of 1 bar. CTAB/Si ratios are 0.05 (a), 0.10 (b) and 0.14 (c). Data presented are the result of the subtraction of the signal for the capillary column minus a reference capillary without stationary phase.

On the other hand, no significant difference with the reference signal was observed for the lowest CTAB/Si ratio, thus suggesting the absence of order for the mesoporous structure (Fig. III.11.a). This absence of order was somehow expected from the literature, as presented in the Fig. III.1 and Fig. III.2.

In the Fig. III.11.b and c, the diffraction rings are slightly distorted at the horizontal plane proximity (more diffuse and larger signal). This anisotropy is certainly due to the confinement of the stationary phase inside the walls of the capillaries, oriented vertically here. Similar observations were also attributed to wall confinement effects in other studies.¹⁰

Radial plots are presented on Fig. III.12. Intensity maxima are found for a vector norm of 1.18 and 1.20 nm⁻¹, which correspond to an average distance between the pores of 5.3 and 5.2 nm. These values were similar to those found in the literature for silica thin film using CTAB as SDA (usually around 4 nm).

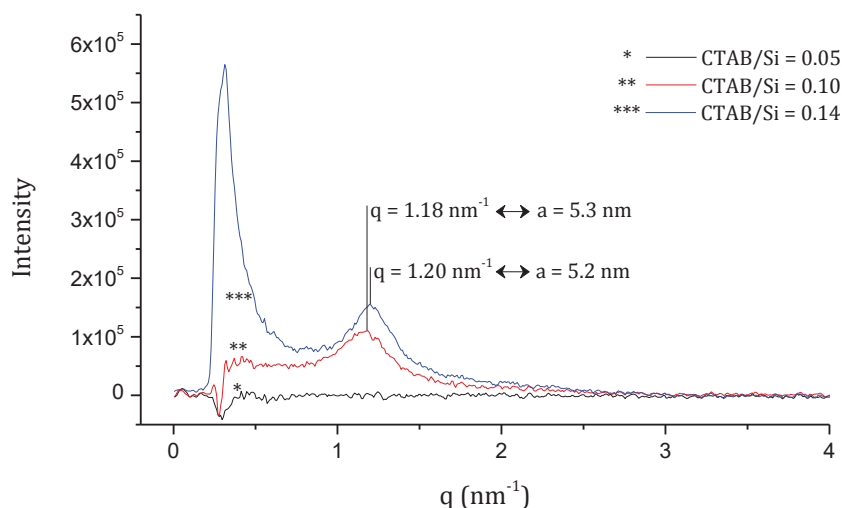


Fig. III.12 – Radial integration of SAXS data for the 3 columns prepared at 1 bar. The signal maximum for the interference ring is found at 1.18 or 1.20 nm^{-1} for the columns prepared with CTAB/Si molar ratios of 0.10 and 0.14 respectively. No peak is observed for the column prepared with a CTAB/Si molar ratio of 0.05.

Powders synthesized in “column like conditions”, were analyzed by XRD and N_2 adsorption. As presented in Fig. III.13, XRD analyses showed similar results as those obtained by SAXS radial integration. However, all the samples presented an interference peak, although of minor intensity for the powder with CTAB/Si = 0.05. This peak accounts for the presence of a constant inter-pore average distance for the silica coatings. The inter-pore distance values are 3, 2.9 and 2.8 nm for CTAB/Si = 0.05, 0.10, 0.14 respectively. These differences can be explained from the relatively different synthesis conditions: also the powder synthesis mimics the conditions inside the column, they are still very different as the thickness of the coating is several order of magnitude greater than that in the column (2 mm compared to few hundreds nm).

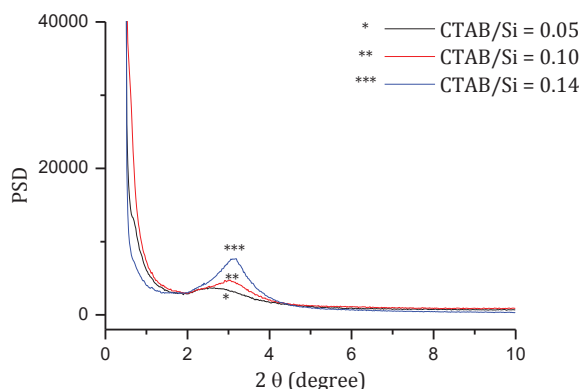


Fig. III.13 – XRD analysis of powders synthesized in “column like conditions” for varying CTAB/Si molar ratios.

However, after annealing, the powders were still dark with organic residues. The annealing program (4h-250°C) was probably not adapted for CTAB removal in the case of

these powders: i) the gas flow during annealing, although similar to that used in the column, was spread on a much larger cross-section, and ii) the powder fragment were more probably around several μm thick, instead of the 100 nm thick stationary phase.

As a result, N_2 adsorption/desorption unfortunately gave misrepresented data (negative C term for the BET). For a CTAB/Si ratio of 0.1 or 0.14, BET values around 800 to 1000 are common and were expected.¹¹ Complementary information could be obtained by increasing drastically the annealing time, but this may be of small interest if the powder composition is different from the film composition inside the columns.

III.2.2.2. Chromatographic performances

Chromatographic properties of the different columns were evaluated for the separation of light alkanes (methane to n-pentane). Methane was considered as unretained and used to calculate the holdup time. Propane retention factor was used to compare the different columns between each other, as it was generally of the order of 1 (smaller retention factors are often less precise and greater retentions are more prone to saturation).

Fig. III.14 present the retention properties of the different stationary phases of CTAB/Si molar ratios from 0.05 to 0.14 and coated at 1 bar for 2 s. Propane retention (black square dots), surprisingly, increased for lower CTAB/Si ratios. As a result the “stationary phase affinity” (red round dots), which is defined as the retention factor divided by the thickness of the stationary phase (with a 100 factor to keep values of the order of unity), followed the same trend.

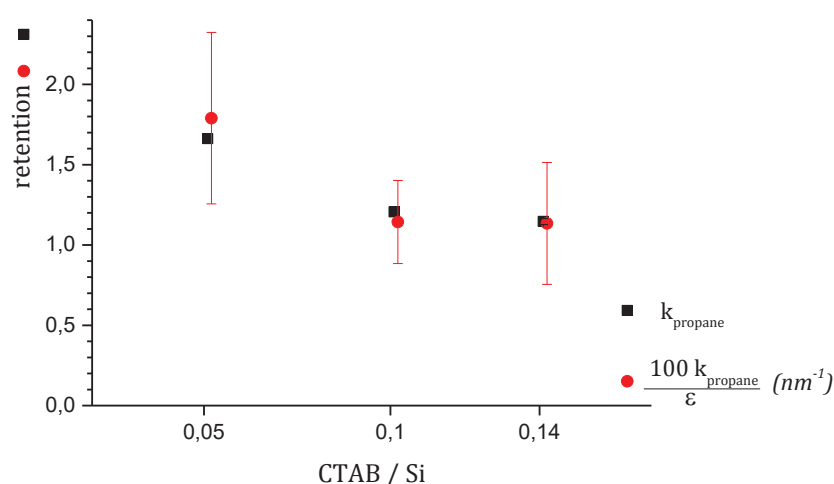


Fig. III.14 – Retention properties of columns coated at 1 bar with a sol gel stationary phase as a function of CTAB/Si molar ratios. Error bars are +/- one standard deviation, they are invisible for retention.

These results confirmed the trend that we observed in a preliminary study on columns coated at a pressure of 0.5 bar. Although the film thickness was lower on these first columns,

their affinities towards propane were really similar to those of the columns coated at 1 bar with the same CTAB/Si ratio (see Fig. III.15).

Nonetheless, no order was found on SAXS data of all the columns coated at 0.5 bar. This result can be related to the absence of silica structuration caused by low pressure coating (0,5 bar) or to the thinness and fickleness of the film that prevent to collect interference signals. To confirm the influence (or not) of pressure on order requires further investigations and this point will be discussed later.

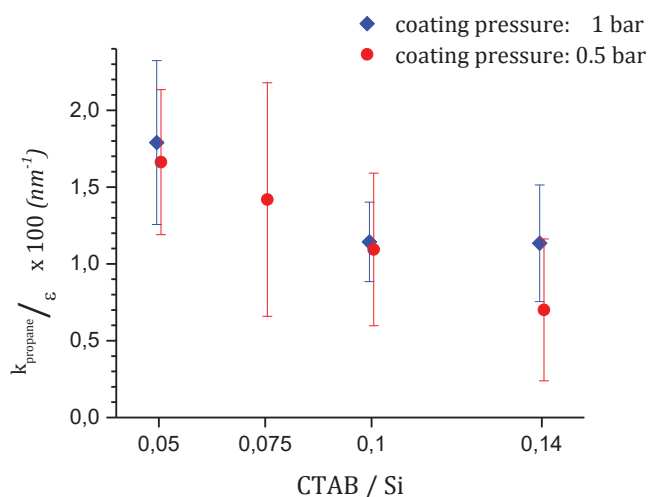


Fig. III.15 – Affinity of the stationary phase towards propane for various CTAB/Si molar ratios. Similar results are observed regardless of the coating pressure used. Error bars are +/- one standard deviation.

The adsorption standard enthalpies of light alkanes (C_2 to C_5) were calculated from the Van't Hoff plots, between 30 and 60°C, for the columns coated at 1 bar (cf Chapter I). They are represented in Fig. III.16. as a function of carbon number for the column of different CTAB/Si ratios.

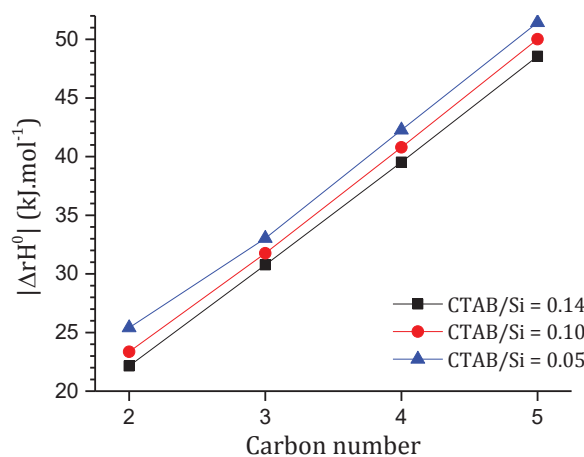


Fig. III.16 – Adsorption standard enthalpy towards light alkanes of the columns coated at 1 bar with a sol gel stationary phase with various CTAB/Si molar ratios.

Adsorption standard enthalpies were found linear with carbon number, in accordance with theory. The lines for the different CTAB/Si ratios had similar slopes ($8.8 \pm 0.1 \text{ kJ}\cdot\text{mol}^{-1}$), which indicates that they have similar physical properties. Moreover, the values found are close to those obtained for porous silica gel with a mean pore diameter of 4.6 nm and specific surface of $650 \text{ m}^2/\text{g}$.¹⁴

III.2.3. Analyses of Pluronic F68 induced structured silica stationary phases

Stationary phases structured using pluronic F68 were coated at 1 bar for 6 seconds, then further stabilized under nitrogen flow for 8 hours at 120°C , and finally annealed at 300°C for 12 hours under wet air flow. 4 different F68/Si ratios from 0,0017 to 0,010 were tested (see Table III-2). An extra column (F68/Si = 0.05) was coated at 4 bar to confirm the influence of the flow gas pressure on film thickness (as seen in Chapter II) and structuration.

F68/Si	0.010	0.005	0.0033	0.0017
Possible mesostructuration	Cubic ¹²	-	-	-

Table III-2 – F68/Si molar ratios that were investigated.

The as-obtained stationary phases showed similar results to those yielded using CTAB: affinity was best for lowest F68/Si ratio although an ordered mesostructure was observed only for the highest F68/Si ratio.

III.2.3.1. Influence of the F68/Si ratio on the physical properties

The thickness of the different films as a function of F68/Si molar ratio are presented in Fig. III.17. The average thickness was found to be more dependent on the SDA content than for CTAB induced films. This is in accordance with results of chapter II which showed that the sol viscosity depends more of the SDA/Si ratio when block copolymers are used (see Table II-3). Film thickness was also found to be more homogeneous for thinner coatings.

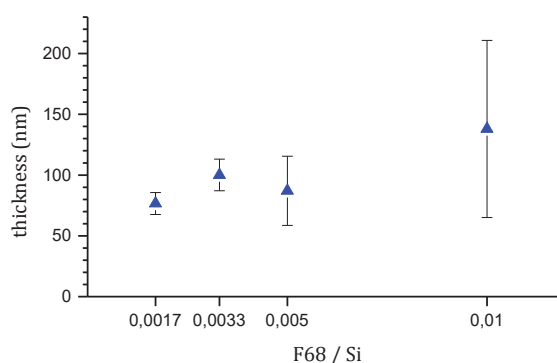


Fig. III.17 – Stationary phase thickness of the films coated with varying F68/Si ratios, measured by SEM.

SAXS pictures (after subtraction of the signal of an uncoated capillary) obtained for different F68/Si ratios and pressures are presented in Fig. III.18. A significant signal was observed for the film with F68/Si ratio of 0.005 coated at 4 bar (a very diffuse ring) and for the film using a F68/Si ratio of 0.01 (a quite complex figure).

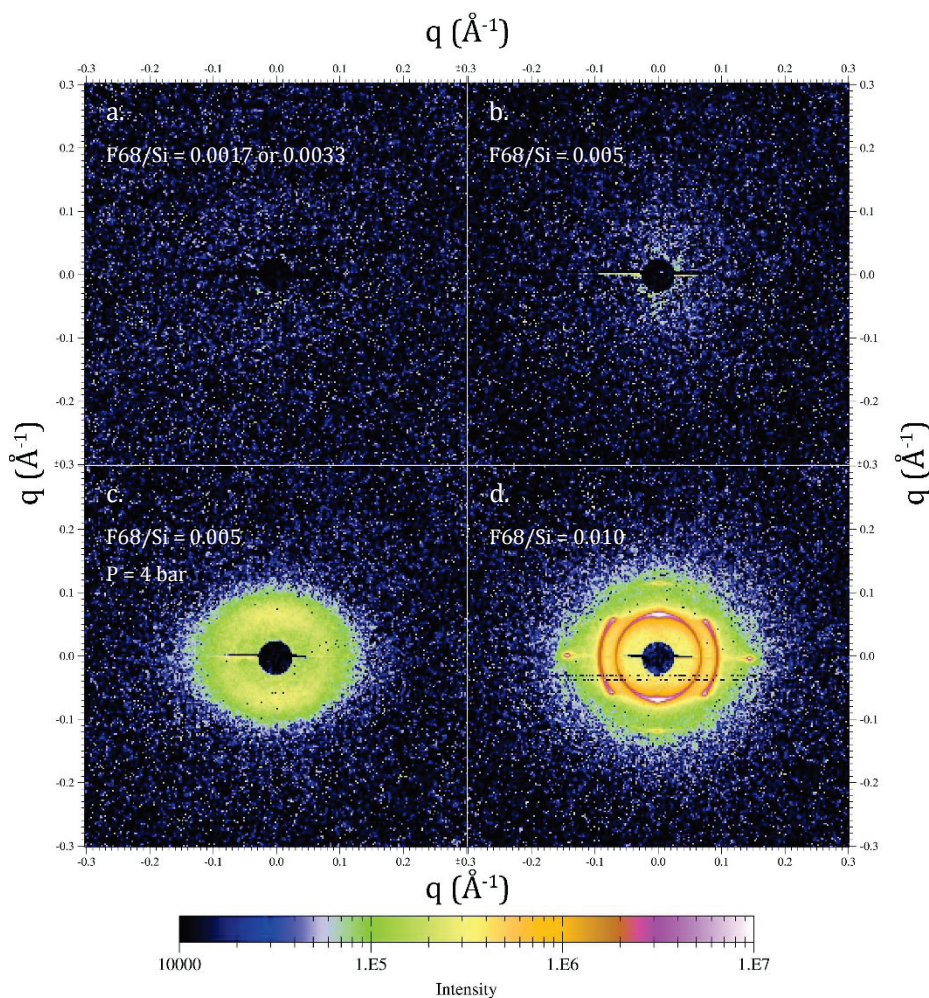


Fig. III.18 – SAXS data for F68 mesoporous stationary phases. (a) F68/Si = 0.0033, coated at 1 bar (the picture is similar to the one with F68/Si = 0.0017, not represented), (b) F68/Si = 0.005, coated at 1 bar, (c) F68/Si = 0.005, coated at 4 bar, and (d) F68/Si = 0.010, coated at 1 bar.

The radial integrations of the signals are presented in Fig. III.19. They confirm the presence of a relatively broad diffraction peak for the column coated at 4 bar which suggests the presence of a poorly ordered porous network (presumably worm-like) with a coherence length (inter-pore distance) of *c.a.* 9.5 nm. This is coherent with the expected larger pores and thicker walls yielded with poloxamers.

The signal for the column with F68/Si ratio of 0.010 exhibit 5 peaks, whose positions are characteristic of a face-centered cubic structure for the reciprocal lattice and corresponding to a body-centered cubic mesostructure, typical of the SBA-16 family, often obtained with pluronic F68.

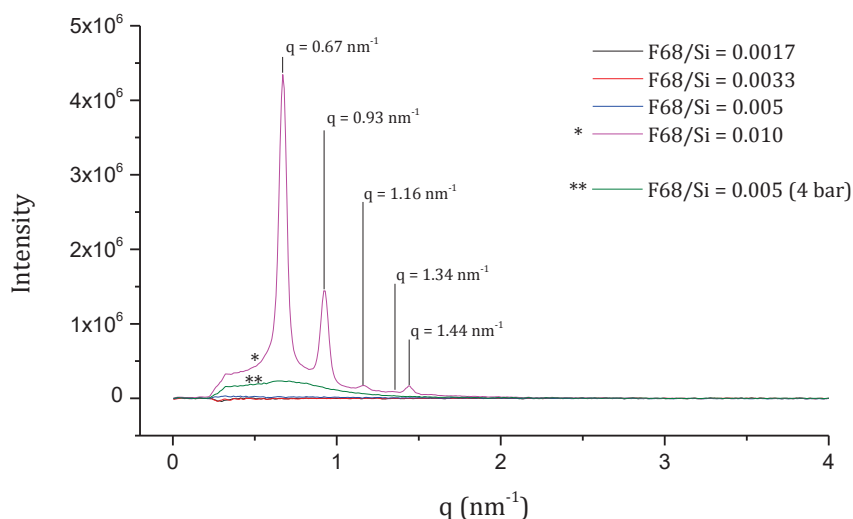


Fig. III.19 – Radial integration of SAXS data for the columns coated with F68. The ratios between peak coordinates (indicated on the figure), for the column coated with F68/Si ratio of 0.010, correspond to a face-centered cubic structure for the reciprocal lattice. The x-coordinate of the first peak coincides with the maximum of the diffuse peak for the column coated at 4 bar, and is centered on 0.66 nm^{-1} .

Complementary SAXS data were recorded for this column with a coaxial position of the capillary with respect to the X-ray beam. Pictures of both configurations, zoomed on the region of interest, are presented in Fig. III.20. On Fig. III.20.b, intense arcs are observed, crossing the pictures by its middle, as explained in III.2.1.3, which make observations more difficult as the diffraction signals is less intense in comparison. As expected with this geometry, the diffraction pattern exhibits rings centered on the direct beam. Only the first two rings are really visible and correspond to the first two diffraction peaks of the Fig. III.19. A third ring is barely visible and corresponds to the fifth diffraction peak.

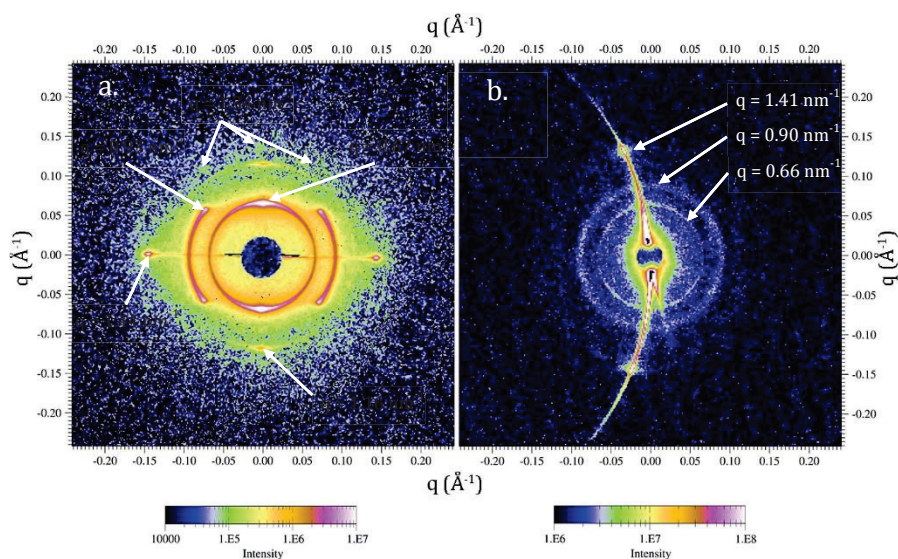


Fig. III.20 – Perpendicular (a) and coaxial (b) SAXS pictures of the column coated with F68/Si = 0.01. There is a small deviation (around 2 or 3 %) between the values measured in the two pictures.

Powders synthesized in “column like conditions” with F68 were analyzed in XRD and N₂ ads./des. measurements. XRD measurements are presented in Fig. III.21. The signal for the powder with F68/Si = 0.010 presented a shoulder peak under one degree (around 0.6°) and a broad peak at 1.1 degree. The powder with F68/Si = 0.005 presented a shoulder peak around 0.9° and a weak and diffuse peak at 2.5°. No peak were observed for the powder with F68/Si = 0.0017, except maybe a really small and diffuse peak at 2.5°.

These results suggest that the powders were not highly structured. We got the most intense signal from the powder with F68/Si = 0.010, as expected by SAXS data on capillaries. However, we expected it to be a highly structured cubic lattice, whereas the XRD data do not suggest a particularly ordered lattice (few peaks, not really distinct).

Once again, the silica powders, although synthesized in conditions mimicking those for yielding column stationary phases, are still quite different.

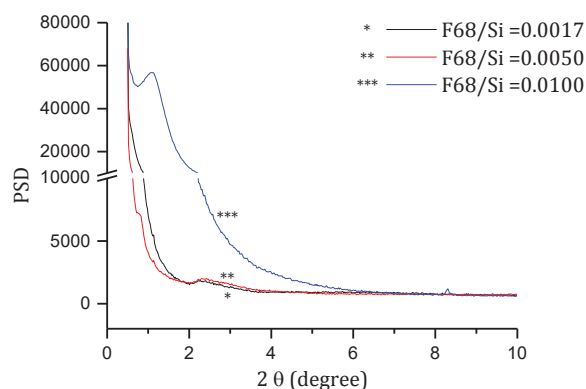


Fig. III.21 – XRD analysis of powders synthesized in “column like conditions” for varying F68/Si molar ratios.

Although bulk silica powders were found to be different from column silica coatings, their textural properties were analyzed by N₂ adsorption/desorption. The textural features and the isotherms are presented in Table III-3 and Fig. III.22 respectively. The sample with F68/Si = 0.010 was found micro-mesoporous (as shown by the type I and type IV shape of their N₂ ads./des. isotherm), although the two others are only microporous (type I isotherm).

Noteworthy, after annealing the materials were brownish, suggesting the presence of organic residues that can modify the intrinsic texture of the samples.

F68/Si	0.0100	0.0050	0.0017
BET surface area (m ² /g)	855	406	379
Total pore volume (cm ³ /g)	0.790	0.211	0.187

Table III-3 – ads N₂ adsorption characteristics for powders synthesized in “column like conditions”.

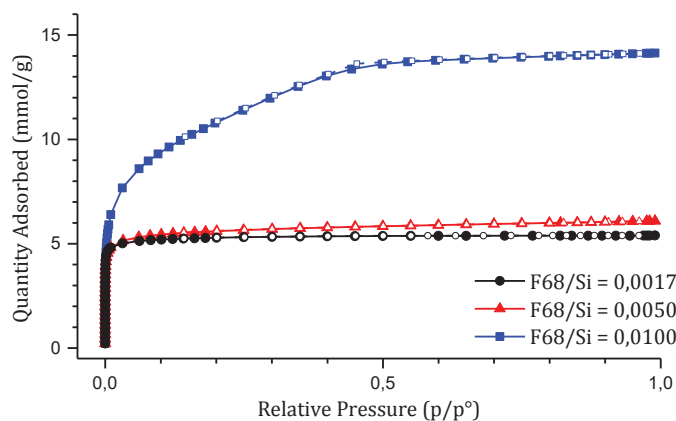


Fig. III.22 – N_2 adsorption/desorption isotherms of the mesostructured powders synthesized in “column like conditions” using F68 as SDA. The desorption isotherms are in open symbols.

III.2.3.2. Chromatographic performances

Like columns coated with CTAB, chromatographic properties of the F68 columns were evaluated for the separation of light alkanes (methane to n-pentane). Columns retention factors for propane were compared, and methane was considered as unretained.

Fig. III.23 present the retention properties of stationary phases coated at 1 bar with different F68/Si molar ratios. Propane retention (black square dots) generally increased as the F68/Si ratio decreased. The stationary phase affinity, (*i.e.* the retention normalized by the thickness - red circle dots, left scale), was highest for the lowest F68/Si ratio and decreased as F68/Si increased. As observed when using CTAB, the most structured column, coated with the highest F68/Si ratio, had the less affinity for propane.

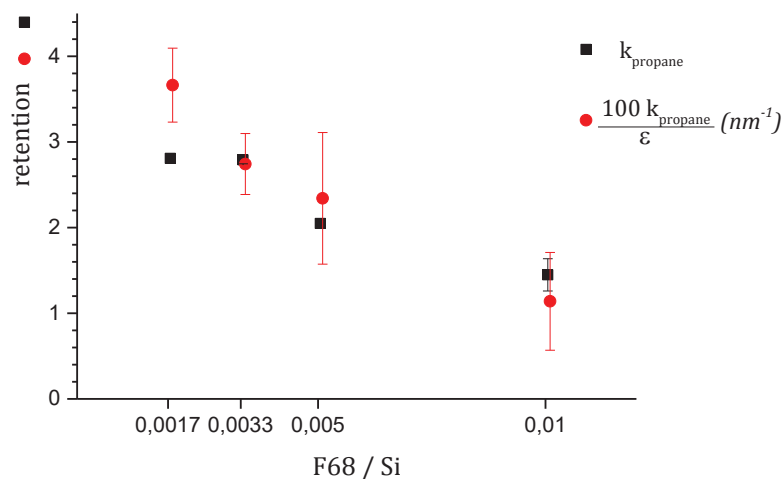


Fig. III.23 – Retention properties towards alkane for columns coated at 1 bar as a function of F68/Si molar ratios. Stationary phase affinity is plotted with red circle dots and retention is plotted with black square dots.

The adsorption standard enthalpies of light alkanes (C_2 to C_5) as a function of F68/Si are illustrated in Fig. III.24 (calculated from the Van't Hoff plots of separations between 30 and 60°C). The lines are parallel (slope at 8.3 kJ.mol⁻¹) and the values obtained are really similar to those obtained for the CTAB induced columns. This suggests that adsorption is dependent mostly upon the material but less on the porous structure.

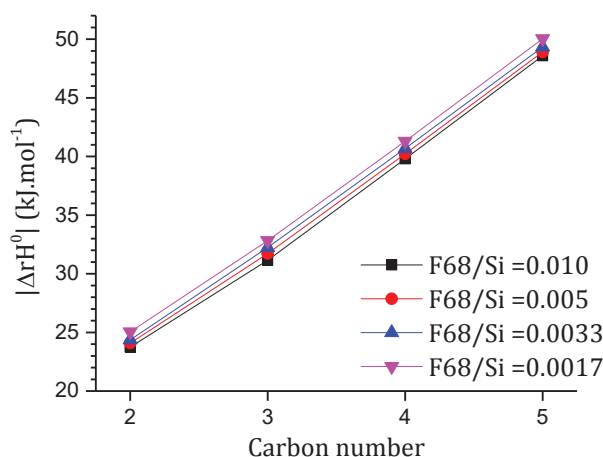


Fig. III.24 – Adsorption standard enthalpy towards light alkanes of the columns coated at 1 bar with a sol gel stationary phase with various F68/Si molar ratios.

III.2.4. Pluronic P123 and F127 induced stationary phases

Columns were prepared using pluronics P123 and F127 as SDAs. The stationary phases were coated at 1 bar for 6 seconds, then stabilized under azote flow for 8 hours at 120°C, and finally annealed at 300°C for 12 hours under wet air flow.

As chromatographic results were not as good as those obtained with pluronic F68 (less retention), only two SDA/Si ratios were explored for each SDA, as presented in Table III-4.

SDA/Si	P123/Si		F127/Si	
	0.0050	0.0025	0.0050	0.0025
Possible mesostructuration	hexagonal ?	-	Cubic or hexagonal	-

Table III-4 – F127/Si and P123/Si molar ratios that were investigated.

III.2.4.1. Influence of the pluronic/Si ratio on the physical properties

Film thickness decreased importantly at lower SDA ratio, as shown in Fig. III.25. This result is in line with that observed for F68 and can be explained by the modification of sol viscosity due by the SDA content.

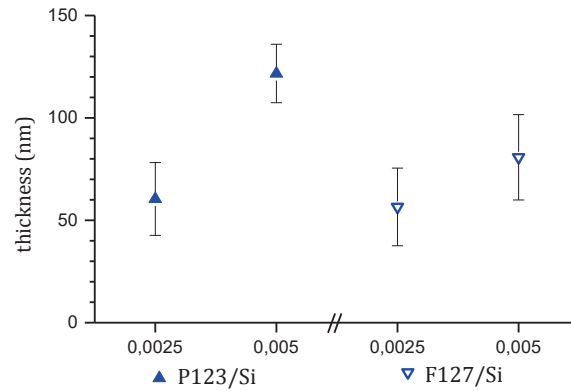


Fig. III.25 – Stationary phase thickness of the films coated with varying P123 or F127/Si ratios, measured by SEM.

As for most of the other stationary phases developed here, no signal was observed on SAXS pictures of phases prepared with pluronic P123 (P123/Si = 0.005 and 0.0025). For F127, the stationary phase exhibited a SAXS signal when F127/Si = 0.005. SAXS pictures of this specific stationary phase are presented on Fig. III.26 (capillary perpendicular (a.) and coaxial (b.) to the X-ray beam).

The SAXS pictures in Fig III.25.a presented a pronounced anisotropy: Two intense arcs of circle are visible on both sides of the horizontal axis, at $q_1 = 0.47 \text{ nm}^{-1}$, and two diffuse arcs at $q_2 = 0.81 \text{ nm}^{-1}$. These four arcs correspond to the two circles, visible on Fig. III.26.b at the same positions. Several intense arcs passing through the center of the figure are also visible. They are probably due to a slight misalignment between the capillary and the beam. Indeed, they also delimit zones where the circles are more intense (top left and bottom right for the extern circle, and bottom left and top right for the intern circle).

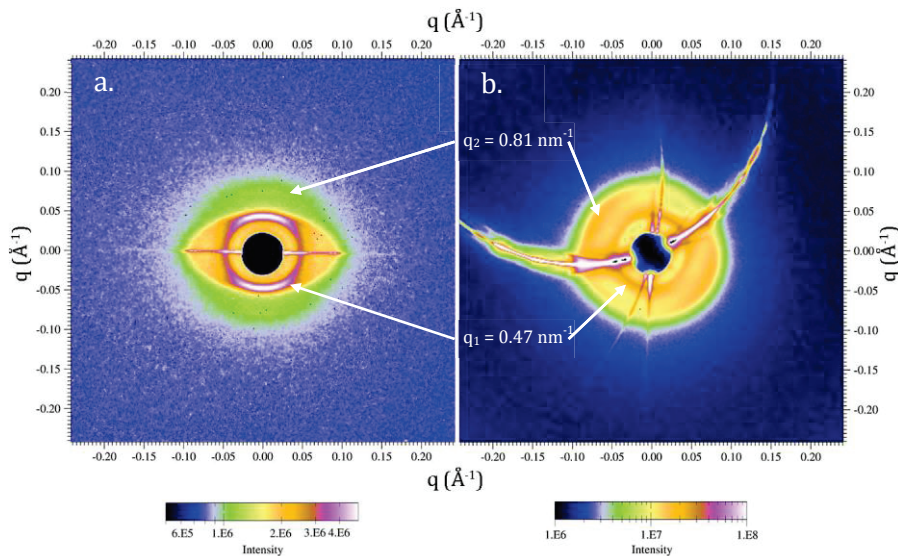


Fig. III.26 – Perpendicular (a) and coaxial (b) SAXS pictures of the column coated with F127/Si = 0.005.

The ratio between q_1 and q_2 ($1.72 \approx \sqrt{3}$) suggest that the stationary phase mesostructure presents a hexagonal geometry. It is more likely to be a 2D hexagonal arrangement, as 3D hexagonal mesostructures are less common and would lead to more diffraction peaks (except in the absence of long range order).

III.2.4.2. Chromatographic performances

Retention properties of the columns towards propane are presented in Fig. III.27 for 2 different P123/Si (filled symbols) and F127/Si (unfilled symbols) molar ratios. As for the other types of SDA, affinity (red round dots) is highest for the lowest pluronic/Si ratios. However, unlike films with previous SDA, propane retention (black square dots) is still lower for the lowest pluronic/Si ratios, as film thickness is more strongly affected by the SDA ratios. Moreover, propane retention is smaller for the film structured with P123 and F127 than those structured with F68. They were therefore not studied in details.

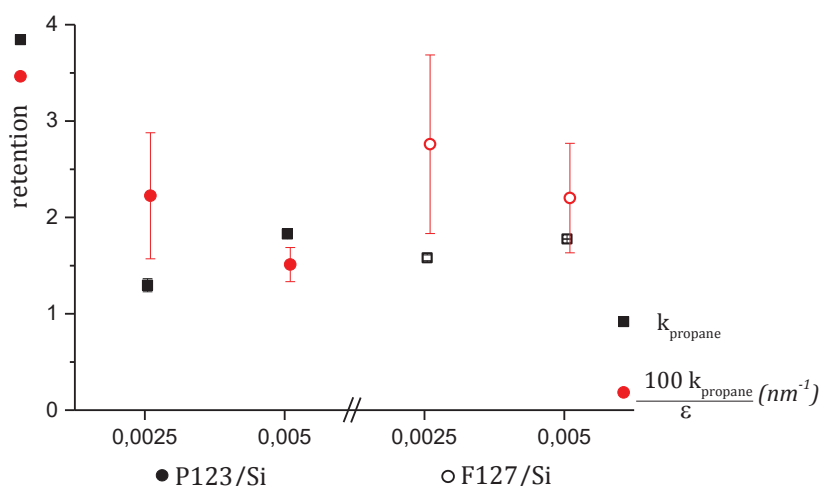


Fig. III.27 – Retention properties of columns coated with a sol gel stationary phase with various P123/Si (in filled symbols) or F127/Si (in unfilled symbols) molar ratios. Retention is plotted with black square dots and the stationary phase affinity is plotted with in red circle dots.

The adsorption standard enthalpies of light alkanes (C_2 to C_5) as a function of the SDA/Si ratio are shown in Fig. III.28 (calculated from the Van't Hoff plots, between 30 and 50°C). The values are very similar to those found with the other SDA, adsorption standard enthalpies increased linearly with the carbon number, and were found roughly parallel to each other (slope around 8.6 kJ.mol⁻¹).

It is noteworthy to notice that the inflexion point that seem to appear for ethane is most likely due to calculation errors. Indeed, as the retention of these column is low, the peaks from methane and ethane overlap at 40°C or higher, and are coeluted at 60°C. As a result, there are not enough precise points on the Van't Hoff plot for a correct linear regression.

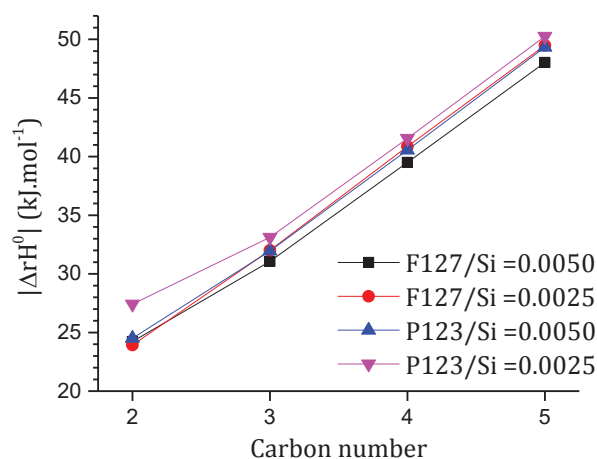


Fig. III.28 – Adsorption standard enthalpy towards light alkanes of the columns coated at 1 bar with a sol gel stationary phase with various P123 and F127/Si molar ratios.

III.3. Comparison between the SDA

III.3.1. Influence of the coating step: SDA content and pressure

First of all, the results suggest that there is no particular interest in having an ordered mesoporous silica stationary phase for gas chromatography. Disordered mesostructured stationary phases achieve similar retentions towards light alkanes.

Moreover, as illustrated in Fig. III.29, the affinity of the silica stationary phases is greatest towards light alkanes when lowest SDA/Si ratios were used and disordered mesostructures obtained.

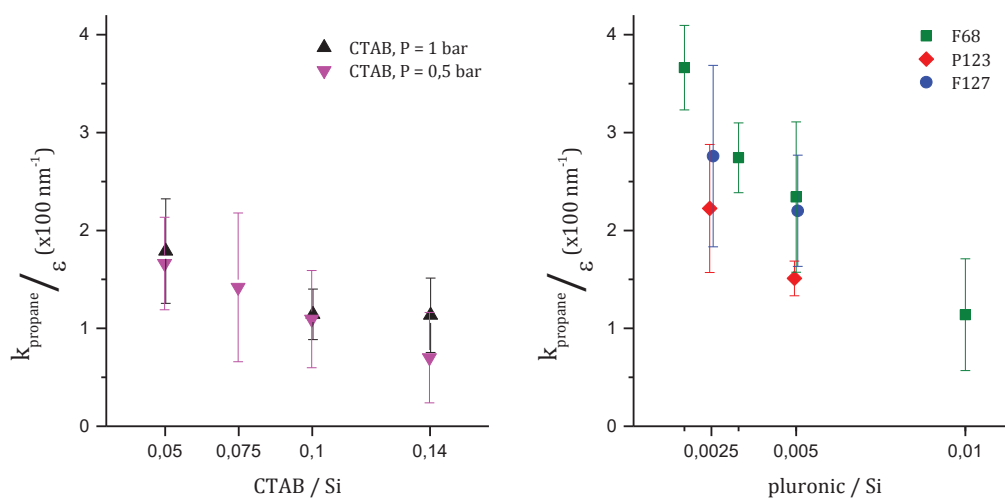


Fig. III.29 – Column affinity for the various SDA and SDA/Si ratios studied in this work.

However, decreasing the SDA content of the sol also decreased its viscosity. As a result, the deposited film was thinner, which is detrimental for column retention. The result of both affinity and thickness variation on retention depends on the SDA:

- For pluronics P123 and F127, the slimming of the stationary phase is greater than the increase in affinity and retention decreases as the SDA content decreases.
- On the other hand, CTAB content has only a limited influence on viscosity and film thickness, so retention increases with affinity, as CTAB content decreases.
- Finally, F68 content influences the sol viscosity and the film thickness significantly, but affinity variations are even more important. As a result, retention increases to a maximum as F68/Si decreases down to 0.003. At lower ratios, film thickness is too thin and retention does not increase anymore.

In Fig. III.30, the chromatographs of a mesostructured silica capillary column is compared to that of a commercial Silica PLOT column (Agilent) of the same length (*i.e.* 1 m). The efficiencies of both columns are similar, although the mesostructured silica capillary is slightly superior for the heavier compounds. Retention is also higher for the mesostructured silica, although the stationary phase thickness is only 100 nm thick compared to the 3 μm of the Silica PLOT.

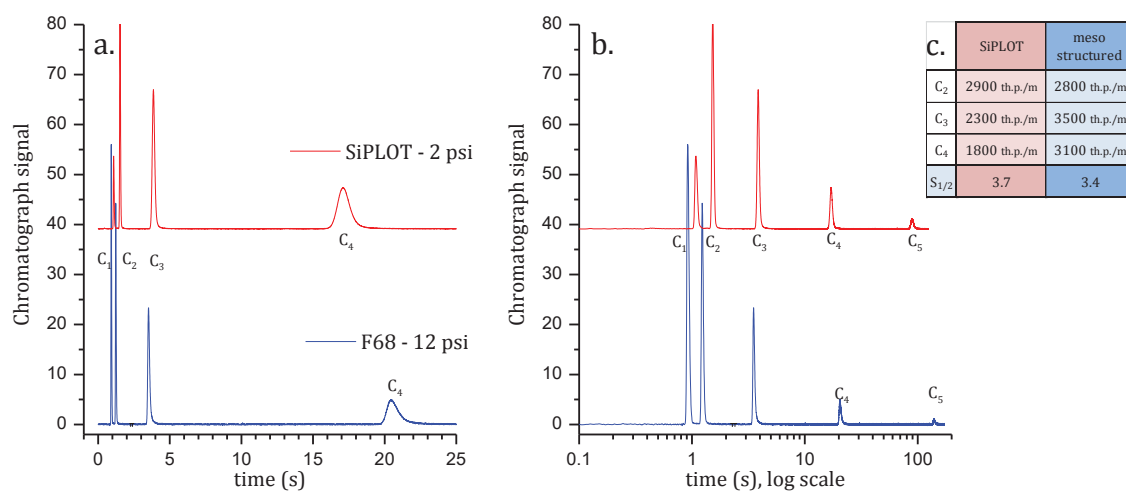


Fig. III.30 – Comparison of the chromatographs of a commercial Silica PLOT column and a mesostructured silica capillary column with F68/Si = 0.0033. Isothermal (30°C) separation of a methane to n-pentane mixture, on 1 meter long column with an internal diameter of 320 μm (Silica PLOT) and 100 μm (mesostructured silica). (a) The time scale is linear, and (b) in logarithmic scale for better readability until C5. (c) Number of theoretical plate per meter for methane to butane, and separation factor between methane and ethane (well over 1.5 for both)

However, it is hard to compare column efficiencies with columns as short as 1 meter. Indeed, on such a short length, the extra column band broadening effects from the apparatus are comparable to band broadening inside the columns, and it is difficult to discriminate

between both. Such a comparison would be clearer on longer columns, at least 5 or 10 meter long. The diameter of both columns is also different, as one of the advantages of the mesoporous silica phase is to be compatible with columns of small diameters (such as 100 μm).

Finally, it was found possible to obtain ordered mesoporous stationary phases by the EISA route inside capillaries. Although the conditions were not ideal to promote long range ordering (relative humidity of the drying gas being at zero), structuration was clearly observed for F68 induced stationary phases, and premises were perceived for CTAB and F127 induced stationary phases.

Ordering is also favored by high pressure coatings. The mechanism at stake is not known and could involve a modification of the drying rate of the stationary phase. It could be investigated by monitoring the outlet gas composition (water and ethanol contents) during drying. High coating pressures could also be used for sol compositions already giving an ordered mesostructure (such as F68/Si = 0.01) to see if the diffraction peak are sharper and thus the mesostructuration more ordered.

III.3.2. Influence of pore size on chromatographic properties

Overall, columns obtained with pluronic SDAs show higher affinities (mostly superior to 2 nm^{-1}) than those obtained with columns using CTAB (between 1 and 2 nm^{-1}). This may result from the presence of extra microporosity yielded by the occlusion of PEO chains of the pluronic SDAs at the surface of the silica mesopores. This hypothesis is supported by the fact that columns prepared with P123 (copolymer exhibiting the smallest PEO chains of the three poloxamers), had a smaller affinity.

One of the aims of the work on powders was to check this hypothesis. However it was not possible to measure the specific surface area and pore characteristics of powders with CTAB, as CTAB removal was unsuccessful. In addition, the mesostructures obtained for the powders were not identical to those of the capillary columns despite efforts to mimic the experimental coating conditions.

Characterization of the stationary phase directly inside the columns remained the major difficulty of this work: we had to rely mostly on chromatographic properties to compare the various SDA conditions, as only the phase thickness was easily and routinely accessible.

The potential influence of micropores is in accordance with the size of light alkanes molecules (the bigger is n-pentane, for an average diameter of 0.546 nm^{13}). It would be interesting to study heavier alkanes to see if retention drops as molecules get bigger.

However, this would require the use of high temperature to maintain short analysis times, and short columns as ours would certainly get saturated pretty fast.

III.4. Conclusion

In this chapter, we have studied the effect of various SDAs on the structuration of mesoporous stationary phases and on the resulting chromatographic properties.

We first described the different features of mesostructures generally obtained by EISA using SDAs (CTAB, pluronics F68, F127 and P123). Two key parameters were found to influence the final mesostructure: i) the relative ambient humidity, which was set to zero in this work for repeatability reasons and ii) the SDA nature and SDA/Si molar ratio.

We also tried to gain insight into the physical characteristics of the as-obtained stationary phases influencing the chromatographic properties by several techniques: SEM, SAXS, and N₂ adsorption/desorption analyses. As N₂ or even Kr adsorption proved not enough sensitive for capillaries, we tried to develop a model powder to gain a better understanding of the porous structures. Unfortunately, the silica powders were not appropriate models for silica coatings as their physical features were too different.

Of the different silica coatings, ordered mesoporous stationary phases were effectively obtained. When a high SDA/Si ratio was used and a coating pressure set to 1 bar or more, worm-like, cubic and hexagonal mesoporous phases were obtained with CTAB, F68, F127 respectively. The coating pressure was found to play an important role for the silica structuration but the reason remains unclear and need to be more extensively studied in a near future.

However, the affinity of the stationary phases with n-alkanes increased as the SDA/Si ratios decreased. Thus affinity was found higher for SDA/Si ratios for which no silica ordering was possible.

Nevertheless, at lower SDA content, the lower viscosity of the sol led to thinner films. As a result, retention was maximal for a compromise between the stationary phase thickness and its affinity towards alkanes. The highest retention was obtained with a F68/Si ratio of 0.003. Indeed, the affinity of the film is higher when pluronic SDA are used. This may be related to the presence of micropores around the silica mesopores.

The SDA nature also influenced the size of the mesopores. Mesopores obtained with pluronics were supposedly bigger than mesopores obtained with CTAB (smaller than 5 nm). This ability to control pore size was interesting considering post-functionalization issues. Indeed, silica is particularly easy to functionalize by silanization reactions, and adding

different chemical functions to the stationary phase could add versatility to the range of possible chemical families that these columns could separate. However, such silanization requires large pores in which the various silanes can diffuse.

After gaining insight into the coating process and the influence of the SDA on the physical and chromatographic properties of the stationary phases, we will present in chapter IV the transposition of the optimized coating process to micro-fabricated columns. An emphasis will be directed to i) the specific coating issues encountered in angular cross-section geometries and to ii) the benchmarking of our prototypes.

III.5. References

1. Zhao, D.; Huo, Q.; Feng, J.; Chmelka, B. F.; Stucky, G. D., *Journal of the American Chemical Society* **1998**, *120* (24), 6024-6036.
2. Besson, S.; Gacoin, T.; Jacquioud, C.; Ricolleau, C.; Babonneau, D.; Boilot, J. P., *Journal of Materials Chemistry* **2000**, *10* (6), 1331-1336.
3. Grosso, D.; Cagnol, F.; Soler-Illia, G. J. D. A. A.; Crepaldi, E. L.; Amenitsch, H.; Brunet-Bruneau, A.; Bourgeois, A.; Sanchez, C., *Advanced Functional Materials* **2004**, *14* (4), 309-322.
4. Cagnol, F.; Grosso, D.; Soler-Illia, G. J. D. A. A.; Crepaldi, E. L.; Babonneau, F.; Amenitsch, H.; Sanchez, C., *Journal of Materials Chemistry* **2003**, *13* (1), 61-66.
5. Besson, S.; Gacoin, T.; Ricolleau, C.; Jacquioud, C.; Boilot, J. P., *Journal of Materials Chemistry* **2003**, *13* (2), 404-409.
6. Grosso, D.; Babonneau, F.; Albouy, P. A.; Amenitsch, H.; Balkenende, A. R.; Brunet-Bruneau, A.; Rivory, J., *Chemistry of Materials* **2002**, *14* (2), 931-939.
7. Matheron, M. *Films mésoporeux hybrides organiques-inorganiques : synthèse, organisation des pores et application en optique ophtalmique*. These de Doctorat, Ecole doctorale de l'Ecole Polytechnique, Palaiseau, **2005**.
8. Kruk, M.; Jaroniec, M.; Ko, C. H.; Ryoo, R., *Chemistry of Materials* **2000**, *12* (7), 1961-1968.
9. Imperor-Clerc, M.; Davidson, P.; Davidson, A., *Journal of the American Chemical Society* **2000**, *122* (48), 11925-11933.
10. Manet, S.; Schmitt, J.; Impéror-Clerc, M.; Zholobenko, V.; Durand, D.; Oliveira, C. L. P.; Pedersen, J. S.; Gervais, C.; Baccile, N.; Babonneau, F.; Grillo, I.; Meneau, F.; Rochas, C., *Journal of Physical Chemistry B* **2011**, *115* (39), 11330-11344.
11. Zhao, D.; Wan, Y.; Zhou, W., *Ordered Mesoporous Materials*. Wiley: **2012**.
12. Besson, S.; Ricolleau, C.; Gacoin, T.; Jacquioud, C.; Boilot, J. P., *Microporous and Mesoporous Materials* **2003**, *60* (1-3), 43-49.
13. Marcus, Y., *The properties of solvents*. Wiley: **1998**.
14. Kiselev, A. V.; Yashin, Y. I., *Petroleum Chemistry: U.S.S.R* **1965**, *4* (3), 221-228.

Chapter IV.

Micro-fabricated columns:

Sol-gel coating

IV.1. Introduction	102
IV.2. Mesostructured silica coating in a micro-fabricated-column	102
IV.2.1. Stationary phase corner pooling phenomenon	102
IV.2.1.1. Flow profile simulation through different cross-section geometries.....	103
IV.2.1.2. Thicker sol-gel deposition in the corner	104
IV.2.1.3. Experimental observations and SDA influence	105
IV.2.2. Connection capillaries influence on chromatographic results	107
IV.2.2.1. Flow calculation in a column with multiple geometrical components....	107
IV.2.2.2. Micro-column coating process adaptation	108
IV.2.2.3. Process for changing the connections	109
IV.3. Micro-column efficiency	110
IV.3.1. Effective theoretical plate number definition	110
IV.3.2. Capillary connections influence on N_{eff}	111
IV.3.2.1. Capillary choice simulation	111
IV.3.2.2. Experimental results on entry shortening.....	113
IV.3.3. Micro-column's kinetic evaluation.....	113
IV.3.3.1. Column optimum efficiency – Golay plot.....	113
IV.3.3.2. Comparison to other published micro-fabricated columns results	114
IV.4. Other chromatographic results	116
IV.4.1. Retention of light alkanes - Temperature influence and Van't Hoff plot.	116
IV.4.2. Separation of natural gas like alkanes mixtures	117
IV.5. Conclusion	118
IV.6. References	119

IV.1. Introduction

In the previous chapters, we have developed a new sol-gel GC stationary phase for the separation of light alkanes in a short capillary column and its coating process:

- First, the different coating parameters of the process were studied and optimized,
- Then, the role of the SDA on the final mesoporous structure of the phase and its retention toward alkanes was examined.

However, GC capillary columns are cumbersome (one of their dimension is really long!) and could be advantageously replaced by more compact micro-fabricated columns, leading to a simpler system integration, a faster and a more efficient thermal management for portable GC system as we saw in chapter I. But since the first micro-fabricated column in the late 1970's,¹ most of the work was focused on intermediate molecular weight hydrocarbons separation, with 5 or more carbon atoms. Only a small number of recent studies have examined applications of micro-fabricated GC columns for lighter hydrocarbons with moderate reported efficiencies (900 to 2500 theoretical plates per meter).²⁻⁶

In this chapter, we propose to transpose our sol-gel process to micro-fabricated columns and to characterize their performances. We will first describe the geometric differences between micro-fabricated and capillary columns and how they affect the flow and the coating itself. Finally, we will illustrate the performances of as-obtained columns and compare them to the state of the art.

IV.2. Mesostructured silica coating in a micro-fabricated-column

IV.2.1. Stationary phase corner pooling phenomenon

The main difference between most micro-fabricated and capillary columns is their cross section geometry. Capillaries' cross section are typically circular, whereas micro-columns fabricated by a DRIE process exhibit square or rectangular cross-sections (as seen in chapter I). This latter system having sometimes really high aspect ratios shows many theoretical advantages⁷⁻⁹ but can lead to some difficulties for coating.

One of the major difficulties for stationary phase liquid coating processes in micro-fabricated columns is the tendency of the deposited film to accumulate in the corners of the channel due to wetting phenomena.¹⁰⁻¹¹

IV.2.1.1. Flow profile simulation through different cross-section geometries

As described previously, Micro-columns, etched on silicon wafer, have square or rectangular cross sections. Noteworthy, if we look closely, the channel bottom angles are not so sharp as the result of etching, contrary to the top angles, which results from the assembly of the top cover plate and the column. Additionally, there might be a slight angle deviation from parallelism for the two sides, but it is usually smaller than 1 or 2°.

These different cross-section shapes have an influence on the flow profile through the column for a laminar flow. Fig. IV.1. shows the velocity profile and the resultant shear stress field that have been computed in COMSOL for the different geometries available for our work. For a circular cross-section, it would have been easy to come up with an analytical solution, but for square or rectangular cross-sections, even if numerical solutions exist as series of functions, it was easier to compute a numerical solution.

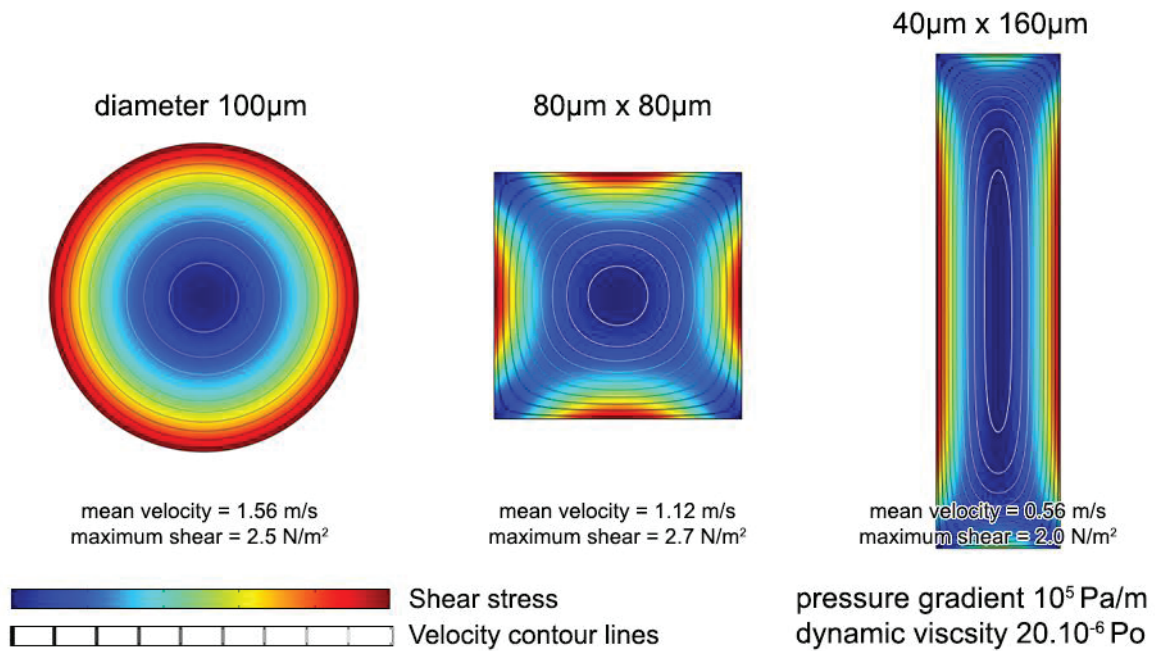


Fig. IV.1 – Flow and shear stress profile through channels of different cross-sections calculated with COMSOL for a pressure gradient of 1 Bar/m and a fluid dynamic viscosity of 2.10⁻⁵ Po (Helium at 30°C)

As observed in Fig. IV.1, while the circular cross section of capillary columns insures a perfectly symmetric flow, the velocity profile in angular cross section takes a circular shape (in square columns) or an oval one (in rectangular columns) in the column center and fits to the cross section profile only near the edges. As a result, the flow velocity decreases faster perpendicular to the large dimension than any diagonals. Besides, the shear stress is much higher on the central part of the edges.

Moreover, for the dimensions that we used and for similar flow mean velocity, the maximum shear stress is higher for micro-columns than for capillary columns (especially for high aspect ratio columns).

In addition to wettability effects, these differences in velocity and shear may also have an impact on corners pooling as it will be discussed now.

IV.2.1.2. Thicker sol-gel deposition in the corner

In chapter II, we have seen that the coating thickness is influenced by the coating speed in a similar way as dip coating, if putting ourselves in the coating fluid referential. In this referential, the dragging speed applied to the coating solution is the reverse of that calculated for Fig. IV.1: it is zero in the center of the column, and maximum at the sides. Thus it follows the shape of the outer velocity contour line and has a round profile in the corners as shown in Fig. IV.2. This inevitably results in a thicker coating in the corners.

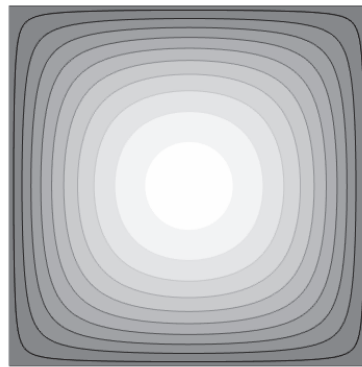


Fig. IV.2 – Coating velocity contour lines in the moving referential attached to the sol for a square column.

The round profile in the corners results in a thicker coating there.

The shear stress, applied by the gas to the sol during drying, is also greater on the sides than on the corners and if gelation is too slow, the sol may be removed from the sides where shear is higher.

This phenomenon is also the result of the coating fluid surface energy minimization (or wettability effects). It leads to the pooling of the fluid in the corners when the contact angle is inferior to 90° , and can be minimized with a fluid of higher viscosity.¹² This effect has already been observed on micro-columns coated by static coating¹⁰ and is one of the major limitations of liquid coatings on micro-columns.¹¹

IV.2.1.3. Experimental observations and SDA influence

Fig. IV.3 shows SEM pictures of the cross section of a micro-column channel coated with a mesoporous stationary phase (TEOS:F68 = 1:0.001, coating at 1 bar for 6 s). The result of the pooling during coating can be observed: a thicker layer in the corners than on the channel walls (a). SEM pictures, taken at the bottom of the channel (b-c) and on the side wall (d-f) (away from the corners) show the stationary phase growing thinner until only the thermal oxide stays visible (f).

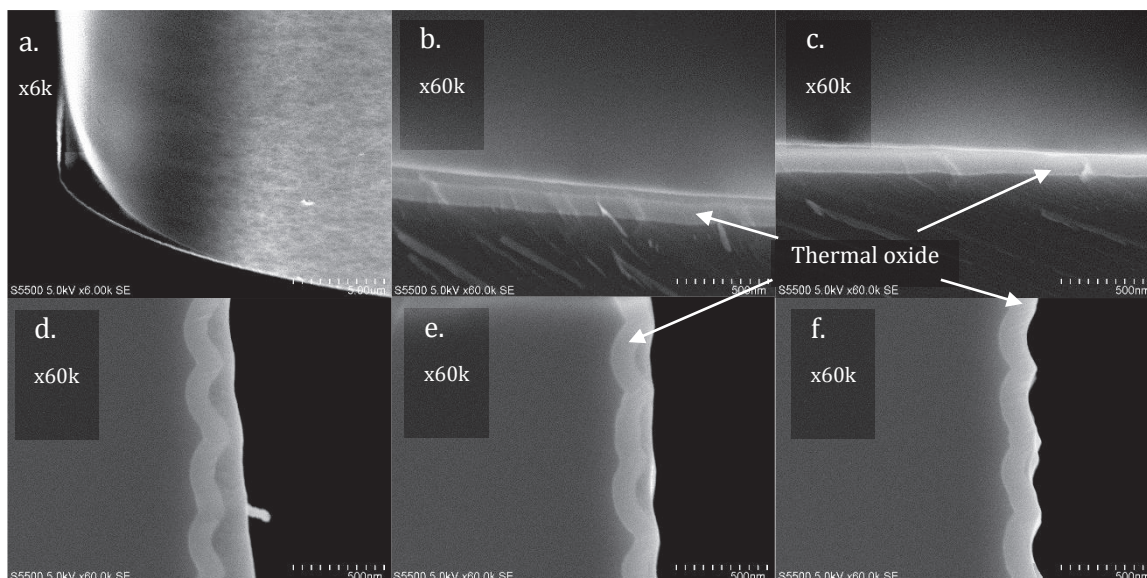


Fig. IV.3 – MEB pictures of the stationary phase in the corner of the channel (a), along the bottom (b-c), and on the sides of the channel (d to f).

In fact, as seen on Fig. IV.4., the stationary phase does not form a continuous film on the bottom (a) or on the sides of the channel (b-c), but forms small beads. This inhomogeneity necessarily has a negative impact on column efficiency, but as this phenomenon is unavoidable with this type of liquid phase coating, columns will be evaluated as such.



Fig. IV.4 – MEB pictures of the bottom (a) and the sides (b-c) of the channel. Stationary phase does not form a continuous film but small beads (in dark in the pictures).

Fig. IV.5. presents extra SEM pictures of micro-columns' channel corners coated with mesoporous stationary phases (TEOS:F68 = 1:0.001 (a), TEOS:CTAB = 1:0.01 (b-f), coating at

1 bar for 6 s). The result of the pooling during coating can be observed as thicker films in the corners. Moreover, one can also observe the silica structure contraction during annealing and SDA removal, resulting in cracks. The structure either comes off the wall (a), breaks in two parts (b) or both at the same time (c-d).

Stationary phase breaking is worse at the top of the channel (e-f), as the junction with the silica cover plate results in a really sharp angle. Fewer breaks are observed at the bottom of the channel, as the column etching results in a smoother angle.

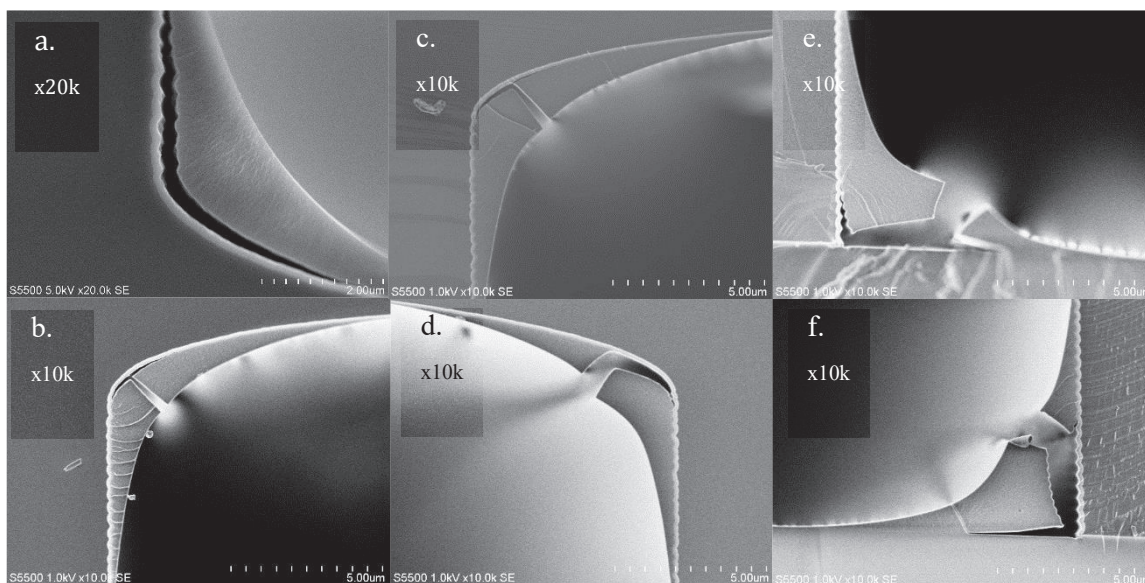


Fig. IV.5 – MEB pictures showing stationary phase pooling in the corners. As the result of gel contraction during gelation and annealing, the stationary phase come off the wall (a), break in two (b) or both (c-f). Pictures (a-d) are taken at the bottom of the channel (silicon part) and corners are slightly round. Pictures (e-f) are taken on the top, at the junction between the silicon and the silica cover plate.

A possible route to limit these phenomena is to increase the viscosity of the sol by changing its composition or the SDA type. Changing the composition would require to re-optimize the sol composition to generate mesostructured phases, the simplest solution is therefore to change the SDA.

Columns coated with F68 looked subjectively better under SEM. The stationary phase still accumulates in the corners of the channel, but it looks like it extends further from it. Another advantage is that the phase in the corner seems to break less (Fig. IV.5.a.), certainly as a result of the thicker walls obtained with tri-block polymer phases. Unfortunately, GC performances of columns coated with the F68 could not be evaluated as the glue used to fix the connection capillaries does not sustain the 300°C temperature required for F68 annealing. It was thus not possible to assess if a more homogeneous coating could have a benefic effect on GC efficiency.

IV.2.2. Connection capillaries influence on chromatographic results

IV.2.2.1. Flow calculation in a column with multiple geometrical components

Another parameter to take into account when working with micro-columns is the required capillary tubing at the extremities for connection to the GC injector and detector. As we are working with relatively short columns (1.33 m long), the length of the tubing is significant as far as we used 25 cm long connection capillaries we used in our work.

In Fig. IV.6, we have computed a helium laminar flow through such multi geometrical component columns, taking into account the compressibility of the carrier gas. The calculation are based on the equations presented in appendix B.2.2.

- The standard configuration is presented in black (square channel 80x80 μm^2 micro-column with 100 μm internal diameter connection capillaries). The ratio between the time spent in the micro-column area and the holdup time (T^*) is 69%.
- A rectangle micro-column (40x160 μm^2) and 100 μm internal diameter connection capillaries (in red). Even though it has the same cross section, it has a higher resistance to flow, and the carrier gas velocity is lower. This means longer holdup times or higher working pressures, but T^* is unchanged.
- A doubled working pressure (in green) approximately doubles the speed of the carrier gas, dividing the holdup time with little changes on T^* . However, high pressures increase the compressibility effects (speed inside the column varying a lot) which have a negative effect on efficiency (through the j and f compression factors)
- The connection capillaries internal diameter also has an effect. If it is higher than 100 μm (in light blue) it increases the speed in the column and T^* drops to only 50%.
- If it is smaller than 100 μm (in deep blue), it reduces the speed of carrier gas inside the micro-column area, and flattens its profile (as the pressure drop inside the micro-column area is smaller in comparison). T^* is also greater (80%).

To avoid resorting to numerical calculations, an approximate value of T^* can be calculated easily with the lengths (l and L) and sections (s and S) of the capillaries of the micro-column as:

$$T^* = \frac{L \cdot S}{L \cdot S + l \cdot s} \quad \text{IV.1.}$$

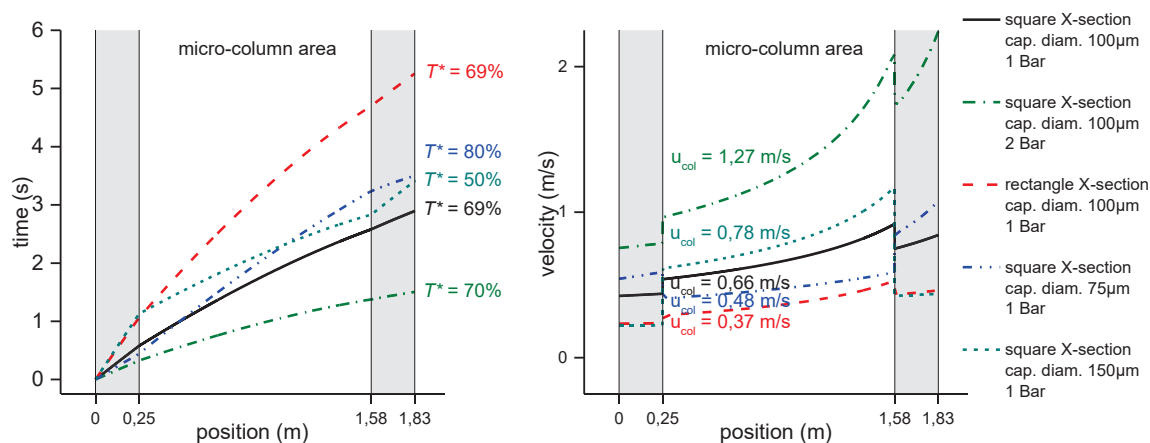


Fig. IV.6 – Time position and speed of an un-retained compound inside a micro-column with 25cm long capillary connections. Square cross section are $80 \times 80 \mu\text{m}$ and rectangle ones are $40 \times 120 \mu\text{m}$. T^* and u_{col} stand for the ratio of time and the average velocity inside the micro-column area.

In any case, we can see that the time spent in the connections is at least 20% of the holdup time (and 30% in average). This means that if the capillary connections are coated with stationary phase, they will have a non-negligible impact on the GC performances, especially as the coating will certainly be different in their circular geometry than in the column.

Moreover, the average velocity in the capillary exit is higher than that in the capillary entry, so both capillaries will not have the same contribution to retention, making hard to consider their intrinsic specific contribution. However, these connection capillaries are necessary for both the coating and the GC performances evaluation, until a compact GC chip including also an injector and a detector can be developed.

IV.2.2.2. Micro-column coating process adaptation

As the whole micro-column system presents a higher flow resistance than the capillary columns as studied in Chapter II and III, it was necessary to modify the coating parameters accordingly.

The coating pressure was kept at 1 Bar, in order to minimize the dragging forces applied by shear during drying. Plug length was chosen to be approximately equal to the length of the connection capillaries, so that the plug velocity was kept approximately constant in the micro-column part of the system. As the cover of the column was made of transparent glass, it was possible to control plug length visually as shown in Fig. IV.7. Coating time was thus approximately equal to 6 seconds for a 2 mL sol solution with 102 mg of CTAB.

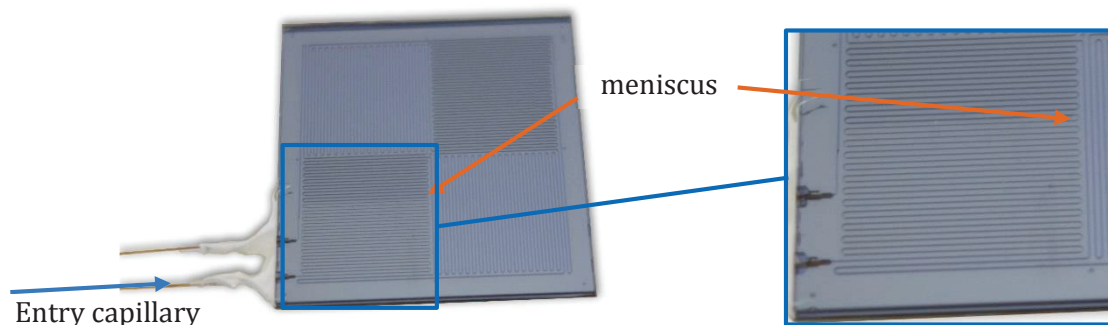


Fig. IV.7 – Picture of a micro-column during coating. The filled part can be seen and controlled by the change of contrast of the channel color.

This ability to see through the cover was also useful to check for inhomogeneities in the coating process and to adjust the parameters accordingly (such as increasing pressure for sol removal when the plug slows down to prevent jam formation).

IV.2.2.3. Process for changing the connections

To minimize the effects of the connection capillaries on micro-column GC performances, they were changed before SDA annealing and GC characterization. Therefore no stationary phase is present in the connection capillaries during the GC performances evaluation. This step requires that the capillaries used for coating can be removed afterwards.

To do that, capillaries are first glued using silicon glue, which stay flexible upon drying. The glue is deposited just on the edges of the chip, all around the capillaries, but not in the holes in which they are inserted (see Fig. IV.8.a). Thus, the gluing is less robust to pressure, but sufficient for the coating pressure used.

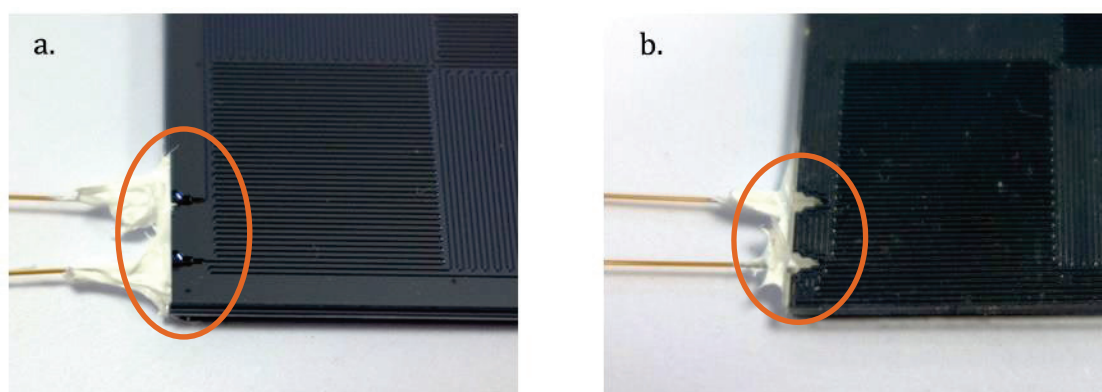


Fig. IV.8 – Pictures of the capillaries glued to the chip for coating (a.). The capillary are plugged but the glue does not fill the holes so it can be removed with a scalpel. Definitive gluing is shown in (b.). The glue fills the holes and the gluing is more resistant to pressure, but it is not reversible.

When the sol is stabilized, and before annealing the SDA, the coating capillaries and the glue are removed and replaced with new capillaries. This time, the glue is introduced in the holes as shown in Fig. IV.8.b, giving a much more robust gluing, which can resist a temperature of 250°C under pressure.

But even uncoated capillaries can have an influence on the chromatographic performances, especially on efficiency and resolution as we will see now.

IV.3. Micro-column efficiency

IV.3.1. Effective theoretical plate number definition

GC column and micro-column efficiencies are often evaluated in terms of theoretical plate number N , or HETP (height equivalent to a theoretical plate), equal to L/N (L being the column length). These definitions are often used as they do not depend much on the retention coefficient.¹³ N is usually used for complex separations requiring a large number of plates, whereas HETP is used for comparing columns of different lengths.

However, if these definitions work well with standard capillary columns, they are not so well suited to micro-columns. Indeed, micro-columns are more complex systems which often include connections, which can distort the meaningfulness of column efficiency. This is illustrated Fig. IV.9.

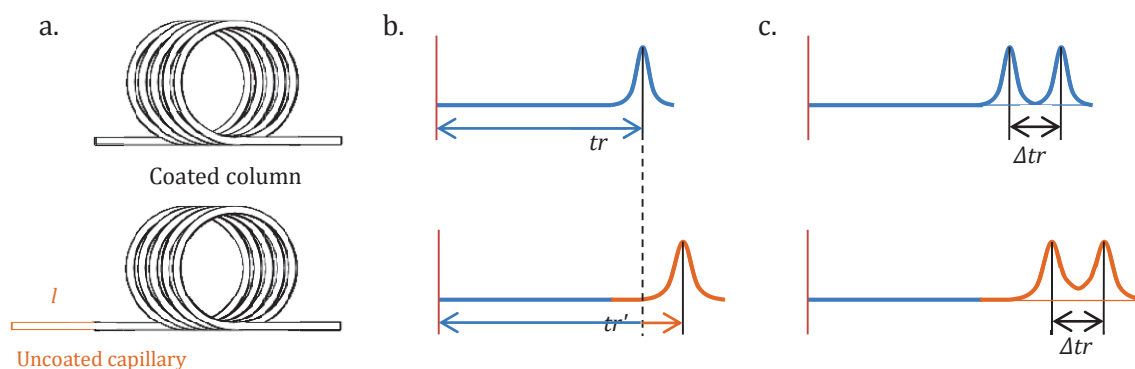


Fig. IV.9 – Illustration of the effect of connections on column efficiency. An uncoated capillary is added at the entry of the column (a). The resulting retention time $t_r' > t_r$ (b), so N is usually higher for the coated column with a capillary connection. But as Δtr is unchanged (the connection is uncoated, so the same time is added to each separation), the separative power of the column is in fact poorer (c).

Adding a capillary connection to a GC column increases the holdup time and all the retention times by the same difference. It also adds some dispersion to each peak, but as the added capillary is uncoated, the added dispersion is small enough that the resulting number of theoretical plate N increases. However, as we see in Fig. IV.9.c, the resolution of the column is in fact poorer (the peaks slightly overlap).

This effect could be corrected if we compare columns HETP and use as column length the total length of the column including the connections. However, connections are infrequently coated or of the same geometry as the column and they are not really part of the column so adding both lengths has little meaning.

Another possibility is to work with the effective theoretical plate number N_{eff} , defined as:

$$N_{eff} = \frac{(tr - t_0)^2}{\sigma^2} \quad IV.2.$$

N and N_{eff} are related by the equation IV.3.:

$$N_{eff} = N \frac{k^2}{(1 + k)^2} \quad IV.3.$$

It seems more appropriate as the addition of uncoated connections does not change the value of $(tr - t_0)$ and reflects more accurately the efficiency of the whole system. Of course, it also has its own limitations:

- The value of N_{eff} is smaller than N
- More importantly, it depends more strongly of the value of k (especially for small k) and it is important to compare different columns for similar k values.
- It is difficult to represent the values of N_{eff} for compounds of different k values in the same graph.

In the following study, we will try to work as much as possible with N_{eff} , but it is not always possible as most of the literature refers preferably to N and H , and most models for column efficiency are developed for H .

IV.3.2. Capillary connections influence on N_{eff}

IV.3.2.1. Capillary choice simulation

As we have seen previously, adding capillary connections to the micro-column increases the number of theoretical plates, but often decreases the effective number of theoretical plates. Nevertheless, there are setups for which the addition of connections, especially at the

end of the column, can improve N_{eff} . This has been extensively studied by A. A. Korolev and coworkers,¹⁴ who added restrictors at the end of their columns to lower their minimum HETP. It is based on the principle that adding a part with some flow resistance at the end of the column increases the pressure at the end of the column, and thus limits the effects of gas dilatation in the column (it modifies the j and f factors, but also the value of gas diffusion D_g).

Of course, this type of column efficiency improvements has drawbacks: the optimal efficiencies are obtained at a higher inlet pressure which leads to higher carrier gas consumption with the split. Moreover, these systems are also much more sensible to pressure shifts from the optimum.

The influence of the entry and exit capillary diameters and lengths is shown in Fig. IV.10. It highlights the fact that the higher values of N_{eff} are obtained for small diameter connection capillaries and that high optimal pressure is required to reach those high N_{eff} . On the other hand, connection capillaries with large diameter lead to poorer efficiencies also for higher working pressures.

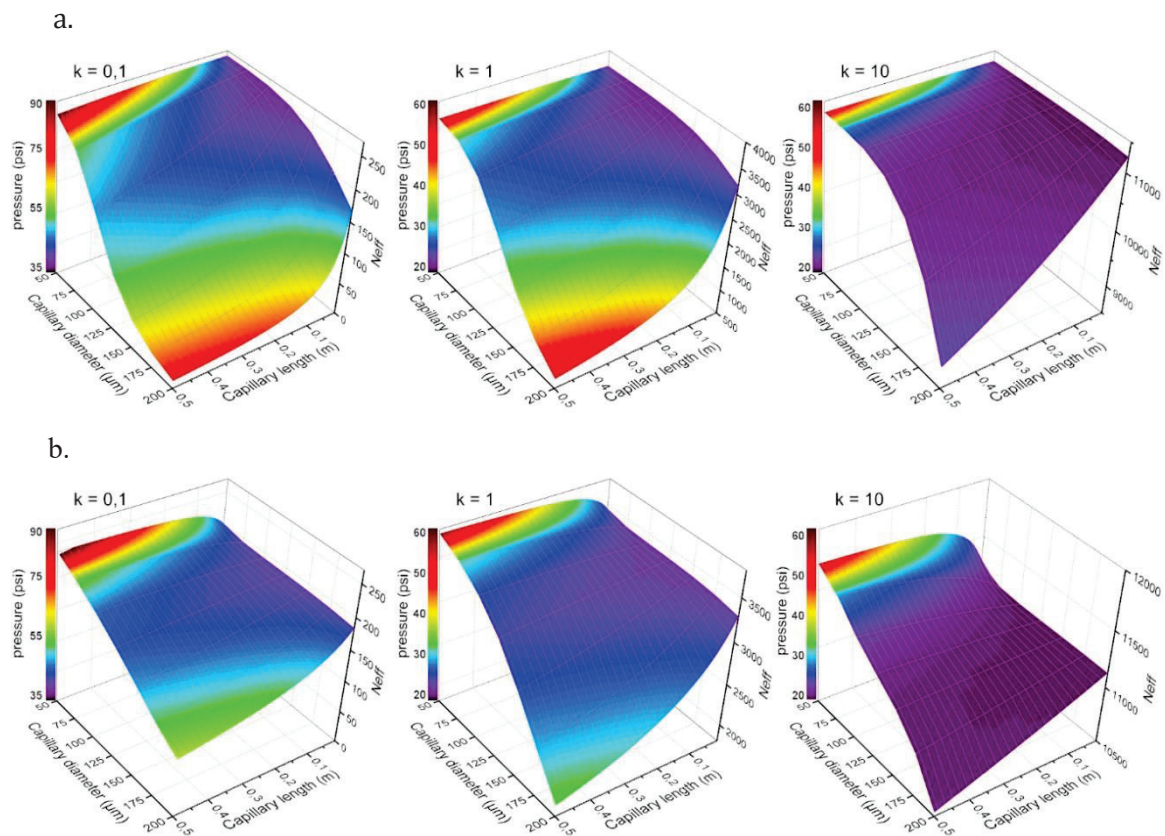


Fig. IV.10 – Influence of diameter and length of the entry (a.) and exit (b.) capillaries on N_{eff} for different values of k , in a square section micro-column ($80\mu\text{m}\times 80\mu\text{m}\times 1.33\text{m}$). Theoretical values are calculated with MATLAB (the model equations are presented in Appendix B.2.3). Optimum N_{eff} is presented in the z-axis, and the optimal working pressure is represented by the color sale.

A good compromise seems the use of 100 μm diameter capillaries with the shortest entry length and a reasonable exit length. Practically, the capillaries used for the connections are 100 μm in diameter and 25 cm long to simplify manipulations and column plugin to the GC apparatus.

IV.3.2.2. Experimental results on entry shortening

It was possible to confirm the predicted trend concerning the influence of the entry capillary length by experimental data (see Fig. IV.11.). However, these data could not be obtained exactly in the same conditions as those used for the model, as it would have required finding the optimum inlet pressure for each compound and for each studied length. We can note that experimental efficiencies are much lower than those predicted by the model, as the latter does not take into account molecular diffusion into the stationary phase, and supposes a perfect coating of the stationary phase.

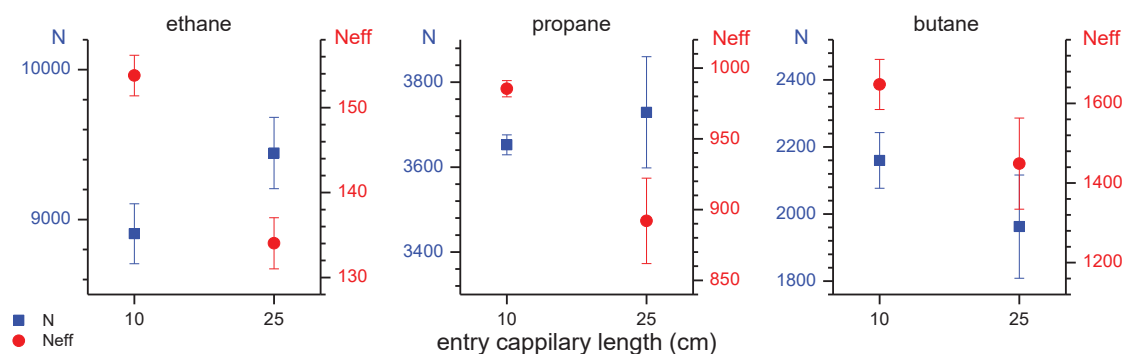


Fig. IV.11 - Entry capillary length influence on efficiency. Carrier speed: 82 cm/s. For ethane and propane, N increases with capillary length whereas Neff decreases, as predicted. For butane, both decreases with capillary length (this can be explained as we are working largely above optimum speed for butane, as we will see in IV.3.3)

IV.3.3. Micro-column's kinetic evaluation

IV.3.3.1. Column optimum efficiency – Golay plot

A typical Golay plot of our micro-columns is presented in Fig. IV.12. The SDA was CTAB with a 0.1:1 molar ratio with respect to Silica precursor. The dilution of the sol is 1:3 in volume with ethanol. The coating pressure was 1 Bar for an approximately 6 s introduction time (as seen in paragraph IV.2.2.2). Methane was considered as un-retained and was used for the determination of the holdup time, which was used to calculate speed and retention coefficients.

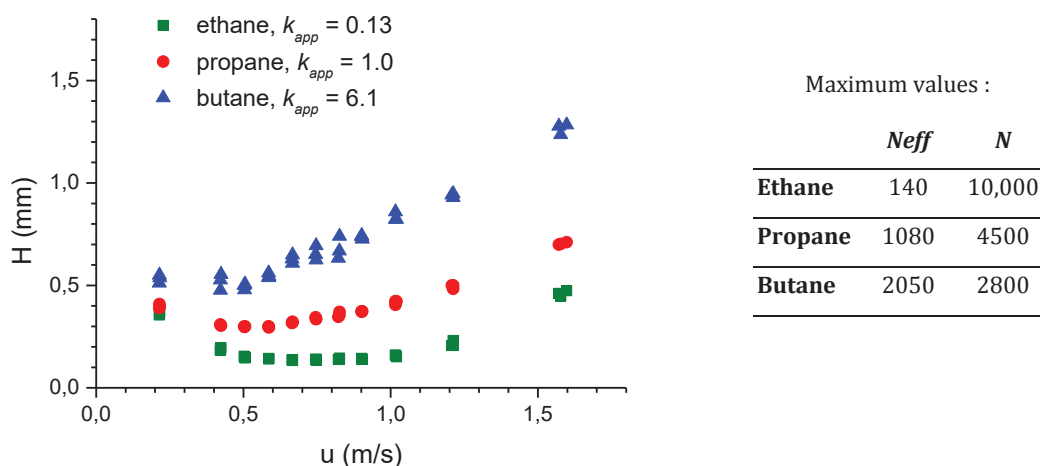


Fig. IV.12 – Golay plot for a micro-column coated with a mesostructured CTAB sol-gel stationary phase. CTAB:Si molar ratio 0.1:1, sol dilution 1:3 in volume with ethanol, coating pressure and introduction time of 1 Bar and approximately 6 seconds. Column dimensions: $80\mu\text{m}\times 80\mu\text{m}\times 1.33\text{m}$, connections: 25cm $100\mu\text{m}$ diameter capillaries. Working pressures between 5 and 40 psi.

We can notice here the difference between the effective number of plates and the number of plates, especially for small k_{app} values (ethane).

Moreover, retention coefficients presented here are under-estimated as they do not take into account the uncoated connections. Retention coefficient of the stationary phase can be accessed through T^* (presented in IV.2.2.1).

$$k = \frac{k_{app}}{T^*} \quad IV.4.$$

We see on the Golay plot Fig. IV.12 that HETP increases faster with carrier gas speed for the heavier alkanes. Consequently, the optimum HETP for these analytes is higher, and at lower carrier gas speed. This effect is certainly due to the slower diffusion speeds of heavier alkanes through the thick stationary phase, accumulated in the corners of the column.

We can also note that the Golay plot is relatively flat for a quite large scale of carrier gas speed. This indicates that the micro-columns can be used in a larger range of carrier gas flow rate than for capillary columns. This result is promising for high speed chromatography applications.

IV.3.3.2. Comparison to other published micro-fabricated columns results

Our stationary phase compares favorably with other published studies on micro-columns as it exhibits 7500 theoretical plates per meter (th.p./m) for ethane. Most reported micro-columns rarely show more than 5500 theoretical plates per meter,¹⁵ except for the work of

the Virginia Tech MEMS lab. on gold nanolayers¹⁶⁻¹⁸ (20,000 th.p./m), and few recent works on semi-packed micro-columns^{10, 19} (around 10,000 th.p./m) or multichannel columns²⁰ (7700 th.p./m).

Furthermore, few works were published for light alkanes' separation on micro-columns. Most attempts were made using packed columns, either with packing materials,²⁻³ or a really recent work with silica monolith.²¹ However, the reported efficiencies do not exceed 1300 and 1750 theoretical plates per meter respectively.

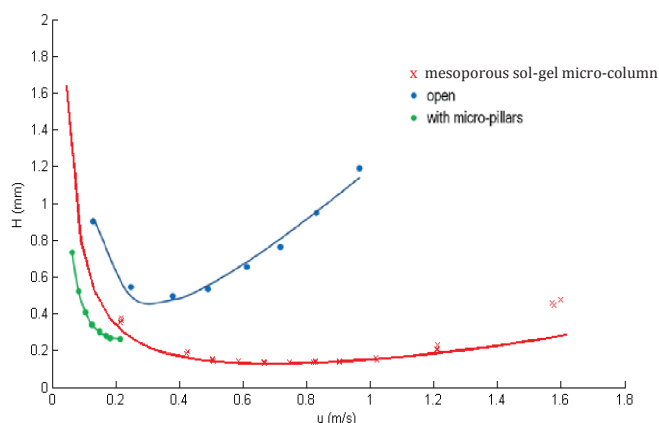


Fig. IV.13 – Comparison of our work with the work of J. Vial and coworkers ⁴.

HETP of ethane for mesoporous sol-gel silica MEMS column (80 μ m \times 80 μ m \times 1.33m) and open or semipacked sputtered-silica MEMS columns (75 μ m \times 100 μ m \times 2.20m). Carrier: He. Temperature: 30°C.

To our knowledge, the more efficient micro-column reported so far for light alkanes separation is the work of the ESPCI-Schlumberger team on sputtered silica.^{4, 22-23} The obtained PLOT like silica stationary phase allows complete isothermal separation of methane to n-butane on 2.2 meter long columns with 2500 th.p./m. The separation was improved with the use of a semipacked design to 5000 th.p./m but it lead to huge pressure drop.

Fig. IV.13. compares the Golay plot for ethane of our mesoporous sol-gel micro-column with the open and a semipacked sputtered silica micro-columns of the ESPCI-Schlumberger team for similar k values ($k = 0.12$, and 0.27 for the open and semipacked design respectively, $k_{app} = 0.13$ for the sol-gel micro-column). It is clear on this graph that our column has a higher efficiency for a broader range of velocities, giving it more versatility, especially for high speed applications.

IV.4. Other chromatographic results

IV.4.1. Retention of light alkanes - Temperature influence and Van't Hoff plot

In a first time, the logarithm of retention coefficients for isothermal separation of C₂-C₅ linear hydrocarbons can be plotted with respect to carbon number, as shown in Fig. IV.14. As expected, the plot is found linear, confirming that the sol-gel stationary phase behaves like conventional column, at least concerning linear saturated hydrocarbons.

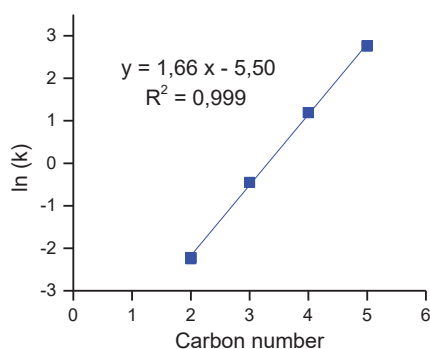


Fig. IV.14 – Kovatz plot for C₂-C₅ n-alkanes at 40°C. The expected linear relationship is verified.

Also as expected, we found that retention decreases as the separation temperature increases. Retention coefficients of C₂ to C₅ decrease from 0.19, 1.4, 8.7 at 30°C and 16 at 40°C, to 0.05, 0.25, 1.0 and 3.7 at 80°C respectively. Van' Hoff plot of ln(*k*) against 10³/RT gives straight lines as seen in Fig. IV.15.

The standard enthalpy obtained (22.9 kJ.mol⁻¹, 30.1 kJ.mol⁻¹, 38.4 kJ.mol⁻¹ and 45.4 kJ.mol⁻¹ for C₂ to C₅ respectively) are similar to those found in the chapter III for capillary columns with the same sol composition. They are also similar to values from the literature for porous silica gels (22.6, 30.1 and 38.3 kJ.mol⁻¹ for C₂, C₃ and C₄ on mesoporous 520 m²/g silica gel with mean pore diameter of 7 nm)²⁴, and quite similar to the one obtained on sputtered silica (23.0, 31.8 and 41.1 kJ.mol⁻¹ for C₂, C₃ and C₄).²³

Moreover, adsorption heat is also a linear function of carbon number in agreement with the literature. It confirms that standard enthalpy is a linear function of hydrocarbon polarizability.

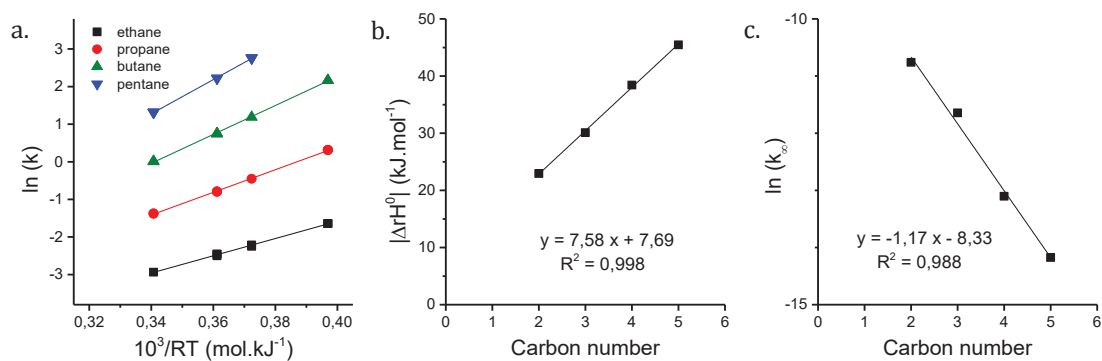


Fig. IV.15 – Thermodynamic evaluation of a sol-gel micro-column. Van't Hoff plots (a) show an expected linear correlation. It gives access to the adsorption heat (b) (slope) and $\ln(k_\infty)$ at infinite temperature (c) (y-intercept) which are both linear function of carbon number

IV.4.2. Separation of natural gas like alkanes mixtures

A more complex separation of C_1 - C_5 light alkanes, with all isomers in natural gas like composition (very different concentrations from one compound to the other) were also attempted with success. A chromatograph of such separation is given in Fig. IV.16. Thermal management of the micro-column was achieved through the GC-oven. However, it was not very adapted to the fast intended separation. Indeed, the maximum temperature increase was limited to $80^\circ\text{C}/\text{min}$ ($1.3^\circ\text{C}/\text{s}$), which is not fast enough compared to the holdup time (slightly over 2 s) and the total separation time (30 to 40 s).

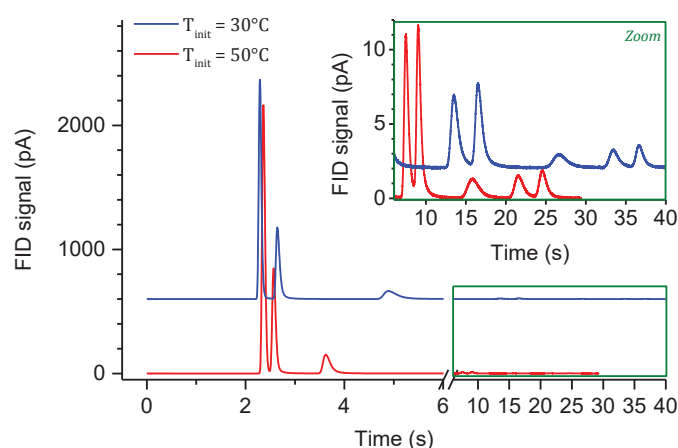


Fig. IV.16 – Separation of a natural gas like mixture of light alkanes: (1) methane (28%), (2) ethane (4%), (3) propane (1%), (4) iso- and n-butane (2000ppm), (5) neo-, iso- and n-pentane (500ppm). Complete separation of all pairs is achieved in 40 s, starting from 30°C with a ramp of $80^\circ\text{C}/\text{min}$. The resolution of the worst pair: n-butane/isobutane $R = 1.8$. Separation could be completed in 30 s, starting from 50°C , but n-butane/isobutane resolution dropped to $R = 1.47$. Inlet pressure = 20psi; $V_{\text{inj}} = 0.2 \mu\text{L}$; column $1.33 \text{ m} \times 80 \mu\text{m} \times 80 \mu\text{m}$.

IV.5. Conclusion

This chapter discussed implementation of the sol-gel process to develop stationary phases on micro-columns. Due to the particular geometry of the DRIE etched channels, obtained stationary phase coating could not be perfectly even and pooling in the channels corner was observed. Added to the film contraction during aging and annealing, the resulted stationary phase often showed cracks. The use of tri-block copolymers as SDAs could strengthen the film and prevent most cracks but the chromatographic performances evaluation was not possible due to packaging issues.

A process to get uncoated capillary connections for the micro-columns was developed so that the observed performances corresponded those of the micro-column itself.

Despite the coating imperfections, the micro-columns obtained with CTAB as SDA showed promising efficiencies and the highest number of theoretical plates per meter reported to date for ethane. Thermal evaluation of the silica stationary phase demonstrated its similarity to porous silica stationary phases described in the literature.

Columns could be used with thermal management for fast and complex separations of natural gas like mixtures. The results suggest that improvement is possible with a faster thermal management of the chip, like resistive heating.

However, this process still shows two main limitations: i) corner pooling effects and connection capillary gluing constraints and ii) it is not yet a collective process that could address several columns (or a full wafer) at the same time. Such a process is not inconceivable but would require the development of specific machinery, for which we did not have the funding and enough dedicated human resources. Thus we present in the next chapter another possible process to coat micro-fabricated columns with a mesostructured silica stationary phase, with the possibility of full wafer coating: the layer by layer coating process.

IV.6. References

1. Terry, S. C.; Jerman, J. H.; Angell, J. B., *IEEE Transactions on Electron Devices* **1979**, *26* (12), 1880-1886.
2. Kaanta, B. C.; Chen, H.; Zhang, X., *Journal of Micromechanics and Microengineering* **2010**, *20* (5).
3. Sklorz, A.; Janßen, S.; Lang, W., *Sensors and Actuators, B: Chemical* **2012**.
4. Vial, J.; Thiébaud, D.; Marty, F.; Guibal, P.; Haudebourg, R.; Nachef, K.; Danaie, K.; Bourlon, B., *Journal of Chromatography A* **2011**, *1218* (21), 3262-3266.
5. Haudebourg, R.; Matouk, Z.; Zoghalmi, E.; Azzouz, I.; Danaie, K.; Sassiati, P.; Thiebaut, D.; Vial, J., *Analytical and Bioanalytical Chemistry* **2014**, *406* (4), 1245-1247.
6. Lehmann, U.; Krusemark, O.; Müller, J.; Vogel, A.; Binz, D., Micro machined gas chromatograph based on a plasma polymerised stationary phase. In *Micro Total Analysis Systems 2000*, van den Berg, A.; Olthuis, W.; Bergveld, P., Eds. Springer Netherlands: **2000**; pp 167-170.
7. Spangler, G. E., *Analytical Chemistry* **2006**, *78* (14), 5205-5207.
8. Spangler, G. E., *Analytical Chemistry* **1998**, *70* (22), 4805-4816.
9. Martin, M.; Jurado-Baizaval, J. L.; Guiochon, G., *Chromatographia* **1982**, *16* (1), 98-102.
10. Ali, S.; Ashraf-Khorassani, M.; Taylor, L. T.; Agah, M., *Sensors and Actuators, B: Chemical* **2009**, *141* (1), 309-315.
11. Dorman, F. L.; Overton, E. B.; Whiting, J. J.; Cochran, J. W.; Gardea-Torresdey, J., *Analytical Chemistry* **2008**, *80* (12), 4487-4497.
12. Bertier, J. *Forces capillaires : une solution d'avenir pour les microsystèmes*. Thèse de Doctorat, UPMC-Sorbonne Universités, Jussieu, **2011**.
13. Grob, R. L.; Barry, E. F., *Modern Practice of Gas Chromatography*. Wiley: **2004**.
14. Korolev, A. A.; Shiryayeva, V. E.; Popova, T. P.; Kurganov, A. A., *Journal of Analytical Chemistry* **2011**, *66* (2), 184-188.
15. Azzouz, I.; Vial, J.; Thiébaud, D.; Haudebourg, R.; Danaie, K.; Sassiati, P.; Breviere, J., *Analytical and Bioanalytical Chemistry* **2014**, *406* (4), 981-994.
16. Zareian-Jahromi, M. A.; Agah, M., *Journal of Microelectromechanical Systems* **2010**, *19* (2), 294-304.
17. Zareie, H.; Alfeeli, B.; Zareian-Jahromi, M. A.; Agah, M. In *Self-patterned gold electroplated multicapillary separation columns*, Proceedings of IEEE Sensors, 2010; pp 1526-1529.
18. Shakeel, H.; Agah, M., *Journal of Microelectromechanical Systems* **2013**, *22* (1), 62-70.
19. Sun, J.; Cui, D.; Chen, X.; Zhang, L.; Cai, H.; Li, H., *Journal of Chromatography A* **2013**, *1291*, 122-128.
20. Zareian-Jahromi, M. A.; Ashraf-Khorassani, M.; Taylor, L. T.; Agah, M., *Journal of Microelectromechanical Systems* **2009**, *18* (1), 28-37.
21. Azzouz, I. *Etude, réalisation et caractérisation de nouveaux supports pour microsystèmes intégrés de chromatographie en phase gazeuse*. **2013**.
22. Haudebourg, R.; Vial, J.; Thiebaut, D.; Danaie, K.; Breviere, J.; Sassiati, P.; Azzouz, I.; Bourlon, B., *Analytical Chemistry* **2013**, *85* (1), 114-120.
23. Haudebourg, R. *Application of sputtering to micro gas chromatography : a novel collective stationary phase disposition technique for micro gas chromatography columns fabrication : feasibility, evaluations and oilfield applications*. **2014**.
24. Kiselev, A. V.; Yashin, Y. I., *Petroleum Chemistry: U.S.S.R* **1965**, *4* (3), 221-228.

Chapter V.

Micro-fabricated columns:

**Nanoparticles layer by layer
coating**

Chapter summary

V.1. Introduction	124
V.1.1. Motivations	124
V.1.2. The layer-by-layer deposition method.....	124
V.1.3. Work presentation.....	125
V.2. Layer-by-layer deposition of non-porous silica nanoparticles	125
V.2.1. LbL deposition process of commercial SNP	125
V.2.1.1. Deposition conditions.....	125
V.2.1.2. LbL coating of micro-columns.....	127
V.2.2. Chromatographic properties of silica nanoparticles	128
V.3. Layer-by-layer deposition of porous silica nanoparticles	129
V.3.1. Mesostructured silica nanoparticles synthesis.....	129
V.3.1.1. State of the art.....	129
V.3.1.2. Mesostructured SNP synthesis.....	130
V.3.2. Mesoporous micro-columns by layer-by-layer deposition.....	133
V.3.2.1. LbL deposition with a cationic polyelectrolyte.....	133
V.3.2.2. LbL deposition with an anionic polyelectrolyte	134
V.3.2.3. Full-wafer mesoporous SNP LbL deposition.....	141
V.3.3. Chromatographic performances.....	144
V.4. Conclusion	145
V.5. References	146

V.1. Introduction

V.1.1. Motivations

Stationary phase porous structures presented in the previous chapters proved quite difficult to characterize directly in the columns. In these conditions it was complex to establish a reliable relationship between their chromatographic properties and their physical features. Therefore, we considered an alternative approach based on the synthesis and characterization of particles in solution and to further coating into columns.

This approach was motivated by the recent work of D. Wang *et al.* on micro-preconcentrators¹ and micro-columns.² In his study, silica nanoparticles (average diameter of 45 nm) were coated on silicon chip by a “layer-by-layer” (LbL) process. Advantages of such process relies on the yielding of silica uniform coatings and therefore the possibility to cover full wafer with controlled stationary phase thickness.

V.1.2. The layer-by-layer deposition method

LbL deposition is a thin film fabrication technique. Although it was reported by Prof. R. K. Iler from the Dupont company with microparticles in 1966,³ it was first used and developed by G. Decher for the self-assembly of polyelectrolyte multilayers.⁴⁻⁵

As a simple description, the LbL deposition process is based on the alternative immersion of the substrate in two polyelectrolyte solutions of opposite charge, yielding the growth of a thin film due to electrostatic interactions between the ground layer and the additional one; only one layer being added at each step. For a better control of the homogeneity and thickness of each layer, a washing step between each deposition washes away the excess of material from the previous stage, while leaving enough surface charges for the next deposition step. The final film thickness is easily controlled by the number of deposited layers (which are often associated by pair and referred as bilayers), which has almost no limit.

In reality, LbL deposition process is much more complex than expected because : i) polyelectrolyte layers are intertwined and not really discernable and ii) a multitude of other attractive forces (Van der Waals forces or hydrophobic interactions) coexist.⁶ However, these different possible interactions allow to extend the LbL process to a wide range of possible substrates such as hydrogen bonded films,⁷ carbon nanotubes,⁸ nanowires⁹ or silica nanoparticles (SNP).^{1-2, 10-11}

SNP LbL deposition can be achieved by the alternative dipping of a substrate in PAH (PolyallylAmine Hydrochloride) and SNP solutions of diameters between 7 and 50 nm.^{1-2, 11} Although other polyelectrolytes than PAH may be used,¹² PAH, a common cationic polyelectrolyte, is often preferred in combination with PSS (PolyStyrene Sulfonate), an anionic polyelectrolyte, to form LbL deposited thin films.¹³ Moreover, PAH is particularly adapted to SNP, which surface is electronegatively charged. Generally, the pH of the PAH and SNP solutions are adjusted between 7 - 7.5 and 9 respectively.

V.1.3. Work presentation

We therefore experienced the LbL method to produce mesoporous silica stationary phases, based on the deposition of mesostructured silica nanoparticles.

In this chapter, non-porous commercial silica nanoparticles were used first to validate the process before focusing our efforts towards the deposition of mesostructured silica nanoparticles.

As commercially available mesostructured SNP were found inappropriate for LbL deposition process, we synthesized our own particles. Two different strategies were investigated to obtain two types of nanoparticles: i) monodispersed nanoparticles of relatively large particle size (100 nm) with a hollow core-shell structure and calibrated pores or ii) amino acid catalyzed mesostructured nanoparticles, of with a smaller diameter (20 nm, more similar to commercial SNPs) with a poorly structured mesoporous network.

Finally the LbL deposition results and the coatings chromatographic properties will be presented.

V.2. Layer-by-layer deposition of non-porous silica nanoparticles

V.2.1. LbL deposition process of commercial SNP

V.2.1.1. Deposition conditions

We first tested and validated the process on commercially available fumed silica nanoparticles (LUDOX™ from Sigma-Aldrich). The nanoparticles have an average diameter of 22 nm and a specific surface area of 140 m²/g. They are available in solution at 50% wt. at pH 9. The SNPs were first deposited on flat control silicon substrates. The deposition of one bilayer, as illustrated on Fig. V.1, consisted in the alternative dipping of the substrate in PAH

solution (1 mg/mL, pH 7), and SNP solution (pH adjusted to 9 with NaOH). Between each dipping step of 3 minutes (or 15 minutes for the first bilayer), the substrate was rinsed three times in deionized water for one minute.

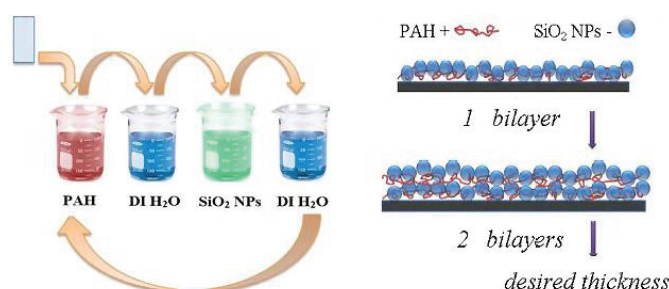


Fig. V.1 – Illustration of the LbL process for the deposition of PAH and SNP bilayers, taken from ¹

The thickness of the deposited film was evaluated with a profilometer. Half of the substrate was covered during the LbL process with kapton tape, which was removed later. As illustrated in Fig. V.2, the film thickness increased exponentially with the number of bilayer if the SNP solution is used as received. It reaches almost 1 μm after 16 bilayers, which is three times what could be expected by multiplying the number of layers with the particles diameter. In contrario, if the SNP solution is diluted to 0.1 % wt., the film thickness was found to increase linearly with the number of bilayers. The final thickness, 453 nm for 30 bilayers, was slightly inferior to the diameter of the particles multiplied by the number of bilayers (660 nm), which was coherent with a non-compact coverage.

These latter conditions were further used in the project, as a linear growth could favor more tunable and reproducible film thicknesses.

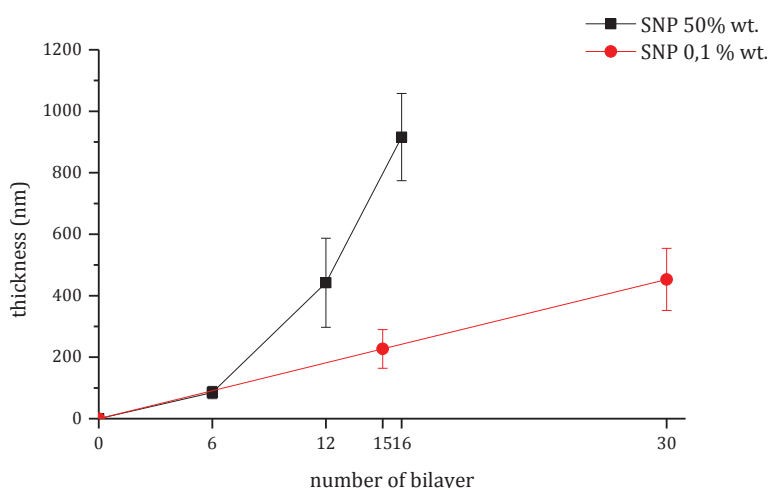


Fig. V.2 – Thickness of the deposited film as a function of the number of bilayers for two SNP solutions.

Ellipsometric porometry measurements were attempted on these substrates but did not give any results since the films are too diffusive and do not reflect light.

Finally, we attempted the deposition of SNPs on silicon substrates with etched microstructures (hexagonal micropillars 20 μm wide, 100 μm high, and spaced 10 μm apart) in order to evaluate the possibility to yield a uniform coating within micro-column channels. The SEM pictures in Fig. V.3, illustrate the uniformity of the coating and its high conformity at the top (b) or bottom (a) of the pillars.

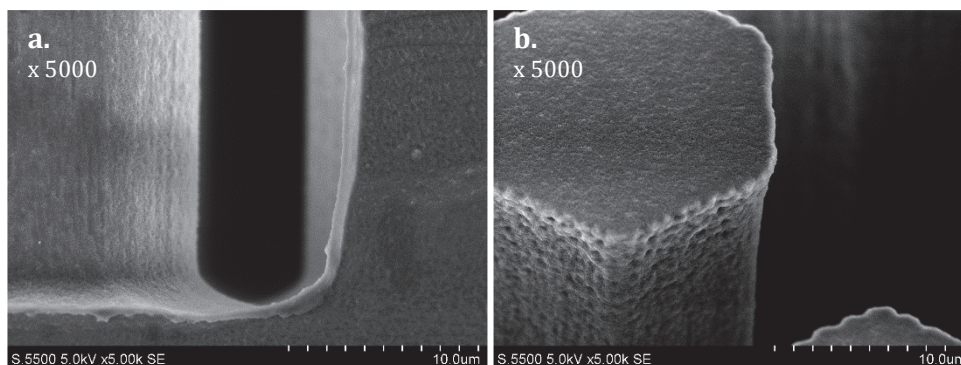


Fig. V.3 – SEM pictures of the SNP LbL coating (30 bilayers) on a silicon chip with micropillars.

V.2.1.2. LbL coating of micro-columns

The coating process was repeated on micro-column silicon chips without any cover. Two columns were coated simultaneously with 30 bilayers of PAH and SNPs, to evaluate the reproducibility of the process and the possibility of full wafer coatings. After the coating, columns were annealed in an oven at 500°C for 4 hours for particle sintering and polyelectrolyte removal (calcination).¹ Then the chips were covered, but as SNPs were also coated on the top of the chip, techniques such as anodic bonding or molecular bonding were not possible for chip packing. Therefore we glued the glass caps with an Ordyl® dry film: the film was first laminated onto the glass substrate, and then applied onto the chip under a metal weight for one night in an oven at 160°C.

As seen in Fig. V.4.a, the capping was successful, but maybe too effective as the Ordyl® film diffused in the channels for several micrometers. The film was found to cover at least 10 μm on each wall (1/8th of their height), and may have diffused further between the particles, although this latter point being difficult to observed by SEM as the polymeric film had the tendency to charge under the electron beam.

As expected, the deposited film thickness was homogeneous inside the channel, and particularly at the channel corners, as shown in Fig. V.4.b. A high magnification picture, presented in Fig. V.4.c showed the SNPs packing. The individual layers did not really stand out as the packing was not dense, but individual particles could be observed.

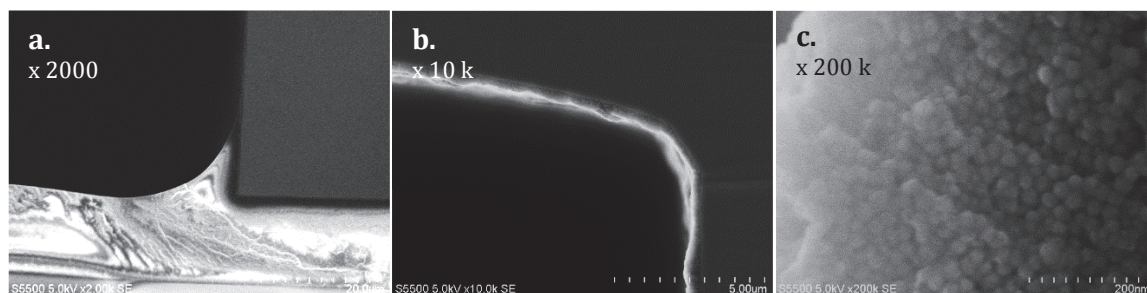


Fig. V.4 – SEM pictures of a micro-column channel cross-section, coated with 30 SNP layers. (a) 10 µm thick ordyl film at the top of the channel, (magnification: 2 k). (b) Picture of a corner at the bottom of the channel (magnification 10 k). (c) Picture of the 30 layers of SNPs at high magnification (200 k)

V.2.2. Chromatographic properties of silica nanoparticles

Similarly to the sol-gel stationary phase columns, the 30 layers SNP stationary phase separation properties were evaluated by GC. However, the retention of these columns was too weak to separate the usual C_1 to C_5 mixture.

This result was not surprising as the estimated total specific surface area of the deposited film was about 20 times lower than the estimated BET surface area of the sol-gel capillaries (0.05 m²). Indeed, if we consider that a particle packing factor of 0.5 (as the particles are not closely packed), and an average film thickness of 500 nm, the specific surface area can be estimated from the particles characteristic to about 0.002 m².

Moreover, the Ordyl® film is certainly detrimental to the chromatographic properties of the columns since:

- It covers most of the top of the channel walls, it further reduces the stationary phase accessible to the gas molecules.
- Moreover, as it starts to degas at 120°C, it limits the column maximum working temperature. This can prevent the quantitative removal of organic products physisorbed on the stationary phase during calcination or further chromatographic use.

The GC properties of the columns were nevertheless evaluated with a mixture of pentane, heptane, octane and toluene, representative of some VOCs (Volatile Organic Compounds). Pentane was not retained but was separated from heptane and octane, although octane and toluene were co-eluted. The chromatograph obtained for the two micro-columns were found very similar, as they had exactly the same retention profile towards these different compounds as shown in Fig. V.5. This is very promising as it suggests a high process repeatability.

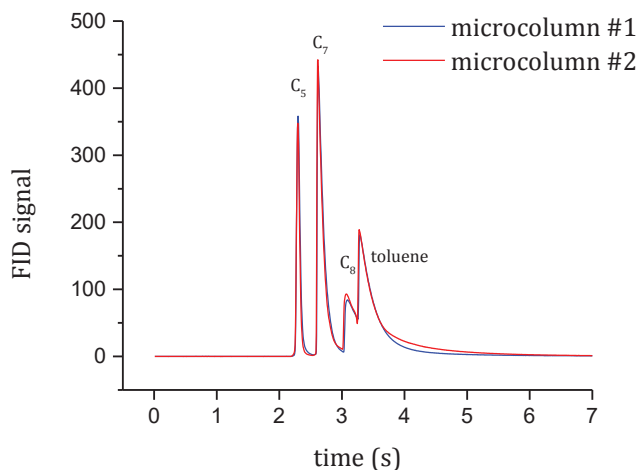


Fig. V.5 – Chromatograms of the two micro-columns with 30 layers of commercial SNPs. Isothermal (30°C) separation of pentane, heptane, octane and toluene at 20 psi.

V.3. Layer-by-layer deposition of porous silica nanoparticles

V.3.1. Mesostructured silica nanoparticles synthesis

V.3.1.1. State of the art

Mesostructured silica nanoparticles have raised increasing interest over the last 10 years. The narrow pore size distribution tunable between 2 and 15 nm, associated with their high specific surface area of such materials offer interesting properties for a wide variety of applications, including drug storage and release,¹⁴ catalysis and gas chromatography. Nonetheless, in many of these applications, the availability of spherical particles with well-defined size is crucial (for mass transport phenomenon, biocompatibility issues, coating processes...).

Spherical mesoporous silica particles were first synthesized by modifying the well-known Stöber process, which is based on a TEOS/ammonia/water/alcohol tertiary system to produce narrowly dispersed silica spheres.¹⁵ The hydrolysis and condensation of the silica precursors, promoted by the basic catalysis, allow the formation of silica nanoparticles with a monodisperse size distribution. By adding structure directing agent such as CTAB, or hexadecylpyridinium chloride, and using isopropanol as co-solvent, 0.2 to 2 μm sized spherical particles were obtained with mesostructured pores between 2 and 5 nm.¹⁶⁻¹⁷ However, the size distribution of the particles was not very narrow. More recently, several articles reported the preparation of nanometer sized (<100 nm) mesostructured,¹⁸⁻²¹ and

ordered mesostructured particles,²² but the synthetic procedures were rather complicated and the control of the nanometer-scale and morphology were not completely satisfying for our targeted application.

By replacing ammonia of the Stöber method, by amino acid such as lysine, small spherical and monodispersed silica nanoparticles were synthesized with a mean size from 5 to 23 nm depending on the experimental conditions.²³⁻²⁴ This approach was extended to the use of other amino acid such as arginine, and opened the way to monodispersed suspension of silica porous particles with size ranging from 15 to 200 nm.²⁵ Further developments yielded mesostructured nanoparticles with calibrated 3 nm pores when CTAB as SDA was used.²⁶

Another approach for the synthesis of monodispersed mesostructured nanoparticles consisted in the growth of silica shell around a template, the latter being eventually further removed to generate hollow core shell particles. “Soft” templates such as surfactant vesicles,²⁷ bacteria,²⁸ or gas bubble²⁹ were used, however they often led to ill-defined shapes and polydispersed particles with a disordered porous arrangement and unpredictable pore sizes. At the reverse, the use of “hard” templates such as polymer latex and surfactants as co-template afforded a more reliable approach for the synthesis of structured silica particles.³⁰⁻³¹ A recent work, from H. Blas *et al.*³² reported the synthesis of individual monodispersed spherical hollow mesostructured silica nanoparticles, with calibrated and oriented pores (perpendicular orientation with respect to the core surface). Such structures could be of great interest for chromatographic applications as it offers to control independently several structural parameters such as the particle diameter and the shell thickness.

V.3.1.2. Mesostructured SNP synthesis

V.3.1.2.1. Core-shell mesostructured SNP

Spherical hollow mesostructured silica nanoparticles were synthesized, *via* a three-step process following the publication of H. Blas *et al.*³² A monodispersed polystyrene latex covered by cationic charges was first synthesized by emulsion polymerization initiated by 2,2'-azobis(2-methylpropionamide) dihydrochloride. CTAB used for the polymerization step was removed by dialysis. The average latex particle diameter determined by DLS was 69 nm with a narrow size distribution (polydispersity factor of 0.038). Hydrolysis-condensation of TEOS in the presence of CTAB was further performed at the surface of the monodispersed cationic polystyrene particles. TEM (transmission electron microscopy) pictures of the particles before the template removal are presented in Fig. V.6. The particle size distribution is slightly polydispersed around 90 nm.

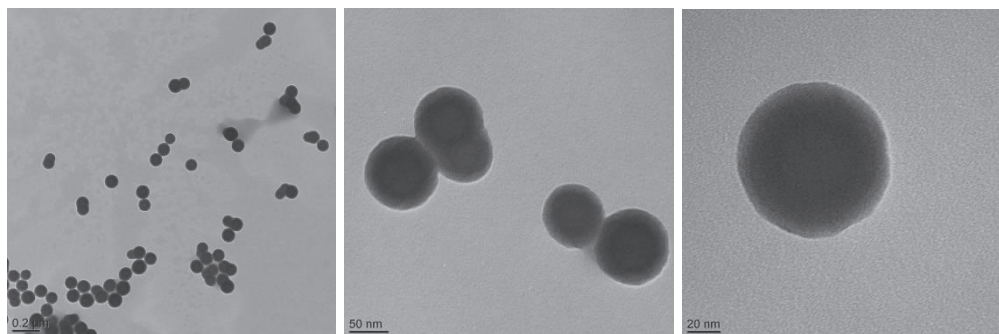


Fig. V.6 – TEM pictures of the core-shell mesostructured SNP before templates removal

Finally, the particles were concentrated to 2.8 % wt. by evaporation of the solvent, for an easier transport and storage. However, this concentration was detrimental to the stability of the solution, as it triggered irreversible aggregate formation, even after dilution and sonication of the mother solution.

LbL deposition of the particles was attempted before template removal by calcination, as it is usually not possible to disperse particles once calcined. In addition, as LbL deposition requires the calcination of the sample to remove the polyelectrolytes, it was easier to remove both polyelectrolyte and templates in one step. Nonetheless, due to the presence of CTAB inside the mesopores and probably on the silica surface, the charge surface of the particles turned to be positive (zeta potential measured around 42 mV), although silicas usually exhibit negative surface charges.

V.3.1.2.2. *Amino acid catalyzed Mesostructured SNP synthesis*

Mesostructured silica nanospheres were synthesized by hydrolysis and condensation of TEOS in an emulsion system containing the silica precursor, water, CTAB and arginine (Arg) under weakly basic conditions, as reported by T. Yokoi *et al.*²⁶

First, we reproduced the optimal synthesis conditions detailed in the publication (*i.e.* TEOS:CTAB:Arg:H₂O = 1:0.13:0.12:2000). However, the deposition of these particles being difficult (§ V.3.2.1.2), we decided to increase particles concentration over 1% wt. by tuning the experimental conditions, to be closer to deposition conditions reported by D. Wang.¹ After several experiments, we prepared silica particles using the following composition TEOS:CTAB:Arg:H₂O = 1:0.07:0.03:250 (Fig. V.8, #2), with a concentration of 1.3% wt. at maximum yield. The average particles size, determined by DLS, was 34 nm (z-average) with a high monodispersity (PDI = 0.11). From SEM pictures (Fig. V.7), particle size was also estimated to about 20 nm. On the SEM picture, the craters at the surface of the particles are clearly visible but it is unclear whether the pores are hierarchically ordered.

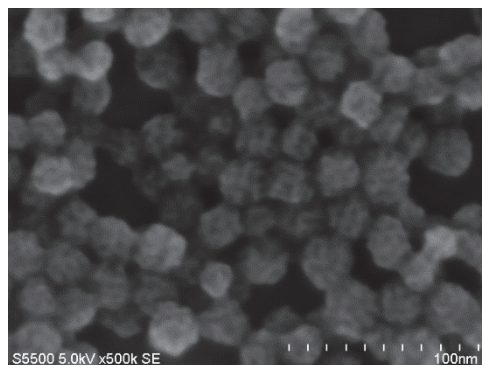


Fig. V.7 – SEM picture of calcined mesoporous SNP. Magnification x 500 k. TEOS:CTAB:Arg:H₂O = 1:0.07:0.03:250.

As shown in Fig. V.8, type IV isotherms were obtained and specific surface area between 370 and 560 m²/g were measured for the particles. Noteworthy, specific surface area seems to be influenced only by the TEOS:Arg ratio: the highest the latter is (conditions #1 and #2), the highest is the surface area. On the other hand, it is mostly independent of the TEOS:CTAB ratio (conditions #1 and #2, or conditions #3 and #4 give similar results). As a result, we favored compositions with higher amounts of Arginine and lower amounts of CTAB. However, the maximal initial amount of arginine was limited as it also plays the role of a weak base and determines the initial and final pH of the solution (for Arg:TEOS ratios over 0.03, unstable solutions with large precipitates were obtained). Similarly, CTAB also plays a crucial role for suspension stabilization, thus the CTAB:TEOS ratio was not reduced under 0.07.

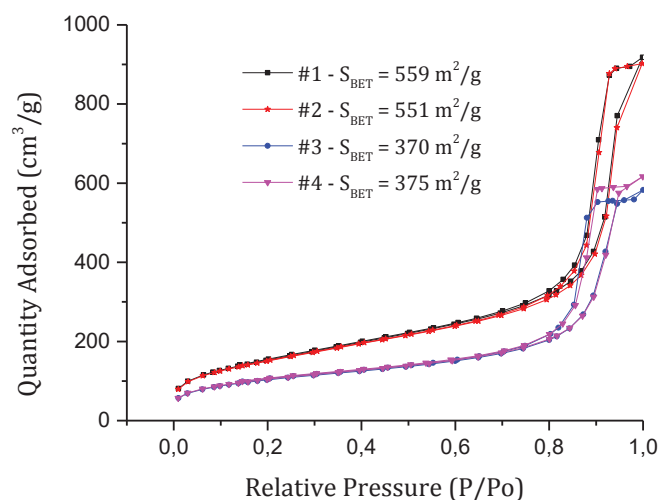


Fig. V.8 – Adsorption isotherms of calcined mesoporous SNP. Formulations are TEOS:CTAB:Arg:H₂O = 1:0.10:0.03:250 (#1), 1:0.07:0.03:250 (#2), 1:0.05:0.015:250 (#3) and 1:0.035:0.015:250 (#4).

Finally, the zeta potential of the as-synthesized particles was measured to 50 mV whatever the pH of the solution (from 3 to 8 adjusted with HCl or NaOH); this positive surface

charge being attributed the presence of CTAB and Arginine. Outside this range of pH, the solution was destabilized and particles formed aggregates.

V.3.2. Mesoporous micro-columns by layer-by-layer deposition

V.3.2.1. LbL deposition with a cationic polyelectrolyte

First, LbL deposition of mesostructured silica nanoparticles was performed with similar deposition conditions as those developed for the commercial LUDOX™ SNPs *i.e.* the use of a the PAH cationic polyelectrolyte as LUDOX™ SNPs have a negative surface charge. However, as mesostructured silica particles exhibited a positive zeta potential (42 mV for core-shell mesoporous SNP, and 50 mV for arginine catalyzed mesoporous SNP) due to the presence of CTAB/arginine, their deposition by LbL process failed.

V.3.2.1.1. Commercial mesoporous silica nanoparticles

LbL coating was first attempted with silica mesoporous nanoparticles purchased from Sigma-Aldrich.³³ The particles were purchased in powder form, and they exhibit an average diameter of 200 nm and pore diameters of 4 nm. Their main advantage was that their zeta potential was negative (measured around -40 mV), however they were quite polydispersed in size, as seen on the SEM pictures in Fig. V.9.a.

Moreover, particles aggregation was also observed and a salt addition (NaCl 3 % and 0.01 % wt.) or filtration in 0.2 μm PTFE filter did not help reducing aggregation. LbL deposition of the particles was however attempted. To maximize the chances of LbL deposition, a saturated particle solution in water was used for coating.

Unfortunately, as shown in Fig. V.9 (b and c), even after 3 deposition cycles a little number of particles were effectively deposited onto the silicon substrate.

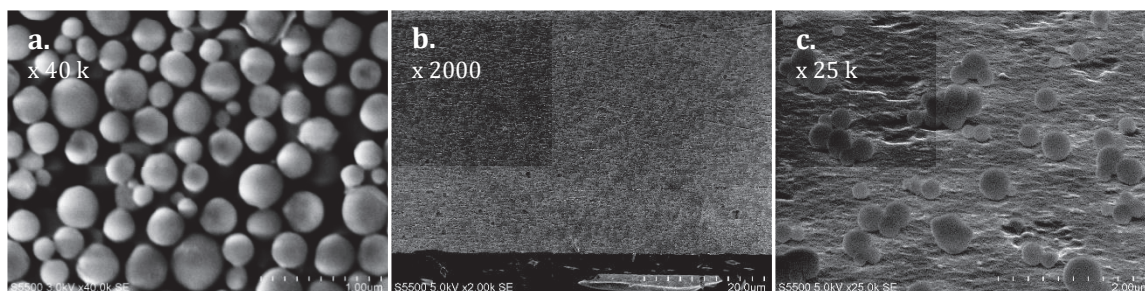


Fig. V.9 – SEM pictures of the commercial mesoporous silica nanoparticles. (a) Commercial mesoporous nanoparticles: the particles are very polydisperse in size. (b and c) Silicon substrate after 3 deposition cycles at different magnification (indicated on the pictures)

Even if it was worth trying the LbL process, this negative result was not surprising because:

- LbL coatings are favored by monodispersed particles,
- The average size of the particles was 200 nm, which is way over the standard size of silica nanoparticles deposited by LbL coating (20 to 50 nm).
- Aggregation of the particles may alter the LbL coating efficiency.

V.3.2.1.2. Core-Shell nanoparticles

We therefore tried to deposit Core-Shell silica particles, which have a narrower size distribution, centered on 100 nm. CTAB removal was undertaken to change their zeta potential back to negative values. The SNPs solution was diluted 10 times in a (1:1 vol.) ethanol:acidic water (pH = 1.25 with HCl) mixture. After one night stirring, the SNPs were washed three times with water by centrifugation. The SNPs zeta potential shifted back to negative values (-40 mV). However, the particles were found to form aggregates after washings. Various strategies were therefore tested to stabilize the SNPS solution: i) addition of a salt, ii) modification of the pH, iii) use of sonication.

Despite those efforts, particles remained partially aggregated and all our attempt to deposit these particles via an LbL process failed. As we had only limited amount of these particles and as their size was still over the standard size of silica nanoparticles deposited by LbL coating (20 to 50 nm), we decided to focus our efforts on arginine catalyzed SNPs.

V.3.2.2. LbL deposition with an anionic polyelectrolyte

After the failure of the LbL deposition with a cationic polyelectrolyte, we decided to use an anionic polyelectrolyte, the polystyrene sulfonate (PSS), to deposit our positively charged nanoparticles and remove these organic materials along with the polyelectrolyte, during the calcination of the film.

We focused our efforts on the arginine catalyzed nanoparticles, as they exhibits similar physical features than the commercial LUDOX™ SNPs (*i.e.* suspension of monodispersed nanoparticle with a size distribution centered at 20 nm).

The standard deposition process was based on the LbL deposition of the LUDOX™ SNPs with PAH. However, as the silica thermal oxide, on top of our silicon substrate, has a negative surface charge, it is not possible to deposit the first PSS layer directly on top of it. Instead, the substrates were first dipped into a Polyethylenimine (PEI) solution (20 mg/mL) for 15 minutes; PEI being a cationic polyelectrolyte which is used routinely with PSS for LbL coatings of polyelectrolytes layers. Then the substrate was alternatively dipped into the PSS

solution (1 mg/mL) and our arginine catalyzed mesoporous SNP solution, with a washing step (three 1 minute long dippings into deionized water) between each step.

Different conditions (dipping reaction times, pH and ionic forces) were experimented to obtain an effective LbL deposition on our silicon substrates. Each time, the quality of the coating (surface coverage, thickness...) was controlled by scanning electron microscopy.

V.3.2.2.1. *LbL deposition of the as synthesized SNPs (arginine use)*

First, the mesoporous SNPs were deposited as synthesized. Silicon substrates underwent 4 LbL deposition cycles. As with LUDOX™ particles, the deposition time of the first cycle was 15 minutes long, and 5 minutes long for the following cycles. The washing steps consisted in 1 minute long bath in deionized water for three times. On one of the substrate, deposition times of 5 minutes long were performed to study the impact of a longer first cycle for the initial layer.

SEM pictures (see Fig. V.10), show that, even after 4 deposition cycles, the coverage of the substrate is not quantitative and the packing of the particles is quite loose. Moreover, the coverage of the first layer of particles is quite low and even weaker for a shorter deposition time (5 min. vs 15 min.).

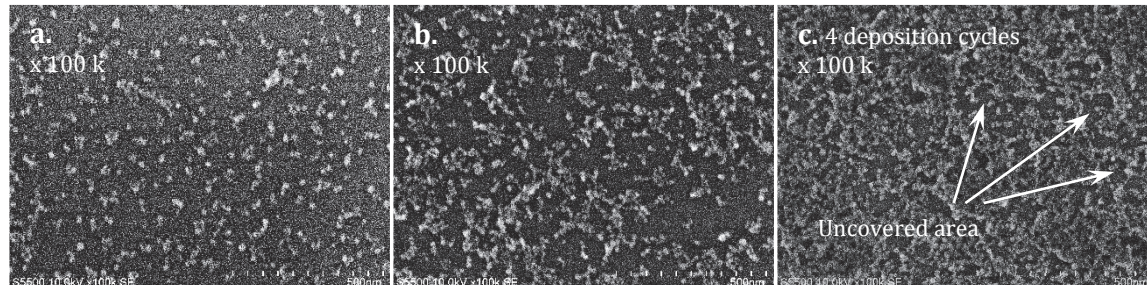


Fig. V.10 – SEM pictures (100 k magnification) of the silicon substrate after 1 deposition cycle of 5 minutes (a) and 15 minutes (b), and (c) after 4 deposition cycles (15 minutes for the 1st, then 5 minutes).

Surface charge (zeta potential) measurements of the substrate between each layer, are represented in Fig. V.11. Surface charge inversion for the PEI layer was for pH slightly over 8, and surface charge is positive. After the addition of a PSS layer, the surface charge effectively changes of sign, becoming negative. Surface charge inversion was shifted to pH slightly under 5. But the addition of a mesoporous SNP layer on top of the PSS layer did not change significantly the zeta potential of the surface: the surface charge inversion is still around 5. This suggests that either the particles layer coverage was too low or that interactions other than electrostatic forces were at stake in this case.

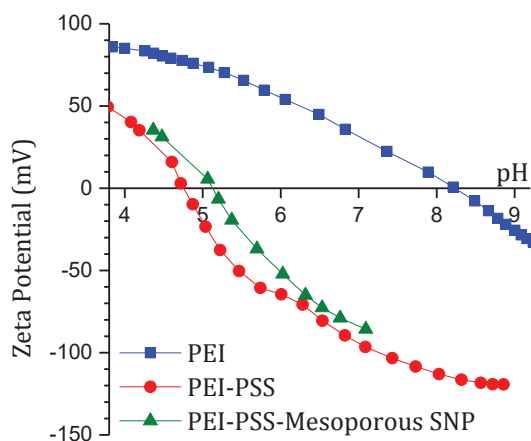


Fig. V.11 – Zeta potential measurements of the silicon substrate surface: 1) after the layer of PEI, 2) after the first layer of PSS, 3) after the first layer of mesoporous SNP.

V.3.2.2.2. Variation of the coating time

The comparison between deposition times of 5 and 15 minutes for the first layer suggested that the nanoparticles deposition was very slow and could be responsible of the deposition failure. With respect to what was observed in classical LbL processes using LUDOX particles of equivalent sizes, the difference in deposition kinetics is probably related to the presence of CTAB/arginine which interact with the polyelectrolyte; such interactions slowing down the the deposition rate.

SEM pictures (see Fig. V.12) show the silicon substrate after one deposition cycle, with SNP deposition times of 30, 45 and 60 minutes. No real difference was observed between the different deposition times, indicating that after 30 minutes, the deposition of the particles was already close to maximum. Although the substrate coverage was much higher than for 15 minutes deposition time (Fig. V.10.b), it was still incomplete and, even after two cycles (Fig. V.12.d), uncovered substrate areas were still be observed.

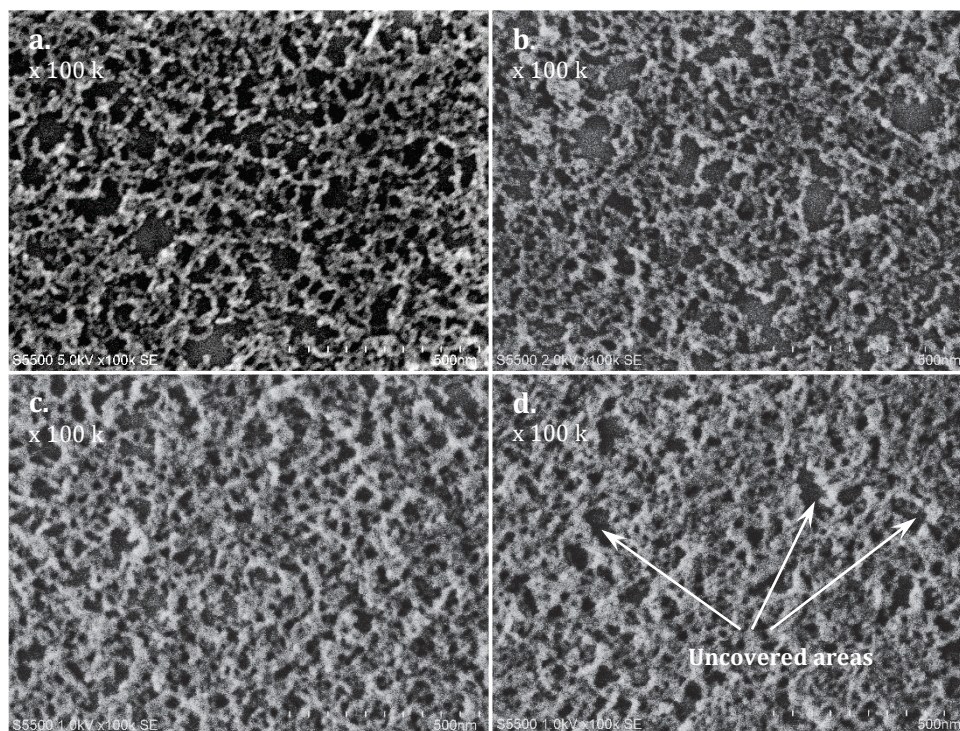


Fig. V.12 – SEM pictures (100 k magnification) of the silicon substrate after 1 deposition cycle, with SNP deposition times of 30 minutes (a) 45 minutes (b), and 60 minutes (c), and after 2 coating cycles with a SNP deposition time of 30 minutes (d).

V.3.2.2.3. Variation of the pH and the NaCl content

Even if longer deposition time could give access to better substrate coverage, deposition times of 30 minutes still lead to relatively sparse mesoporous SNP coatings. These slow kinetics and incomplete coatings can be due to inter-particle repulsion forces. Therefore, we tried to modify the coating conditions (pH or ionic forces) to improve coating within a reasonable coating time.

As other forces than electrostatic ones could be at stake, the pH of the SNP solution was set at 4, in order to be the closest possible to the silica isoelectric point without destabilization of the suspension. Moreover, we added 10^{-1} M NaCl to the suspension to weaken inter-particles repulsion with stronger ionic forces. Such a salt addition noticeably destabilized the nanoparticles suspension (small white flakes became clearly visible to the eye), the coating was tried anyway. Fig. V.13 presents the SEM pictures of substrate with one coating cycle of 15 minutes deposition time at pH 4 with or without the addition of NaCl 10^{-1} M.

At pH 4, the surface charge of the PSS layer changed from negative to positive (Fig. V.11), which should have a repulsive effect on the SNPs, which have also a positive surface charge.

However, no significant difference were observed between depositions at pH 4 or 7, without (Fig. V.13.a is similar to Fig. V.10.b) or with NaCl addition (Fig. V.13.c is similar to b). This suggests that forces other than electrostatic are playing a key role for the SNPs for the deposition.

Noteworthy, the addition of NaCl has clearly an effect on substrate coverage as it changed the aspect of the deposited layer: areas of dense substrate coverage were clearly visible on the SEM pictures (Fig. V.13.c), next to areas with much more sparse coverage.

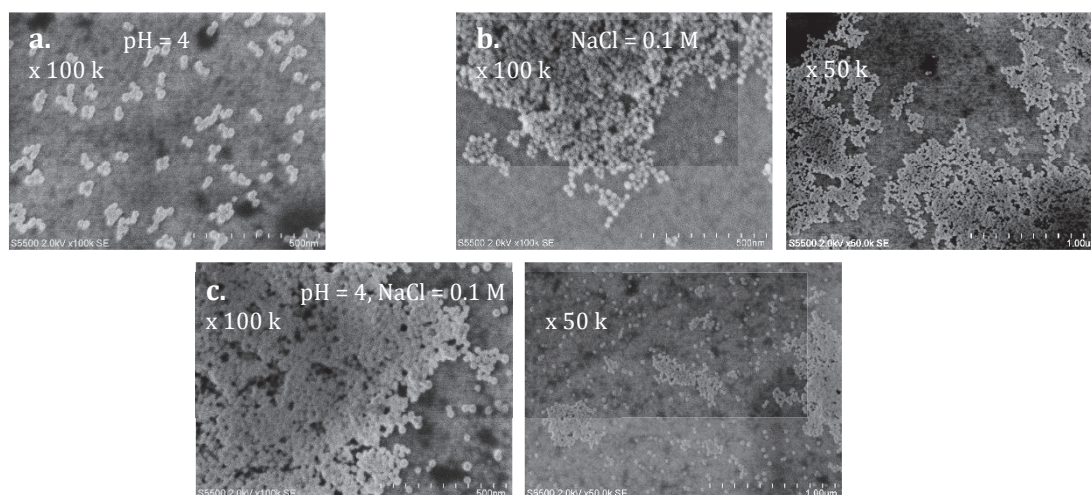


Fig. V.13 – SEM pictures of the silicon substrate after 1 deposition cycle. HCl (until pH = 4) (a and c) or NaCl (0.1 M) (b and c) was added to the mesoporous SNP solution before coating.. Magnification is indicated on the pictures.

Thus, we investigated the influence of NaCl on a larger range of concentrations: from 10^{-2} to 10^{-4} M. At 10^{-2} M, the destabilization effect of the NaCl on the suspension was barely noticeable. Nevertheless, as shown in Fig. V.14, the best coverage of the substrate was obtained for this concentration: although the substrate was still visible, areas of dense coating were more present. At 10^{-3} and 10^{-4} M, the particle coverages were sparser, and similar to those obtained without NaCl addition.

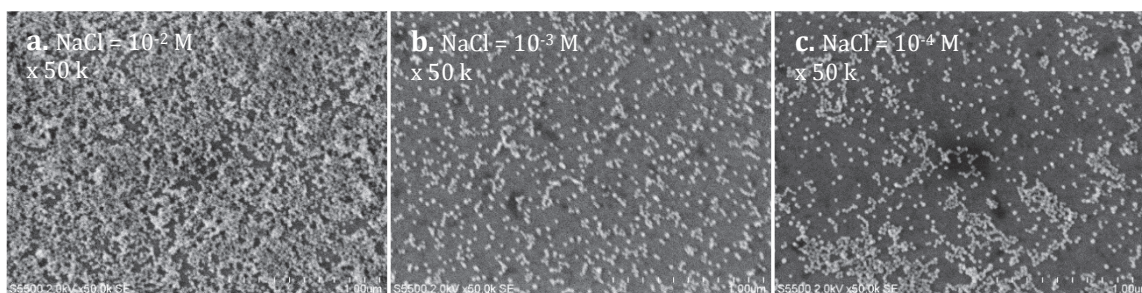


Fig. V.14 – SEM pictures (50 k magnification) of the silicon substrate after 1 deposition cycle of 15 minutes. NaCl 10^{-2} M (a), 10^{-3} M (b) and 10^{-4} M (c) was added to the mesoporous SNP solution prior to coating.

We also measured the surface charge of the substrates after the deposition of one or two layers of SNPs, as shown in Fig. V.15. The surface charge of the substrate after the PEI deposition was positive under pH 8. After the deposition of a PSS layer, it shifted to negative values over pH 5. However, after the addition of a SNP layer, the surface charge is still negative (only slightly less). The same observation can be made after two layers of SNPs. Moreover, No difference in surface charge was observed between a substrate with two layers of SNPs, and a substrate with an additional layer of PSS on top.

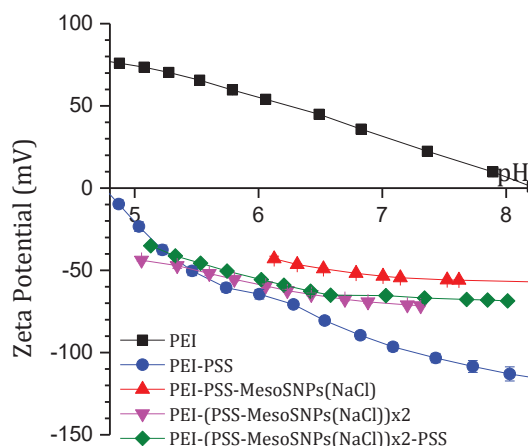


Fig. V.15 – Zeta potential measurements of the silicon substrate surface charge 1) after the layer of PEI, 2) after the first layer of PSS, 3) after the first layer of mesoporous SNP (deposited with NaCl = 10^{-2} M). The measure is repeated 4) after 2 complete deposition cycles, and 5) after the addition of a third layer of PSS.

As the surface charge of the polyelectrolyte layer seemed to play a secondary role, we also tried the same deposition protocol with PAH instead of PSS (and no PEI layer, which is no more necessary). But in this case, the coatings were sparser, even with addition of 10^{-2} M of NaCl to the SNP solution.

V.3.2.2.4. LbL deposition in micro-columns

After experiencing the LbL deposition process on silicon flat substrates, we implemented our protocol to silicon micro-columns. As the presence of aggregates could lead to channel obstruction, two nanoparticles solution were tested: i) One standard solution with the addition of 10^{-2} M of NaCl (already tested on flat silicon substrate) and ii) a second solution, diluted 4 times with deionized water to limit the presence of aggregates, before adding 10^{-2} M of NaCl.

20 deposition cycles were performed on two separate micro-columns with each solution. SEM pictures of both coatings are presented in Fig. V.16 and Fig. V.17, respectively. Despite the presence of aggregates, the coating in the standard conditions was more efficient than the

diluted conditions. In standard conditions, coating was dense (Fig. V.16.d) and the walls were not visible under the coating (Fig. V.16.f), although less than 20 layers were visible on a side view. The coating was approximately 200 nm thick (10 times the diameter of a single particle) and followed the channel profiles (as seen in Fig. V.16.c). Last but not least, the coating thickness was greater at the top corner of the channels (Fig. V.16.e).

Oppositely in diluted conditions, the micro-column walls were still visible through holes in the coating (Fig. V.17.c), the deposited layer was also thinner and more fickle (usually under 100 nm thick), although it still followed the channel profile.

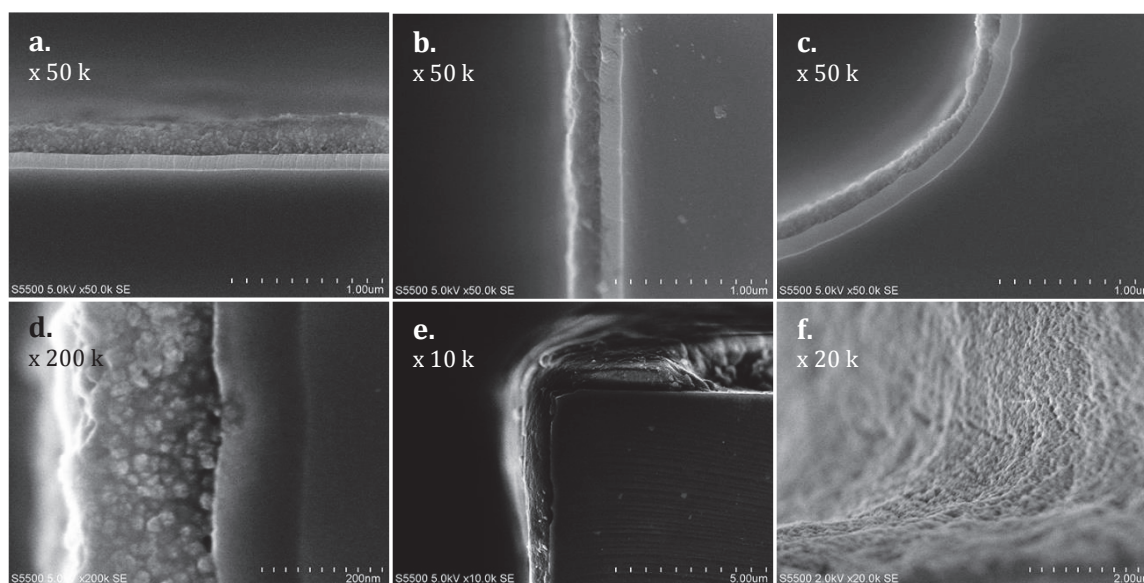


Fig. V.16 – SEM pictures of the coating obtained inside the channels of a micro-column after 20 deposition cycles with PSS 1 mg/mL and arginine catalyzed mesoporous SNP with 10^{-2} M of NaCl. (a), (b) and (c) present respectively the channel bottom, side and bottom corner. (d) is a zoomed picture of the coating, (e) top corner and (f) side view of a channel bottom. Magnification is indicated on the pictures.

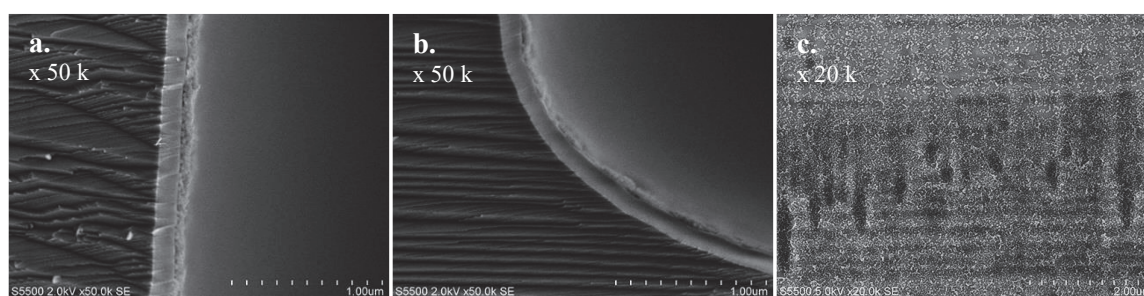


Fig. V.17 – SEM pictures of the coating obtained inside the channels of a micro-column after 20 deposition cycles with PSS 1 mg/mL and arginine catalyzed mesoporous SNP diluted 4 times in deionized water, before addition of 10^{-2} M of NaCl. (a) and (b) present respectively the channel side and bottom corner. (c) Side view of a channel.

Magnification is indicated on the pictures.

Unfortunately, it was not possible to test the chromatographic performances of these micro-columns as the application of the Ordyl® film on top of the chip did not stick correctly, resulting in multiple leaks.

V.3.2.3. Full-wafer mesoporous SNP LbL deposition

To avoid the use of Ordyl® dry film for top sealing, we decided to try a similar process than that developed by D. Wand *et al.*¹

The principle of this process is schematized on Fig. V.18. This process is based on the deposition of a 8 µm thick layer of photoresist on each 200 mm wafer by spin coating. Photoresist is further exposed to UV through a mask, and developed to reveal the channel design. The channels are then etched by anisotropic DRIE (Direct Reactive Ion Etching). Before photoresist removal in acetone with ultra-sonication, the stationary phase is deposited by the developed LbL process, thus no coating is left on the top of the wafer. Then the stationary phase is calcined at 550°C for 5 hours, and the glass top is sealed by anodic bonding (700 V at 400°C). Finally, chips are diced and capillary tubing added for GC connections.

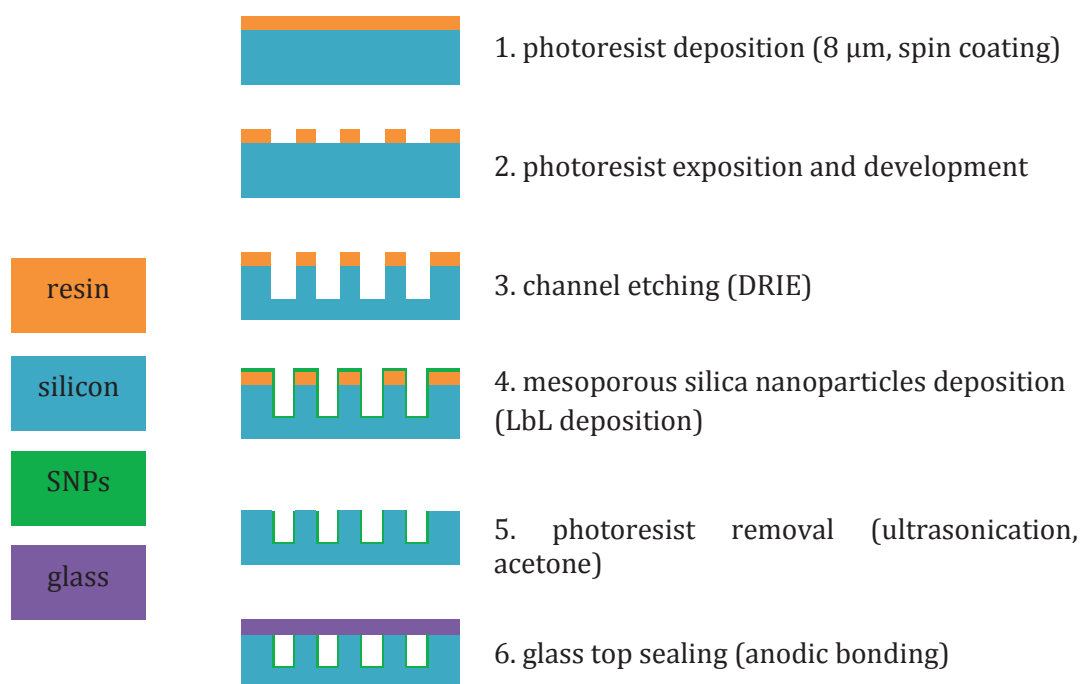


Fig. V.18 – Process flow for the realization of full wafer LbL deposited stationary phase for micro-columns with anodically bonded cover plate.

Unfortunately, the photoresist we used here to protect the top of our wafer appeared to be sensible to the polyelectrolyte solutions and, as a result, peeled off from the wafer during the first stage of the LbL process (see Fig. V.19).



Fig. V.19 – Picture of a wafer after the deposition of the first PEI layer.

To solve this problem, the concentration of PEI solution was decreased (2 mg/mL instead of 20 mg/mL) and a silica layer was added by a molecular vapor deposition process, routinely used in the laboratory on top of the wafer and the photoresist coating. We started with a 20 nm thick silica layer to allow the easy removing of the photoresist. As expected, the photoresist removal was quite easy (several seconds in acetone) but the protection given by the silica layer to the photoresist was barely sufficient: during the first stage of the LbL coating, it peeled off, entirely on one of 2 wafers, and partially on the 2nd wafer (on the top of some walls between channels). A thicker silica layer (50 to 100 nm thick) would have probably given more robustness to the photoresist without drastic difficulty for further photoresist removal.

On top of the silica layer, a PEI layer was deposited, and after rinsing, 15 LbL deposition cycles were performed with PSS (1mg/mL) and mesoporous silica nanoparticles (with NaCl 10^{-2} M). After the coating, the photoresist along with the silica and particles on top was removed by ultrasonication in acetone. Then, the wafer was calcined at 550°C and the glass top was sealed by anodic bonding. Due to the presence of particles between some of the channels, anodic bonding was not perfect on the whole wafer and defects were visible as iridescent halos (see Fig. V.20).

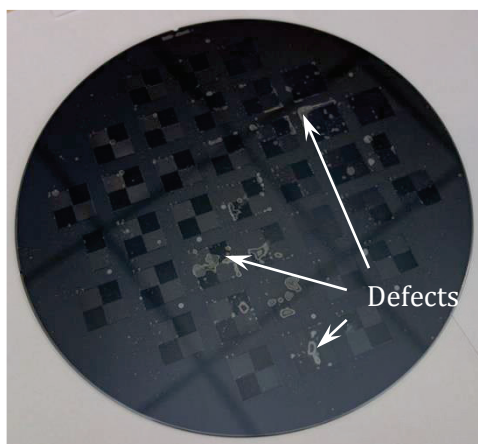


Fig. V.20 – Picture of the wafer after glass cover plate anodic bonding.

Some columns of the wafer were sacrificed for imaging with SEM. On the pictures (Fig. V.21), we can see that the coating was unfortunately not as successful as with individual micro-columns. Most of the wall surface was not covered or only sparsely (Fig. V.21.a). Dense nanoparticles layers were seen on some areas at the top of the channels (in white on Fig. V.21.b and c), coexisting with uncoated areas. Some really thick (800 nm thick) and dense areas were observed at the bottom of the channel (Fig. V.21.d and e). On the median part of the walls, almost no particles were seen (Fig. V.21.g), except really few and small clusters (one of which is shown in Fig. V.21.f).

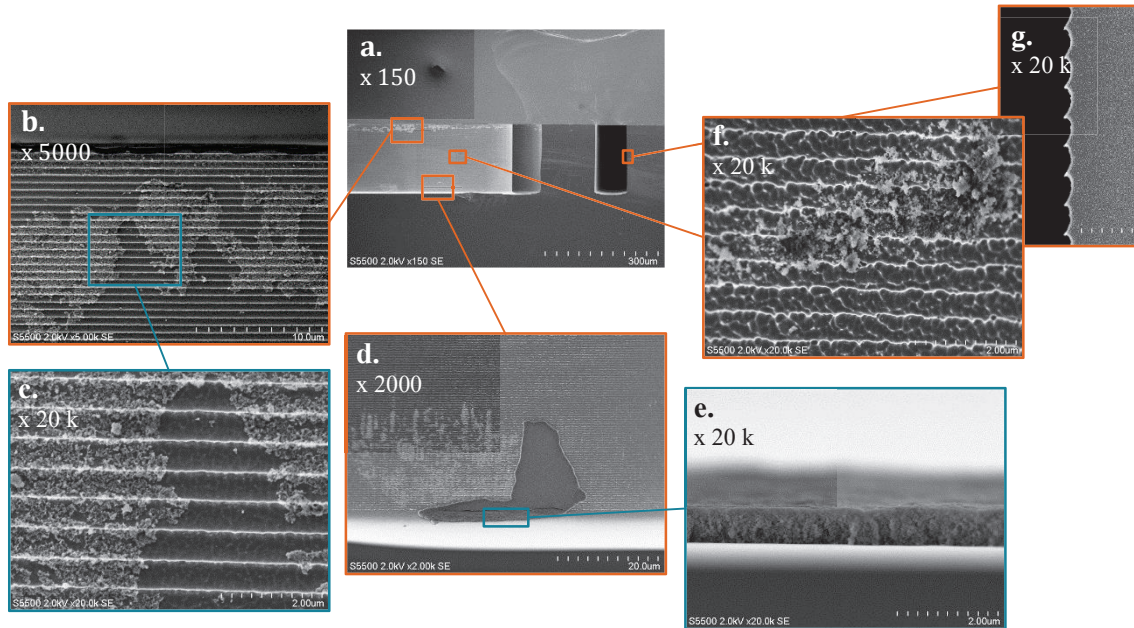


Fig. V.21 – SEM pictures of the stationary phase deposited by LbL full wafer coating. (a) Large view. (b and c) Pictures in the top first 20 μm of the channel. (d and e) Bottom of the channel, and zoom on a coated area. Zoom on a particle cluster (f) and cross section view (g) of the median part of the channel.

Several hypotheses could explain such results:

- Polymer residues from the DRIE process may have change the surface state of the columns and block the LbL deposition. These residues are usually removed by deoxidation and reoxidation steps which were not done on this wafer as it could damage the photoresist.
- The influence of decrease in the concentration of the PEI solution (from 20 mg/mL to 2 mg/mL) may have been underestimated, although it should be sufficient for coating, especially as electrostatic forces may not be the predominant forces at stake.
- For this full wafer deposition, it was not possible to shake the solution during the deposition process as it was usually done (orbital shaker to 80 rpm.) because of

the geometry of the container (flat with low edges). Thus it is possible that particle diffusion was too slow (compared to mixing), and particles only went to the top edge of the channels or sedimented in the bottom as an effect of gravity.

V.3.3. Chromatographic performances

Nevertheless, GC performances of 3 columns without sealing defects were tested. The separation of a mix of methane to n-pentane is shown in Fig. V.22, for various injected concentration. Propane was not retained, and not separated from methane and ethane. However, n-butane and n-pentane were successfully separated. This is very promising regarding the fact that mesoporous SNP were only coated on less than 10% of the surface of the channel walls. If a correct coating of several hundred nm could be achieved, the alkane mixture would certainly be completely separated.

As a result of the stationary phase low coverage, it is also possible to observe the overloading the column with pentane: the peak maxima is shifted to lower elution times as the quantity of pentane injected increases.

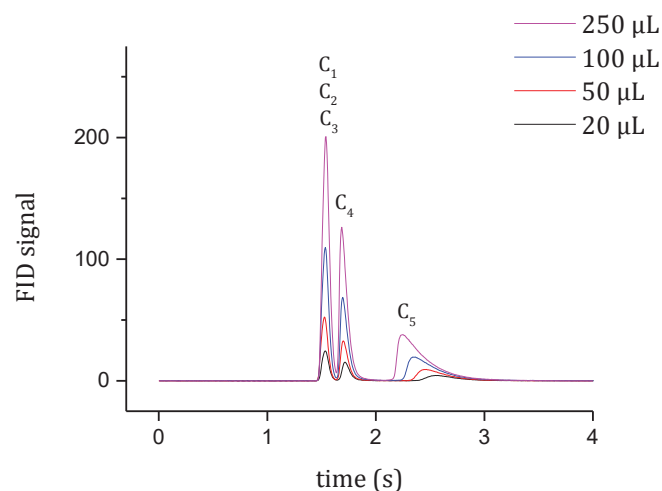


Fig. V.22 – Isothermal (30°C) separation of methane to n-pentane (500 ppm each) at 20 psi. Butane and pentane are separated from the others. The saturation of the stationary phase is clearly visible on the quantity of sample introduced increases.

Interestingly, retention properties of the 3 columns were really similar for the separation of light alkanes. Thus it appears that even if the coatings are not perfect, they appear to be similar in average (integrated over the column length), confirming the potential for repeatability of the process.

V.4. Conclusion

In this chapter, we investigated an alternative process to coat GC micro-columns with a mesoporous silica stationary phase. Instead of synthesizing the porous medium directly into the columns, we explored a method which comprises first the synthesis of mesoporous silica nanoparticles which can be fully characterized, and their further coating into the column by an LbL approach.

In the first part, we rapidly described the LbL process and its application for the deposition of nanoparticles onto substrates.

Using commercially available silica particles, we demonstrated the possibility to use this process for the realization of micro-columns. However, although the chromatographic performances of the micro-columns were encouraging (moderate efficiency and high reproducibility of the separation), the as-developed stationary phases failed to separate light alkanes. This lack of separation could arise from the low specific surface area of the stationary phase coated in the column.

Therefore we focused our efforts into the coating of silicon chips with mesoporous/mesostructured silica nanoparticles. As such, particles were not commercially available with a satisfying narrow size distribution. We therefore synthesized our own particles. Two routes were explored: i) the synthesis of hollow core-shell mesostructured nanoparticles as developed by H. Blas and coworkers,³² and ii) the synthesis of mesostructured silica nanoparticles catalyzed by amino acids as reported by T. Yokoi and coworkers.²⁶ The as-obtained particles had satisfying physical characteristics (narrow size distribution and high surface area) but the cationic SDA needed for mesostructuring modified the particles charge surface and thus their reactivity and the interactions involved in LbL deposition.

Therefore, from unsuccessful LbL deposition with cationic polyelectrolyte, we modified the process to coat mesostructured silica particles onto flat silicon micro-columns: i) An anionic polyelectrolyte was used, ii) experimental parameters such as coating time, pH and ionic forces in the nanoparticles solution were adjusted and iii) NaCl (10^{-2} M) was added to the nanoparticle solution. With these conditions, the coatings were successful on individual silicon micro-columns. They were however not tested chromatographically due to packaging issues.

Specific wafers were fabricated so that the coating could be removed from the top of the wafer, through a photoresist lift-off process, and glass covers could be anodically bonded. Even though, the protecting photoresist did not withstand the deposition process and needed

to be reinforced. Although this step could be improved, micro-columns were successfully fabricated and tested in GC. The results were particularly promising considering that the coating was eventually not optimum. Several ideas were evocated at the end of the chapter to improve the results for future attempts.

V.5. References

1. Wang, D.; Muhammad, A.; Heflin, J. R.; Agah, M. In *Novel layer-by-layer silica nanoparticles as an adsorbent bed for micro-fabricated preconcentrators*, Proceedings of IEEE Sensors, 2012.
2. Wang, D.; Shakeel, H.; Lovette, J.; Rice, G. W.; Heflin, J. R.; Agah, M., *Analytical Chemistry* **2013**, *85* (17), 8135-8141.
3. Iler, R. K., *Journal of Colloid and Interface Science* **1966**, *21* (6), 569-594.
4. Decher, G.; Hong, J. D.; Schmitt, J., *Thin Solid Films* **1992**, *210-211*, Part 2 (0), 831-835.
5. Decher, G.; Hong, J.-D., *Makromolekulare Chemie. Macromolecular Symposia* **1991**, *46* (1), 321-327.
6. Kotov, N. A., *Nanostructured Materials* **1999**, *12* (5-8), 789-796.
7. Laschewsky, A.; Wischerhoff, E.; Denzinger, S.; Ringsdorf, H.; Delcorte, A.; Bertrand, P., *Chemistry - A European Journal* **1997**, *3* (1), 34-38.
8. Taylor, A. D.; Michel, M.; Sekol, R. C.; Kizuka, J. M.; Kotov, N. A.; Thompson, L. T., *Advanced Functional Materials* **2008**, *18* (19), 3003-3009.
9. Srivastava, S.; Kotov, N. A., *Accounts of Chemical Research* **2008**, *41* (12), 1831-1841.
10. Lvov, Y.; Ariga, K.; Onda, M.; Ichinose, I.; Kunitake, T., *Langmuir* **1997**, *13* (23), 6195-6202.
11. Bravo, J.; Zhai, L.; Wu, Z.; Cohen, R. E.; Rubner, M. F., *Langmuir* **2007**, *23* (13), 7293-7298.
12. Wang, F.; Peters, S.; Guzda, J.; Blunk, R. H.; Angelopoulos, A. P., *Langmuir* **2009**, *25* (8), 4384-4392.
13. Antipov, A. A.; Shchukin, D.; Fedutik, Y.; Petrov, A. I.; Sukhorukov, G. B.; Möhwald, H., *Colloids and Surfaces A: Physicochemical and Engineering Aspects* **2003**, *224* (1-3), 175-183.
14. Vallet-Regí, M.; Balas, F.; Arcos, D., *Angewandte Chemie International Edition* **2007**, *46* (40), 7548-7558.
15. Stöber, W.; Fink, A.; Bohn, E., *Journal of Colloid and Interface Science* **1968**, *26* (1), 62-69.
16. Grün, M.; Lauer, I.; Unger, K. K., *Advanced Materials* **1997**, *9* (3), 254-257.
17. Unger, K. K.; Kumar, D.; Grün, M.; Büchel, G.; Lüdtke, S.; Adam, T.; Schumacher, K.; Renker, S., *Journal of Chromatography A* **2000**, *892* (1-2), 47-55.
18. Möller, K.; Kobler, J.; Bein, T., *Advanced Functional Materials* **2007**, *17* (4), 605-612.
19. He, Q.; Cui, X.; Cui, F.; Guo, L.; Shi, J., *Microporous and Mesoporous Materials* **2009**, *117* (3), 609-616.
20. Qiao, Z. A.; Zhang, L.; Guo, M.; Liu, Y.; Huo, Q., *Chemistry of Materials* **2009**, *21* (16), 3823-3829.
21. Yu, M.; Zhou, L.; Zhang, J.; Yuan, P.; Thorn, P.; Gu, W.; Yu, C., *Journal of Colloid and Interface Science* **2012**, *376* (1), 67-75.
22. Zhang, K.; Xu, L. L.; Jiang, J. G.; Calin, N.; Lam, K. F.; Zhang, S. J.; Wu, H. H.; Wu, G. D.; Albela, B.; Bonneviot, L.; Wu, P., *Journal of the American Chemical Society* **2013**, *135* (7), 2427-2430.
23. Davis, T. M.; Snyder, M. A.; Krohn, J. E.; Tsapatsis, M., *Chemistry of Materials* **2006**, *18* (25), 5814-5816.
24. Yokoi, T.; Sakamoto, Y.; Terasaki, O.; Kubota, Y.; Okubo, T.; Tatsumi, T., *Journal of the American Chemical Society* **2006**, *128* (42), 13664-13665.
25. Hartlen, K. D.; Athanopoulos, A. P. T.; Kitaev, V., *Langmuir* **2008**, *24* (5), 1714-1720.
26. Yokoi, T.; Karouji, T.; Ohta, S.; Kondo, J. N.; Tatsumi, T., *Chemistry of Materials* **2010**, *22* (13), 3900-3908.
27. Feng, Z.; Li, Y.; Niu, D.; Li, L.; Zhao, W.; Chen, H.; Gao, J.; Ruan, M.; Shi, J., *Chemical Communications* **2008**, (23), 2629-2631.
28. Davis, S. A.; Burkett, S. L.; Mendelson, N. H.; Mann, S., *Nature* **1997**, *385* (6615), 420-423.
29. Wang, J.; Xia, Y.; Wang, W.; Poliakoff, M.; Mokaya, R., *Journal of Materials Chemistry* **2006**, *16* (18), 1751-1756.

30. Tan, B.; Rankin, S. E., *Langmuir* **2005**, *21* (18), 8180-8187.
31. Wu, X.; Tian, Y.; Cui, Y.; Wei, L.; Wang, Q.; Chen, Y., *Journal of Physical Chemistry C* **2007**, *111* (27), 9704-9708.
32. Blas, H.; Save, M.; Pasetto, P.; Boissière, C.; Sanchez, C.; Charleux, B., *Langmuir* **2008**, *24* (22), 13132-13137.
33. SigmaAldrich
<http://www.sigmaaldrich.com/catalog/product/aldrich/748161?lang=fr®ion=FR>.

Conclusion

The objective of this work, realized in collaboration with the laboratory LC2P2 in Lyon (C2P2: Chemistry, Catalysis, Polymers and Processes), was to study mesostructured silica materials as a stationary phases in micro-fabricated silicon columns. Thus we developed two processes: i) the *in-situ* deposition of a silica sol by dynamic coating directly in capillary or in micro-fabricated columns, detailed in the first part of the manuscript (chapters II to IV) and ii) the layer-by-layer deposition of silica nanoparticles on micro-fabricated columns, detailed in a second part (chapter V).

In chapter I, we briefly presented gas chromatography and highlighted the central role play by the column. We described the Golay theory for columns performances as it was used to compare our work to the state of the art. Finally, we focused our review on GC micro-systems and specifically on micro-fabricated columns as they show great promise for the future of GC.

In chapter II, we studied and optimized the sol-gel thin film coating process. We added a structure-directing agent (SDA), the CTAB, to the sol composition to increase the porosity and generate the structuration of the final stationary phase. We also chose to use a low dilution for the sol to maximize the quantity of silica per volume of sol deposited. The process was found to be more similar to a dip coating process than a spin coating one with respect to the influence of the coating speed on the coating thickness. A high coating speed, obtained with a high pressure flow and a low sol introduction time, led to efficient columns with high retentions. However, a process with an average coating speed was finally favored as it proved much more reproducible: retention coefficient variations of only several percent were observed. It also allowed the fabrication of a double-layer-stationary phase with twice the retention of single layer-stationary phase, without decrease of the efficiency.

Then, in chapter III, we studied the effects of various SDAs and SDA/Si molar ratio on the structuration of mesoporous stationary phases and on the resulting chromatographic properties. Besides chromatographic properties, we tried to gain insight into influence of the physical characteristics of the as-obtained stationary phases onto chromatographic performances by several techniques: SEM, SAXS, gas adsorption. The development of a model powder silica was attempted but unfortunately its physical features were too different from those of the silica coatings. Ordered mesoporous (worm-like, cubic and hexagonal) stationary phases were effectively obtained with CTAB, pluronic F68 and F127 respectively, when a high

SDA/Si ratio was used. However, the chromatographic affinity of the stationary phases with n-alkanes proved to be higher for low SDA/Si ratios for which no silica ordering was observed. Columns obtained with F68 showed similar retention coefficient towards light n-alkanes as commercial Si-PLOT columns, but with a stationary phase 30 times thinner, *i.e.* a 30 times greater affinity.

The transfer of the process to micro-fabricated columns was the object of chapter IV. Due to their particular geometry, the stationary phases could not be perfectly conformal and pooling in the channels corner was observed. Our investigations were however limited to the use of CTAB as SDA since pluronic SDAs could not be removed without damaging the glue used in column packaging. However the obtained micro-columns showed promising efficiencies and the highest number of theoretical plates per meter reported to date for ethane (7500 th.p./m.). They were also used with thermal management for fast and complex separations of natural gas like mixtures.

In chapter V, we investigated an alternative way to coat GC micro-columns with mesostructured silica nanoparticles (SNPs). We demonstrated the possibility to use this process using commercially available nonporous silica particles and a cationic polyelectrolyte. Although the chromatographic performances of the micro-columns were encouraging, the as-developed stationary phase failed to separate light alkanes, possibly because of their low specific surface area. As mesostructured silica nanoparticles were not commercially available with a satisfying narrow size distribution, we focused our efforts on the synthesis of our own particles, following two possible route i) the synthesis of hollow core-shell mesostructured nanoparticles and ii) the synthesis of mesostructured silica nanoparticles catalyzed by amino acids. However, the cationic SDA needed for mesostructuration modified the particles charge surface and thus we had to switch to an anionic polyelectrolyte to promote the SNPs surface adsorption and to adjust the ionic forces of the solution, by adding 10^{-2} M of NaCl. With these conditions in hands, the coatings were successful on individual silicon micro-columns. They were however not tested chromatographically due to packaging issues with the cover plate. Specific wafers were fabricated so that the wafer cover plate could be anodically bonded. The full wafer was successfully coated and micro-columns tested in GC. The results were particularly promising considering that the coating was eventually not optimum.

Overall, this work proved the efficiency of mesostructured silica as a stationary phase for the separation of light alkanes in micro-fabricated columns. It opens up new perspectives for

stationary phase design, especially as the sol-gel process proved to be a quite versatile route, with the possibility of tuning the final pore structure with different possible SDAs. Moreover, as silica is particularly easy to functionalize by silanization reactions with various chemical functions, it could be used as a base for a wide range of separations.

To improve the thin film sol-gel coating throughput, full-wafer coating is to be investigated in a near future. This could be done similarly to capillary coating by coating a longer column, etched in a wafer in such a way that it can be diced into smaller separated columns afterwards.

On the other hand, the alternative use of full wafer LbL deposition for yielding stationary phases was also demonstrated. Gaining insights into the exact mechanism at stake for the coating would be of interest to further extend this process to a wider range of nanoparticles for a gain in versatility.

In future work, thermal monitoring integration should also be considered to propose a faster separation of samples with a wider range of volatility and a lower power consumption. Finally, the integration of the column in a miniaturized system, including an injector and detector, should be studied to propose a complete and compact GC system for on-line LPG monitoring, or other applications.

Appendix A.

Experimental part

Summary

A.1.	Sol synthesis	159
A.1.1.	Acidic water solution	159
A.1.2.	Sol preparation.....	159
A.1.3.	SDA preparation.....	160
A.2.	Stationary phase coating	161
A.2.1.	Coating apparatus	161
A.2.1.1.	<i>Apparatus tubing</i>	161
A.2.1.2.	<i>The vial chamber</i>	162
A.2.2.	Capillary column coating.....	162
A.2.2.1.	<i>Column preparation</i>	162
A.2.2.2.	<i>Column pretreatment</i>	162
A.2.2.3.	<i>Column coating</i>	163
A.2.3.	Micro-fabricated column coating.....	164
A.2.3.1.	<i>Micro-column fabrication process</i>	164
A.2.3.2.	<i>Column pretreatment</i>	164
A.2.3.3.	<i>Column coating</i>	165
A.2.4.	Coating post-treatment.....	165
A.2.4.1.	<i>Sol-gel aging</i>	165
A.2.4.2.	<i>Stationary phase annealing</i>	165
A.3.	Column's characterizations	166
A.3.1.	Chromatographic properties	166
A.3.1.1.	<i>GC setup</i>	166
A.3.1.2.	<i>Results analysis</i>	166
A.3.2.	SEM observations.....	166
A.3.2.1.	<i>Sample preparation</i>	166

A.3.2.2.	SEM measurements.....	167
A.3.3.	SAXS analysis.....	167
A.3.3.1.	Sample preparation.....	167
A.3.3.2.	SAXS measurements	167
A.3.4.	BET analysis on capillary columns	168
A.4.	Powder synthesis (capillary like coating conditions)	168
A.4.1.	Powder BET analysis.....	169
A.4.2.	Powder XRD analysis	169
A.5.	Ludox particles deposition	169
A.5.1.	Solution preparation	169
A.5.2.	Layer-by-layer deposition.....	170
A.5.3.	Micro-column packing.....	170
A.6.	Hollow core-shell mesoporous nanoparticles synthesis	170
A.6.1.	Polystyrene cationic latex synthesis.....	170
A.6.2.	Mesoporous shell synthesis	171
A.7.	Layer-by-layer deposition of mesoporous silica nanoparticles.....	171
A.7.1.	Amino acid catalyzed Mesoporous silica nanoparticles synthesis.....	171
A.7.2.	Mesoporous silica nanoparticles layer by layer deposition.....	172
A.7.2.1.	Solution preparation.....	172
A.7.2.2.	LbL deposition.....	172
A.7.2.3.	Surface zeta penitential measurements	172
A.7.3.	Full wafer deposition	172

Appendix A.

As sol-gel synthesis are easily affected by external conditions such as room temperature and relative humidity, all synthesis were carried out in the lab's clean room. Its temperature, pressure and relative humidity are regulated to 21 ± 0.5 °C and 45 ± 0.5 % respectively.

Unfortunately, sol-gel aging and annealing could not be done in the clean room as no nitrogen inflow was near enough a programmable oven. Therefore, columns were carried to another room at proximity for aging. Once connected to the nitrogen line, the gas is flushed in several seconds, so any water (or other compounds) intake during the transfert should not hinder much the aging.

A.1. Sol synthesis

A.1.1. Acidic water solution

Hydrochloric acid (HCl) standard solution (1 M) was purchased from Sigma-Aldrich®.

0.560 μ L of this solution was added to 9.44 mL of deionized water (from a PureLab station) to obtain 10 mL of an HCl solution in water at pH 1.25.

A.1.2. Sol preparation

Tetraethyl orthosilicate (TEOS), reagent grade, 98%, and absolute ethanol >99.8%, were purchased from Sigma-Aldrich®.

1.8 mL of the HCl solution pH 1.25 was added and mixed to 4.4 mL of ethanol in a round bottom flask. 4.4 mL of TEOS is then added slowly to the flask, under magnetic stirring at 200 rpm. The final molar ratios are TEOS:H₂O:EtOH = 1:5:3.8.

The sol is aged for 1 hour, still under stirring, at 60°C (± 2 °C) in a water bath. A condenser is placed on top of the flask, run by a cool water flow.

A picture of the experimental set-up is presented in Fig. A.1

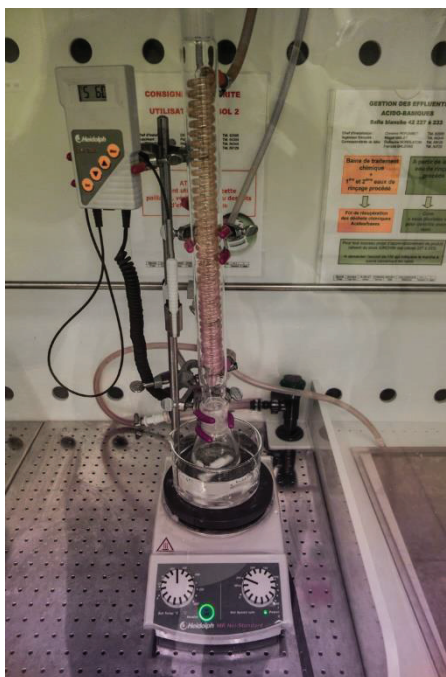


Fig. A.1 – Experimental set-up for the sol preparation

A.1.3. SDA preparation

The SDA used for the sol-gel mesostructure is dissolved in ethanol for at least 30 minutes in an ultrasonic bath. The quantities used depend of the desired dilution of the sol, and of the SDA/Si molar ratio. They are summarized in the table below:

Dilution	EtOH	CTAB/Si	CTAB	F68/Si	F68	F127/Si	F127	P123/Si	P123
D1:2	3 mL	0.14	142 mg	0.010	234 mg	0.010	176 mg	0.0050	81 mg
D1:1	1.5 mL	0.10	102 mg	0.0050	117 mg	0.005	88 mg	0.0025	40 mg
D3:1	0.5 mL	0.075	76 mg	0.0033	78 mg				
		0.05	51 mg	0.0017	40 mg				

Table A-1 – Ethanol and SDA quantities used for the synthesis

The final temperature of the bath (due to ultrasounds) is generally around 35°C, which also helps for the dissolution of some particularly high SDA concentrations.

A.2. Stationary phase coating

A.2.1. Coating apparatus

As seen on the picture Fig. A.2, the coating apparatus that we used is composed of two main parts: i) the apparatus tubing, linking the nitrogen outlet to the ii) vial chamber pressurized by the nitrogen flow and closed by a septum cap through which is connected the column(s) to be coated.

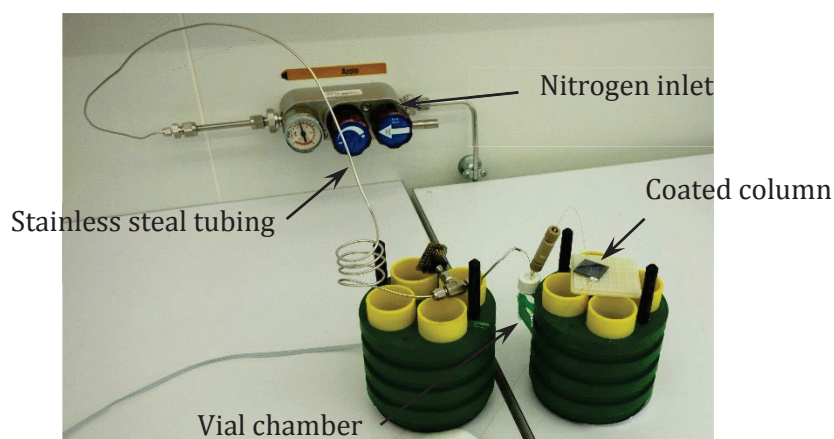


Fig. A.2 - Picture of the coating apparatus.

A.2.1.1. Apparatus tubing

The coating apparatus is composed of a 67 cm long stainless steel tubing (internal diameter 0.5 mm) connected to the nitrogen inlet, equipped with a manometer, on one side and to a junction on the other. The junction is equipped with a pressure sensor and lead to a small 5 cm stainless steel tubing (same characteristics), at the end of which a fused silica capillary is glued.

Unfortunately the pressure sensor was not working properly (nonlinear response under 2 bar, in the region of interest for the study, and signal drift), and was not used. Therefore the pressure was set with the manometer integrated to the nitrogen inlet. As the pressure drop in the tubing part is negligible, the value at the manometer is representative of the pressure in the vial chamber.

For a Poiseuille nitrogen flow, the pressure drop (ΔP) in the tubing part can be calculated:

$$\Delta P = 0.08 \% \text{ (incompressible flow)}$$

$$\Delta P = 0.06\% \text{ (compressible flow, pressure 1 bar)}$$

$$\Delta P = 0.10\% \text{ (compressible flow, pressure 2 bar)}$$

Appendix A.

It is even smaller during coating, as viscosity of the coated liquid is far greater than nitrogen, or for micro-fabricated columns, as they have a greater resistance to flow than capillary columns.

A.2.1.2. The vial chamber

The vial chamber is a 2 mL glass vial, closed by a screw-top cover with a septum.

It may contain a liquid that need to be pushed through the column. An absorbent fabric is placed into the top part of the vial, and used to wipe the column's end when it is removed from the liquid.

Capillaries go into the vial through the septum. Special care must be taken when piercing it not to jam septum pieces into the capillary.

The nitrogen capillary inlet is above the liquid inside the vial. It can be immersed if needed only when pressure is on to control the flow by bubble formations (if pressure is off, liquid could flow upstream with capillary forces).

The column inlet is also inside the vial. If immersed, the liquid is propelled through the column under the pressure gradient; else, it is nitrogen that flow through.

The airtightness of the system was confirmed up to 5 bar, by immersing it into a water bath and looking for bubble formations, and by looking at the manometer needle.

A.2.2. Capillary column coating

A.2.2.1. Column preparation

Flexible fused silica capillary tubing was purchased from Polymicro Technology™. The internal and external diameters of the capillary are given by the manufacturer as $100 \pm 4 \mu\text{m}$ and $363 \pm 10 \mu\text{m}$ respectively. They are composed of a silica core, and a 20 μm thick polyimide coating, given to withstand temperatures up to 400°C.

Column 1.5 m long are cut from the primary bobbin with a ceramic blade. The length of the columns is measured between two marks, and has a precision of $\pm 5 \text{ mm}$ (less than 0.5 % of total length).

A.2.2.2. Column pretreatment

While preparing and aging the sol initial solution, the column internal silica surface is activated (by surface hydration).

An activation solution is prepared from 75 mL of water (deionized water from a PureLab station), 100 mL of ethanol (absolute, >99.8%, Sigma Aldrich®) and 0.7 g of sodium hydroxide anhydrous pellets ($\geq 97\%$, Sigma Aldrich®).

Approximately 1 mL of this solution is placed in a vial, which is pressurized to 1 bar. The capillary column inlet is immersed inside the vial for 35 minutes. Assuming the mixture has a maximum viscosity of 1.2×10^{-3} Po (viscosity of ethanol), this corresponds to a flow of 8.2 $\mu\text{L}/\text{min}$, or 1.6 column volume every minute (55 column volumes in total).

The vial is then replaced by one with water (from PureLab station) and the column is rinsed for 15 minutes. The pressure is the same and the flow is 9.8 $\mu\text{L}/\text{min}$, for a total of 28 column volumes.

Finally, the column is dried with a nitrogen flow at 1 bar for 15 minutes.

A.2.2.3. Column coating

After aging 1 hour at 60°C , the 1.5 mL is pipetted from the sol mother solution and added to the solution of SDA in ethanol. The solution is mixed with a vortex mixer for 10 seconds, and filtrated (Polytetrafluoroethylene membrane, 0.2 μm). Approximately 1 mL of this final solution is placed in the bottom of a vial, which is connected to the coating apparatus.

The pressure is set to the coating pressure (generally 1 bar) and the vial is left still for 5 minutes to achieve pressure stabilization. The column inlet is then immersed for the coating time (generally between 2 and 6 seconds), and finally wiped with the adsorbent fabric.

The column is left for 15 more minutes inside the vial at the same, flushed by nitrogen, then it is unplugged and carried to the oven room.

The coating parameters for the Table II-1 (Chapter II) are as follow:

Conditions	Coating pressure	Coating time
#1	1 bar	1 minute
#2	0.5 bar	1 minute
#3	2 bar	5 sec
#4	1 bar	6 sec

Table A-2 – coating parameters used for the study of dilution influence on column's retention (Chapter II.3.1.2)

A.2.3. Micro-fabricated column coating

A.2.3.1. Micro-column fabrication process

Columns' channel is etched by deep reactive-ion etching (DRIE) in a 540 μm thick wafer. A two steps etching procedure is used to have 200 μm deep channel inlets although GC channel depth is only 80 μm (Fig. A.3.a). Channel is 1,33m long, 80 μm wide and 80 μm in serpentine four-leaf clover design (Fig. A.3.b). The micro-column is then covered by a 200 nm thick thermal oxide, and sealed by a silica glass cover plate by anodic bonding.

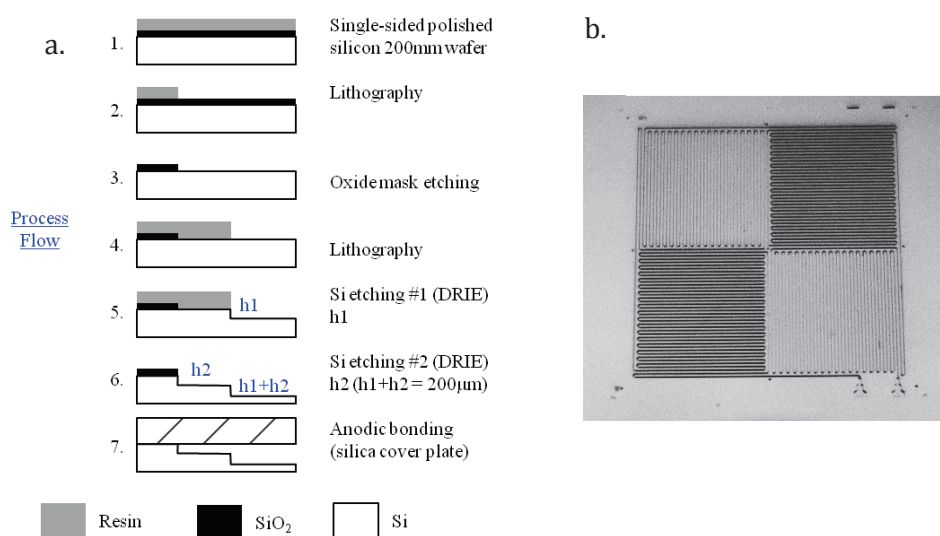


Fig. A.3 – (a) process flow and (b) picture of a column illustrating the serpentine four-leaf clover design

25 cm long fused silica capillaries (100 μm inner diameter and 170 μm outer diameter) are cut with a ceramic blade. Special care is taken to have a particularly clean cut so they will fit more closely to their holes. They are glued using silicon glue, which stay flexible upon drying. The glue is deposited just on the edges of the chip, all around the capillaries, but not in the holes in which they are inserted.

Thus they can be removed and replaced by new uncoated ones before stationary phase annealing. When replaced, the glue is introduced into the holes, giving a much more robust gluing, which can resist a temperature of 250 $^{\circ}\text{C}$ under pressure.

A.2.3.2. Column pretreatment

Micro-column pretreatment is similar to capillary column pretreatment. However, as column resistance to flow is higher, the activation time is also longer: 60 minutes.

In addition, as there are stagnant areas for the flow in the micro-column (channel corners, turns, entries), and it is important to rinse it with more care. Therefore, the rinsing step is 60

minutes long. If there are areas with basic pH remaining in the column, it will make the sol-gel precipitate in the columns and plug it.

Finally, the drying step must also be longer, 30 minutes, as water sticks into the corners of the channel and takes more time to evaporate.

A.2.3.3. Column coating

Micro-column coating is similar to capillary coating. The only difference is that the entry capillary of the column is connected with a short 5 cm long sturdier capillary (100 μm inner diameter and 363 μm outer diameter), which is more adapted to pierce the septum of the vial.

The coating pressure is 1 bar, and the coating time 6 seconds for a typical sol-gel solution with 102 mg of CTAB.

A.2.4. Coating post-treatment

A.2.4.1. Sol-gel aging

The column is connected to a nitrogen line (1 bar) and placed in a programmable oven.

Temperature is increased from ambient to 120°C in 30 minutes, and kept at 120°C for 8 hours. Cooling is not monitored.

A.2.4.2. Stationary phase annealing

Stationary phase annealing process depends on the SDA used for the mesostructure formation:

- If pluronic (F68, F127 or P123) is used, annealing is done in the same oven, still under nitrogen flow, at the same pressure. Temperature is increased to 300°C in 270 minutes (approximately 1°C per minute) and held at 300°C for 12 hours. Cooling is not monitored
- If CTAB is used, columns are directly connected to the GC apparatus. Annealing is done under helium flow (12 psi, 0.84 bar). Temperature is increased to 120°C at 5°C/min, then to 230°C at 1°C/min, it is held at 230°C for 30 min then increased to 250°C at 1°C/min and held at 250°C for 240 min. In this configuration annealing is monitored by following the FID signal.

At the end of annealing, 25 cm of each column end is cut to reduce the total length to 1 meter. Then it is connected to GC apparatus for GC analyses.

A.3. Column's characterizations

A.3.1. Chromatographic properties

A.3.1.1. GC setup

Micro-columns are evaluated on a conventional GC (Agilent 6850 Series II), with a split-splitless injector and a flame ionization detector (FID) both set at 250°C. Helium is used as carrier gas. The temperature of the separations is controlled by the GC oven. Data are recorded by Agilent Chemstation software and exported to be processed with Origin 8.6.

For GC analyses, pressure is set generally to 12 psi for capillary columns or 20 psi for micro-columns. Tedlar bags are filled every two days with a mixture of methane to n-pentane (500ppm of each) in nitrogen from a main bottle provided by Air Liquid. 100 μ L of this mixture is injected with a gastight syringe through the split injector. Split ratio is 500 for capillary columns. For micro-columns, as it is not possible to compute the flow, the split flow is set to 500 mL/min.

A.3.1.2. Results analysis

Result are exported from Chemstation, imported to Origin 8.6 and analyzed with the peak analyzer algorithm. In general, injections were repeated at least 3 times for each column to determine the retention and efficiency of the separation for each species. However, the retention coefficients were highly stable as they did vary from less than 0.1% between injections.

A.3.2. SEM observations

A.3.2.1. Sample preparation

Columns are cut into 8 segments of 12.5 cm. At each segment end, the polyimide coating is removed either with a scalpel blade, or burned with a lighter flame and whipped with a tissue soaked with ethanol.

9 small capillary pieces (one every 12.5 cm) are then cut, approximately 4 mm long, and stuck on a 4 mm by 6 mm piece of silicon with a double-faced carbon scotch tape, parallel to each other, and perpendicular to the large side of the silicon piece.

Appendix A.

A.3.2.2. SEM measurements

SEM observations are realized on the high resolution Hitachi S 5500 scanning electron microscope of the Nanocharacterization Platform at MINATEC. Accelerations voltage is set between 0.5 keV and 2 keV and intensity to 15 mA.

The thickness of the stationary phase inside each columns was estimated from the mean and standard deviation of the nine thickness values measured every 12.5 cm.

A.3.3. SAXS analysis

A.3.3.1. Sample preparation

Two types of sample were prepared for 2 different setups.

- Long capillary segments (10 cm long) with the end stripped from the polyimide coating (with a lighter's flame and ethanol soaked tissue)
- Small capillary segments (approximately 4 mm long) also stripped from the polyimide coating, placed side by side as a mean to be coaxial within each other.

A.3.3.2. SAXS measurements

SAXS measurements were carried out at the ESRF (European synchrotron radiation facility). The wavelength for the measurement was set to 0.0574 nm, and the distance from the sample to the detector to 900 or 1395 mm.

2 setups were investigated:

- Long capillary segments are perpendicular to the beam as illustrated in Fig. A.4.a
- Short capillary segments are presented coaxial to the beam, as illustrated in Fig. A.4.b

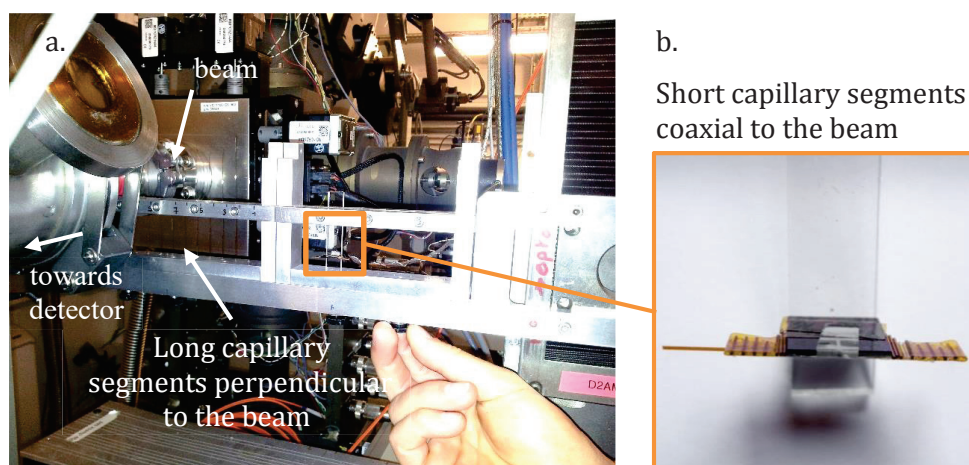


Fig. A.4 - SAXS experimental set-up with capillaries perpendicular (a) or coaxial (b) to the beam.

A.3.4. BET analysis on capillary columns

We tried to do BET analysis directly on the capillary columns, with an ASAP® 2420 from Micromeritics™:

The 1 m long capillary columns were cut in small pieces (approximately 1 to 2 cm long), and introduced in the analysis chamber. It was degased at 150°C for 24 hours under secondary vacuum and analyzed with krypton (as the specific surface is too low for nitrogen analysis).

A.4. Powder synthesis (capillary like coating conditions)

The sol synthesis is the same as for columns:

1.8 mL of the HCl solution pH 1.25 was added and mixed to 4.4 mL of ethanol in a round bottom flask. 4.4 mL of TEOS is then added slowly to the flask, under magnetic stirring at 200 rpm. The sol is aged for 1 hour, still under stirring, at 60°C (\pm 2°C) in a water bath. A condenser is placed on top of the flask, run by a cool water flow.

6 SDA conditions were investigated (SDA is dissolved with ultrasounds for at least 30 minutes in 1.5 mL of ethanol):

CTAB/Si			F68/Si		
0.14	0.10	0.05	0.0100	0.0050	0.0017
426 mg	306 mg	153 mg	702 mg	351 mg	120 mg

Table A-3 – SDA quantities, dissolved in 4.5 mL of ethanol, for powder synthesis.

At the end of sol aging, 4.5 mL of the sol solution is added to the SDA in ethanol, and mixed with a vortex mixer for 10 seconds, and filtrated (PTFE membrane, 0.2 μ m).

The solution is then introduced in a glass container, and introduced in the oven under nitrogen flow Fig. A.5. Temperature is increased to 120°C in 30 minutes and kept at 120°C for 8 hours. Then the cap are closed and the container is placed in a glove box where the powder is gathered and stored for further use.

Powders are placed into high temperature tube furnace, under dry air flow and annealed. Temperature program depends on the SDA:

- For CTAB: 1°C/min until 230°C held for 30 min, then 1°C/min until 250°C held for 240 min. Cooling is not monitored.
- For F68: 1°C/min until 300°C held for 12 hours. Cooling is not monitored.

Powders are gathered in a glove box and stored into vials until further characterization.



Fig. A.5 – Picture of the glass container, placed into the oven for powder synthesis in “column like” conditions.

A.4.1. Powder BET analysis

Powders are degassed at 150°C for 3 days under secondary vacuum and analyzed on the ASAP® 2420 from Micromeritics™.

A.4.2. Powder XRD analysis

Powders XRD analyses are done at the diffractometry center Henri Longchambon at Lyon, on a Bruker D8 Advance diffractometer.

A.5. Ludox particles deposition

A.5.1. Solution preparation

LUDOX® TM50 (50% wt. in water) and Poly allylamine hydrochloride (PAH, $M_v \sim 58,000$), were purchased from Sigma-Aldrich®.

1g of PAH and 5.8 g of NaCl (0.1 M) was mixed in 1 L of deionized water from a Pure-lab station.

1.4 mL of LUDOX TM50 was added to 1 L of deionized water from a Pure-lab station. NaOH (0.1M in water) was added drop by drop until the solution reached pH = 9 (± 0.1).

A.5.2. Layer-by-layer deposition

5 glass crystallizers were filled with approximately 100 mL of the PAH solution, the LUDOX particles solution and deionized water from PureLab station (3 crystallizers).

Silicon substrates were alternately dipped into the crystallizers for several cycles. A cycle consists in the following steps, realized under slow orbital stirring (75 rpm):

- 5 minutes in the PAH solution (15 minutes for the first cycle)
- 1 minute in each water solution
- 5 minutes in the LUDOX particles solution (15 minutes for the first cycle)
- 1 minute in each water solution

The water contained in the 3 crystallizers is replaced each time the substrates are in the LUDOX particles or PAH solutions (twice per cycle).

A.5.3. Micro-column packing

An Ordyl® film was laminated onto glass substrate (of the size of the micro-columns chip), and applied under a metal weight (10 kg, distributed between 2 chips) in an oven at 160°C for one night (16 hours).

Then capillaries are glued at the inlet and outlet of the column with a silicon glue, similarly to micro-columns coated with sol-gel.

A.6. Hollow core-shell mesoporous nanoparticles synthesis

Styrene was purchased from Aldrich (99%) and distilled under reduced pressure before use to remove the inhibitor. Tetraethoxysilane (TEOS, Fluka, >99%), cetyltrimethylammonium bromide (CTAB, Sigma-Aldrich, 99%), ammonium hydroxide (28-30% in water, Sigma-Aldrich), 2,2'-azobis(2-methylpropionamide) dihydrochloride (V50, Aldrich, 97%), and ethanol (VWR, > 99%) were used as received.

A.6.1. Polystyrene cationic latex synthesis

The initiator, 84.5 mg of 2,2'-azobis(2-methylpropionamide) dihydrochloride, was dissolved in 5.50 g of water.

Appendix A.

0.403 g of CTAB was mixed with 175 g of deionized water and 20.1 g of styrene. The biphasic medium was degassed under stirring (300 rpm) by nitrogen bubbling during 30 min and heated up to 90 °C before adding the initiator.

The polymerization was carried out at 90 °C at 300 rpm during 6 h, and the final conversion was 97%. After dialysis against water during 3 days to remove the surfactant and the residual monomer, the PS-cat particles exhibited a z-average diameter of 78 nm measured by DLS and a number-average diameter of 60 nm.

The final solids content was 7.8 % wt.

A.6.2. Mesoporous shell synthesis

3.2 g of CTAB was mixed in 100 mL of deionized water under stirring.

It was added to a solution of 6.0 g of latex particles (7.8 % wt. of solids), 600 mL of deionized water, 199 mL of ethanol and 7.5 g of ammoniac solution (28-30 % wt.), and stirred for 30 minutes at 100 rpm.

5.4 g of TEOS was added drop by drop to the preparation, which was left to react at room temperature for 60 hours. The TEOS/CTAB/NH₃/EtOH/H₂O molar ratio was 1:0.34:5.3:168:1320, and the TEOS/polystyrene weight ratio 11.4.

After the reaction, the particles were concentrated to 2.8 % wt. with a rotary evaporator under vacuum.

A.7. Layer-by-layer deposition of mesoporous silica nanoparticles

A.7.1. Amino acid catalyzed Mesoporous silica nanoparticles synthesis

1080 mg of CTAB and 232 mg of L-arginine (reagent grade, > 98%, Sigma-Aldrich) were mixed in 200 mL of water by ultra-sonication (30 minutes). The solution is then placed under stirring (100 rpm) in a water bath at 60°C for another 30 minutes.

9.6 mL of TEOS were added drop-by-drop to the solution, which was left to react one night at 60°C under vigorous stirring (600 rpm).

The TEOS/CTAB/Arg/H₂O molar ratio was 1:0.07:0.03:250.

Appendix A.

A.7.2. Mesoporous silica nanoparticles layer by layer deposition

A.7.2.1. Solution preparation

Polyethyleneimine (PEI, 50 % wt. in water) and polystyrene sulfonate (PSS, M_w 70,000) were purchased from Sigma-Aldrich.

40 g of PEI solution was placed into a 1 L volumetric flask, and completed to 1 L with deionized water (final PEI content 20 mg/mL).

1 g of PSS was dissolved in 1 L of deionized water.

328 μ L of NaCl (saturated solution in water) was added to the 200 mL of mesoporous nanoparticles solution.

A.7.2.2. LbL deposition

LbL deposition of the mesoporous silica nanoparticles was similar to that of LUDOX particles, except an additional step of PEI deposition (15 minutes and 3 times 1 minute washing) is realized before the first cycle.

Cycles consist in the deposition of a polyelectrolyte layer for 5 minutes, 3 one minute long rinsing steps, the deposition of a nanoparticle layer for 5 minutes and 3 more rinsing step. Deposition and rinsing are done under orbital stirring (75 rpm) when possible (*i.e.* not for full wafer deposition), and deposition times for the first cycle are longer: 15 minutes.

A.7.2.3. Surface zeta potential measurements

To measure the surface zeta potential of the different layers, the coating was also realized on pairs of silicon flat substrates (5mm x 10mm). These substrates were inserted in the cell of the SurPASS Zeta meter from ANTON-PAAR. The gap between the two plates was set as close as possible from 100 μ m and the apparatus measured the streaming current of a NaCl solution of varying pH (adjusted with HCl or NaOH).

A.7.3. Full wafer deposition

Specific wafer were prepared for the LbL full wafer deposition. Columns' channel is etched to 200nm by deep reactive-ion etching (DRIE) in a 540 μ m thick wafer. The photoresist was not removed after DRIE as illustrated in Fig. A.6, but kept so it can be removed with the nanoparticle coating deposited on top of it. Before the LbL deposition, the

photoresist was reinforced by the addition of a 20 nm thick silica layer by molecular vapor deposition.

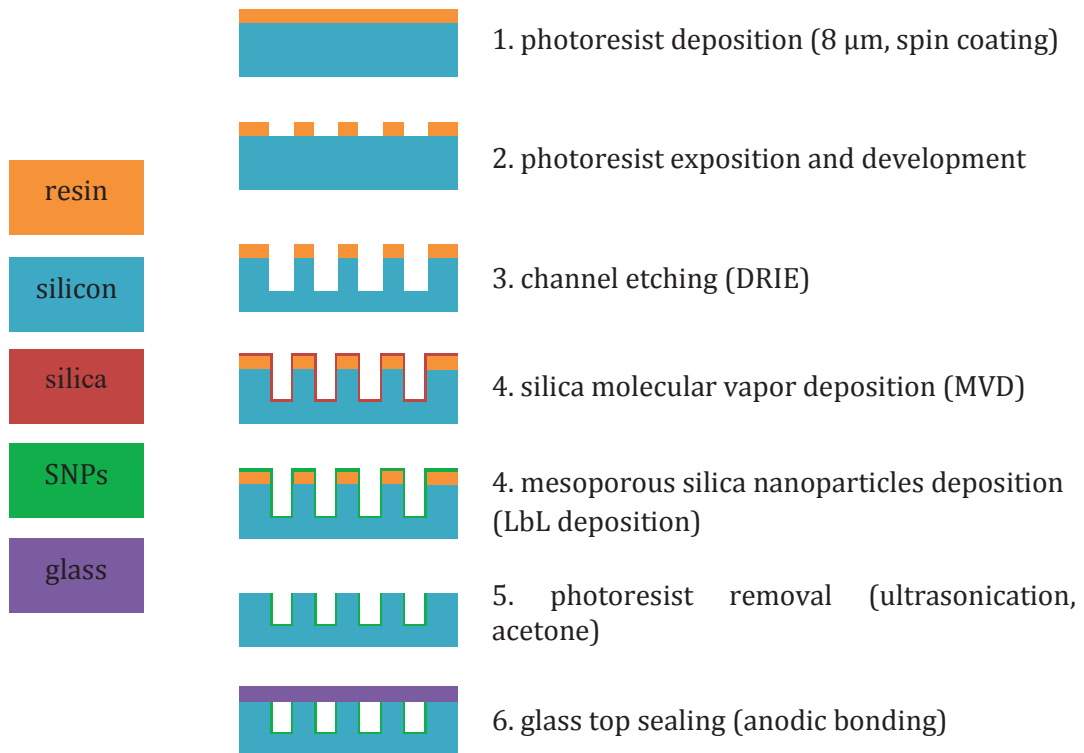


Fig. A.6 – Process flow for the full wafer LbL deposition of mesoporous silica nanoparticles.

After the deposition, the wafer is immersed into acetone and sonicated for few seconds, rinsed with deionized water and dried by spinning. It is then sealed by a glass cover plate by anodic bonding, before 25 cm long fused silica capillaries (100 μm inner diameter and 170 μm outer diameter) are glued to its inlet and outlet.

For full wafer deposition, LbL deposition defers slightly from single chip deposition: the PEI solution for the first layer is less concentrated (2 mg/mL) and there is no orbital stirring during deposition and rinsing.

Appendix B.

Laminar flow through columns

Summary

B.2.	Poiseuille flow through a capillary column	178
B.2.1.	Incompressible flow.....	178
B.2.2.	Compressible flow	179
B.2.3.	Multiple fluid flow.....	179
B.3.	Laminar flow through micro-columns.....	180
B.3.1.	Velocity profile through a rectangular cross section.....	180
B.3.2.	Compressible flow through the micro-column.....	181
	<i>B.3.2.1. Incompressible flow through multiple column segments.....</i>	<i>181</i>
	<i>B.3.2.2. Compressible flow through multiple column segments.....</i>	<i>181</i>
B.3.3.	Micro-column HETP calculation	182
	<i>B.3.3.1. Theoretical model for HETP calculations</i>	<i>182</i>
	<i>B.3.3.2. HETP of a column with multiple segments.....</i>	<i>183</i>
	<i>B.3.3.3. Capillary influence on HETP.....</i>	<i>184</i>
B.4.	References	187

Appendix B.

Assuming that the flow through the column is laminar (Poiseuille flow in the case of a cylindrical capillary column), it is possible to calculate the flow, velocity, travel time *etc.* of a fluid through the column, knowing its geometry.

A flow is generally laminar if its Reynolds number is under 2000, although in some geometries the flow can take various transition forms between a laminar flow ($Re < 1$) and a turbulent flow ($Re > 2000$).

$$Re = \frac{\rho \cdot u \cdot l}{\mu} \quad B.1.$$

Where ρ is the fluid density (approximately 10^3 kg/m³ for liquids and 1 kg/m³ for gas), l the characteristic dimension of the system (here the diameter of the columns, 10^{-5} m), μ the dynamic viscosity of the fluid (generally higher than 10^{-3} Po for liquids, $1.7 \cdot 10^{-5}$ Po for nitrogen and $2 \cdot 10^{-5}$ Po for helium).

Thus, in our case, it is reasonable to assume that the flow will be laminar for fluid velocities (u) inferior to 200 m/s for liquids and 1000 m/s for nitrogen or helium.

B.2. Poiseuille flow through a capillary column

B.2.1. Incompressible flow

For a laminar flow of an incompressible fluid, such as liquids, through a capillary (length L and inner diameter $2r$) under a pressure gradient ΔP , it is possible to calculate easily its following characteristics: flow, F , and average velocity, u .

$$F = \frac{\pi r^4 \Delta P}{8\mu L} \quad B.2.$$

$$u = \frac{r^2 \Delta P}{8\mu L} \quad B.3.$$

For a pressure gradient of 1 bar (10^5 Pa), it corresponds to average velocities of 0.03 m/s for a liquid ($Re = 0.3$), and 1.5 m/s for helium ($Re = 3$).

B.2.2. Compressible flow

As a result of their compressible nature, gas compartments are different from liquids. Their density is proportional to pressure, thus, the gas flow varies through the column: it is lower near the entry where the pressure is higher and the gas denser, and it is higher near the outlet of the column where the pressure is near atmospheric pressure (P_0). Thus the higher is p , the ratio between the inlet and outlet pressure $(P_0 + \Delta P)/P_0$

The flow and velocity at the outlet can be calculated as follow:

$$F_o = \frac{\pi r^4 \Delta P}{8\mu L} \frac{p + 1}{2} \quad B.4.$$

$$u_o = \frac{r^2 \Delta P}{8\mu L} \frac{p + 1}{2} \quad B.5.$$

As a result, the velocity at the outlet is higher than average velocity $\langle u \rangle$ of the gas through the column. It can be calculated as the inverse of the average travel time (T) of a gas molecule through the column.

$$\frac{L}{\langle u \rangle} = T = \int_0^L \frac{dz}{u(z)} = \frac{1}{u_o} \int_0^L \left((p^2 - 1) \left(1 - \frac{z}{L} \right) + 1 \right)^{1/2} dz \quad B.6.$$

$$\langle u \rangle = j u_o \quad \text{where} \quad j = \frac{3p^2 - 1}{2p^3 - 1} \quad B.7.$$

j is called the Giddings-Golay compression factor.

B.2.3. Multiple fluid flow

During column coating, a liquid plug is pushed under constant pressure, P_e , through a column initially filled with nitrogen. In this case, we are confronted to a flow with 2 fluids, one compressible and one not, with different viscosities and length.

By considering that the interface between the two fluids is flat, it is possible to calculate the plug length l , and interface velocity as a function of time t .

$$\frac{dl}{dt} = \frac{r^2}{8\mu_l l} (P_e - P_l) \quad B.8.$$

$$\text{where } P_l = \frac{\mu_g(L-l)P_e}{\mu_l l + 2\mu_g(L-l)} + \sqrt{\left(\frac{\mu_g(L-l)P_e}{\mu_l l + 2\mu_g(L-l)}\right)^2 + \frac{\mu_l l P_0^2}{\mu_l l + 2\mu_g(L-l)}} \quad B.9.$$

Where the index l stand for the liquid, and g for the nitrogen gas whose viscosity at 20°C is $1.75 \cdot 10^{-5}$ Po. As the analytical solution to this problem is not trivial, we used MATLAB to generate a numerical solution.

Knowing the column dimensions, the pressure, and the total time to fill the column, it is possible to access to the viscosity of the liquid. Inversely, knowing the viscosity of the liquid and the introduction time, it is possible to access to the length of the plug and the interface velocity.

B.3. Laminar flow through micro-columns

B.3.1. Velocity profile through a rectangular cross section

Contrary to the simple case of a capillary, where the velocity profile is easy to calculate due to the cylindrical geometry, the velocity profile of a laminar flow through a rectangular (of height h and width w) or square cross-section is less trivial, even if the equation to solve is the same:

$$\Delta_{x,y} u = \frac{1}{\mu} \frac{dP}{dz}, \text{ and } F = \iint u. dx. dy \quad B.10.$$

With the condition that the velocity is null at the walls.

Although we will prefer a numerical solution calculated in COMSOL for the sake of simplicity, this equation has an analytical solution as a Fourier series:¹

$$F = \frac{8 \Delta P}{\mu L} \frac{h}{w} \sum_{n=1}^{\infty} \left(\left(\frac{1}{(2n-1)\frac{\pi}{w}} \right)^4 \left(1 - \frac{2w}{(2n-1)\pi h} \tanh \left(\frac{(2n-1)\pi}{2} \right) \right) \right) \quad B.11.$$

B.3.2. Compressible flow through the micro-column

B.3.2.1. Incompressible flow through multiple column segments

In addition to their rectangular cross section, one has also to take into account the connection capillaries to calculate the flow and the average velocity of the carrier gas through the column. Each part of the column can be considered as a segment. For each segment i , it is possible to calculate the flow as a function of the pressure drop between its extremities:

$$F = \frac{\Delta P_i}{R_i} \quad B.12.$$

$$\text{where } R_i = \frac{8\mu L_i}{\pi R_i^4} \quad B.13.$$

The expression of R_i (equation B.13) is more complicated in the case of the micro-column, and its rectangular cross-section, but it can be calculated as well. As flow conservation is required from one segment to the other, F is constant. Thus, in equation B.12, it is possible to recognize an analogy with an electric circuit of multiple resistor in series, with ΔP_i being the tension, and F the intensity.

Thus, for a column with 3 segments, we have:

$$F = \frac{\Delta P}{R_1 + R_2 + R_3}, \text{ and } \Delta P_i = \frac{R_i \Delta P}{R_1 + R_2 + R_3} \quad B.14.$$

B.3.2.2. Compressible flow through multiple column segments

In the case of a compressible flow, it is no more F that is constant but $P \times F$. This changes slightly the equation but analytical solutions are still simple to get:

$$F_0 = \frac{1}{R_1 + R_2 + R_3} \frac{P_e^2 - P_0^2}{2P_0} \text{ (outlet flow)} \quad B.15.$$

$$\text{and } P_1^2 = \frac{R_1 P_0^2 + (R_2 + R_3) P_i^2}{R_1 + R_2 + R_3}, \quad P_2^2 = \frac{(R_1 + R_2) P_0^2 + R_3 P_i^2}{R_1 + R_2 + R_3}, \quad P_3^2 = P_0^2 \quad B.16.$$

Where P_i is the pressure at the end of the segment i .

It is also possible to calculate the gas velocity inside each segment and the average velocity of the carrier gas for each segment, as a function of the velocity at the outlet $u_0 = F_0/\pi r^2$ (where r is the radius of the outlet capillary).

$$\langle u_1 \rangle = \frac{3}{2} \frac{p^2 - p_1^2}{p^3 - p_1^3} u_0, \langle u_2 \rangle = \frac{3}{2} \frac{p_1^2 - p_2^2}{p_1^3 - p_2^3} u_0, \langle u_3 \rangle = \frac{3}{2} \frac{p_2^2 - 1}{p_2^3 - 1} u_0, \text{ where } p_i = \frac{P_i}{P_0} \quad B.17.$$

$$\text{and } \langle u \rangle = \frac{L_1 + L_2 + L_3}{\frac{L_1}{\langle u_1 \rangle} + \frac{L_2}{\langle u_2 \rangle} + \frac{L_3}{\langle u_3 \rangle}} \quad B.18.$$

B.3.3. Micro-column HETP calculation

B.3.3.1. Theoretical model for HETP calculations

Most of the actual theoretical models for the prediction of HETP (height equivalent to a theoretical plate) in capillary and micro-fabricated columns have been presented in Chapter I. Briefly, the general form of the equation is recalled here (where D_m , D_s , w , d_s and k are respectively the diffusion coefficients of the analyte in the mobile, and stationary phase, the width of the column channel (or its diameter), the stationary phase thickness and the retention coefficient)

$$H = \frac{2D_m}{\langle u \rangle} j f + C_m \frac{w^2}{D_m} \langle u \rangle \frac{f}{j} + \frac{2k}{3(k+1)^2} \frac{d_s^2}{D_s} \langle u \rangle \quad B.19.$$

$$\text{where } j = \frac{3(p^2 - 1)}{2(p^3 - 1)} \text{ and } f = \frac{9(p^4 - 1)(p^2 - 1)}{8(p^3 - 1)^2} \quad B.20.$$

C_m represents the resistance to mass transfer in the mobile phase:

$$C_m = \frac{A + B k + C k^2}{96(k+1)^2} \quad B.21.$$

The values of the coefficient A , B and C depend of the geometry of the column. For a capillary columns, their values are:

$$A = 1, B = 6 \text{ and } C = 11 \quad B.22.$$

For a rectangular geometry, we used the most recent model from H. Ahn and S. Brandani² with coefficients that vary as a function of $\alpha = h/w$:

$$\begin{aligned} \text{with } A(\alpha) &= \frac{32}{35} \left[\frac{6.192(\alpha - 1)^2}{(\alpha - 0.1)^2} + 1.759 \right] \\ B(\alpha) &= \frac{64}{35} \left[\frac{6.192(\alpha - 1)^2}{(\alpha - 0.1)^2} + 1.759 \right] + \frac{32}{5} \left[\frac{3.213(\alpha - 1)^2}{(\alpha + 0.2)^2} + 0.938 \right] \\ C(\alpha) &= 16 \left[\frac{2\alpha^2}{(\alpha + 1)^2} \right] + \frac{32}{35} \left[\frac{6.192(\alpha - 1)^2}{(\alpha - 0.1)^2} + 1.759 \right] + \frac{32}{5} \left[\frac{3.213(\alpha - 1)^2}{(\alpha + 0.2)^2} + 0.938 \right] \end{aligned} \quad B.23.$$

B.3.3.2. HETP of a column with multiple segments

Another form for H is:

$$H = L \frac{\sigma^2}{t_r^2} \quad B.24.$$

Where t_r is the average time for the analyte to go through the column:

$$t_r = (k + 1)t_0 = (k + 1) \frac{L}{\langle u \rangle} \quad B.25.$$

And σ^2 the dispersion of the peak (i.e. the variance of the Gaussian), assumed to have a Gaussian shape. Consequently, the total dispersion of the peak at the end of the column is equal to the sum of the dispersion it acquired in all the segment.

$$\sigma^2 = \sigma_1^2 + \sigma_2^2 + \sigma_3^2 \quad B.26.$$

Where:

$$\sigma_i^2 = \frac{(k_i + 1)^2 L_i}{\langle u_i \rangle^2} H_i \quad B.27.$$

And H_i is calculated with equation B.19, by replacing $\langle u \rangle$ by $\langle u_i \rangle$, p by p_i in the calculation of j and f , and D_m by D_m/p_i (to take into account the compressibility of the gas).

B.3.3.3. Capillary influence on HETP

We developed a MATLAB model, using the equations presented in this section, to calculate the HETP as function of the inlet pressure, for various geometries of columns. In this example, we study the capillary influence on HETP and optimal pressure.

We will interest ourselves to a GC column with 3 segments, like the ones we used:

- One capillary at the inlet without stationary phase ($k = 0$), of various length and diameter.
- A micro-fabricated column of square cross section ($80 \times 80 \mu\text{m}^2$), and 1.33 m long. It is coated with a stationary phase of average thickness 100 nm, k variable (0.1, 1 or 10).
- A second capillary at the outlet, without stationary phase ($k = 0$), of various length and diameter.

B.3.3.3.1. MATLAB code (function names called in the code are in red)

```
%% MAIN
clear all
global gas_Po gas_psi gas_mu gas_Dm gas_Ds

% gas definitions
gas_Po = 101325; % outlet pressure : 1 atm (in Pa)
gas_psi = 6804.6; % 1 psi (in Pa)

% dynamic viscosity of He
gas_mu = 20*10^-6;

% analytes definitions
gas_Dm = 42 * 10^-6; gas_Ds = gas_Dm/100;% diffusion coefficient
gas_k = [0.1, 1, 10]; % retention coefficient

% column definitions
col_aspect = 1; % alpha = h/w
col_L = 1.33; % (in m)
col_w = 80*10^-6; % (in m)

cap_length = 0.25; % (in m)
cap_diam = 100 * 10^-6; % (in m)

var_diameter = [50:25:200] * 10^-6; %in m
var_length = [1:1:50] * 10^-2; %in m

% Initialization
N = zeros (length(var_length),length(var_diameter),length(gas_k),2);
P = zeros (length(var_length),length(var_diameter),length(gas_k),2);
t_0 = zeros (length(var_length),length(var_diameter),length(gas_k),2);
k_app = zeros (length(var_length),length(var_diameter),length(gas_k),2);

% Calculation
for a = 1:length(var_length)
    for b = 1:length(var_diameter)
        for c = 1:length(gas_k)
            [N(a,b,c,1),P(a,b,c,1),t_0(a,b,c,1),k_app(a,b,c,1)] = f_optimum ([0, ...
                col_aspect, 0; var_length(a), col_L, cap_length; var_diameter(b), ...
                col_w, cap_diam; 0, gas_k(c), 0]);
            [N(a,b,c,2),P(a,b,c,2),t_0(a,b,c,2),k_app(a,b,c,2)] = f_optimum ([0, ...
                col_aspect, 0; cap_length, col_L, var_length(a); cap_diam, col_w, ...
                var_diameter(b); 0, gas_k(c), 0]);
        end
    end
end
```

Appendix B.

```
%% function f_optimum (returns Nmax and P optimal as a fonction of the
system geometry)
function [Nmax, Popt, t_0, k_app] = f_optimum( M )
step = 0.1;

P = step;
[Nmax, t_0, k_app] = f_efficiency ( P, M );
N = Nmax-1;

while Nmax > N
    P = P+pas;
    N = Nmax;
    [Nmax, t_0, k_app] = f_efficiency ( P, M );
end

Nmax = N;
Popt = P-pas;
end

%% function f_efficiency (returns the number of theoretical plates N as a
function of the system geometry and the pressure P (in psi))
function [N, t_0, k_app] = f_efficiency( P, M )

[col_P, col_j, col_f, col_uo, col_um] = f_flow ( P, M );

A = length(M(1,:));
t0 = 0;
tr = 0;
sig = 0;
for a=1:A
    if M(2,a) == 0 % no calculation for length = 0
    else
        t0 = t0 + M(2,a) / col_um(a);
        tr = tr + M(2,a) * (M(4,a)+1) / col_um(a);
        sig = sig + f_sig(col_P(a+1), col_j(a), col_f(a), col_uo(a), col_um(a), M(:,a));
    end
end

N = (tr)^2/sig;
k_app = (tr-t0)/t0;
t_0 = t0;
end

%% function f_flow (returns the flow characteristics as a function of the
column geometry and the pressure gradient)
function [col_P, col_j, col_f, col_uo, col_um] = f_flow( P, M )

global gas_Po gas_psi

A = length(M(1,:));

for a = 1:A
    col_R(a) = f_res ( M (:,a) );
end

for a = 1:A
    col_R1 = 0;
    for b = A:-1:a
        col_R1 = col_R1 + col_R(b);
    end
    col_R2 = sum(col_R) - col_R1;

    col_P(a) = sqrt ((col_R1*(1+P*gas_psi/gas_Po)^2+col_R2)/sum(col_R));
end
col_P(A+1) = 1;

Qo = 1/sum(col_R)*(col_P(1)^2-1)*gas_Po/2;
for a = 1:A
    col_j(a) = 3/2*(col_P(a)^2-col_P(a+1)^2)/(col_P(a)^3-col_P(a+1)^3);
    col_f(a) = 9/8*(col_P(a)^2+col_P(a+1)^2)*(col_P(a)^2-col_P(a+1)^2)^2/(col_P(a)^3-
col_P(a+1)^3)^2;
    col_uo(a) = Qo / (f_section(M(:,a))*col_P(a+1));
    col_um(a) = col_j(a) * Qo / f_section(M(:,a));
end
end
```

Appendix B.

```
%% function f_res (returns the fluidic resistance to flow as a function
of the column geometry)
function R = f_res( M )

global gas_mu

if M(1) == 0
    R = 8*gas_mu/pi * M(2)/(M(3)/2)^4;
else
    R = 12*gas_mu * M(2) / (M(1) * M(3)^4 );
    % flow correction factor for side effects (calculated with COMSOL)
    if M(1) == 1
        R = R / 0.42173 ;
    elseif M(1) == 4
        R = R / 0.84244 ;
    elseif M(1) == 8
        R = R / 0.92122 ;
    elseif M(1) == 16
        R = R / 0.96061 ;
    end
end
end

%% function f_section (returns the section of the column segment)
function [ S ] = f_section( M )

if M(1) == 0
    S = pi*M(3)^2/4;
else
    S = M(1) * M(3)^2;
end
end

%% function f_sig (returns the number of theoretical plates N as a fonction
of the system geometry and the pressure P)
function [sig ] = f_sig( col_P, col_j, col_f, col_uo, col_um, M )

global gas_Dm gas_Ds

col_B = col_f * 2 * (gas_Dm/col_P) / col_uo ;
col_C1 = col_f * col_uo * M(3)^2/(gas_Dm/col_P) * f_Cm(M(4), M(1));
col_C2 = (col_j/col_P) * col_uo * 2/3 * M(4)/(1+M(4))^2 * (10^-7)^2/gas_Ds;

sig = (col_B + col_C1 + col_C2) * (1+M(4))^2 * M(2) / col_um^2;
%sig^2=H * (1+k)^2L/<u>^2
end

%% function f_Cm (returns Cm as a function of k and the aspect ratio of
the column / Capillary column : alpha = 0)
function [Cm] = f_Cm( k, alpha )

if alpha == 0
    Cm = (1 + 6*k + 11*k^2) / (96 * (1 + k^2));
else
    g1 = 2*alpha^2 / (alpha + 1)^2;
    g2 = (1.759 + 6.192*(alpha-1)^2/(alpha-0.1)^2);
    g3 = (0.938 + 3.213*(alpha-1)^2/(alpha+0.2)^2);

    A = 32/35 * g2;
    B = 64/35 * g2 + 32/5 * g3;
    C = 16 * g1 + 32/35 * g2 + 32/5 * g3;

    Cm = (A + B*k + C*k^2) / (96 * (1 + k^2) );
end
end
```

B.3.3.3.2. Results

This code gives back two 4 dimensions matrix N and P, which are respectively the maximum number of theoretical plate and associated optimal pressure, which were used for the realization of Fig.IV.10.

The first dimension correspond to the length of inlet or outlet capillary between 1 and 50 cm (the other is fixed to 25 cm), the second dimension to the inlet or outlet capillary diameter between 50 and 200 μm (the other is fixed to 100 μm), the third dimension to the retention coefficient of the micro-column, 0.1, 1 or 10, and the fourth to the inlet or outlet.

The viscosity of the carrier gas was set to $2 \cdot 10^{-5}$ Po, the viscosity of Helium at 30°C. And the diffusion coefficients of the analyte through the mobile phase to $4.2 \cdot 10^{-5}$ m^2/s , which is close to the diffusion coefficient of propane in helium. However, as it is not possible to measure the diffusion coefficients of the analyte through the stationary phase, it was set arbitrarily to one hundredth of the one in the mobile phase.

B.4. References

1. Tabeling, P., *Microfluidique*. Belin: **2003**.
2. Ahn, H.; Brandani, S., *AIChE Journal* **2005**, 51 (7), 1980-1990.